Advances in Digital Breast Tomosynthesis: Image Reconstruction, Artifact Correction, and Dose Reduction

by

John W. Garrett

A dissertation submitted in partial fulfillment of
the requirements for the degree of

Doctor of Philosophy
(Medical Physics)

at the
University of Wisconsin–Madison
2017

Date of final oral examination: May 10, 2017

The dissertation is approved by the following members of the Final Oral Committee:

Guang-Hong Chen, Ph.D., Professor, Medical Physics
Edward F. Jackson, Ph.D., Professor, Medical Physics
Ke Li, Ph.D., Assistant Professor, Medical Physics
Amy M. Fowler, M.D., Ph.D., Assistant Professor, Radiology
Michael A. Speidel, Ph.D., Assistant Professor, Medical Physics

For my family and friends.

Acknowledgements

*"Knowing is not enough; we must apply. Willing is not enough; we must do." - Johann Wolfgang von Goethe (*Wilhelm Meisters Wanderjahre*, 1821)*[i]

It is no exaggeration to say this dissertation would never have been written and that I would never have been in a position to write it without the guidance and support of many people.

First and foremost I would like to thank my advisor, Dr. Guang-Hong Chen. He is a mentor who leads by example, and his enthusiasm, motivation, and creativity are contagious. He has taught me the value of rigorous scientific methodology and always aiming to perform paradigm shifting work rather than settling for incremental progress. He also taught me that to be a successful scientist takes living and breathing science. I will strive throughout my scientific career to continue to follow his advice and strive to change the field of medical imaging for the better.

I would also like to express my gratitude to my dissertation defense committee, Dr. Amy Fowler, Dr. Ke Li, Dr. Edward Jackson, and Dr. Michael Speidel. I appreciate their time and interest taken in my research project, their thoughtful questions and critiques, and their mentorship.

There are many other faculty who have been mentors to me during my time here. I appreciate the Medical Physics faculty whose courses provided the foundation for my research, Dr. Elizabeth Burnside and Dr. Mai Elezaby who patiently answered clinical questions for me as I learned about digital breast tomosynthesis, and all the other professors and clinicians who have offered advice and guidance over the years.

My colleagues in the UW X-ray CT group have been mentors, collaborators, and friends. I thank all of the group members, past and present, who have provided good scientific discussion, advice, and companionship. I would like to specifically thank Yongshuai Ge, Dr. Ran Zhang, Yinsheng Li, and Dr. Ke Li for their tireless support on this project. They spent many hours helping me acquire data, work through implementations, and discussing results; without their help this work would not have been possible.

[i] Original text: "Es ist nicht genug, zu wissen, man muß auch anwenden; es ist nicht genug, zu wollen, man muß auch tun."

My parents, Dr. John Garrett and Dr. Janet Garrett, have supported me and served as an inspiration to me over the years. During my time as a doctoral student (and my whole life prior) they have offered their advice and support. They are my personal and professional role models, and I hope that in my career and life I am able to positively impact as many lives as they have.

Finally, I owe a special thanks to my fiancée, Allison. She is an incredibly caring, patient, and supportive partner. Without her companionship, my life would be unfulfilling.

— John W. Garrett (2017)

Abstract

Advances in Digital Breast Tomosynthesis: Image Reconstruction, Artifact Correction, and Dose Reduction
John W. Garrett

Breast cancer is the second most prevalent cancer, globally, with millions of new cases identified each year. Since the introduction of widespread screening for breast cancer, there has been a steady decline in breast cancer mortality. In order to reliably detect breast cancers, breast screening methods need to offer high spatial resolution, low dose, high patient throughput, and excellent low contrast detectability. Mammography has been the gold standard in breast cancer screening since it was introduced, however many new technologies have emerged recently that offer many additional benefits when compared with mammography. One such method, digital breast tomosynthesis (DBT) builds on existing equipment and techniques used in mammography by incorporating three dimensional (3D) information. Clinically available in the United States since 2011, the addition of DBT has been shown to improve both sensitivity and specificity for breast screening when compared with two dimensional (2D) mammography alone. However, due to the unique requirements of breast imaging, image reconstruction, processing, and analysis for DBT is quite challenging. In this dissertation, several research areas are explored with the overarching goal of improving DBT imaging in a clinical setting. First, a novel image reconstruction algorithm and implementation strategy are introduced for DBT. Second, a technique to assess and understand the anatomical noise in the breast with respect to these new reconstruction methods is described. Finally, a platform-agnostic post-processing technique to reduce image noise and potentially reduce dose for DBT exams is presented. The tools presented in this work have been found to improve through-plane spatial resolution, reduce anatomical clutter, and potentially enable significant dose reduction for DBT. These are all very important steps in providing effective and safe breast cancer screening in the future.

Contents

Tables

Figures

1 Introduction

Breast cancer is the second most prevalent type of cancer, globally, with nearly 1.7 million new cases identified in 2012 alone (almost 12% of all cancers)[1]. In 2013 in the United States alone, around 230,000 diagnoses of breast cancer were made with over 40,000 women dying of breast cancer. In fact, nearly 1 in eight women (and 1 in 1000 men) will develop invasive breast cancer over her (or his) life, which is a staggering figure. Fortunately, there is some good news: since widespread screening for breast cancer began in the 1990s, there has been a steady decline in breast cancer mortality of approximately 2% per year from 2001-2010 according to the Centers for Disease Control and Prevention (CDC)[2]. More recently, a massive study of 400,000 women showed a reduction of greater than 30% in the incidence of stage II+ cancers in women who underwent screening[3]. This decline is attributable to a few factors: improved screening and diagnosis, advances in treatment, and increased awareness.

Due to the prevalence of the disease, contemporary breast cancer research covers a wide range of topics including genomics, diagnosis, treatment, cellular composition, detection, and many more. The majority of breast cancer research currently falls into the following categories: understanding the mechanisms causing breast cancer, determining how to best treat patients presenting with breast cancer, and finding new ways to detect breast cancer in the first place. In this dissertation, the focus is on one of the aforementioned active research areas: the earlier detection of breast cancer by developing improved imaging for breast cancer detection.

The most common imaging modality for breast screening today is x-ray mammography, a modality which provides morphological and anatomical information about breast tissue non-invasively. Mammography is a fast and relatively low-dose x-ray exam that can be performed at very low cost

(average Medicare reimbursement rate for bilateral screening exam ≈ \$170[4]). Mammography has been shown to reduce breast cancer mortality by as much as 30% in women[5] and is the current clinical standard in breast cancer imaging. However, the use of mammography is not without controversy. In Table 1.1, we can see the wide variety of screening guidelines currently provided in the United States. The disparities in these expert recommendations indicate there is still no expert consensus regarding the efficacy of mammographic screening; practically, this means there is no consensus as to the age groups to whom breast cancer screening should be recommended[5–14].

One major reason for this variability in expert consensus is that despite the benefits of mammography, its sensitivity and specificity are inherently limited, especially in radiologically dense breasts. As a result, its use is more challenging and less reliable in patients with dense breasts, breast implants, or following breast surgery[15]. The successful diagnosis of breast cancers at early stages is the goal of breast screening. However, the psychological distress associated with a call back from a screening exam, the potential overdiagnosis of some potentially non-fatal cancers (the labeling of true positive cancer diagnoses as "overdiagnosis" remains another highly contentious point)[16], and the immense cost of follow-up care for women with false positive screening are major

Table 1.1: Expert recommendations for screening mammography from different sources.

Organization	Issued (Year)	Screening ages	Frequency
American College of Obstetricians and Gynecologists[8]	2003	1. 40-49 years; 2. $\geq$ 50 years	1. Every 1-2 years; 2. Annually
American College of Physicians[8]	2007	1. 50-74 years; 2. 40-49 years	1. Every 1-2 years; 2. Individual decision (every 1-2 years, if performed)
National Cancer Institute[8]	2010	$\geq$ 40 years	Every 1-2 years
National Comprehensive Cancer Network[8]	2011	$\geq$ 40 years	Annually
National Health Service, UK[8]	2011	47-73 years	Every 3 years
American College of Radiology[6]	2015	$\geq$ 40 years	Annually
American Cancer Society[7]	2015	1. 45-54 years; 2. $\geq$ 55 years; 3. 40-44 years	1. Annual; 2. Biennial with opportunity for annual; 3. Opportunity to begin annual screening
U.S. Preventive Services Task Force[14]	2016	1. 50-74 years; 2. 40-49 years; 3. $\geq$ 75 years	1. Biennial; 2. Individual decision (every 2 years, if performed); 3. Not sufficient evidence to provide recommendation

issues. In fact, much of the controversy surrounding screening mammography focuses not only on the limited sensitivity of the modality (leading to missed cancers), but rather on the negative impact of false-positive screening results (caused by limited specificity). Thus, improving both the sensitivity and specificity of screening exams is necessary to limit these issues in the future. One measure taken to help alleviate some of these issues is that nearly half of the states in the US have passed legislature requiring that women with mammographically dense breasts be notified that mammograms are less sensitive in this group and that supplemental techniques for screening may be beneficial for patients with elevated risk[17].

In addition to mammography, many additional breast imaging techniques have been developed over the years. One alternative, ultrasound, is commonly used in breast cancer detection and has a specificity and sensitivity comparable to mammography[18]. The advantages of ultrasound include the absence of ionizing radiation and uncomfortable compression, as well as a relatively low cost (average Medicare reimbursement rate for unilateral breast exam including axilla $\approx$ \$110[4]). However, ultrasound is highly dependent on operator experience, and the studies performed thus far suggest that operator expertise may not be reproducible[19,20]. A second modality, breast MRI, was recommended by the American Cancer Society in 2007 for breast cancer screening in high-risk women[21–27]. Studies have consistently demonstrated that although expensive (average Medicare reimbursement rate for a contrast-enhanced breast MRI exam is >\$600 on average[4]), contrast-enhanced MRI may detect breast cancers that are mammographically and sonographically occult. Despite its high sensitivity however, MRI has a high rate of false positive diagnoses[22,27–42]. Additionally, neither MRI nor ultrasound is well suited to the detection of fine micro-calcifications, hindering the early detection of breast cancer. Other attempts to improve sensitivity and specificity of breast cancer diagnosis via functional and molecular imaging techniques using PET and scintimammography[21,28,43] are also under investigation. The various pros and cons of these systems are the major motivation in pursuing additional imaging modalities; a system that is practical for screening applications, but can help improve sensitivity and specificity, simplify breast screening and diagnostic imaging, and eliminate the need to have each patient undergo multiple imaging procedures.

It should be emphasized that mammography is already achieving many of the goals of screening. It is eminently practical, fast, and cheap while still providing high quality radiographic images of

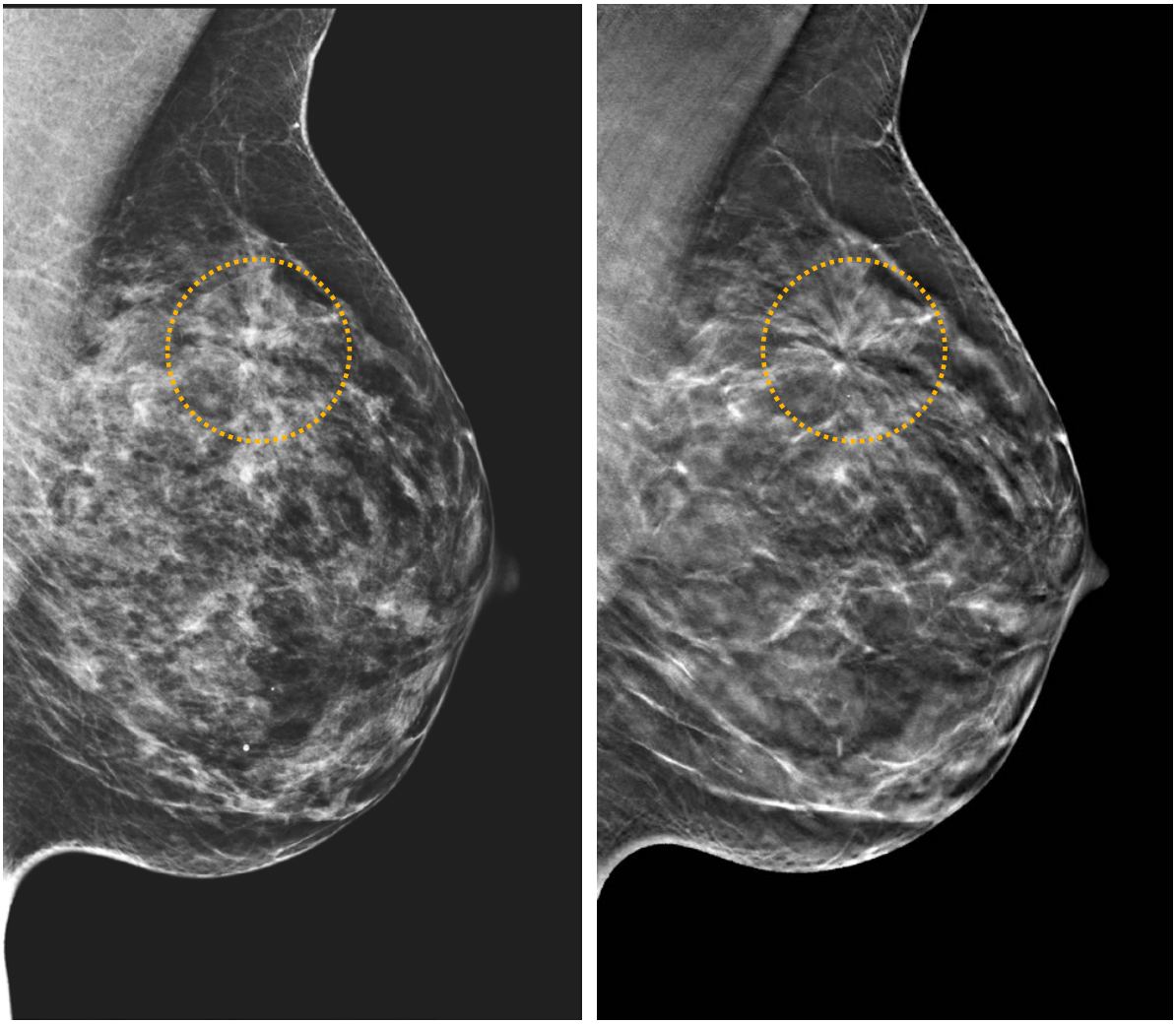

Figure 1.1: An example of the limitations of 2D mammography (a) compared with DBT (b). In the mammogram, the overlapping tissues make it difficult to identify any pathology in the breast parenchyma. In the corresponding slice from the DBT acquisition the overlapping tissues are largely removed, exposing an area of architectural distortion indicated in the dashed circle.

the breast. However, we should point out that standard mammography has two major limitations: 1) It is a 2D imaging modality, and 2) It depends entirely on contrast generated by x-ray absorption. The 2D nature of mammography results in the inevitable superposition of normal breast structures, hindering the detection of lesions and other features of interest [44]. In projection imaging, breast tissues form a low-frequency anatomical noise background, which often dominates other noise sources, such as quantum or electronic noise, and confounds the detection and classification of breast lesions

Table 1.2: Sensitivity and specificity for different breast cancer screening modalities.

Modality	Sensitivity (%)	Specificity (%)
Mammography[80,81]	87	58
DBT+Mammography[80,81]	89	69
DBT+Synthesized Mammography[80,81]	88	71
MRI[42]	61.7-98.4	72.0-79.1
Mammography+US[42]	76	84
Mammography+MRI[42]	84-94	86-95

and microcalcifications[44–46]. Absorption contrast is also problematic in breast imaging as dense glandular tissue in the breast and tumor tissue have very similar linear attenuation coefficients in the diagnostic x-ray regime[47]. As a result, even with artifact-free and low-noise images, the inherent contrast of tumor masses in the breast is limited. To overcome this, radiologists utilize morphology, asymmetry, and longitudinal changes to diagnose malignancies in many cases, although as we have just argued, the anatomical clutter can limit diagnoses based on morphology.

In an attempt to alleviate tissue superposition, recent developments in volumetric x-ray breast imaging methods include digital breast tomosynthesis (DBT)[48–57] (see Figure 1.1) and dedicated breast cone-beam computed tomography (CBCT)[58–66]. Dedicated breast CBCT remains a promising and active area of research, although DBT has already found a home in the clinic and is being used globally. Since DBT is performed using a patient setup and equipment similar to mammography, it is also relatively low cost (average Medicare reimbursement rate for bilateral DBT screening exam is $\approx$ \$230[4]). DBT is currently still used in conjunction with two-dimensional mammograms, however synthesized mammography (generating a single two-dimensional image of the breast from a tomosynthesis acquisition) is an alternative way to provide a 2D overview of the breast[67,68].

There is also a great deal of active research currently attempting to improve contrast for breast cancers with x-ray imaging. This work includes the introduction of exogenous contrast agents[69–73] as well as the introduction of interferometer based x-ray phase contrast imaging[74–79]. These methods have the potential to improve cancer detection with x-ray imaging by boosting contrast, however each comes with its own challenges and limitations that need to be addressed for future clinical translation. A summary of the specificities and sensitivities of the various breast cancer imaging modalities is provided in Table 1.2.

In this dissertation, several research areas will be explored with the overarching goal of improving DBT imaging in a clinical setting. First, several image reconstruction methods and artifact correction schemes will be explored for DBT. Second, a technique to assess the anatomical noise in the breast will be introduced and used to understand how new methods might improve detection performance in digital breast tomosynthesis. Finally, a platform agnostic post-processing technique to reduce image noise and potentially reduce dose for DBT exams will be introduced.

2 Background

X-ray breast imaging is a huge part of modern medicine, with nearly 40 million mammograms performed annually in the United States alone[82]. The goal of x-ray breast imaging is to detect and diagnose pathologies of the breast, most commonly breast cancers. Breast imaging technology is highly specialized and uniquely regulated compared with other diagnostic imaging equipment. In the 1980s, the American College of Radiology (ACR) introduced a mammography accreditation program which had a major impact on the practice of mammography by recommending new minimal standards for both quality control and practice[47]. This program led to the development of specialized phantoms, new imaging equipment, and eventually the emergence of the federally mandated Mammography Quality Standards Act (MQSA) in 1992[47]. Part of the MQSA requirements is that a specific phantom (see Figure 2.1) be imaged weekly, and certain features in that phantom must be visible. This phantom features small and low contrast objects similar to those found clinically, and in addition to routine quality assurance (QA), serves as a useful test object for breast imaging studies. These programs have changed and evolved over the years to keep up with new recommendations from expert panels as well as continuously changing technology.

2.1 Breast anatomy

In a normal breast, there are several anatomical components. Cooper's ligaments form a network of fibrous structures which support adipose background tissue. Suspended in the fatty tissue are a variety of glandular elements. These elements include lactiferous ducts (leading from the nipple), excretory ducts, interlobular ducts, and terminal ducts. The terminal ducts lead into structures known as acini, where milk is produced. The ducts of the breast form a divergent structure branching

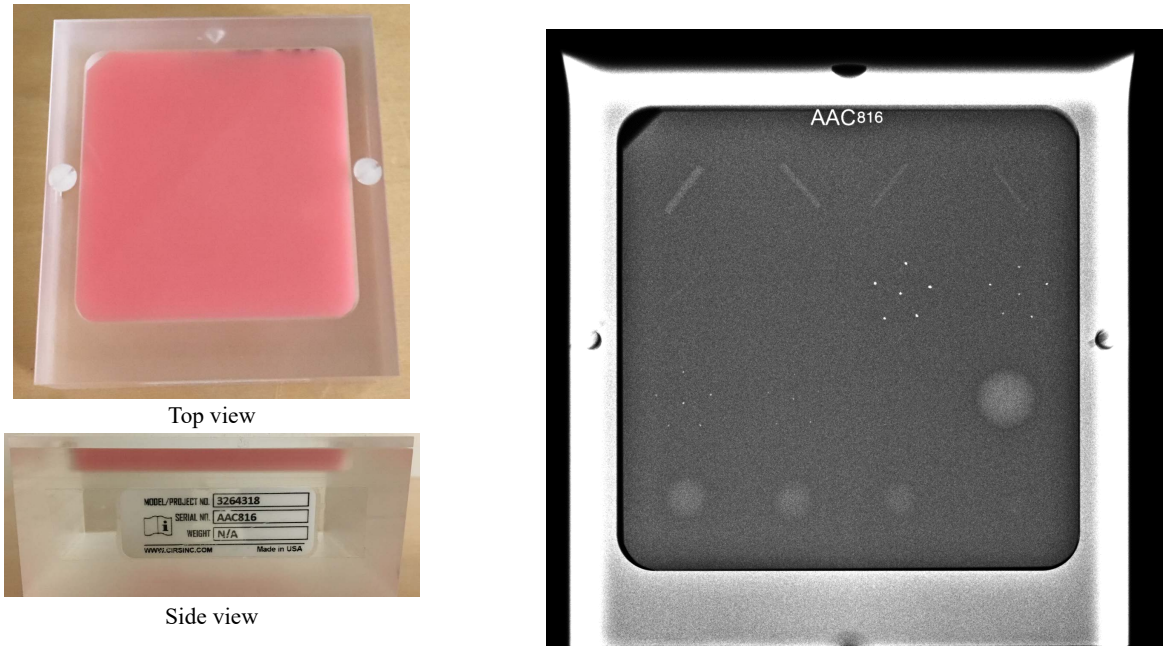

Figure 2.1: The ACR mammography accreditation phantom in our lab (CIRS Model 3254318, CIRS, Norfolk, VA). Both photos (a) and a mammogram (b) of the phantom show the composition of the phantom. The calcifications, masses, and fibers are visible in the mammogram.

outward towards the chest wall from the nipple. This distribution is typically composed of about 15-20 lobes, each of which drains a lactiferous duct. The majority of the dense breast tissue is in the upper outer quadrant of the breast (region nearest to the axilla). Anterior to the pectoralis muscle posterior to the bulk of the glandular tissue is a layer of retroglandular fat. In general, this region should not contain any glandular tissue[83].

The proportion of fatty tissue to glandular tissue in the breast varies, even in normal breasts. In addition to making radiographic imaging more challenging, large proportions of dense breast tissue are also a significant risk factor (5.0 relative risk factor)[8]. Since it is important to assess and classify breast density, the ACR provides a classification scheme to describe the composition of the breast which includes four categories[84]:

(a) The breasts are almost entirely fatty

(b) There are scattered areas of fibroglandular density

(c) The breasts are heterogeneously dense, which may obscure small masses

(d) The breasts are extremely dense, which lowers the sensitivity of mammography

These categories provide a standardized method to categorize breast density. This is especially important when it comes to recommending additional imaging and determining additional breast cancer risk factors for screening patients.

2.2 Mammographic imaging

A standard screening examination consists of four mammograms or DBT acquisitions of the breast [83]. Typically, each breast is imaged in two views, cranio-caudal (CC) and mediolateral oblique (MLO) [83]. On the CC projection, the breast can undergo substantial compression, however the breast tissue adjacent to the chest wall is not always visible. In the MLO view, the compression is typically slightly less, however this view allows for tissue adjacent to the chest wall and in the axilla to be imaged. Normal lymph nodes are commonly seen in the axilla and overlying the pectoralis muscle. One additional advantage of utilizing two approximately orthogonal views is localization. A suspicious feature seen in both views can be stereotactically localized reasonably well, allowing for follow-up imaging with ultrasound or biopsy.

The most common features used to identify breast cancers on mammograms are pleomorphic calcifications and spiculated margins of masses (see Figure 2.2) [83]. Other common features include asymmetry between breasts or longitudinal changes in the breast. Screening images are typically reviewed in such a way that at some point an overview is provided with all four views from the current exam (RCC, RMLO, LCC, and LMLO) as well as all four views from a prior study are visible at once. This allows the radiologist to more easily detect either asymmetry between breasts or changes in the breast since the previous exam. To maximize image contrast, the x-ray beam energy used for breast imaging is very low compared to other radiographic modalities. In addition, digital detectors used for full-field digital mammography (FFDM) have very high spatial resolution, with very good detective quantum efficiency (DQE).

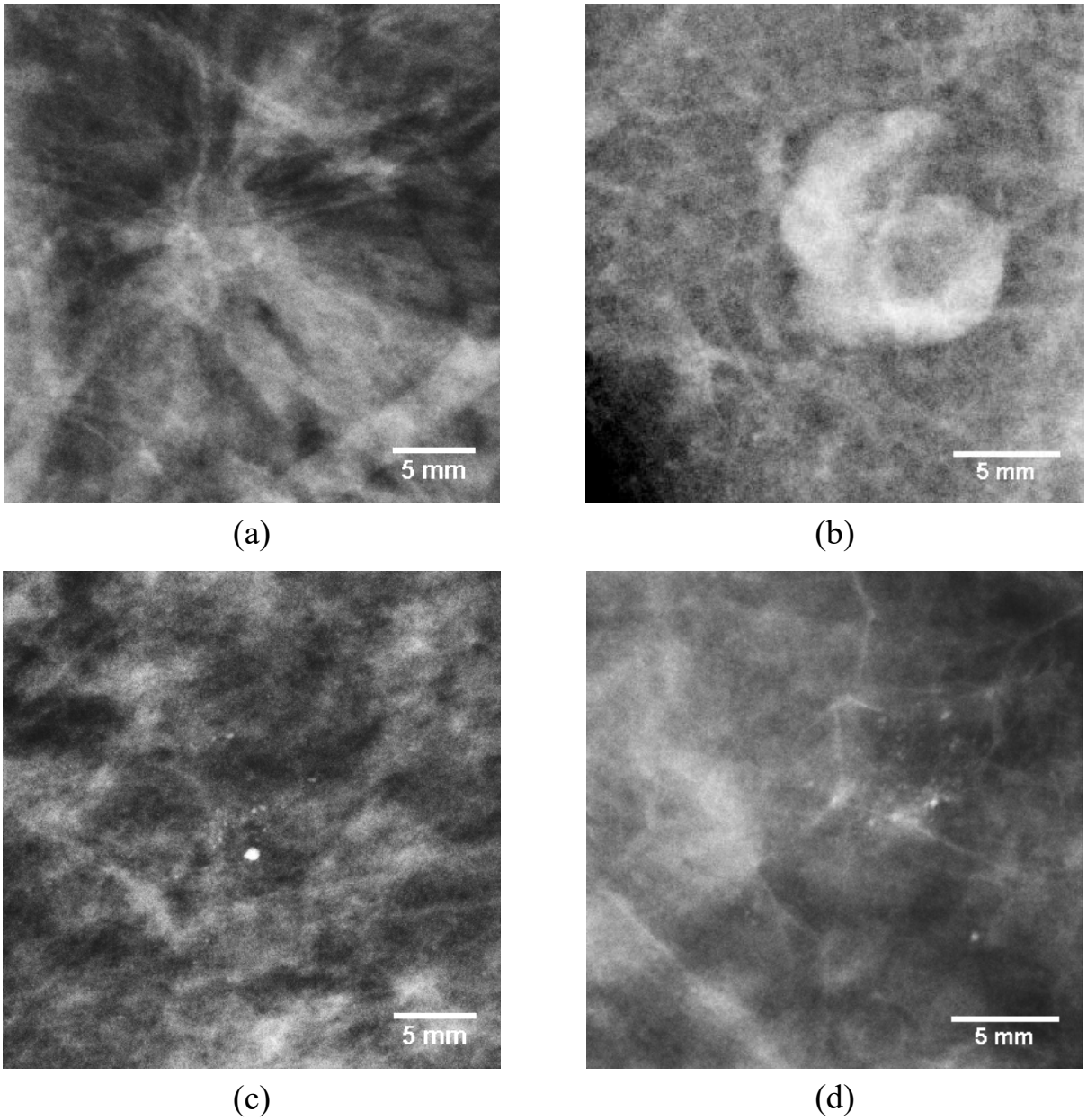

Figure 2.2: Examples of typical features of interest taken from clinical mammograms. The top row provides two examples of mass-like features: a spiculated mass (a) and a well circumscribed lymph node with a fatty hilum (b). The bottom row provides two examples of calcifications: a group of small punctate calcifications (c) and a group of poorly defined pleomorphic calcifications (d).

2.3 Digital breast tomosynthesis

Digital breast tomosynthesis (DBT) is an emerging breast imaging modality that builds on existing equipment and techniques used in mammography by incorporating three dimensional (3D) information[51]. Tomosynthesis is another name for limited view angle tomography, where the gantry is rotated about a limited angular span (typically $< 50°$). The total angular span is referred to as the tomo angle (θ_{tomo}) in this work[i]. Because of the limited angular span required, tomosynthesis can be performed using more conventional radiographic imaging equipment compared with computed tomography (CT). In tomosynthesis, the limited angular span of the acquisition results in limited resolution along the slice direction, but typically offers superior spatial resolution to CT in the plane of the reconstructed slices. In addition, tomosynthesis is very easily performed in conjunction with conventional radiography since the equipment used to perform tomosynthesis is typically standard radiographic equipment with minor modifications[85].

Tomosynthesis was first described in the 1930s by Ziedses Des Plantes[86], however digital detectors had not yet been developed, so a practical implementation of tomosynthesis was not possible when the idea was first conceived. The term "tomosynthesis" was first used in an early paper describing a simple reconstruction method for tomosynthesis by Grant[87] in 1972. Various early forms of tomosynthesis have been developed over the years, such as ectomography[88], which aimed to reconstruct a single slice from many projections with an arbitrary thickness, and flashing tomosynthesis[89], a rapid tomosynthesis technique which was developed to reduce the contrast dose level needed to perform coronary angiography. Tomosynthesis has been applied to many different clinical applications: chest imaging (pulmonary nodule detection)[85,90,91], cardiac imaging (including real-time catheter tracking and anatomical mapping)[92–96], dental applications[97], and, of course, breast imaging.

2.3.1 DBT: State-of-the-art

DBT has been clinically available in the United States since 2011[8], and offers spatial resolution comparable to that of mammography while simultaneously alleviating two major problems inherent

[i] In the literature the tomo angle is sometimes also defined as half the complete angular span.

Table 2.1: System parameters for FDA approved DBT systems in the US.

System	Hologic Selenia Dimensions	GE SenoClaire	Siemens Mammomat Inspiration	Fujifilm ASPIRE Cristalle (HR*)
Date of FDA Approval	02/11/2011	08/26/2014	04/21/2015	01/10/2017
Tomo. angle	15°	25°	50°	15° (40°)
Projection number	15	9	25	15 (15)
X-ray tube motion	Continuous	Step-and-shoot	Continuous	Continuous
Detector motion	±2.1° rotation	Static	Static	Static
Acquisition time	3.7 s	<10 s	21 s	4 s (9 s)
X-ray tube anode material	W	Mo/Rh	W	W
X-ray filter material	Al	Mo/Rh	Rh	Al
Detector type†	a-Se DC	CsI(Tl) coupled to a-Si IC	a-Se DC	a-Se DC‡
Native detector element size	70 μm	100 μm	85 μm	50 μm
Actual detector pixel size	140 μm w/ 2×2 binning	100 μm	85 μm	150 μm w/ 3×3 binning (100 μm w/ 2×2 binning)
Recon. method	FBP	Iterative (ASiR-DBT)	FBP	FBP

* The Fujifilm system may be operated in an additional high-resolution (HR) mode. Values used for this mode are shown in parentheses.

† For the detector type, DC indicates a direct conversion detector and IC indicates an indirect conversion detector. Additionally, the prefix, a- indicates an amorphous (ie. non-crystalline or lacking long range order) structure for the scintillator/semi-conductor.

‡ The Fujifilm detector uses a hexagonal pixel pattern known as hexagonal close pattern (HCP)[100] rather than a square pixel grid.

to two-dimensional (2D) imaging modalities: overlaying structures obscuring important pathology (false negatives leading to decreased sensitivity) and simulating pathology when none is present (false positives leading to decreased specificity)[49,90,98,99]. DBT with clinical equipment was first proposed by Niklason *et al.*[49] in 1997. Since its clinical introduction, DBT has changed the field of clinical breast imaging dramatically. In addition to its impact in the clinic, DBT remains a very active area of research: a recent PubMed search for articles with the phrase "Digital breast tomosynthesis" published since 1997 reveals over 425 publications.

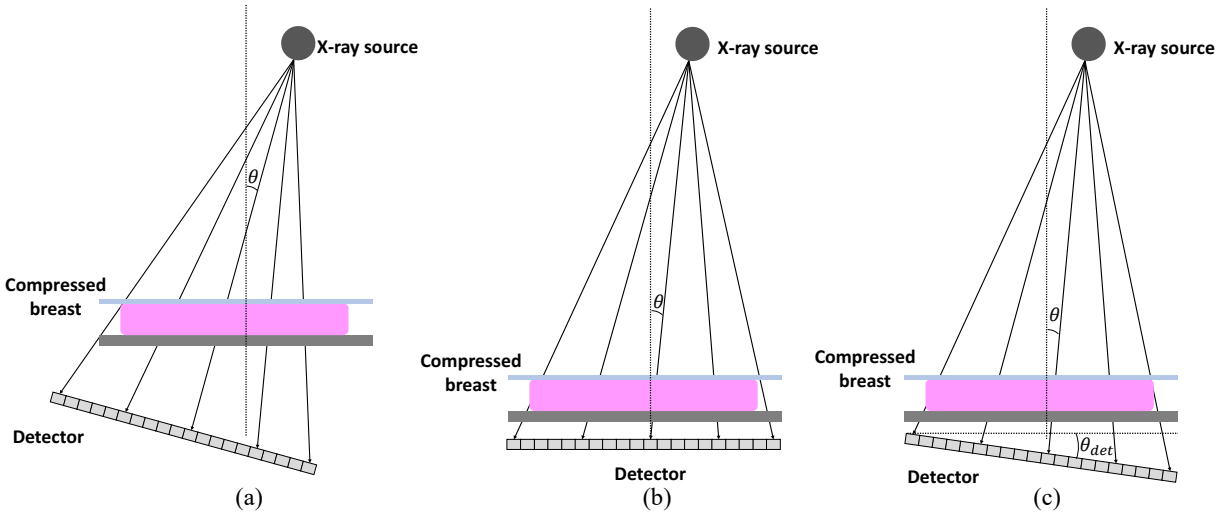

Figure 2.3: Example geometries for DBT systems. The Grossman geometry is shown in (a), while (b) and (c) demonstrate clinically implemented geometries with stationary (b) and semi-mobile (c) detectors.

A summary of current clinical DBT systems with US Food and Drug Administration (FDA) approval[ii] is provided in Table 2.1 [101–103]. The major differences between clinical systems are the angular span of the acquisition (from 15° up to 50°), projection number, continuous vs. step-and-shoot gantry motion, acquisition time (from 3.7 s up to 21 s), detector type, material, and pixel size, reconstruction method, and pre- and post-processing techniques. There are several possible schemes available in clinical systems to perform DBT [90]. If the detector and tube move together, the geometry is known as the Grossman geometry [90]. An illustration of several possible ways to achieve DBT is shown in Figure 2.3.

Unless otherwise specified, all the data used in this work were acquired using a research dedicated Hologic Selenia Dimensions DBT system (Hologic Inc., Bedford, MA) located in 1242 WIMR. This system is shown in Figures 2.4, 2.5, and 2.6. In addition to the information provided in Table 2.1, more details for this system are provided in Table 3.1.

[ii] One other system, the GE Senographe Pristina recently received FDA approval (03/03/2017), however only the 2D component of the system has been approved for use in the United States at this point so we won't consider it here.

Figure 2.4: The Hologic Selenia Dimensions digital breast tomosynthesis unit in 1242 WIMR.

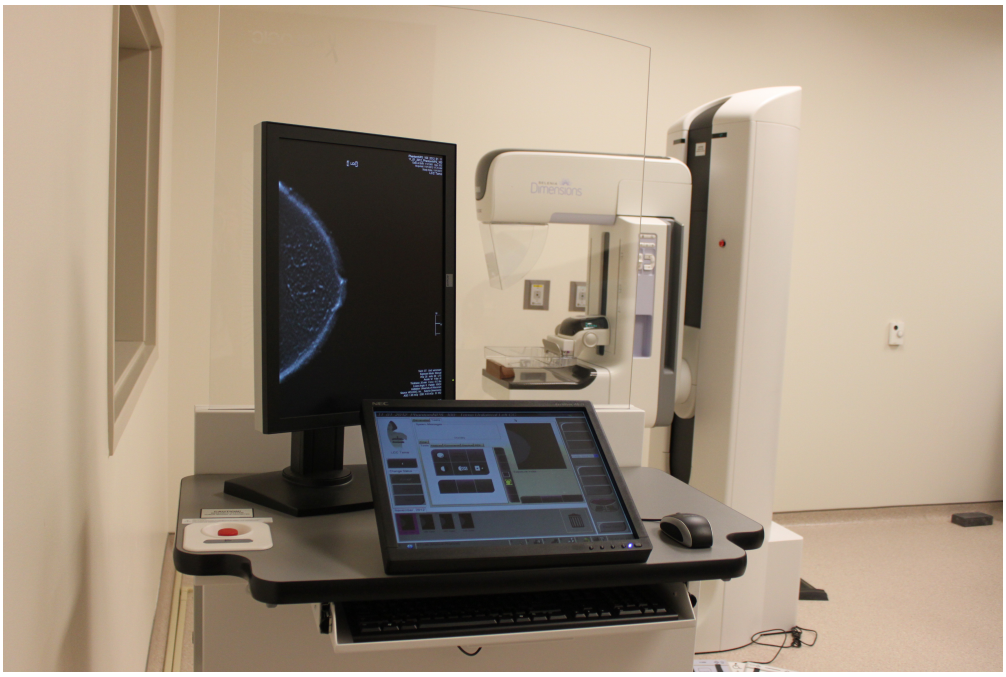

Figure 2.5: The acquisition workstation located in 1242 WIMR used to acquired data using the Hologic Selenia Dimensions DBT unit shown in Fig. 2.4. The display is showing a reconstruction of an anthropomorphic breast phantom positioned on the system.

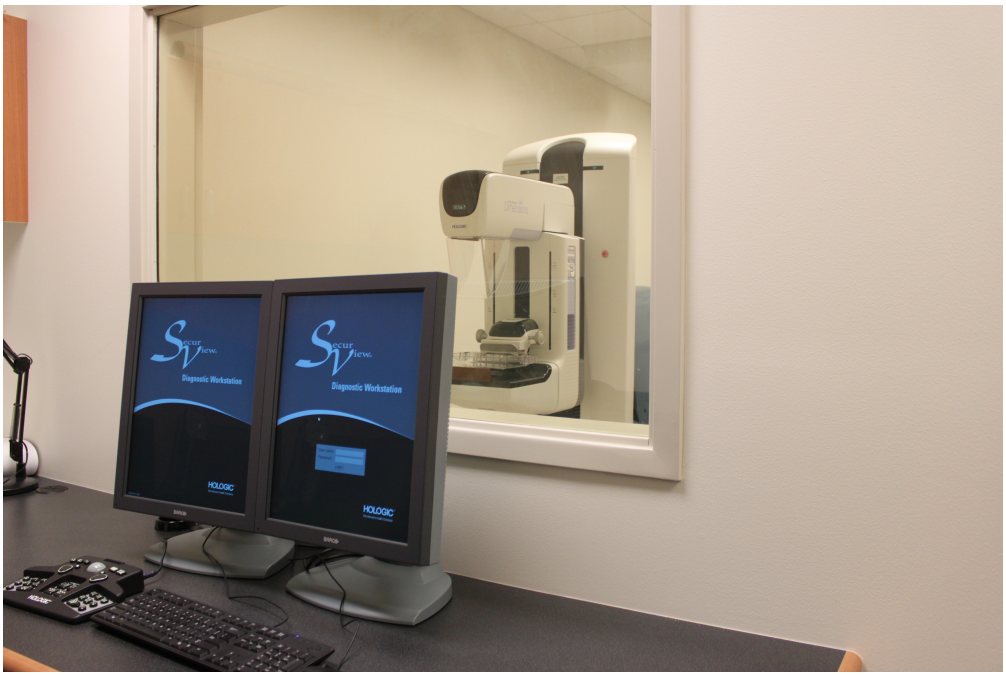

Figure 2.6: The SecurView® workstation located in 1242 WIMR used for image review and analysis.

2.3.2 DBT: Research Systems

In addition to the systems already in clinical practice, a great deal of work is currently being done in research environments. One unique system being developed currently at the University of North Carolina in conjunction with Hologic utilizes an array of carbon nanotube solid-state x-ray sources[104–106]. In this system, no tube motion is required at all. Instead,the x-ray sources (located in a line above the detector) are activated sequentially to achieve different x-ray source positions. This has the major benefit of being able to acquire images very quickly and with no blurring due to motion of the x-ray source during the acquisition. Currently, the nanotube sources are limited in output power, however this is a promising area of research. Another system being developed at the University of Pennsylvania allows for unique x-ray trajectories[107]. In this system, the x-ray tube motion isn't limited to an arc parallel to the chest wall, but is also capable of motion in the anterior-posterior direction. The goal of this system is to eliminate some blurring artifacts and allow for higher resolution reconstructions.

Another unique system is being developed at Philips (Philips Mammography Solutions, Kista, Sweden) using a slit scanning technique and a photon counting detector[108]. The so called, MicroDose SI system has been approved by the FDA for use as a 2D mammography unit[103], however it is also capable of performing tomosynthesis. The photon-counting silicon slit detector has 21 rows, so as the slit is scanned across the object each point in the breast is seen from a variety of relative source/detector positions, so DBT is possible with a tomo angle of $\approx 11^{\circ}$. As far as DBT is concerned, this system is still a prototype, however the unique geometry (slit scanning) and photon-counting detector offer non-trivial benefits of scatter rejection, reduced noise (photon-counting detector can reject electronic noise), and multiple energy levels for single-shot multi-energy imaging.

2.4 Tomographic reconstruction

2.4.1 X-ray data acquisition

X-ray photons are attenuated as they pass through matter, undergoing both scattering and absorption events. Before discussing image reconstruction, a model of x-ray attenuation and detection is needed. We can first define an image object as an energy (ε) dependent function with compact spatial support: $\mu(r;\varepsilon) : r \mapsto \mathbb{R}$ where $\varepsilon \geq 0$ and the object's spatial support is $r \subset \mathbb{R}^3$. The attenuation of x-ray photons along a path $\ell \subset \mathbb{R}^3$ through an object can be described using the Beer-Lambert law[47]:

$$\bar{\mathrm{I}} = \bar{\mathrm{I}}_0 \int_0^{\varepsilon_{\max}} \mathrm{d}\varepsilon \Omega(\varepsilon) e^{-\int_{\ell \cap r} \mu(r;\varepsilon)\mathrm{d}s}, \tag{2.1}$$

where I is the x-ray fluence exiting the object, I_0 is in incident x-ray fluence, and $\Omega(\varepsilon)$ is the normalized x-ray spectrum. If we assume monochromatic photons of energy ε, this can be written in the following form:

$$\bar{\mathrm{I}} = \bar{\mathrm{I}}_0 e^{-\int_{\ell \cap x} \mu(r)\mathrm{d}s}. \tag{2.2}$$

If we divide both sides by the incident x-ray fluence, I_0, and take a logarithm this expression can be written as follows:

$$-\log \frac{\bar{\mathrm{I}}}{\bar{\mathrm{I}}_0} = \int_{\ell \cap r} \mu(r)\mathrm{d}s. \tag{2.3}$$

Equation 2.3 is the fundamental imaging equation for tomographic x-ray imaging, as it tells us the path integrals of the linear attenuation coefficients can be related to the measured x-ray fluence (intensity) at the detector, provided a flat-field (no object present) image is available ($\bar{\mathrm{I}}_0$). In practice, we acquire many measurements over many line integrals, $\{\ell_j \subset \mathbb{R}^3 : j \in [1, N_p]\}$, where N_p is the total number of measurements. Each measurement follows Equation 2.3, and may be written as follows:

$$\bar{y_j} = -\log \frac{\bar{\mathrm{I}}_j}{\bar{\mathrm{I}}_{0,j}} = \int_{\ell_j \cap r} \mu(r)\mathrm{d}s. \tag{2.4}$$

2.4.2 Analytical image reconstruction

If Equation 2.4 is left in its integral form, an analytical solution is possible provided several conditions are met, most notably the so-called Tuy data-sufficiency condition[109]. This analytical solution is known as filtered backprojection or FBP and for many years has been the standard reconstruction method in computed tomography (CT). In FBP, the measured projection data are weighted, filtered, and backprojected. During backprojection, the data are distributed along the x-ray paths calculated using the system geometry.

This analytical process offers several nice features. First, this process can be performed very quickly. A graphics processing unit (GPU) implementation of FBP can reconstruct a single slice CT image (512×512) in less than a tenth of a second[iii] Second, because FBP is a linear procedure, many aspects of the output images can be reliably predicted using linear cascaded systems analysis[110–113]. Thirdly, by modifying the filter used for FBP reconstruction different image characteristics may be achieved.

Unlike traditional CT, tomosynthesis is inherently an under-determined problem. In CT, the Tuy data sufficiency condition requires that at least a short scan is completed (with parallel beam geometry this is 180° or with fan beam geometry 180°+ fan angle)[109]. If this condition is satisfied, the Fourier Slice theorem[114] tells us that Fourier space is filled approximately isotropically, in a radial fashion with denser sampling at lower frequencies and sparser sampling as the radial frequency increases (see Figure 2.7). As a result, approximately isotropic voxels can be reconstructed, resulting in true 3D reconstructions. In tomosynthesis on the other hand, the Fourier domain is incompletely sampled (see Figure 2.7). As a result, the reconstructed voxels are highly anisotropic. To counteract this incomplete sampling, the reconstruction method used should be modified for tomosynthesis, as the assumptions made in conventional FBP reconstructions are no longer valid.

[iii] This timing reflects my own implementation of the FBP algorithm, performed on my local workstation rather than timing for a clinical system.

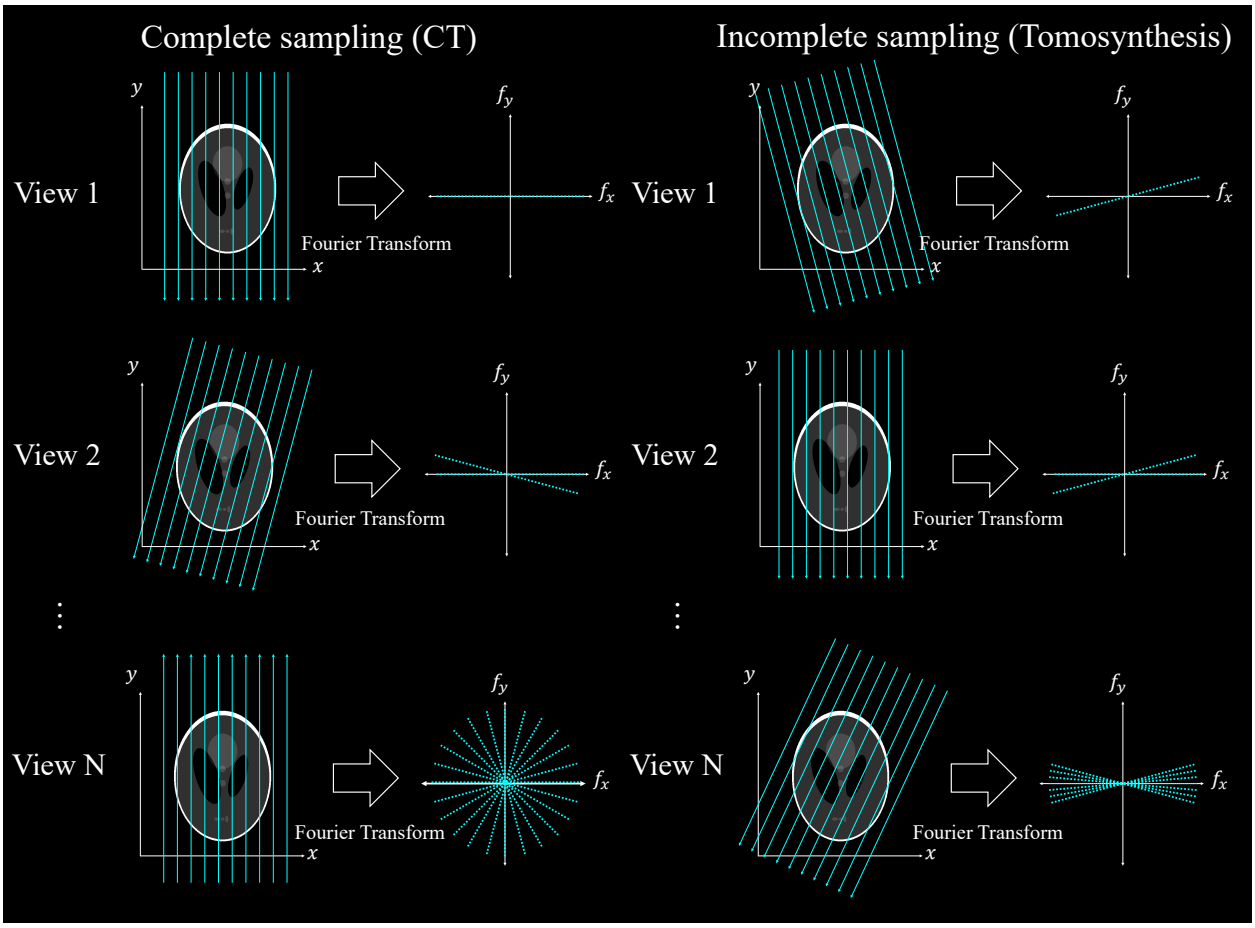

Figure 2.7: An illustration of the Fourier domain sampling of tomographic imaging as described using the Fourier Slice Theorem.

2.4.3 Algebraic or iterative image reconstruction

In practice, medical images are always discrete. With this in mind, we can consider solving Equation 2.4 by rewriting the integral in a digitized/discrete fashion. In order to achieve this, the distribution of attenuation coefficients can be discretized using basis functions, $B_i : \mathbb{R}^3 \mapsto \mathbb{R}$. These basis functions can be used to describe an $M \times N \times P$ voxelized image, $\mathbf{x} \in \mathbb{R}^{MNP}$. Each image voxel may be approximated as follows:

$$\mu(r) \approx \sum_{i=1}^{MNP} x_i B_i(\mathbf{x}), \tag{2.5}$$

where $[\mathbf{x}]_i = x_i$. We can now write an approximation (indicated by the tilde) of each of the N_p projection measurements from Equation 2.4 as follows:

$$\begin{aligned} \tilde{y}_j &= \int_{\ell_j \cap r} \sum_{i=1}^{MNP} x_i B_i(\mathbf{x}) \mathrm{d}s \\ &= \sum_{i=1}^{MNP} x_i \int_{\ell_j \cap r} B_i(\mathbf{x}) \mathrm{d}s \\ &= \sum_{i=1}^{MNP} x_i A_{j,i}, \end{aligned} \tag{2.6}$$

where $A_{j,i}$ indicates the approximate intersection length of path j with voxel i. It is important to emphasize here that in this notation $A_{j,i}$ has nothing to do with the image object at all. Rather, $A_{j,i}$ describes a discrete representation of the imaging system for a given set of basis functions. As a result, A (where $[A]_{j,i} = A_{j,i}$) is known as the system matrix.

If we combine all N_p of the projection measurements into a vector, we can write the following expression to describe our problem:

$$\begin{pmatrix} \tilde{y}_1 \\ \tilde{y}_2 \\ \vdots \\ \tilde{y}_j \end{pmatrix} = \begin{pmatrix} \sum_i A_{1,i} x_i \\ \sum_i A_{2,i} x_i \\ \vdots \\ \sum_i A_{j,i} x_i \end{pmatrix}. \tag{2.7}$$

We can define the vector of measurements on the left-hand side as $\tilde{\mathbf{y}}$ and the right size of this

expression can be expanded as follows:

$$\tilde{\mathbf{y}} = \begin{pmatrix} A_{1,1}x_1 & A_{1,2}x_2 & \dots & A_{1,i}x_i \\ A_{2,1}x_1 & A_{2,2}x_2 & \dots & A_{2,i}x_i \\ \vdots & \vdots & \ddots & \vdots \\ A_{j,1}x_1 & A_{j,2}x_2 & \dots & A_{j,i}x_i \end{pmatrix} = \begin{pmatrix} A_{1,1} & A_{1,2} & \dots & A_{1,i} \\ A_{2,1} & A_{2,2} & \dots & A_{2,i} \\ \vdots & \vdots & \ddots & \vdots \\ A_{j,1} & A_{j,2} & \dots & A_{j,i} \end{pmatrix} \begin{pmatrix} x_1 \\ x_2 \\ \vdots \\ x_i \end{pmatrix}. \tag{2.8}$$

We can define the matrix on the right-hand side as $A \in \mathbb{R}^{N_p \times MNP}$ and the vector on the right-hand side as $\mathbf{x}$. With this notation, we can model our image acquisition in the following discrete fashion as a system of linear equations:

$$A\mathbf{x} = \tilde{\mathbf{y}}. \tag{2.9}$$

Using this digital representation/model allows us to perform a so-called model-based reconstruction since the solution will be based on a model of the imaging system. This system of linear equations can be solved in one of two ways: algebraically or iteratively. In either method, the measured projection data, $\mathbf{y}$, are substituted for $\tilde{\mathbf{y}}$ in order to solve for the image $\mathbf{x}$. In the algebraic solution, this system is inverted:

$$\mathbf{x} = A^{-1}\mathbf{y}, \tag{2.10}$$

where the superscript, $^{-1}$, indicates the matrix inverse. This inversion can be achieved provided A is not singular (viz. $\det A \neq 0$), although even for singular matrices a pseudoinverse may be calculated using a singular value decomposition (SVD) procedure[iv]. However, determining x using an inverse or pseudoinverse is typically a poorly posed problem in practice. For one thing, the

[iv] The pseudoinverse is defined for an $m \times n$ matrix A as $A^\dagger = V\Sigma^\dagger U^*$, where U, V, and Σ are defined such that $A = U\Sigma V^*$. The superscript * indicates the conjugate transpose in the most general case. U is a unitary $m \times m$ matrix and V is a unitary $n \times n$ matrix. In addition, Σ is a diagonal $m \times n$ matrix with non-negative values along its diagonal (zeros are permitted). The pseudoinverse of Σ (viz. $\Sigma^\dagger$) is obtained by replacing each non-zero diagonal element with its reciprocal and taking a transpose of the result.

problem is likely to be either over- or under-determined, and in either case an inverse approach may be unstable. A second concern is that the physics governing photon interactions and detection, the polychromatic spectra, finite acquisition time, patient motion, and safety-limited dose means the measured data will be be noisy and may potentially be inconsistent from view to view. Thus, even for a well determined problem, the algebraic solution to the problem may not be a diagnostic quality image. Finally, due to computational limitations, inverse based approaches may not be achievable.

A practical solution to deal with this is to pose the problem instead as an optimization problem which can be solved iteratively with the following cost function:

$$\tilde{\mathbf{x}} = \arg\min_{\mathbf{x}} ||A\mathbf{x} - \mathbf{y}||_p^p, \tag{2.11}$$

where $||\mathbf{x}||_p^p = (\sum_i x_i^p)^{\frac{1}{p}}$ indicates the p-norm. The most common solution to this problem is a least-squares solution ($p = 2$), however there are many different ways to find an optimal. In practice, this problem is often subjected to additional constraints which constrain or regularize the solution. The cost function for a regularized reconstruction can be described as follows:

$$\mathbf{x}^* = \arg\min_{\mathbf{x}} ||A\mathbf{x} - \mathbf{y}||_2^2 + \sum_{i=1}^{N} \lambda_i R_i(\mathbf{x}), \tag{2.12}$$

where there are N regularization terms, each with a corresponding weight, λ. A common example of a regularizer for image reconstruction is a constraint enforcing smoothness to reduce image noise, but a plethora of regularization methods have been implemented for various applications.

Given the additional complexity (computational as well as theoretical) of iterative reconstruction methods, one might ask, why isn't FBP good enough? This is a fair question, however there are many motivating factors for introducing iterative reconstruction methods. FBP solves a mathematical problem for image reconstruction, however it isn't able to take into account physical properties of the system. This can result in images which have inaccurate values, limited spatial resolution, and potentially severe artifacts. On the other hand, so called model-based iterative reconstruction methods are able to model various aspects of the system to alleviate these issues. Examples of this include the introduction of statistical models for measurements, accounting for the finite size of x-ray sources, detector elements, and reconstructed voxels, the x-ray spectrum, detector physics,

and more[115]. In addition to eliminating artifacts caused by imperfections (compared with the mathematical model) in a physical system, iterative reconstruction methods can also enable image reconstruction when the measured data would otherwise be insufficient for FBP reconstructions. This includes undersampled data, data acquired from less than a short-scan acquisition (required for FBP reconstruction), as well as extremely noisy data. Iterative reconstruction methods have been introduced clinically in diagnostic CT, however they also potentially have a tremendous amount to offer DBT, which is inherently both undersampled and acquired over an angular span much shorter than the required short scan for CT.

2.5 Image quality assessment

It is important with any imaging modality to understand the diagnostic strengths and limitations of that modality. Many traditional image quality metrics, such as contrast-to-noise ratio (CNR), are based on the simple Rose model for detection. This model assumes that object size and contrast along with background noise determine detection performance[116–119]. Unfortunately, this model is an oversimplification of the actual task typically performed in imaging. As Barrett *et al.* point out, "The task in imaging is always to draw inferences about the object that produced an image"[120]. As a result, understanding the practical performance of an imaging system requires a much more comprehensive understanding of the system than is provided by the Rose model. One solution to understanding how an imaging system works is to use human reader studies. Reader studies offer a true measurement of practical performance for a system, and account for many features of the imaging system that are difficult to measure independently: the reader and his/her environment, the imaging task, and technical aspects of the system. Since reader studies provide such a comprehensive picture of imaging systems, they remain the gold standard in defining performance and bringing novel imaging technologies to clinical settings.

Unfortunately, reader studies require a large time commitment from experienced readers and it is difficult to direct the design and optimization of a system using reader studies. To help alleviate some of these problems, task-based objective image quality metrics are increasingly being utilized and explored in medical imaging[120–126]. The benefits of task-based assessment are many, but some

of the major ones include: the ability to include observer performance, the ability to incorporate a specific imaging task, the ability to explore a variety of system parameters prospectively, and, perhaps most importantly, the ability to include all of these aspects of the imaging system and more without requiring the recruitment of trained observers for each and every study. For obvious reasons, in order to be trusted these metrics need to be validated and calibrated against true human observer performance for a given imaging modality, but once a validated model is in place further system optimization and performance evaluations can be quickly performed for a wide variety of system parameters and imaging tasks.

In order to implement most task-based image quality metrics, a rigorous measurement of the system's noise power spectrum (NPS) is needed. For 3D digital images, the 3D NPS may be calculated as follows[127]:

$$\mathrm{S}\left(f_x, f_y, f_z\right) = \frac{\Delta_x \Delta_y \Delta_z}{N_x N_y N_z} \left\langle \left| \mathrm{DFT}\left\{ \mathrm{V}_i\left(x, y, z\right) - \left\langle \mathrm{V}_i\left(x, y, z\right) \right\rangle \right\} \right|^2 \right\rangle, \tag{2.13}$$

where Δ_i is the pixel pitch in the i direction, N_i is the number of pixels in the region used to estimate the NPS in the i direction, V_i is a noise instance, $\langle \cdot \rangle$ is the average operation, and DFT is the 3D discrete Fourier transform.

Although the 3D NPS provides a comprehensive understanding of the stochastic noise of the system, in practice the image volume is not read as a whole, but rather a slice by slice assessment is performed by radiologist reviewers. Thus, assessing the in-plane 2D NPS is a more accurate measure of the noise performance as the images are read. As a result, it is desirable to reduce the 3D NPS to the 2D (central slice)[127]. The 2D NPS is given by the following expression:

$$\mathrm{S}_{\mathrm{2D}}\left(f_i, f_j\right) = \int \mathrm{S}\left(f_i, f_j, f_k\right) \mathrm{d}f_k. \tag{2.14}$$

The 3D NPS can be further reduced to a 1D case with an additional integration as follows:

$$\mathrm{S}_{\mathrm{1D}}\left(f_i\right) = \int \int \mathrm{S}\left(f_i, f_j, f_k\right) \mathrm{d}f_k \mathrm{d}f_j. \tag{2.15}$$

The 1D NPS is useful for exploring the peak frequency of the NPS and quantitatively comparing

spectra from different imaging methods.

In addition to the NPS, the system modulation transfer function (MTF) is needed to fully characterize an imaging system. The MTF is a normalized description of the signal transfer properties at different spatial scales, and is typically presented as a plot showing MTF as a function of spatial frequency; alternatively, the frequency value at a certain percent of the peak value of the MTF may also be presented[47].

2.5.1 Anatomical noise in breast imaging

The anatomical background noise plays a significant role in breast imaging. According to the Rose model for signal detection, smaller objects should be less easy to detect when the CNR for those objects is fixed. However, Burgess *et al.* showed that for mammography, the anatomical background leads to the opposite[44]. They found using human observers that the anatomical background of the breast in mammography meant larger masses (diameters ranging from 1-10 mm) needed to be relatively higher contrast to be detectable. The impact of the anatomical background noise on detection performance has been quantified using several techniques[44,45,128–130], including a spatial frequency dependent power spectrum, viz., the anatomical background noise power spectrum[44,45,130]. In this framework, the overall detectability for a specific imaging task is jointly impacted by a generalized NPS that consists of two major components: quantum and anatomical background noise[44,45,130]. The quantum noise depends on the imaging system itself (such as the quantum detection efficiency of the detector), the image acquisition parameters (such as the overall radiation exposure level and tube potential), and the breast itself (such as breast density and compressed thickness). Conversely, the anatomical background noise is primarily dependent on the breast parenchymal structure, imaging conditions, and imaging geometry (CC vs. MLO planar view), although the impact of acquisition parameters on image contrast may lead to some minor variation in the measured anatomical noise background[131]. It has been shown that the power spectrum of anatomical background noise in the breast may be empirically modeled as[44] :

$$\mathrm{NPS_a}(f) \approx \alpha f^{-\beta} \tag{2.16}$$

where f is the spatial frequency, and α and β are two parameters determined by fitting the measured and radially averaged $\mathrm{NPS_a}(f)$ to the model given in Eq. (2.16). In reality, the parameters α and β may change from one imaging method to another and from patient to patient, but these deviations should fall within a range of typical values for a given modality. Typical values for β in absorption x-ray mammography imaged using a cranio-caudal geometry with compression have been reported to be around $\beta_{\mathrm{mammo}} \approx 3.2$ [44,45,130]. Recently, β has also been measured for digital breast tomosynthesis (DBT) [132] and breast cone-beam CT (BCT) [131,133], yielding values of $\beta_{\mathrm{tomo}} \approx 3.1$, and $\beta_{\mathrm{BCT}} \approx 2.0$ respectively. Not only does β depend on the imaging modality, but it also varies with the x-ray beam energy [131], the breast density [46], and even the imaging plane (CC vs. MLO for mammography and DBT) [133]. Despite its many dependencies on specific imaging conditions, it is well documented that β is strongly correlated with lesion detection performance [44,46,133–135]. Therefore, quantitative assessment and prediction of diagnostic performance for mammography should take into consideration not only imaging system/acquisition parameters, but also this beta-power law of the anatomical background. As an example, the concept of a generalized NPS including the anatomical noise background has been developed and incorporated into the model observer framework [121,136].

For a given imaging method, β can be estimated from local anatomical background power spectra for different regions of interest (ROIs) in a given breast, followed by an ensemble average over many local regions in many breast imaging datasets [44,137]. The resulting power spectrum is then radially averaged and fitted to the model given in Eq. (2.16). From this fit, the value for β may be extracted. The steps of this process implemented experimentally may be found in Garrett *et al.* [137] as well as Chapter 5 of this dissertation. We should note that extremely low and extremely high frequencies do not correspond to the spatial scales of anatomical structures, and as a result the linear regression is most appropriately performed over a limited range of frequencies. In our experience, this range was typically determined to be $\approx [0.4, 3]$ mm^{-1}. In practice, this range should be chosen to provide the maximum r^2 value (coefficient of determination) for the least square fitting (the most linear range of the data).

2.6 Dose reduction

Understanding the noise and spatial resolution characteristics of a system along with the impact of anatomical noise is critical in understanding how an imaging system will perform. However, in any medical system utilizing ionizing radiation, another question arises. How does the system perform with respect to radiation dose? Good practice guidelines are to follow the As Low As Reasonably Achievable (ALARA) principle[138]. As a result, it is always desirable to reduce the required radiation exposure for an imaging procedure to the lowest possible level without sacrificing diagnostic quality. In any x-ray based imaging technique, the patient exposure can be reduced via several different techniques[115].

For tomographic imaging techniques, such as computed tomography (CT) or DBT, the number of view angles can be reduced while keeping other imaging parameters fixed. Although this reduces dose, it can result in image artifacts due to aliasing and angular under-sampling. Our current clinical DBT system (Hologic Selenia Dimensions) only acquires 15 projections with a limited angular range of $\approx [-7.5°, 7.5°]$. Further reducing the number of views or decreasing the angular range has a negative impact on the reconstructed images' spatial resolution and localization accuracy[48,139,140]. Another common technique is to reduce the x-ray tube current (and thus x-ray photon output) for the acquisition. This reduces the x-ray tube output fluence and results in a more or less linear reduction in patient exposure[47]. There is still a compromise, however, since reduced x-ray fluence provides fewer quanta, and thus noisier images. Increased image noise results in reduced detectability of masses and fine structures. There are many post-processing techniques for decreasing image noise, however most conventional de-noising techniques remove noise while introducing spatial blur. In breast imaging, spatial resolution is very important; identification of small clusters of microcalcifications or spiculated margins of lesions can lead to the discovery of early stage breast cancers[8,47]. Thus, any technique to reduce image noise in DBT must not sacrifice diagnostic value by reducing the spatial resolution of the system.

One image de-noising technique that has been recently introduced to reduce image noise while retaining spatial resolution is the Dose Reduction with Prior Image Constrained Compressed Sensing algorithm (DR-PICCS)[141–145]. This technique has found several applications within diagnostic

CT[143–147], but shows promise in other imaging applications as well[148]. With an emphasis on retaining spatial resolution and noise texture while reducing the overall image noise level, DR-PICCS is a good candidate for reducing dose in breast imaging applications. The Prior Image Constrained Compressed Sensing (PICCS) algorithm was developed initially as a reconstruction technique for highly under-sampled projection data sets in computed tomography (CT)[141,142,145,147]. PICCS can be performed by iteratively solving the following unconstrained minimization problem:

$$\tilde{\mathbf{x}} = \arg\min_{\mathbf{x}} \left[\frac{\lambda}{2} \left(A\mathbf{x} - \mathbf{y} \right)^T \mathbf{Q} \left(A\mathbf{x} - \mathbf{y} \right) + \alpha \Psi \left| \mathbf{x} \right|_{\ell_1} + (1-\alpha) \Psi \left| (\mathbf{x} - \mathbf{x}_p) \right|_{\ell_1} \right] \tag{2.17}$$

where $\mathbf{x}$ is the image solution, $\mathbf{x}_p$ is a prior image, $\mathbf{y}$ is a projection dataset, $\mathbf{Q}$ is a statistical weighting matrix, A is the system matrix that defines the geometry used to generate $\mathbf{y}$, Ψ is a sparsifying transform, α is a weighting term, and the ℓ_1-norm is defined as: $|\mathbf{x}|_{\ell_1} = \sum_{n=0}^{N} |\mathbf{x}_n|$. Commonly, the total variation (TV) is chosen as a sparsifying transform (we can recall the TV is defined as the ℓ_1-norm of an image bidimensional spatial gradient ℓ_2-norm), defined as follows for a discrete image of dimension $M \times N$:

$$TV(\mathbf{x}) = \sum_i \sqrt{(x_{i+1} - x_i)^2 + (x_{i+M} - x_i)^2}, \tag{2.18}$$

where i and j denote the pixel location in the discrete image, $\mathbf{x}$.

The PICCS framework was originally intended to reconstruct CT datasets, however it has been shown that the adaptation of PICCS to dose reduction (DR-PICCS) can operate directly in the image domain to reduce noise while retaining important imaging features[143,145]. In this framework, a noisy image of interest is forward projected to generate a synthesized projection dataset, Y, and a prior image can be generated by using a conventional image denoising technique. One preferred method to generate the prior image is an automated 3D anisotropic diffusion filter using a slice-by-slice noise estimate[149,150].

2.6.1 Anisotropic Diffusion in Image Denoising

Anisotropic diffusion has been used in image denoising for over 25 years[149]. Diffusion denoising is derived from the following partial differential equation:

$$\frac{\partial u}{\partial t} = \operatorname{div}\left(c\left(|\nabla u|\right)\nabla u\right) \tag{2.19}$$

where u is the image volume (function of x, y, z, t) , div is the divergence operator, and ∇ is the gradient operator. The function, $c(|\nabla u|)$, controls the strength of diffusion and is known as the diffusion coefficient. Two common choices for $c(|\nabla u|)$ that solve this equation are:

$$c(|\nabla u|) = e^{-\left(\frac{|\nabla u|}{\kappa}\right)^2} \tag{2.20}$$

and

$$c(|\nabla u|) = \frac{1}{1+\left(\frac{|\nabla u|}{\kappa}\right)^2}, \tag{2.21}$$

where κ is a parameter that can be tuned for different applications. The goal of κ is to normalize the update strength; as such, κ should be chosen to be as close as possible to the image noise standard deviation. If κ is selected appropriately, regions of the image with gradient magnitudes on the order of noise ($|\nabla u| \leq \kappa$) will be smoothed, but edges ($|\nabla u| > \kappa$) will be preserved.

In practice, diffusion is implemented by performing the following updates:

$$u^{t+1} = u^t + \frac{\partial u}{\partial t} \tag{2.22}$$

$$= u^t + \operatorname{div}\left(c\left(|\nabla u|\right)\nabla u\right) \tag{2.23}$$

$$= u^t + \sum_{k=1}^{N_k} c(|\nabla_k u^t|)\nabla_k u^t, \tag{2.24}$$

where u^t is the image at a given "time"[v], t, and the subscript k indicates each possible direction out of N_k directions. In the 2D case, $N_k = 8$ (8 adjacent pixels) and in 3D $N_k = 26$ (26 adjacent voxel elements).

[v]Time is used to describe the iterative procedure for diffusion since in physical systems diffusion proceeds with time.

We claimed before that it is desirable to establish a κ value on the order of the image noise. However, a single fixed value is inappropriate for many iterations as we expect the image noise to decrease as the process proceeds. Ideally, κ will be updated at each iteration to reflect the local image noise. One method to estimate image noise is achieved by taking an image gradient, calculating a histogram of the gradient, and identifying a certain percentile value of that gradient, commonly around the 90^{th} percentile[150].

3 Image reconstruction for digital breast tomosynthesis

3.1 Introduction

Due to the limited angular range and specific requirements of breast imaging, reconstruction for digital breast tomosynthesis (DBT) is a challenging and unique problem. Unlike conventional computed tomography (CT) which offers isotropic 3D spatial resolution, due to the significantly reduced angular range used to acquire tomosynthesis data (as little as 15° in clinical systems), tomosynthesis can only offer highly anisotropic 3D spatial resolution in which the in-plane spatial resolution is comparable to that of 2D mammography while through-plane spatial resolution is significantly poorer than that of the in-plane resolution, albeit much better than that of 2D mammography. In a clinical DBT reconstruction, the typical voxel size is approximately $0.1 \times 0.1 \times 1$ mm^3, providing good resolution in-plane, and much more limited through-plane resolution along the slice direction. In practice, although the reconstructed slice thickness is about 1 mm, the actual slice thickness can be much larger. It is worth emphasizing here that performing a reconstruction to an image grid with smaller voxels in the through-plane direction does not indicate a true improvement in through-plane resolution. The true physical through-plane resolution is jointly defined by the data acquisition hardware and image reconstruction method, not the reconstructed voxel size. This increased slice thickness manifests itself as through-plane blurring or signal leakage in the reconstructed volumes as demonstrated in Figure 3.1.

Many different methods to perform reconstruction for DBT exist [151], and a great deal of work

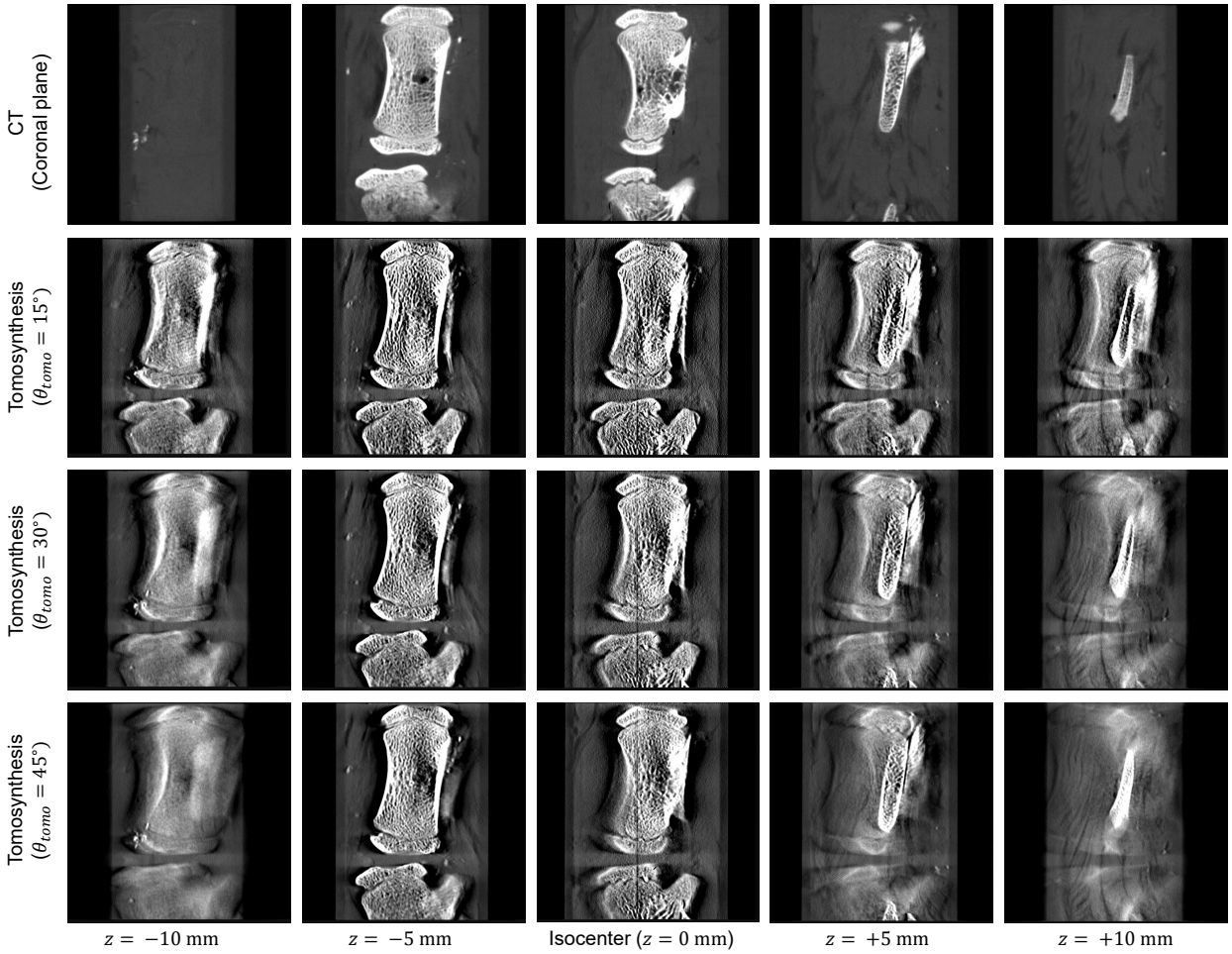

Figure 3.1: FBP reconstructed slices spaced 5 mm apart of a pig bone imaged on a benchtop system for several acquisition methods. CT and tomosynthesis acquisitions were performed with a full scan and tomo angles of 15°, 30°, and 45°, respectively. Through-plane blurring is evident in all of the tomosynthesis reconstructions and is more pronounced with smaller tomo angles.

has been done to identify optimal reconstructions for DBT. Analytical reconstruction methods, such as shift-and-add backprojection (SAA) and filtered backprojection (FBP), are common choices to perform image reconstruction for tomosynthesis in many applications. SAA can be performed very quickly and results in relatively low noise images[152], however the images produced with SAA reconstruction have significant image blurring and through-plane blurring artifacts. When the data are filtered prior to back projection (FBP) the image sharpness is dramatically improved[153], however image noise is significantly amplified and through-plane blurring artifacts remain. These through-plane blurring artifacts are very damaging in the images because they make object localization

more difficult and can obscure low contrast objects above or below higher contrast objects. DBT specific filters have been developed to try and balance image contrast/noise characteristics and through-plane blurring artifacts[153], however regardless of filter choice, some compromise is made.

On the other hand, iterative reconstructions have been shown to offer many benefits in DBT imaging. Iterative methods are able to simultaneously provide both good contrast-to-noise ratio (CNR) and spatial resolution characteristics in images[152,154–156]. Iterative reconstruction methods are flexible and able to incorporate a variety of system and object models to improve image quality. In DBT, some of these features include: breast boundaries[156], task specific regularization such as anisotropic diffusion[139], a statistical noise model[157], as well as spectral information[158]. They can also provide reduced through-plane blurring artifacts.[152,157] Together, these benefits offer improved image quality for a given image acquisition, and some have argued this may permit dose reduction with iterative reconstruction method[159]. Recent work has demonstrated that the reconstruction method (FBP vs iterative) and parameters can have a significant influence on human observer performance[160].

3.2 Data acquisition

All datasets used in this work (unless otherwise indicated) were acquired using a Hologic Selenia Dimensions (Hologic, Inc. Bedford, MA) DBT imaging system (see Figures 2.4, 2.5, and 2.6). The coordinate system used in this work is depicted in Figure 3.2. The system parameters used for image acquisitions are shown in Table 3.1. A few comments on the system should be made: 1) For tomosynthesis the detector is operated in a 2×2 binned mode; the native pixel pitch is 70×70 μm^2. 2) Although the only beam filter available for tomosynthesis is aluminum, both rhodium (0.05 mm) and silver (0.05 mm) filters are available for mammographic acquisitions. 3) For tomosynthesis acquisitions, only the large focal spot (0.3 mm) for the system is available, however for mammographic acquisitions an additional small (0.1 mm nominal) focal spot size is available. The reconstructed volumes were reconstructed to a projective pixel grid (see Figure 3.3), in which the pixel size at each slice location is the magnified pixel pitch at the detector. In this method, pixels further from the detector (closer to the focal spot) are smaller than those closer to the detector.

Table 3.1: Parameters for tomosynthesis acquisitions with Hologic Selenia Dimensions system.

Parameter	Value
Number of views	15
Tomo. angle	15°
Tube motion	continuous
Acquisition time	3.7 s ($\approx$ 4.1 degrees/s)
Detector type	direct conversion
Conversion material	amorphous selenium (A-Se)
Detector pixel pitch	140×140 μm^2
Detector dimensions	23.3×28.5 cm^2
Detector bit depth	14 bits
Source-detector distance	700 mm
Source-isocenter distance	633 mm
Anode material	W
Focal spot size	0.3 mm (nominal)
Filter	0.7 mm Al

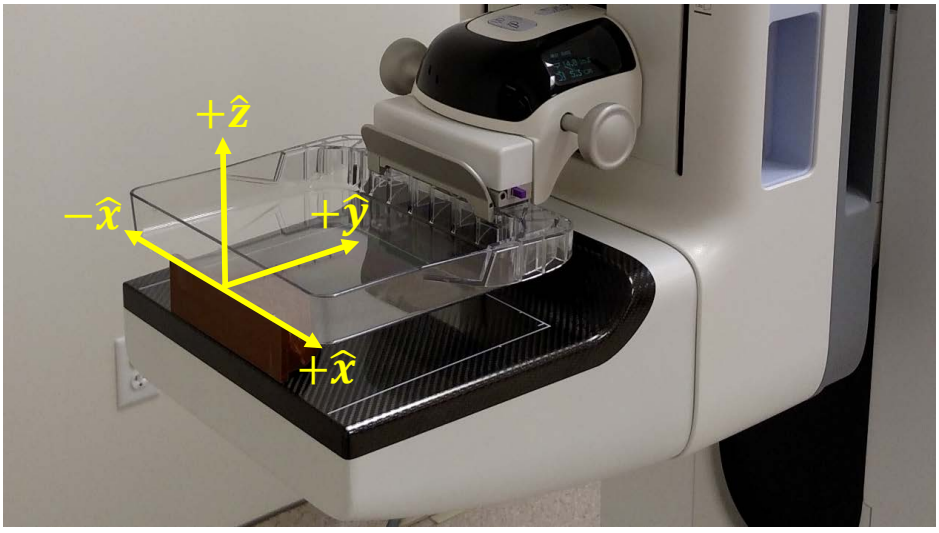

Figure 3.2: The coordinate system used in this work.

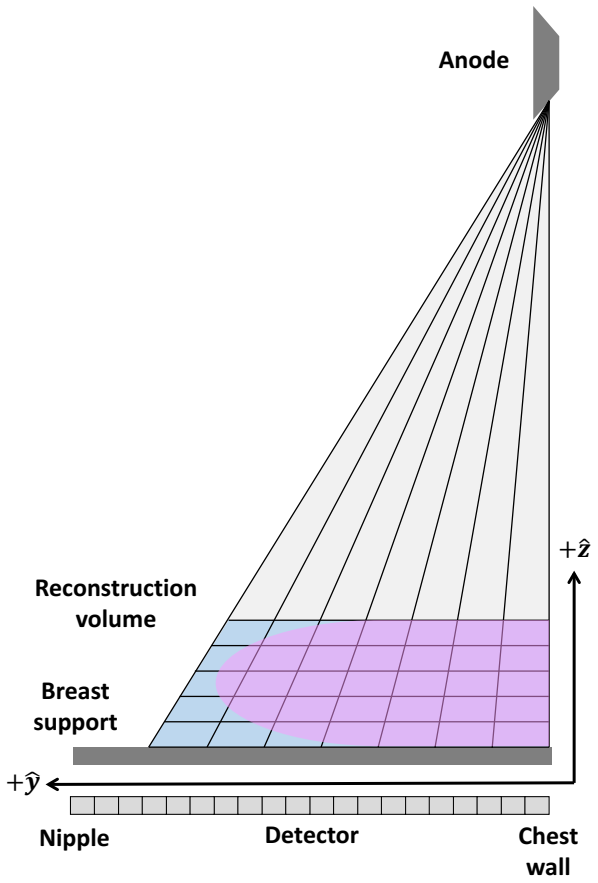

Figure 3.3: An illustration of the projective pixel grid used in this work.

3.2.1 Test objects

Using this system, a variety of test objects were imaged for this work. These test objects included: the ACR mammography accreditation phantom (CIRS Model 3254318, CIRS, Norfolk, VA, see Figure 2.1), a custom anthropomorphic phantom (see Figure 3.4), as well as several clinical breasts shown in Figure 3.20.

3.3 Forward- and back-projection

All reconstructions (iterative or analytical) performed for the Hologic Selenia Dimensions system in this work were implemented using projection matrices[161] (commonly just called P-matrices) to perform both forward and back-projection operations. The details of how those projection matrices

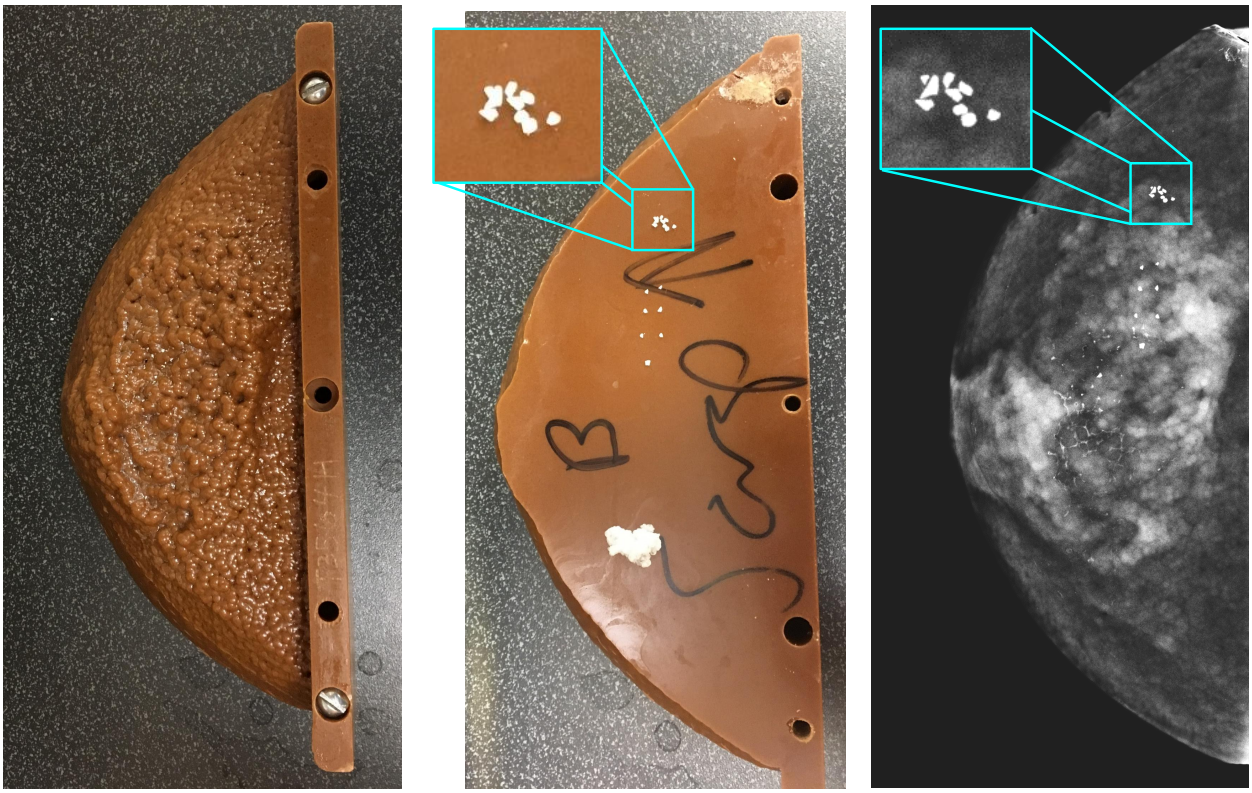

(a) (b) (c)

Figure 3.4: The anthropomorphic phantom used in this work. A photograph of the outside of the phantom (a), a photo of the interior of the phantom including a close up of the calcification cluster used for measurements (b), and a mammogram (28 kV, Rh filter, 81 mAs, anti-scatter grid present) of the phantom (c) are shown. Note: the lighter brown material at the top corner visible in (b) is epoxy used to repair the corner of the phantom.

were used are described in Appendix A.1. The calibration for these P-matrices is embedded in the DICOM header exported from any Hologic Selenia Dimensions DBT system and a script was written to extract the relevant parameters from that header automatically during reconstruction.

In this implementation, projection matrices were used to perform both forward- and back-projection[161]. Projection matrices provide a calibrated mapping from the image domain to the projection domain. In other words, for a given view angle, i, there is a one-to-one correspondence

between a location on the detector (u, v) and a pixel location (x, y, z):

$$\begin{pmatrix} u \times s \\ v \times s \\ s \end{pmatrix} = \mathbf{M_{i,BP}} \begin{pmatrix} x \\ y \\ z \\ 1 \end{pmatrix} \tag{3.1}$$

where u and v are coordinates on the detector, x, y, and z are image volume coordinates, s is a scalar, and $\mathbf{M_{i,BP}}$ is a 3×4 matrix where the subscript i indicates the current projection number and **BP** indicates the matrix corresponds to the backprojection operation. Although $\mathbf{M_{i,BP}}$ itself is not square, if we choose a fixed location, z, we can invert the matrix algebraically (see Appendix A.1) and use a similar formulation to perform the forward projection as follows:

$$\begin{pmatrix} x \times s' \\ y \times s' \\ s' \end{pmatrix} = \mathbf{M_{i,FP}}(z) \begin{pmatrix} u \\ v \\ 1 \end{pmatrix} \tag{3.2}$$

where s' is a scalar and $\mathbf{M_{i,FP}}(z)$ is a 3×3 z-dependent matrix where the subscript i indicates the current projection number and **FP** indicates the matrix corresponds to the forward projection operation.

The use of projection matrices for this system is advantageous for several reasons. First, the system has an unusual geometry (recall the detector is almost stationary during the gantry rotation) which makes modeling the system geometry somewhat more challenging that a conventional CT system. Second, the use of projection matrices provides a very robust means of accounting for slight changes in system geometry or instability. Since the projection matrices are calibrated using the system itself (rather than a schematic or model of the system), they can achieve good quality reconstructions even for systems that may change over time. Third, the implementation of forward- and back-projection using projection matrices can be very fast. Finally, the projection matrices themselves are quite small. As a result, they can be embedded directly in the DICOM header information of the images and shared with the image data. Thus, datasets can be shared and

reconstructed anywhere with the relevant calibration information.

3.4 FBP Reconstruction

Images reconstructed using filtered backprojection (FBP) were used in this work to seed the iterative reconstructions and as a prior image in some implementations. In order to achieve rapid convergence, a good seed image is important. Ideally, that image should not have any major artifacts and should have a manageable noise level. There are many possible options, but FBP is a common method in most clinical systems, and as a linear process is a good reference which is well understood.

3.4.1 FBP Filter Design

The FBP images were reconstructed using tomosynthesis-specific filters[153,162]. The filter design is essentially a ramp filter with spectral windowing to account for the limited angular sampling and high noise introduced by the ramp filter (through-plane and in-plane, respectively). The $\hat{x}$, $\hat{y}$, and $\hat{z}$ directions are indicated in Figure 3.2, with corresponding frequency coordinates: ω_x, ω_y, and ω_z, respectively. In this case, all filtering is performed along detector rows (x-direction). Before defining our filters, we can consider the following coordinate transformations in the frequency domain (illustrated in Figure 3.5):

$$\omega_r = \sqrt{\omega_x^2 + \omega_z^2} \tag{3.3}$$

$$\theta = \tan^{-1}\left(\frac{\omega_z}{\omega_x}\right) \tag{3.4}$$

$$\omega_x = \omega_r \cos\theta \tag{3.5}$$

$$\omega_z = \omega_r \sin\theta \tag{3.6}$$

In a parallel beam approximation, ω_r corresponds to the row direction of the detector directly, u (see Figure 3.5). Thus, in the Fourier domain (for a parallel beam geometry), the overall filter is defined as the product of three filters as follows:

$$H_F(\omega_r, \theta) = H_{ramp}(\omega_r) H_{\mathrm{IP}}(\omega_r, \theta, A) H_{\mathrm{TP}}(\omega_r, \theta, B) \tag{3.7}$$

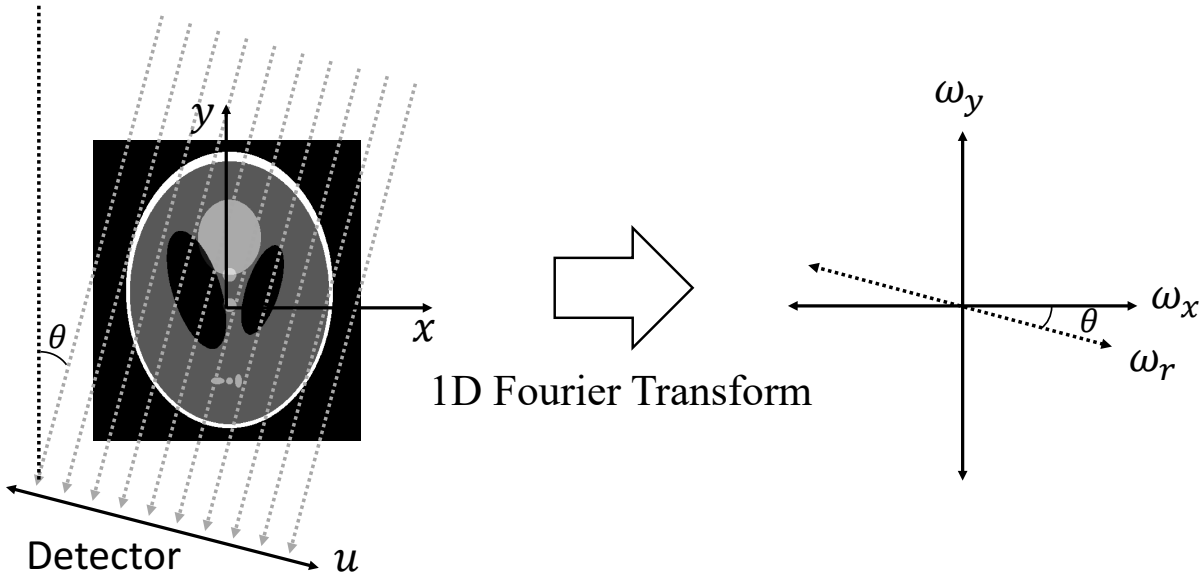

Figure 3.5: An illustration of the Fourier slice theorem. The parallel beam measurement in the left of the panel results in a 1D vector measurement at the detector. The 1D Fourier transform of that vector corresponds to the region of Fourier space occupied by the dashed arrow in the right hand side of the diagram.

where

$$H_{ramp}(\omega_r) = 2\left(\frac{\theta_{tomo}}{2}\right)|\omega_r| \tag{3.8}$$

$$\begin{aligned} H_{\mathrm{IP}}(\omega_r,\theta,A) &= \begin{cases} 0.5\left(1+\cos\left(\frac{\pi\omega_s}{A}\right)\right) & \omega_y < A \\ 0 & \text{else} \end{cases} \\ &= \begin{cases} 0.5\left(1+\cos\left(\frac{\pi\omega_r\cos\theta}{A}\right)\right) & \omega_r\cos\theta < A \\ 0 & \text{else} \end{cases} \end{aligned} \tag{3.9}$$

$$\begin{aligned} H_{\mathrm{TP}}(\omega_r,\theta,B) &= \begin{cases} 0.5\left(1+\cos\left(\frac{\pi\omega_z}{B}\right)\right) & \omega_z < B \\ 0 & \text{else} \end{cases} \\ &= \begin{cases} 0.5\left(1+\cos\left(\frac{\pi\omega_r\sin\theta}{B}\right)\right) & \omega_r\sin\theta < B \\ 0 & \text{else} \end{cases} \end{aligned} \tag{3.10}$$

The subscripts, IP and TP, indicate an in-plane and through-plane apodization, respectively, and the parameters A and B are scalars used to determine the strength of the filter in the in-plane and

through-plane cases, respectively. Both A and B are chosen as a percent of the Nyquist frequency for the projection data ($\omega_N \frac{1}{2\delta u}$).

In practice, the filtration is performed in the spatial, rather than Fourier, domain, and can achieved by convolving the projection data by each component subsequently. Recall, the following property of the Fourier transform: $A(x) * B(x) = \text{IFT}\left(\tilde{A}(f) \times \tilde{B}(f)\right)$, where $*$ denotes a convolution operation, IFT indicates the inverse Fourier transform operation, and $\tilde{A}(f)$ is the Fourier transform of $A(x)$. By using this property, we can equivalently perform the filtration of the projection data, $P(u)$, in the following two ways:

$$\begin{aligned} P'(u) &= \text{IFT}\left(H_{ramp}(\omega_r) H_{\text{IP}}(\omega_r, \theta, A) H_{\text{TP}}(\omega_r, \theta, B) \tilde{P}(\omega_r)\right) \\ &\text{or} \\ P'(u) &= H_{ramp}(\omega_r) * H_{\text{IP}}(\omega_r, \theta, A) * H_{\text{TP}}(\omega_r, \theta, B) * P(u). \end{aligned} \tag{3.11}$$

3.4.2 FBP Filter Parameter Selection

To determine the optimal values for A and B, FBP reconstructions were performed for an anthropomorphic phantom with calcifications (see Figure 3.4) using a range of A ($A/\omega_n \in [0.5, 1.5]$) (increment 0.05) and B ($B/\omega_n \in [0.02, 0.2]$) (increment 0.02) values (see Figure 3.6 for several representative cases). To quantify through-plane blurring, the artifact spread function (ASF) may be used. The ASF is defined as follows:

$$\text{ASF}(z) = \frac{I_{Max}(z) - \bar{I}_{bkg}(z)}{I_{Max}(z_0) - \bar{I}_{bkg}(z_0)}, \tag{3.12}$$

where I_{max} denotes the maximum intensity value in the region containing the feature of interest, $\bar{I}_{bkg}$ denotes the background value near the object, z denotes the slice index, and z_0 denotes the slice index of the object of interest. The ASF width for the calcifications, calcification CNR, and the width of one calcification in the cluster were all measured at each set of reconstruction parameters. Contour plots of these three measurements are shown in Figure 3.7. We can see that reducing either parameter too dramatically will boost the CNR, but at the cost of dramatically reduced image

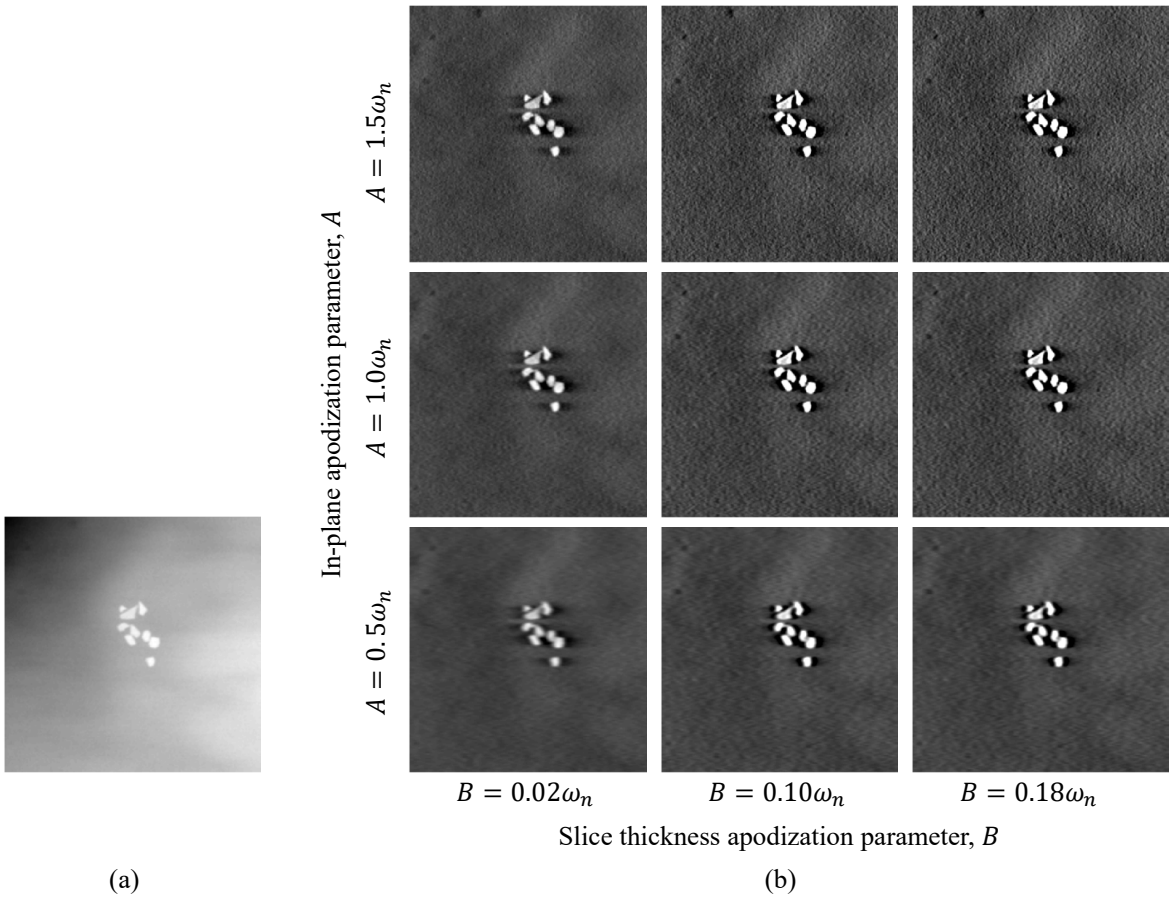

Figure 3.6: The cluster of calcifications in the phantom reconstructed using direct backprojection (a) as well as FBP (b) with several representative parameters. The W/L for all FBP images is the same.

sharpness both in- and through-plane. Based on this study, approaching the upper left corner of the plot maximizes CNR while allowing for a reasonable ASF width and calcification width as long as $B \geq\approx 0.05\omega_n$. Although these results can help describe the overall quality of the reconstructed images, it is not easy to identify a single optimal point from them. In order to identify an optimal parameter set we can introduce another metric to assess image quality, the so called quality factor (QF) introduced by Mertelmeier *et al.*[163]. The QF is defined as follows:

$$\mathrm{QF} = \frac{\mathrm{CNR}}{\mathrm{ASF}_{20}}, \tag{3.13}$$

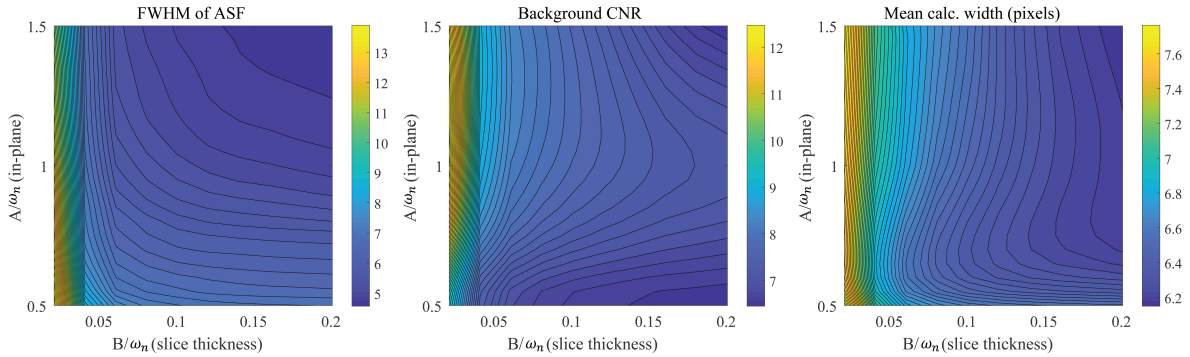

Figure 3.7: The measured ASF width, calcification CNR, and calcification width for the FBP reconstructions as a function of the apodization parameters, A, and B.

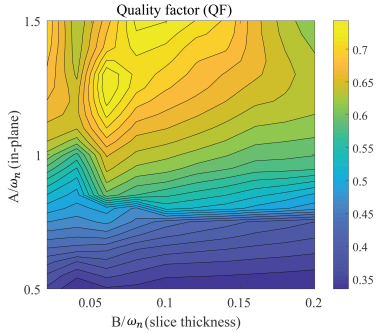

Figure 3.8: The measured quality factor (QF) for the FBP reconstructions as a function of the apodization parameters, A, and B.

where CNR indicates the in plane CNR for an image feature and the ASF_{20} is the width of the ASF curve at 20% of its maximum (in other words the full width 20% max). The QF was measured for the calcifications in the anthropomorphic phantom as well, and the results are shown in Figure 3.8. In this plot, an optimal value can be identified in the region where $A \approx 1.3\omega_n$ and $b \approx 0.06\omega_n$. These values are consistent with optimal values found by Mertelmeier *et al.* for a prototype clinical system[153], and will be used for the remainder of this study.

3.5 Model-Based Iterative Reconstruction

Although many modern iterative reconstruction algorithms can offer improved image quality and physical/statistical system modeling, these algorithms typically come with a major cost:

computational expense[157]. In this work, the denoised ordered-subset statistically penalized algebraic reconstruction technique (DOS-SPART) algorithm is adapted for use in digital breast tomosynthesis imaging[164]. DOS-SPART is able to incorporate the desirable aspects of many different published iterative reconstruction methods, and due to its unique implementation strategy (which is discussed in the subsequent section), can be a very efficient iterative reconstruction method. Thus, iterative reconstruction of large volumes such as those common in digital breast tomosynthesis (≈1996x2457x60 voxels) may be feasible in a clinical setting. Previous work has demonstrated the feasibility of implementing DOS-SPART for DBT[165], and in this chapter the details of the implementation, convergence, and quantitative image quality assessment are provided.

3.5.1 DOS-SPART Algorithm

Given a system matrix A to model the forward projection of an image volume and a diagonal matrix $\mathbf{Q}$ to model the statistical counts of the measured projection data, the log-processed projection data vector, $\mathbf{y}$, can be used to reconstruct a vectorized image vector, $\mathbf{x}$, by solving the following convex optimization problem:

$$\tilde{\mathbf{x}} = \arg\min_{\mathbf{x}} \left[\frac{1}{2} ||A\mathbf{x} - \mathbf{y}||^2_{\mathbf{Q}} + \lambda R(\mathbf{x}) \right], \tag{3.14}$$

where λ is the parameter to control the regularization strength.

The first-order optimality condition of the problem yields:

$$0 \in A^T Q(A\mathbf{x} - \mathbf{y}) + \lambda \partial R(\mathbf{x}), \tag{3.15}$$

where $\partial R(\mathbf{x})$ is the subdifferential of the regularizer. By multiplying each side by an arbitrary positive semi-definte matrix, $\mathbf{P}$, in the above equation and by adding and subtracting the minimizer $\tilde{\mathbf{x}}$, one has the following equation for the minimizer $\mathbf{x} = \tilde{\mathbf{x}}$:

$$\left[\tilde{\mathbf{x}} - \mathbf{P}A^T Q(A\tilde{\mathbf{x}} - \mathbf{y}) \right] - \tilde{\mathbf{x}} \in \lambda P \partial R(\tilde{\mathbf{x}}). \tag{3.16}$$

Using the definition of the proximity operator, $\text{prox}_{\lambda PR}(\mathbf{x})$, the above equation can be written as

the following fixed point equation for the minimizer $\tilde{\mathbf{x}}$:

$$\tilde{\mathbf{x}} = \text{prox}_{\lambda PR}\left[\tilde{\mathbf{x}} - \mathbf{P}A^T Q(A\tilde{\mathbf{x}} - \mathbf{y})\right]. \tag{3.17}$$

The fixed point, $\tilde{\mathbf{x}}$, can be determined iteratively using the following sequences:

$$\begin{aligned} \mathbf{u}_{k+1} &= \mathbf{x}_k - s\mathbf{P}A^T\mathbf{Q}\left(A\mathbf{x}_k - y\right), & (3.18)\\ \mathbf{x}_{k+1} &= \text{prox}_{\lambda PR}(\mathbf{u}_{k+1}), & (3.19)\\ &= \arg\min_{\mathbf{x}}\left[\frac{1}{2}||\mathbf{x} - \mathbf{u}_{k+1}||^2_{\mathbf{P}^{-1}} + \lambda R(\mathbf{x})\right]. \end{aligned}$$

Eq. (3.18) represents a generalized gradient descent update with a statistical penalty to the measured projection data and a positive semidefinite matrix, $\mathbf{P}$, to provide variable update step size for each individual image voxel[i]. Eq. (3.19) represents a generalized denoising problem using a $\mathbf{P}^{-1}$-norm distance between $\mathbf{x}$ and $\mathbf{u}_{k+1}$. The ordered-subset method can be readily introduced in Eq. (3.18) in numerical implementation, and thus this algorithm has been referred to as Denoised Order-Subset Statistically Penalized Algebraic Reconstruction Technique (DOS-SPART) by Li *et al.*[166].

3.5.1.1 Regularization

The formalism presented in Equations. 3.18 and 3.19 is so far completely generic with respect to the actual regularizer used. In practice, a specific regularizer should be chosen, and the goal of that regularizer will determine its form. As previously discussed, a common goal of regularization is to reduce/limit image noise. Thus, a regularizer that promotes smoothness such as total variation (TV) is commonly used. We can recall, in a two-dimensional (2D) $M \times M$ vectorized image, the total variation is defined as follows:

$$TV(\mathbf{x}) = \sum_i \sqrt{(x_{i+1} - x_i)^2 + (x_{i+M} - x_i)^2}. \tag{3.20}$$

[i] A matrix, A, is said to be positive semidefinite iff for every non-zero column vector, z, it is true that $z^*Az \geq 0$, where * indicates a complex conjugate. If it is true that $z^*Az > 0$ for all non-zero column vectors, z, that matrix is said to be positive definite.

This straightforward regularizer inherently promotes image smoothness while preserving edges. TV regularization is very common in tomographic reconstruction methods[167–174]. An alternative regularization scheme which can be used in this framework is the so called prior image constrained compressed sensing (PICCS) regularization[142,175–177]. The PICCS framework has been used extensively in CT applications for diagnostic multi-detector CT (MDCT)[175–177], interventional c-arm CT[178,179], as well as CT image-guided radiation therapy[142,180]. The regularization in the PICCS framework is given generally by the following:

$$R(\mathbf{x}) = \left[(1-\alpha)\left|\left|\Psi(\mathbf{x})\right|\right|_p^2 + \alpha\left|\left|\Psi(\mathbf{x}-\mathbf{x}_P)\right|\right|_p^2\right], \tag{3.21}$$

where α is a parameter determining the relative weight of the two terms ($\alpha \in [0,1]$), $\mathbf{x}_P$ is a prior image, and Ψ indicates a sparsifying transformation. A common choice for Ψ is the TV as described in Eq. 3.20 (an ℓ_1-norm), allowing this to be rewritten as:

$$R(\mathbf{x}) = \left[(1-\alpha)TV(\mathbf{x})^2 + \alpha TV(\mathbf{x}-\mathbf{x}_P)^2\right] \tag{3.22}$$

We can see that this PICCS-TV regularizer is actually a generalization of the standard TV regularizer, and reduces to Eq. 3.20 when $\alpha = 0$.

3.5.1.2 Statistical penalization

As described in Eq. 3.14, the matrix Q is a diagonal matrix which models the statistical counts of the measured projection data and is used to penalize rays during the reconstruction according to their noise. In other words, a noisy ray with very few photons arriving at the detector (very noisy) is given a smaller weight than a ray where the photon number arriving at the detector is high (low noise).

In practice, a weighting scheme is used to achieve an approximately linear weight for the meaningful rays in the projection data. That is achieved by finding the minimum and maximum values of rays passing through the breast object (as opposed to rays passing through air alone) and using a piecewise linear model. In this model, the weights should be linear within the breast down to a lower threshold (fixed at 0.2). The lowest weights should be greater than zero so that no

rays are completely discarded. The maximum weight allowed is 1, so rays outside the breast (high photon numbers) are updated with a weight of 1.

This weighting scheme works reasonably well for many cases, however in the event that there is metal present in the images the scheme causes problems (see Figure 3.9). Since metal is much more highly attenuating than breast tissue, metal in the projection images will cause some rays to have very few or even no photons arriving at the detector. This lowers the floor for the weighting scheme dramatically and thus squeezes the linear range of the weighting scheme. The result is that normal breast tissues are all pushed to the top or bottom of the linear range.

To avoid this scaling, an additional step was added in the weight map generation in the event that metal is present. First, a simple step was taken to determine if metal is present in the projection data. This was accomplished by calculating the approximate maximum linear attenuation coefficient in the projection data as follows:

$$\mu_{max} \geq \max\left(\frac{\mu\ell}{Z_t}\right) = \max\left(\frac{-\log(I/I_0)}{Z_t}\right) \tag{3.23}$$

where μ_{max} indicates the maximum linear attenuation coefficient in the projection data, Z_t is the compressed thickness of the breast, $\mu\ell$ is the measured projection datum calculated by taking the negative log transformation of the quotient of the raw projection and the flat field image ($-\log[I/I_0]$). The max operation was taken over all measured rays in the projection dataset to determine a single μ_{max} value per projection dataset. The measured μ_{max} value was then compared to a threshold. If $\mu_{max} \geq \mu_{thresh}$ that dataset is treated as containing metal; if $\mu_{max} < \mu_{thresh}$ the statistical weights were generated using the method described above. Using a cohort of clinical breast cases (two examples shown in Figure 3.9), a threshold of 0.04 mm^{-1} was empirically determined to be a suitable value for differentiating projections containing metal from those without (see Figure 3.10).

If metal was identified in the projection data, a piecewise linear weighting scheme was still used, however the endpoints of the linear segment were determined using the values bounding the central 90% of the non-air image values. This was accomplished by generating a histogram of all the non-air values, and determining the photon numbers corresponding to the 5th and 95th percentiles. Those intensities were then used to determine the lower and upper limits to the linear segment of the

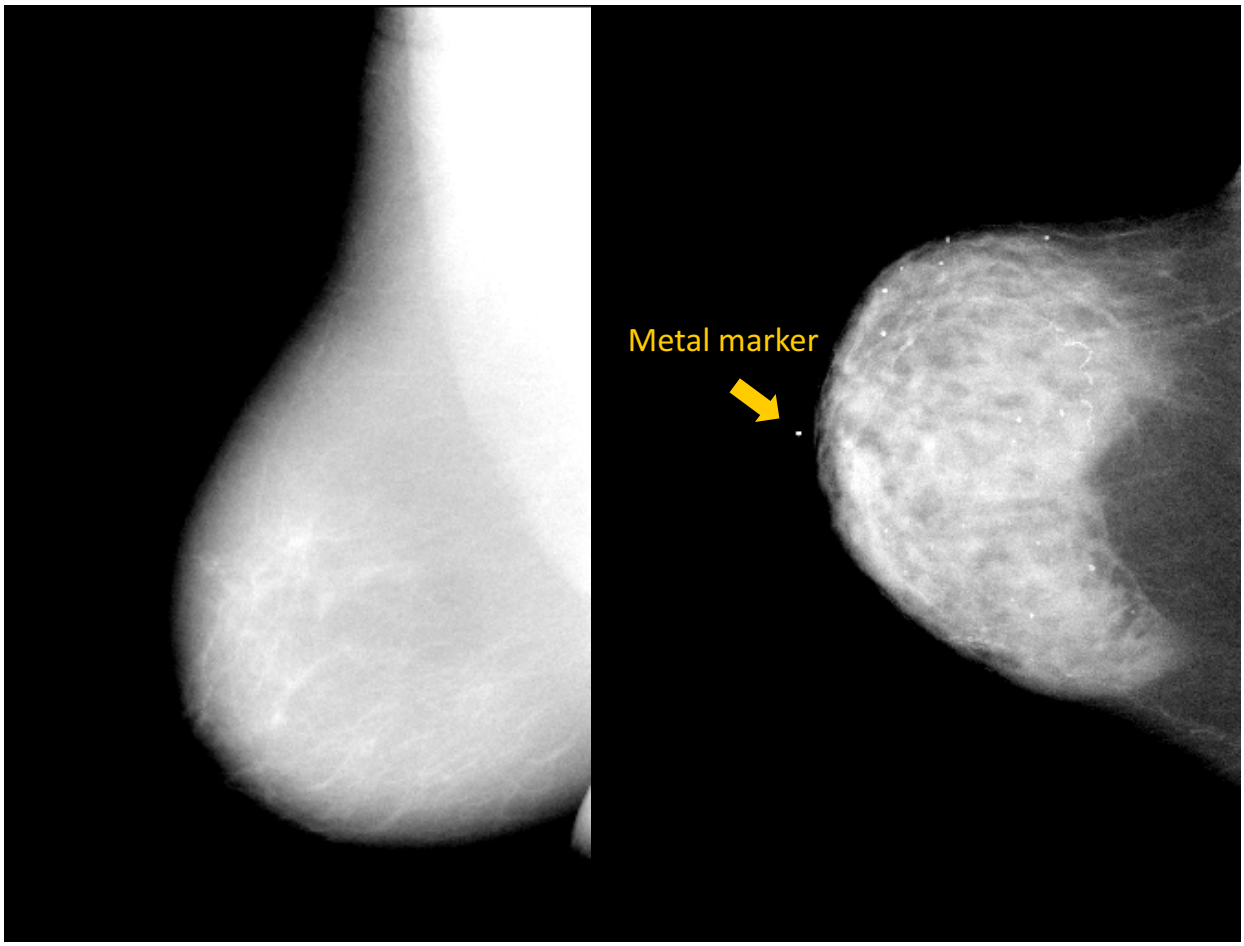

Figure 3.9: Two example projection images to demonstrate the presence and absence of metal. The corresponding μ_{max} values are shown for each.

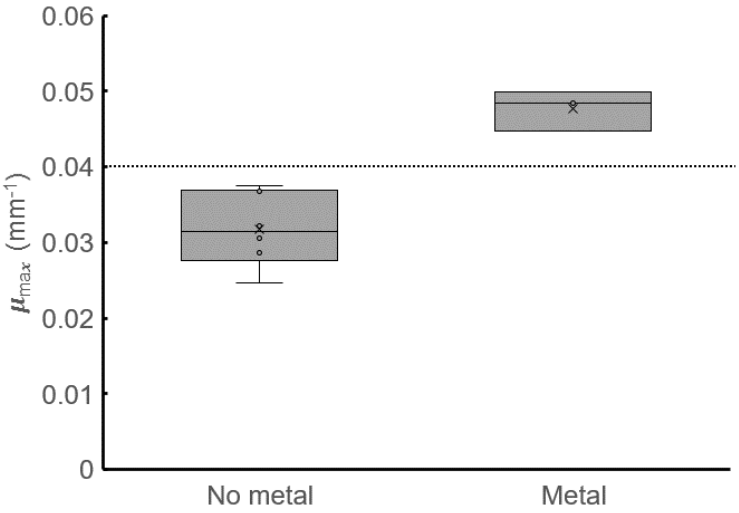

Figure 3.10: A box-plot of the measured μ_{max} values from a clinical breast cohort including cases both with and without metal present. The dashed line indicates $\mu_{max} = 0.04\text{mm}^{-1}$, the empirically chosen threshold.

weighting scheme, respectively.

3.5.1.3 Breast masking

A common problem with iterative reconstruction methods in DBT imaging is severe shading at the breast boundary (see Figure 3.11). One way to both deal with these artifacts and speed up computation is to introduce a 3D breast mask to constrain the reconstruction[156,181]. By preventing updates outside the image object, the reconstruction time is reduced substantially. This improvement is inversely proportional to the fraction of the detector area covered by the breast and in our experience typically reduces the reconstruction time by almost a factor of two. In addition, since voxels outside the object are not being updated, the entire line integral measured through the breast is correctly attributed to the breast voxels, restoring contrast at the edges as shown in Figure 3.11.

In this work, we developed a method to calculate the breast mask. In this method, the mask was generated by identifying the breast boundaries in the projection domain, backprojecting the borders, and filling in to the chest wall. The calculated breast mask was used as the image domain weight, $\mathbf{P}$, in the OS-SPART framework in Equation 3.16. We can recall that we required that P

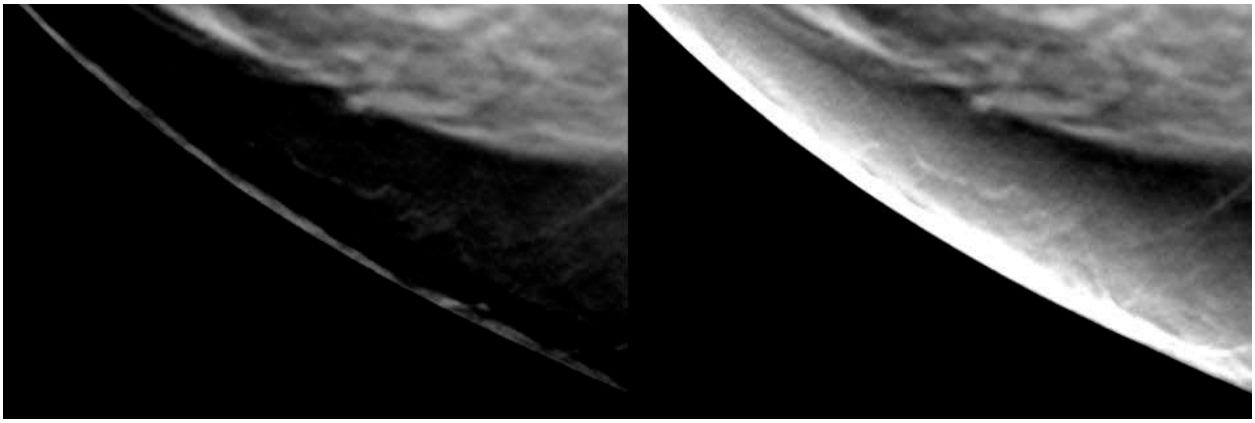

(a) No breast masking (a) With breast masking

Figure 3.11: An example of a breast reconstructed with DOS-SPART reconstructed without (a) and with (b) the breast mask used to constrain the reconstruction. Both images are reconstructed with the same reconstruction parameters out to 250 iterations to ensure convergence. Both images are shown with the same W/L.

be positive semi-definite. In our definition here of $\mathbf{P}$ as a binary breast mask, we meet those criteria since $\mathbf{P}$ is diagonal with diagonal elements of either 0 or 1. A schematic illustrating this workflow is shown in Figure 3.12 and described in detail in Algorithm 1.

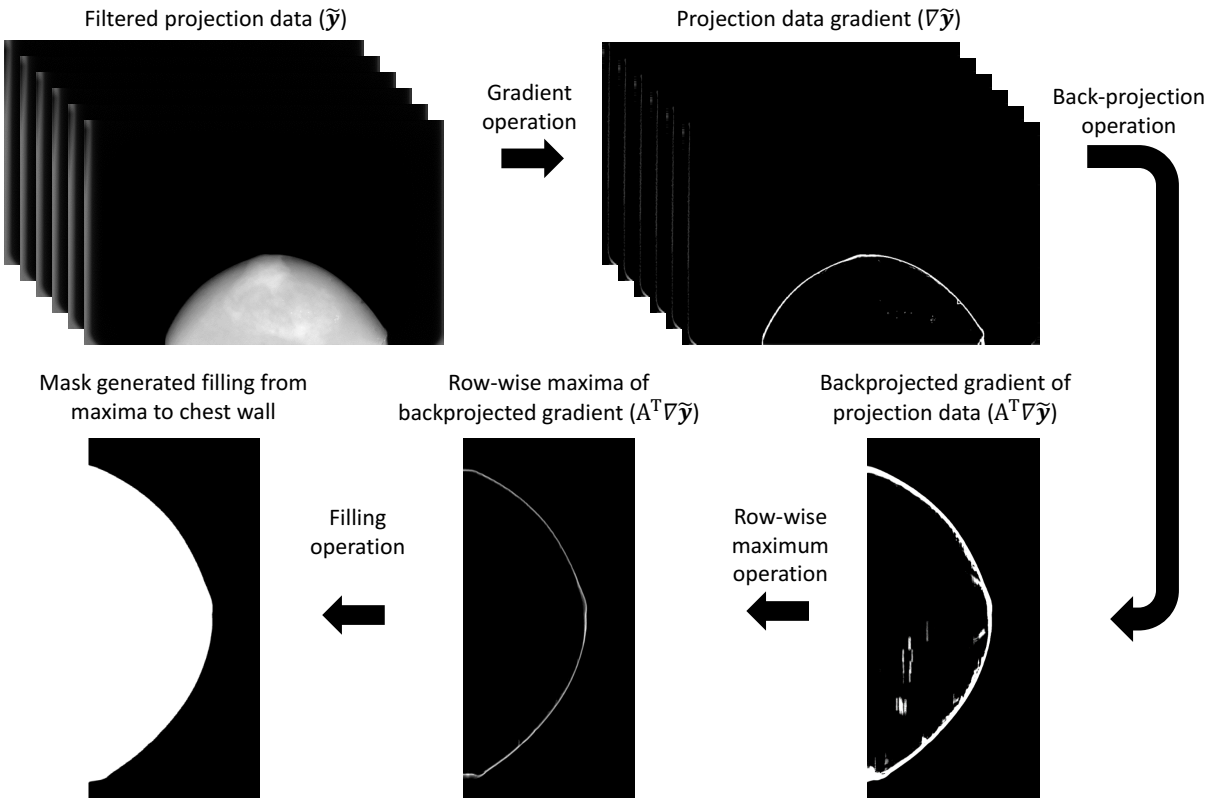

Figure 3.12: The workflow used to calculate the 3D breast mask volume.

Algorithm 1 Breast mask generation

procedure INITIALIZE BREAST MASK($\mathbf{y}, A, thresh_{proj}, thresh_{im}$)
  Blur and threshold projection data:
  $\tilde{\mathbf{y}} = \text{Rect2D} * \mathbf{y}$ ▷ Convolve projection data with box-car filter
  for Each projection datum, i **do**
    if $\tilde{\mathbf{y}}_i < thresh_{proj}$ **then**
      $\tilde{\mathbf{y}}_i = 0$
  Backproject gradient of smoothed projection data:
  $I_{Border} = A^T \nabla \tilde{\mathbf{y}}$ ▷ ∇ indicates the local 2D gradient
  Find and smooth row-wise maximum of gradient volume:
  for iterator $slice = 0; slice < N_s; slice++$ **do** ▷ N_s = number of slices in the image volume
    for iterator $row = 0; row < N_r; row++$ **do** ▷ N_r= number of rows in each image slice
      if $\max\left[I_{Border}(x, row, slice)\right] \geq thresh_{im}$ **then**
        $\mathbf{i}_{max}(row, slice) = \arg\max_x I_{Border}(x, row, slice)$
      else
        $\mathbf{i}_{max}(row, slice) = row_{max}$ ▷ If maximum value below threshold, assign max. index to edge of detector (assume that row has no object present)
    $\tilde{\mathbf{i}}_{max} = \text{Rect1D} * \mathbf{i}_{max}$
  Fill from breast edge to detector edge:
  for Each voxel, $i, row, slice$ **do**
    if $i > \tilde{\mathbf{i}}_{max}(row, slice)$ **then**
      $\mathbf{P}_{i,row,slice} = 1$
    else
      $\mathbf{P}_{i,row,slice} = 0$
  Smooth breast mask:
  for iterator $slice = 0; slice < N_s; slice++$ **do**
    $\tilde{\mathbf{P}}_{slice} = \text{Rect2D} * \mathbf{P}_{slice}$
  $\mathbf{P} \leftarrow \tilde{\mathbf{P}}$
  return P

3.5.1.4 Convergence analysis

In order to determine the appropriate number of iterations needed to achieve convergence, an appropriate convergence criterion needs to be determined. In this work, we use the normalized and averaged variation in the objective function as our criterion [182]. We can recall our objective function from Eq. 3.14 is given as

$$\Phi(\mathbf{x}) = \frac{1}{2}||A\mathbf{x} - \mathbf{y}||^2_{\mathbf{Q}} + \lambda R(\mathbf{x}). \tag{3.24}$$

This can be written explicitly for the two regularizers used in this work as follows:

$$\text{TV}: \ \Phi(\mathbf{x}_k) = \frac{1}{2}||A\mathbf{x}_k - \mathbf{y}||^2_{\mathbf{Q}} + \lambda TV(\mathbf{x}_k) \tag{3.25}$$

and

$$\text{PICCS}: \ \Phi(\mathbf{x}_k) = \frac{1}{2}||A\mathbf{x}_k - \mathbf{y}||^2_{\mathbf{Q}} + \lambda \left[(1-\alpha)TV(\mathbf{x}_k) + \alpha TV(\mathbf{x}_k - \mathbf{x}_P)\right] \tag{3.26}$$

This can be used to calculate the convergence criterion at iteration k as follows:

$$\epsilon(\mathbf{x}_k) = \frac{1}{2}\frac{\left[|\Phi\left(\mathbf{x}_{k-1}\right) - \Phi\left(\mathbf{x}_k\right)|\right] + \left[|\Phi\left(\mathbf{x}_k\right) - \Phi\left(\mathbf{x}_{k+1}\right)|\right]}{\epsilon(\mathbf{x}_{k=1})}, \tag{3.27}$$

where $\mathbf{x}_k$ is the image at iteration k ($k \in \mathbb{N}$). The convergence was investigated initially to determine the required number of iterations needed to achieve empirical convergence, defined here as $\epsilon \leq 10^{-3}$. Convergence was measured in 5 repeated acquisitions of the ACR mammography accreditation phantom acquired at the standard clinical dose where the iteration number was allowed to run out to 250 iterations. The resulting curves were averaged to determine the approximate number of iterations required to achieve empirical convergence.

3.5.1.5 Parameters

The proposed algorithm has many parameters that must be tuned in order to maximize performance. However, in practice it isn't practical to try and optimize the image reconstruction with respect to every possible parameter. Instead, the majority of parameters are fixed in a stable range, and the remaining free parameters are tuned to optimize image quality. The reconstruction parameters used

Table 3.2: Reconstruction parameters.

Parameter	Value
Number of iterations	>50
Number of regularization steps per iteration	10
Number of ordered subsets (views per subset)	5 (3)
Step size (s)	0.75
λ	25
μ	1.25
α (for PICCS regularization)	0.5
Breast mask calculation thresholds	Projection domain: 0.02; Image domain: 0.05
Extrapolation width for truncation correction	400 pixels on each edge of the detector

in this work are summarized in Table 3.2.

3.5.1.6 Implementation

The algorithm described in Section 3.5.1 can be implemented according to the following pseudo-code shown in Algorithm 2 and Algorithm 3 for the TV and PICCS regularizers, respectively. The pseudo-code for the OS-SPART implementation used to perform the data fidelity updates can be found in Algorithm 4. In the implementations described here, a variable-splitting technique along with a soft-shrinkage thresholding operation as described by Li *et al.*[164] is used. The soft-shrinkage operator, $S_\mu(x)$, is defined as follows:

$$\begin{aligned} S_\mu(x) &= x\left(1-\frac{\mu}{|x|}\right)_+ \\ &= \begin{cases} x\left(1-\frac{\mu}{|x|}\right) & \frac{\mu}{|x|}\in(0,1] \\ 0 & \text{else} \end{cases}, \end{aligned} \tag{3.28}$$

where μ is a threshold value selected for a given application. A visual representation of the use of the shrinkage operator is shown in Figure 3.13.

The algorithm was coded in Visual C (Microsoft, Inc., Redmond, WA) and CUDA (NVIDIA Corporation, Santa Clara, CA) and executed on a local workstation. With the current implementation, a single GPU (GTX 1070, NVIDIA, Santa Clara, CA) is used and the total reconstruction time for a standard sized breast ($\approx$ 6 cm) is approximately 70 s to achieve empirical convergence (defined in Section 3.5.1.4).

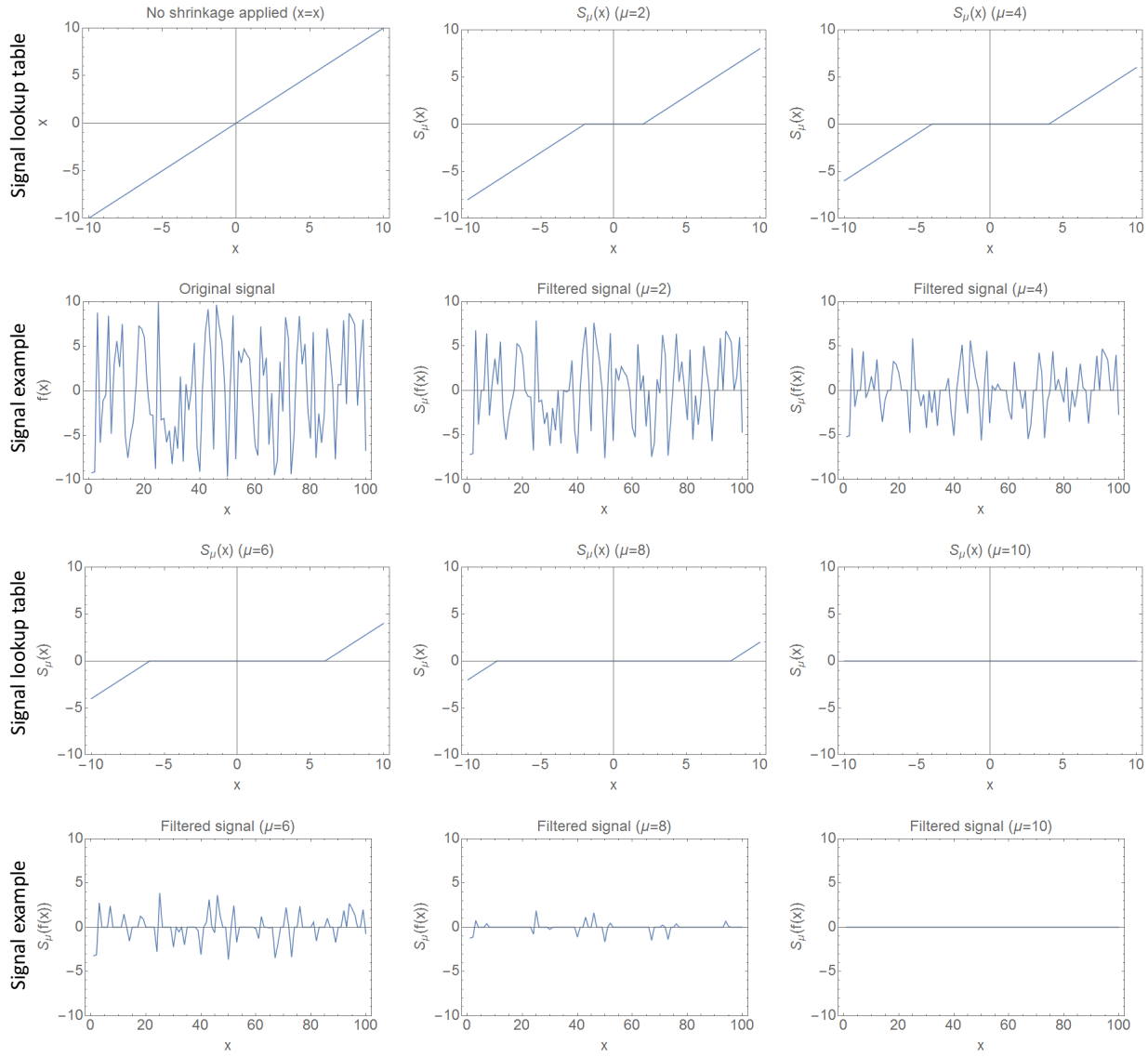

Figure 3.13: An example of the use of the soft-shrinkage operator described in Eq. 3.28. This example illustrates how the shrinkage operator "shrinks" values down as the threshold increases.

Algorithm 2 DOS-SPART: TV Regularizer

$\mathbf{P} \leftarrow$ Breast Mask

$\mathbf{Q} \leftarrow$ Projection counts

$\mathbf{x}^{k=0} \leftarrow \text{FBP}(\mathbf{y})$ ▷ Image can be initialized to zeros, FBP image, etc.

procedure DOS-SPART($\mathbf{x}^k, \mathbf{y}, \mathbf{Q}, \mathbf{P}, A, \lambda, \mu$)

  $k \leftarrow 0$

  while $\epsilon(\mathbf{x}^k) > \epsilon_{\text{Thresh}}$ **do**

    Perform data fidelity update:

    $\mathbf{u}^{k+1} \leftarrow \text{OS} - \text{SPART}(\mathbf{x^k}, \mathbf{y}, \mathbf{Q}, \mathbf{P}, A)$

    Number of regularization steps: N_{ADMM} (N_{ADMM} chosen empirically)

    Initialize intermediate matrices:

    for Each voxel, i **do**

      $\mathbf{D}^{n=0} = \left[u_{i+1}^{k+1} - u^{k+1}, u_{i+M}^{k+1} u_i^{k+1}\right]$

      $\mathbf{B}^{n=0} = [0, 0]$

    Perform regularization:

    $\tilde{\mathbf{x}}^{n=0} = \mathbf{u}^{k+1}$ ▷ ˜ indicates the regularized image

    for iterator $n = 0; n < N_{ADMM}; n++$ **do**

      for Each voxel, i **do**

        $\bar{x}_i^n = 1/4 \left(\tilde{\mathbf{x}}_{i+1}^n + \tilde{\mathbf{x}}_{i+1}^n + \tilde{\mathbf{x}}_{i+M}^n + \tilde{\mathbf{x}}_{i-M}^n\right)$

        $h_i^n = 1/4 \left[\left(D_{x,i-1}^n - D_{x,i}^n\right) + \left(D_{y,i-M}^n - D_{y,i}^n\right) + \left(B_{x,i-1}^n - B_{x,i}^n\right) + \left(B_{y,i-M}^n - B_{y,i}^n\right)\right]$

        $\tilde{\mathbf{x}}_i^n = \frac{\frac{\lambda\mu}{P_i}}{\frac{\lambda\mu}{P_i}+4} \mathbf{u}_i^{k+1} + \frac{4}{\frac{\lambda\mu}{P_i}+4} \left(\bar{x}_i^n + h_i^n\right)$

        $\mathbf{E}_i^n = \left[\left(\tilde{\mathbf{x}}_{i+1}^n - \tilde{\mathbf{x}}_i^n\right) - \mathbf{B}_{x,i}^n, \left(\tilde{\mathbf{x}}_{i+M}^n - \tilde{\mathbf{x}}_i^n\right) - \mathbf{B}_{y,i}^n\right]$

        $||\mathbf{E}_i^n||_2 = \sqrt{\left(\mathbf{E}_{x,i}^n\right)^2 + \left(\mathbf{E}_{y,i}^n\right)^2}$

        $\mathbf{D}_i^n = \left[\left(S_\mu\left(\left|E_{x,i}^n\right|\right) \frac{E_{x,i}^n}{||\mathbf{E}_i^n||_2}\right), \left(S_\mu\left(\left|E_{y,i}^n\right|\right) \frac{E_{y,i}^n}{||\mathbf{E}_i^n||_2}\right)\right]$

        $\mathbf{B}_i^n = \mathbf{D}_i^n - \mathbf{E}_i^n$

    $k++$

    $\mathbf{x}^k = \tilde{\mathbf{x}}^n$

  return $\mathbf{x}^k$

  Notes:

  1. Anywhere the "Each pixel" notation is used, the implementation is pixel parallel and well suited to GPU implementation.

  2. We assume row-wise ordering for image matrices and that each image row contains M elements; thus, the index $i + M$ corresponds to the location one row down from the location i.

  3. We assume the matrices $\mathbf{B}$, $\mathbf{D}$, and $\mathbf{E}$ each have two elements at each pixel location, x, and y such that: $\mathbf{D^n} = [D_x^n, D_y^n]$.

Algorithm 3 DOS-SPART: PICCS Regularizer

1: $\mathbf{P} \leftarrow$ Breast Mask
2: $\mathbf{Q} \leftarrow$ Projection counts
3: $\mathbf{x}^{k=0} \leftarrow \text{FBP}(\mathbf{y})$ ▷ Image can be initialized to zeros, FBP image, etc.
4: $\mathbf{x}_p \leftarrow \mathbf{x}^k$ ▷ Here we use the FBP image as a prior
5: **procedure** DOS-SPART($\mathbf{x}^k, \mathbf{x}_p, \mathbf{y}, \mathbf{Q}, \mathbf{P}, A, \lambda, \mu, \alpha$)
6: $k \leftarrow 0$
7: **while** $\epsilon(\mathbf{x}^k) > \epsilon_{\text{Thresh}}$ **do**
8: **Perform data fidelity update:**
9: $\mathbf{u}^{k+1} \leftarrow \text{OS} - \text{SPART}(\mathbf{x}^{\mathbf{k}}, \mathbf{y}, \mathbf{Q}, \mathbf{P}, A)$
10: Number of regularization steps: N_{ADMM} (N_{ADMM} chosen empirically)
11: **Initialize intermediate matrices:**
12: **for** Each voxel, i **do**
13: $\mathbf{D}^{n=0} = \left[u_{i+1}^{k+1} - u^{k+1}, u_{i+M}^{k+1} u_i^{k+1}\right]$
14: $\mathbf{D}_p^{n=0} = \left[\left(u_{i+1}^{k+1} - u^{k+1}\right) - \left(\mathbf{x}_{p,i+1} - \mathbf{x}_{p,i}\right), \left(u_{i+M}^{k+1} - u_i^{k+1}\right) - \left(\mathbf{x}_{p,i+M} - \mathbf{x}_{p,i}\right)\right]$
15: $\mathbf{B}^{n=0} = [0,0];\ \mathbf{B}_p^{n=0} = [0,0]$
16: **Perform regularization:**
17: $\tilde{\mathbf{x}}^{n=0} = \mathbf{u}^{k+1}$
18: **for** iterator $n = 0; n < N_{ADMM}; n++$ **do**
19: **for** Each voxel, i **do**
20: $\bar{x}_i^n = 1/4\left(\tilde{\mathbf{x}}_{i+1}^n + \tilde{\mathbf{x}}_{i+1}^n + \tilde{\mathbf{x}}_{i+M}^n + \tilde{\mathbf{x}}_{i-M}^n\right)$
21: $\bar{x}_{p,i}^n = 1/4\left(\mathbf{x}_{p,i+1} + \mathbf{x}_{p,i+1} + \mathbf{x}_{p,i+M} + \mathbf{x}_{p,i-M}\right)$
22: $h_i^n = 1/4\left[\left(D_{x,i-1}^n - D_{x,i}^n\right) + \left(D_{y,i-M}^n - D_{y,i}^n\right) + \left(B_{x,i-1}^n - B_{x,i}^n\right) + \left(B_{y,i-M}^n - B_{y,i}^n\right)\right]$
23: $h_{p,i}^n = 1/4\left[\left(D_{p,x,i-1}^n - D_{p,x,i}^n\right) + \left(D_{p,y,i-M}^n - D_{p,y,i}^n\right)\right.$
24: $\left. + \left(B_{p,y,i-1}^n - B_{p,x,i}^n\right) + \left(B_{p,y,i-M}^n - B_{p,y,i}^n\right)\right]$
25: $\tilde{\mathbf{x}}_i^n = \frac{\frac{\lambda\mu}{P_i}}{\frac{\lambda\mu}{P_i}+8}\mathbf{u}_i^{k+1} + \frac{4}{\frac{\lambda\mu}{P_i}+8}\left(2\bar{x}_i^n + \mathbf{x}_{p,i} - \bar{x}_{p,i}^n + h_i^n + h_{p,i}^n\right)$
26: $\mathbf{E}_i^n = \left[\left(\tilde{\mathbf{x}}_{i+1}^n - \tilde{\mathbf{x}}_i^n\right) - \mathbf{B}_{x,i}^n, \left(\tilde{\mathbf{x}}_{i+M}^n - \tilde{\mathbf{x}}_i^n\right) - \mathbf{B}_{y,i}^n\right]$
27: $\mathbf{E}_{p,i}^n = \left[\left(\tilde{\mathbf{x}}_{i+1}^n - \tilde{\mathbf{x}}_i^n\right) - \mathbf{B}_{p,x,i}^n - \left(\mathbf{x}_{p,i+1} - \mathbf{x}_{p,i}\right), \left(\tilde{\mathbf{x}}_{i+M}^n - \tilde{\mathbf{x}}_i^n\right) - \mathbf{B}_{p,y,i}^n - \left(\mathbf{x}_{p,i+M} - \mathbf{x}_{p,i}\right)\right]$
28: $||\mathbf{E}_i^n||_2 = \sqrt{\left(\mathbf{E}_{x,i}^n\right)^2 + \left(\mathbf{E}_{y,i}^n\right)^2}$
29: $\mathbf{D}_i^n = \left[\left(S_{(1-\alpha)\mu}\left(\left|E_{x,i}^n\right|\right)\frac{E_{x,i}^n}{||\mathbf{E}_i^n||_2}\right), \left(S_{(1-\alpha)\mu}\left(\left|E_{y,i}^n\right|\right)\frac{E_{y,i}^n}{||\mathbf{E}_i^n||_2}\right)\right]$
30: $\left|\left|\mathbf{E}_{p,i}^n\right|\right|_2 = \sqrt{\left(\mathbf{E}_{p,x,i}^n\right)^2 + \left(\mathbf{E}_{p,y,i}^n\right)^2}$
31: $\mathbf{D}_{p,i}^n = \left[\left(S_{\alpha\mu}\left(\left|E_{p,x,i}^n\right|\right)\frac{E_{p,x,i}^n}{||\mathbf{E}_{p,i}^n||_2}\right), \left(S_{\alpha\mu}\left(\left|E_{p,y,i}^n\right|\right)\frac{E_{p,y,i}^n}{||\mathbf{E}_{p,i}^n||_2}\right)\right]$
32: $\mathbf{B}_i^n = \mathbf{D}_i^n - \mathbf{E}_i^n;\ \mathbf{B}_{p,i}^n = \mathbf{D}_{p,i}^n - \mathbf{E}_{p,i}^n$
33: $k++$
34: $\mathbf{x}^k = \tilde{\mathbf{x}}^n$
35: **return** $\mathbf{x}^k$
36: **Notes:**
37: 1. The PICCS parameter, α, is only seen in the the soft shrinkage operations performed in lines 29 and 31.

Algorithm 4 OS-SPART

procedure OS-SPART($\mathbf{x}^k, \mathbf{y}, \mathbf{Q}, \mathbf{P}, A$)
  $k \leftarrow 0$
  $\mathbf{x}' \leftarrow \mathbf{x}^k$ ▷ $'$ notation here indicates a temporary variable, not a differential
  For 15 view DBT:
  Number of subsets : $\mathrm{N_{SS}} = 5$
  Number of views per subset : $\mathrm{N_{VSS}} = 3$
  for iterator $nS = 0; nS < N_{SS}; nS++$ **do**
    for iterator $nView = 0; nView < N_{VSS}; nView++$ **do**
      Calculate current view number, i: $i = nS + nView \times (N_{SS})$
      Forward projection: $\mathbf{y_i'} = A_i\mathbf{x}$'
      Calculate and weight difference projection: $\mathbf{y_i}'' = Q_i\left(\mathbf{y} - \mathbf{y_i}'\right)$
      Backproject difference onto image volume: $\mathbf{x}' = \mathbf{x}' + \mathbf{P}A_i^T\mathbf{y}''$
  $\mathbf{u}^{k+1} \leftarrow \mathbf{x}'$
  return $\mathbf{u}^{k+1}$

3.5.2 Image quality assessment

3.5.2.1 Through-plane blurring

Through-plane blurring in the reconstructed images was assessed using the ASF defined in Equation 3.12. In this work, both the 540 and 400 μm microcalcifications in the ACR mammography accreditation phantom were used to measure the ASF. The ASF was measured for all 6 of the calcifications of each size in 5 separate acquisitions. The measured full width half maximum (FWHM), full width quarter maximum (FWQM), and full width tenth maximum (FWTM) were measured to perform a quantitative comparison.

A two-sample t-test was used to compare the means of the measured values for each metric and determine statistical significance. In all cases, the null hypothesis was that the means were the same, $H_0 : \mu_1 = \mu_2$, and thus the alternative hypothesis was a difference in the mean measured value, $H_1 : \mu_1 > \mu_2$.

3.5.2.2 Spatial resolution characteristics

In addition, the spatial resolution was measured using a line profile through the high contrast 540 μm and 400 μm calcifications in the ACR mammography phantom, corresponding to the two largest clusters of calcifications seen in Figure 2.1. The spatial resolution was measured using a

radial average line profile through the high contrast 540 μm and 400 μm calcifications in the ACR mammography phantom. To calculate this profile, the center of mass of the calcification was found and a radial profile about that center was computed. Each profile was then normalized such that the peak had a value of 1 and the tail a value of 0. This was performed for each of the six calcifications of each size in all five repeated scans, so the final curves are the average of 30 total curves at each dose level. To quantify the width of the curve, the half width half maximum (HWHM) in each case was measured. A two-sample t-test was used to compare the mean widths for each DOS-SPART method with the commercial method and determine statistical significance. In all cases, the null hypothesis was that the mean widths were the same, $H_0 : \mu_1 = \mu_2$, and thus the alternative hypothesis was a difference in the mean measured value, $H_1 : \mu_1 > \mu_2$.

3.6 Results

3.6.1 Convergence

Using the convergence criteria defined in Eq. 3.27, it was found that the stopping criterion of 10^{-3} was achieved in approximately 30-50 iterations for both regularizers. Nevertheless, each method approaches convergence as defined by small variation in the objective function value for large iteration numbers. The PICCS regularized reconstructions more rapidly achieved the desired threshold of 10^{-3}, however both achieve that threshold by around 50 iterations. For the remainder of the work presented here, 50 iterations were used to ensure empirical convergence was achieved.

3.6.2 Image quality assessment

3.6.2.1 Through-plane blurring

The larger (540 μm) calcification cluster from the ACR phantom is shown in focus and in planes 5 and 10 mm above and below the focal plane using each of the three reconstruction methods in Figure 3.15. The residual signal artifacts in the commercial reconstruction method are still quite strong at $\pm$10 mm, whereas in the DOS-SPART reconstructions (TV or PICCS regularization) the signal leakage is almost negligible already at $\pm$5 mm. The measured ASF curves for the 540

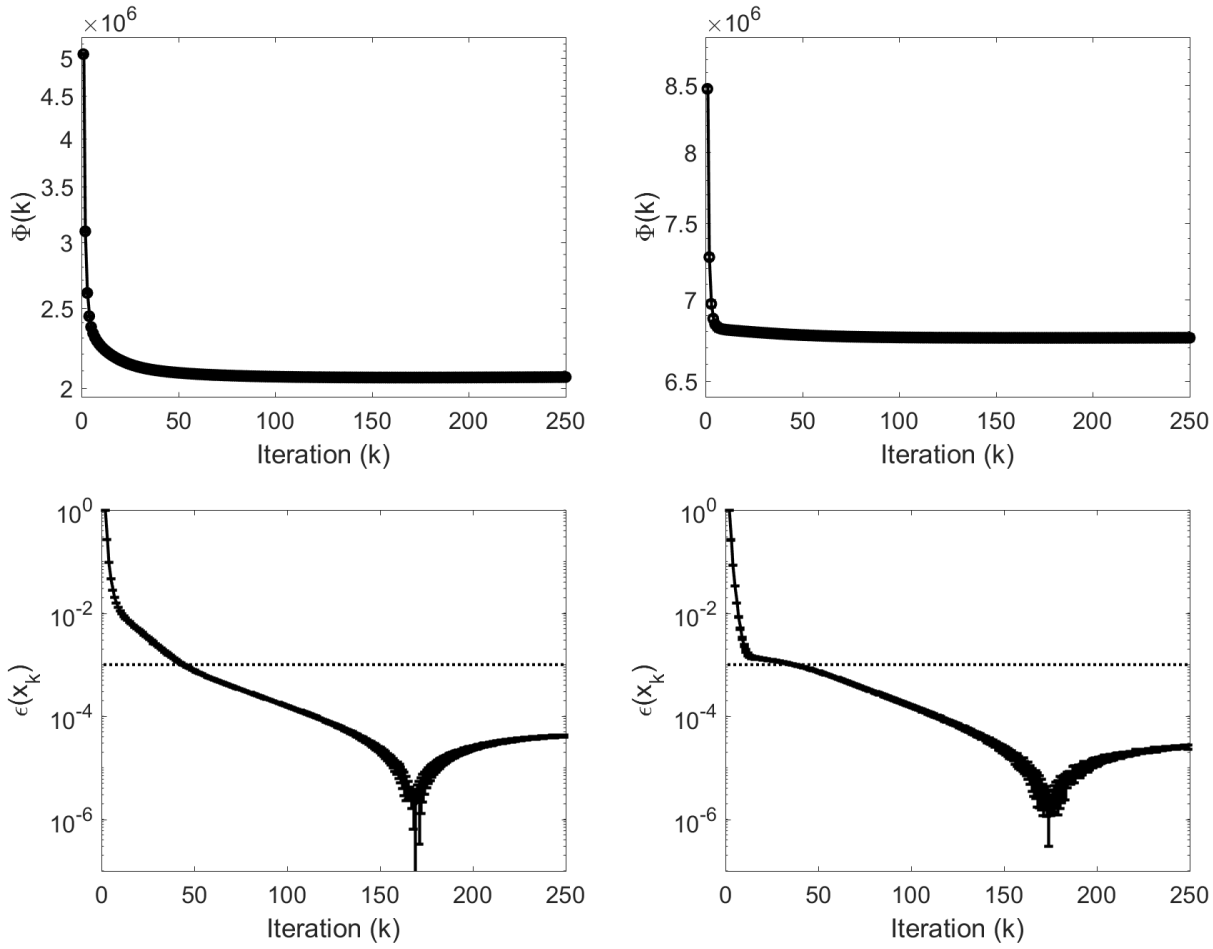

Figure 3.14: Plots of the objective function (top) and normalized convergence criteria (bottom) from Eq. 3.27 is shown for the TV (a) and PICCS (b) regularized implementations. Error bars denote the measured standard deviation between measured curves. The dashed line in the plots in the bottom row indicates 10^{-3}.

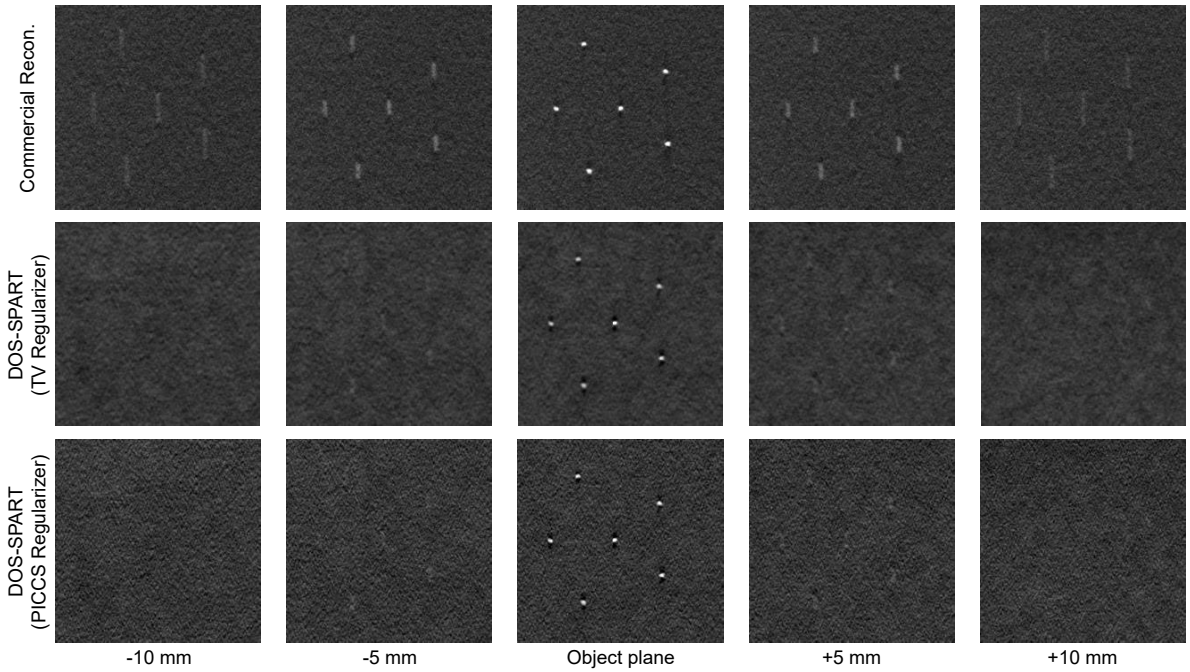

Figure 3.15: The calcification objects in the ACR phantom used for the ASF measurements. The objects are shown in focus as well as ±5 and ±10 mm away. The images shown are from the same acquisition and all images are shown with the same W/L.

μm and 400 μm calcification objects are shown in Figure 3.16, while the corresponding FWHM, FWQM, and FWTM measurements are shown in Figure 3.17. The statistical significance of the differences in ASF width measurements is shown in Table 3.3. We can see from the ASF curves and box plots that DOS-SPART (regardless of regularizer) improved the tails of the ASF compared with the commercial reconstruction method. This improvement over the commercial reconstruction was statistically significant in all cases for the FWTM value, the greatest extent of the artifacts. The difference in ASF width between the two regularizers was much less dramatic, and wasn't statistically significant in all cases, however the measured width parameters were slightly smaller using the PICCS regularizer rather than the TV only regularizer in each case except the FWHM for the smaller calcifications.

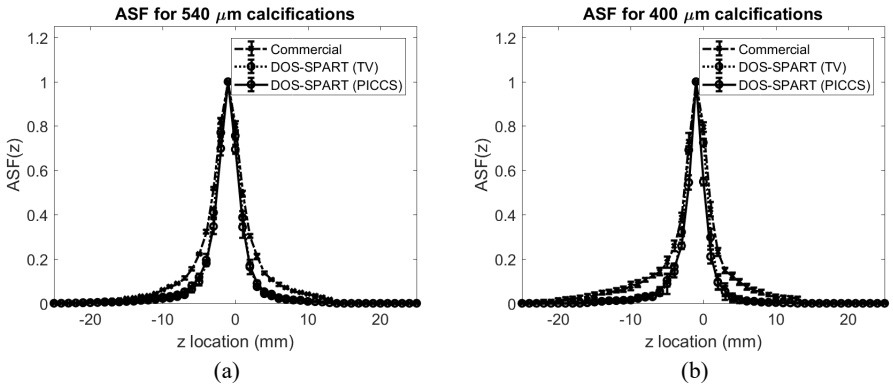

Figure 3.16: The mean measured ASF in the reconstructed images using each reconstruction method. Error bars denote the standard deviation of the measurement.

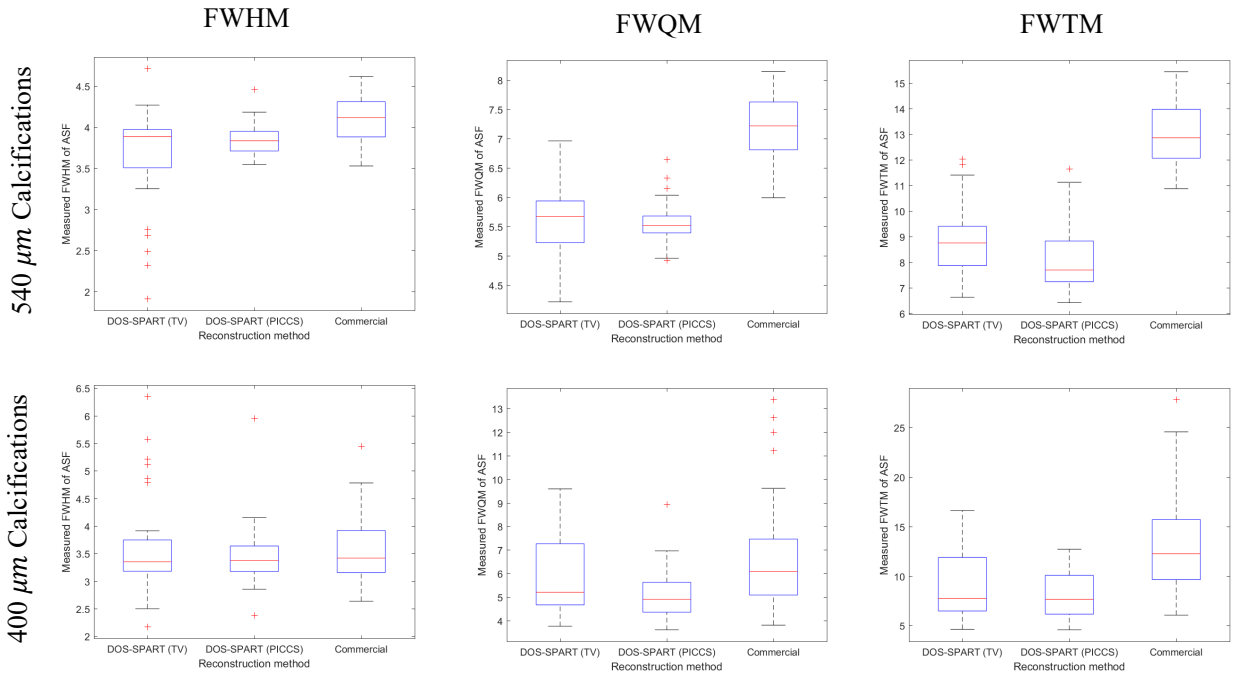

Figure 3.17: Distribution of the measured widths of the ASF curves for the three reconstruction methods.

Table 3.3: The statistical significance of the differences in measured ASF widths for the different reconstruction methods. Cases where the null hypothesis could not be rejected (95% confidence) are indicated in bold.

540μm Calcifications			
Measurement	Commercial> DOS-SPART (TV)	Commercial> DOS-SPART (PICCS)	DOS-SPART(PICCS)≠ DOS-SPART (TV)
FWHM	p<0.001	p<0.001	**p > 0.05**
FWQHM	p<0.001	p<0.001	**p > 0.05**
FWTM	p<0.001	p<0.001	p<0.04
400μm Calcifications			
Measurement	Commercial> DOS-SPART (TV)	Commercial> DOS-SPART (PICCS)	DOS-SPART(PICCS)≠ DOS-SPART (TV)
FWHM	**p > 0.05**	**p > 0.05**	**p > 0.05**
FWQHM	**p > 0.05**	p<0.02	p<0.04
FWTM	p<0.02	p<0.001	**p > 0.05**

Table 3.4: The measured HWHM of the average radial profile through the 540 μm calcification at each dose level. A smaller HWHW indicates improved spatial resolution. An asterisk indicates the measurement is significantly different from the commercial value (p<0.01).

	HWHM (mm)				
Relative dose	100%	80%	60%	40%	20%
Commercial recon.	0.12 ± 0.01	0.12 ± 0.01	0.13 ± 0.01	0.13 ± 0.02	0.13 ± 0.03
DOS-SPART (TV)	0.12 ± 0.02	0.12 ± 0.02	0.13 ± 0.01	0.13 ± 0.02	0.13 ± 0.02
DOS-SPART (PICCS)	$0.11 \pm 0.01^*$	$0.11 \pm 0.02^*$	$0.11 \pm 0.02^*$	$0.11 \pm 0.02^*$	$0.11 \pm 0.03^*$

3.6.2.2 Spatial resolution characteristics

The measured profiles through the calcifications are shown in Figures 3.18 and 3.19. The corresponding width measurements are shown in Table 3.4 and Table 3.5. The measurements show that regardless of regularizer, DOS-SPART was able to at least maintain spatial resolution for small high contrast objects compared with the commercial reconstruction. In addition, for all dose levels and calcification sizes considered here, the spatial resolution using the PICCS regularization was actually improved (statistically significant in all cases with p<0.01) compared with the commercial reconstruction.

3.6.2.3 Clinical image results

Four clinical examples are presented in Figure 3.20. In the first case (Figure 3.21), a cluster of calcifications in a heterogeneously dense breast (BIRADS density: (c); R CC view) from a 40-year-old

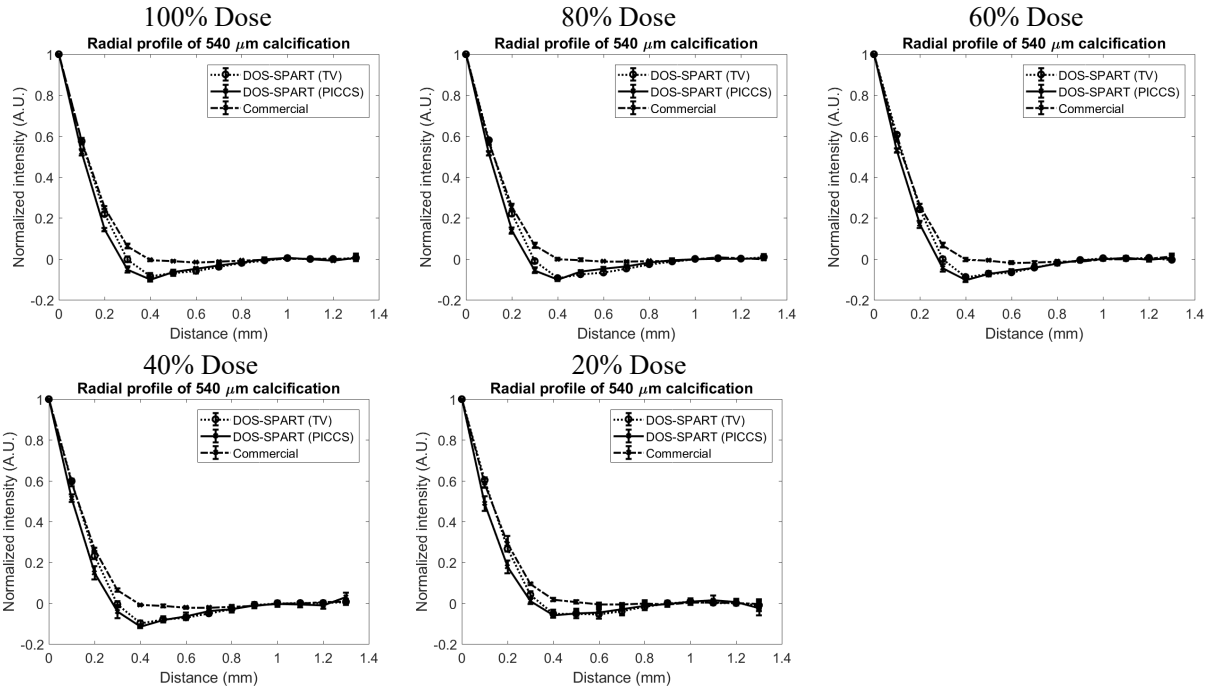

Figure 3.18: The average radial profiles through the 540 μm calcifications in the ACR accreditation phantom at each dose level. Error bars denote the standard deviation.

Table 3.5: The measured HWHM of the average radial profile through the 400 μm calcification at each dose level. A smaller HWHW indicates improved spatial resolution. An asterisk indicates the measurement is significantly different from the commercial value ($p<0.01$).

	HWHM (mm)				
Relative dose	100%	80%	60%	40%	20%
Commercial recon.	0.09 ± 0.01	0.09 ± 0.01	0.09 ± 0.01	0.09 ± 0.02	0.09 ± 0.02
DOS-SPART (TV)	0.10 ± 0.01	0.10 ± 0.01	0.09 ± 0.01	0.10 ± 0.02	0.10 ± 0.02
DOS-SPART (PICCS)	$0.08 \pm 0.01^*$	$0.08 \pm 0.01^*$	$0.07 \pm 0.01^*$	$0.08 \pm 0.01^*$	$0.07 \pm 0.02^*$

woman is shown. This cluster of calcifications is well focused and conspicuous in the focal plane in all of the reconstructions, however in the commercial reconstruction the residual signal from the cluster is clearly visible and distracting in the reconstructed slices 10 mm above and below the cluster.

In the second case (Figure 3.22), a highly calcified dense mass in a fatty breast (BIRADS density: (a); R CC view) of a 69-year-old woman is shown. Subjectively, this is a very interesting pathology with many different high contrast features present. However, the superposition of the high contrast features in the commercial reconstruction leads to substantial signal leakage and reduced sharpness.

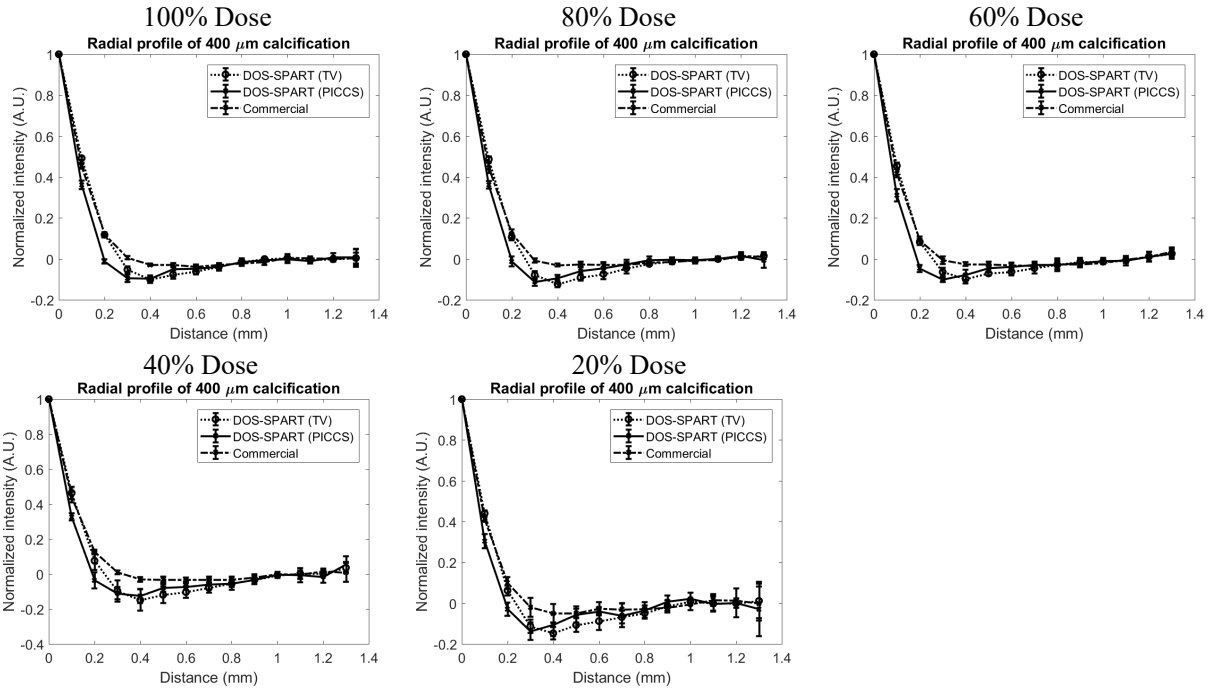

Figure 3.19: The average radial profiles through the 400 μm calcifications in the ACR accreditation phantom at each dose level. Error bars denote the standard deviation.

The margins of the mass as well as the calcified structures are difficult to distinguish, and the different layers of the mass are not well separated. In the DOS-SPART reconstructions, the signal leakage is substantially reduced, and the individual layers of the mass may be clearly seen.

In the third case (Figure 3.23), a spiculated mass with calcifications in a breast with scattered fibroglandular tissue (BIRADS density: (b); R CC view) of a 67-year-old woman is shown. In this case, as with the previous, the high density tissue and calcifications result in substantial through plane blurring in the commercial reconstruction. The result is sharper in-focus high contrast objects in the DOS-SPART reconstructions.

In the fourth case (Figure 3.24), a spiculated mass with calcifications in a breast with scattered fibroglandular tissue (BIRADS density: (c); R CC view) of a 67-year-old woman is shown. This case demonstrates some of the issues with FBP at the boundaries of the breast, where the skin line is incorrectly visualized, and through plane blurring obscure the subcutaneous fat.

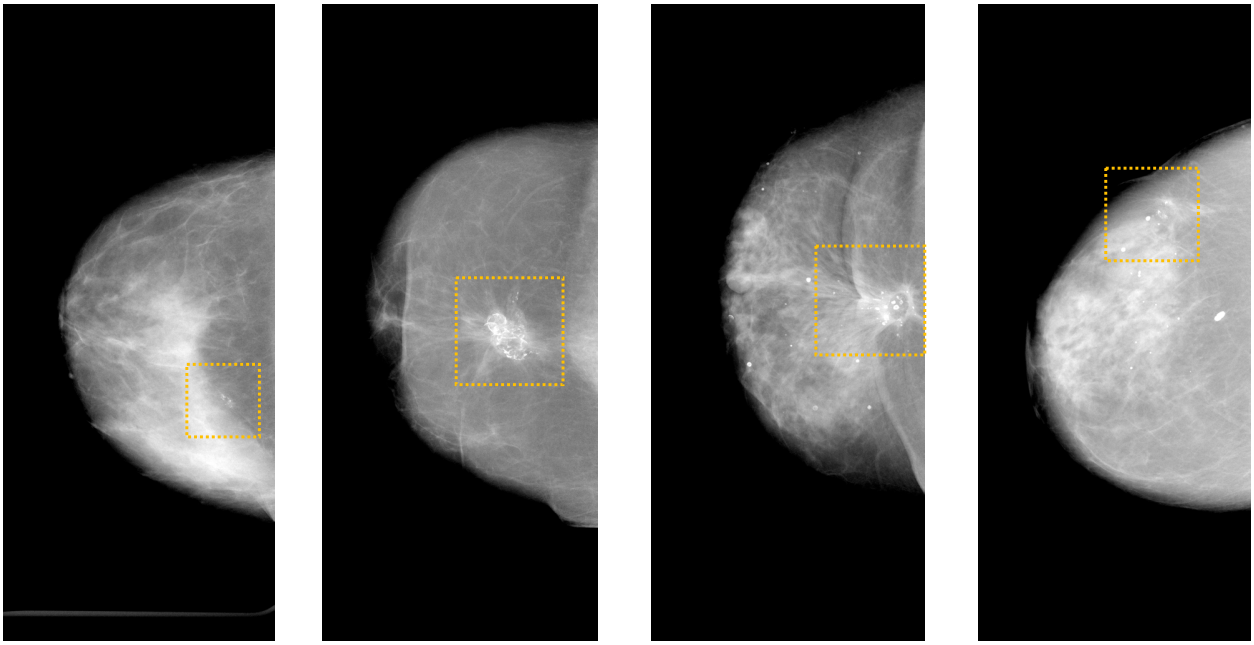

Figure 3.20: Projection images of the four clinical breast examples. The gold square indicates the region depicted in Figures 3.21, 3.22, 3.23, and 3.24.

3.7 Discussion and conclusions

We have demonstrated that the DOS-SPART algorithm may be applied to DBT acquisitions with a clinical system. The resulting images feature significantly reduced through plane blurring and can be achieved in a clinically relevant time of a minute or two for a clinical case. The major benefit DOS-SPART offers is that it (and potentially other model based iterative reconstruction techniques) can be used to reduce the effective slice thickness in DBT acquisitions for DBT systems with smaller angular spans used to acquire data. To alleviate the through-plane signal leakage problem in other clinical systems, both hardware and software solutions have been investigated in the past several years. For example, some commercial systems have increased the angular span of the acquisition since larger tomo-angles lead to better through-plane spatial resolution. However, this method does have some other concerns. First, increasing the angular span requires a prolonged data acquisition time, thus increasing inadvertent motion artifacts. For patient safety, in clinical systems the gantry's speed is limited. Thus, increasing the tomographic angle requires a longer scan as seen in Table 2.1.

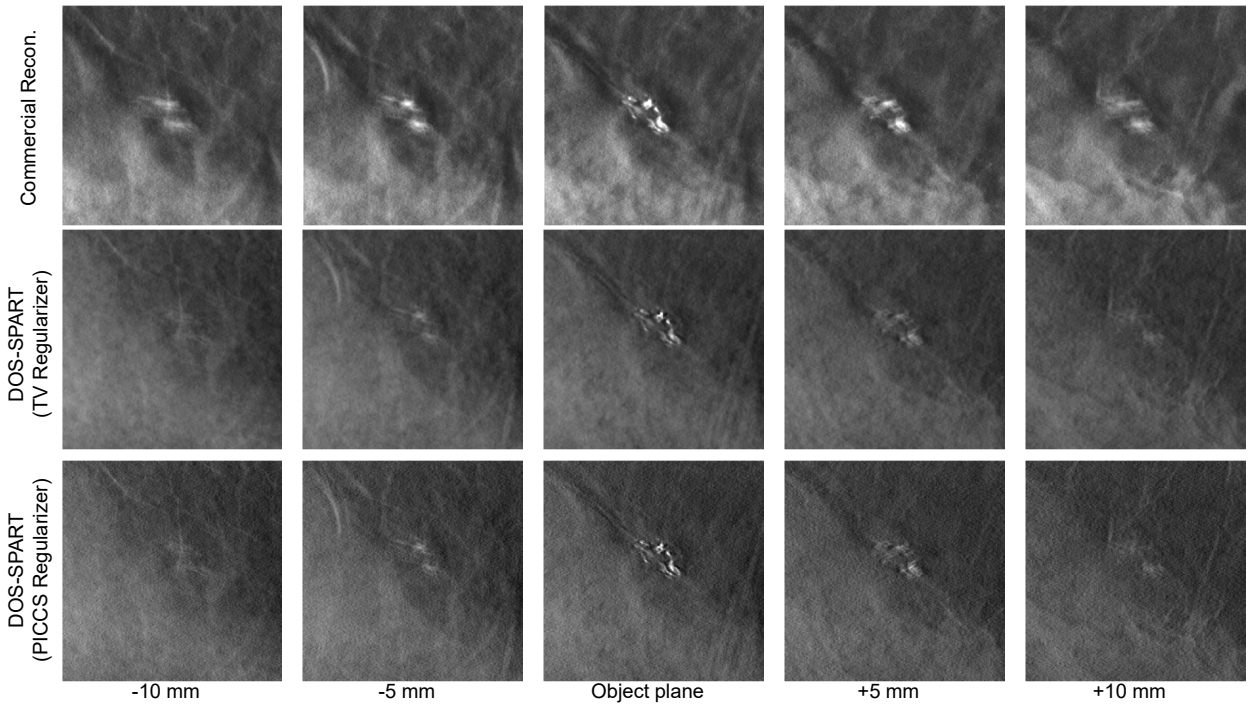

Figure 3.21: A cluster of calcifications in a clinical DBT exam reconstructed with the commercial reconstruction engine (top), DOS-SPART (TV Regularizer) (middle), and DOS-SPART (PICCS Regularizer) (bottom) is shown in focus and at locations above and below the focal plane in the z direction. All image shown with the same W/L.

Second, the view angle sampling rate is often reduced at the cost of increasing view angle span. This reduction in view angle sampling rate exacerbates view angle aliasing artifacts in the reconstructed images. Third, if the view angle sampling rate remains unchanged, then the radiation exposure level at each view angle must be reduced due to the overall dose constraint of the total DBT acquisition. The reduced exposure level at each view angle leads to more severe photon starvation artifacts, especially at more oblique view angles which have longer path lengths for a compressed breast. Fourth, the increased view angle span may also lead to a reduced effective detector pixel size for a rocking acquisition geometry [152]. Due to these potential challenges, a smaller angular span in clinical DBT systems is highly desirable, provided the through-plane artifacts level can be reduced, improving its through-plane resolution.

An interesting comparison which can be made as well is between the two regularizers used in this work. The most significant through plane artifacts were mitigated, regardless of regularizer

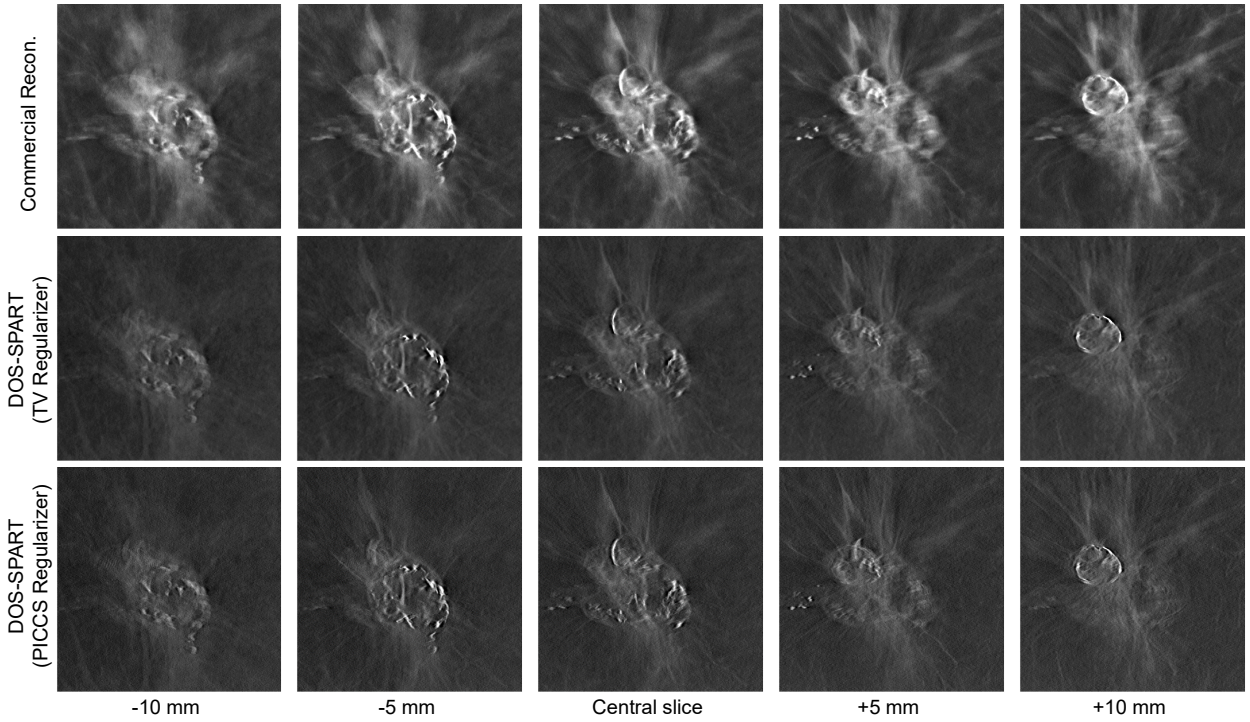

Figure 3.22: A highly calcified dense mass in a clinical DBT exam reconstructed with the commercial reconstruction engine (top), DOS-SPART (TV Regularizer) (middle), and DOS-SPART (PICCS Regularizer) (bottom) is shown at different z locations. All image shown with the same W/L.

used, however the PICCS regularization not only improved spatial resolution compared the the TV only regularization, it actually was able to further reduce the through plane blurring as well. In addition, it showed a more rapid convergence, with the PICCS regularized images approaching the empirical convergence criteria on average in around 35-40 iterations rather than 50.

Interestingly, if we recall the convergence plots shown in Figure 3.14, we may have noticed there is some odd behavior in the curves once they hit a small enough value ($\approx 10^{-5} - 10^{-6}$). We see the curve drops rapidly before a small "bounce". This shouldn't happen for a convex optimization problem, and merits further investigation, however one reason this could occur is that when the image approaches convergence the relative update size approaches numerical precision. The objective function is evaluated for the entire image volume ($1890 \times 2457 \times 62$ voxels). We can thus elect to modify our definition of the convergence criteria from Equation 3.27, by normalizing by the number of voxels rather than the value at the first iterations (providing an approximation of the update

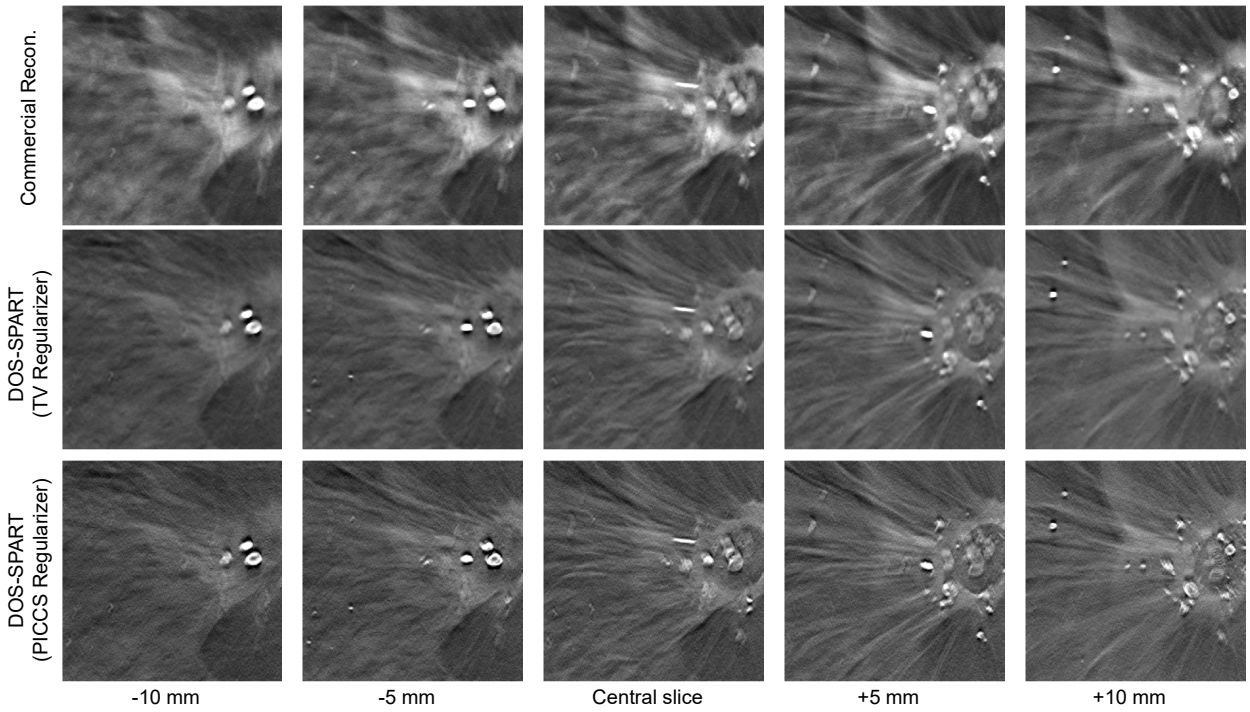

Figure 3.23: A dense, spiculated mass in a clinical DBT exam reconstructed with the commercial reconstruction engine (top), DOS-SPART (TV Regularizer) (middle), and DOS-SPART (PICCS Regularizer) (bottom) is shown at different z locations. All image shown with the same W/L.

magnitude in each voxel), as follows:

$$\epsilon_{mod}(\mathbf{x}_k) = \frac{1}{2}\frac{[|\Phi(\mathbf{x}_{k-1}) - \Phi(\mathbf{x}_k)|] + [|\Phi(\mathbf{x}_k) - \Phi(\mathbf{x}_{k+1})|]}{\mathrm{N}_{\mathrm{voxels}}}. \tag{3.29}$$

The convergence values using this new metric are shown in Figure 3.25. We can see here that the update size per voxel is approaching $\approx 10^{-8} - 10^{-9}$. Per the current IEEE standard[183] (used in Visual C and CUDA) for 32-bit precision floating point numbers, the mantissa (significand field) of the number is stored using 23 bits plus one implicit bias or offset digit (inherent to compiler) for a total of 24 bits of precision. The remaining bits are used to indicate the sign (1 bit) and exponent (8 bits) for a total of 32 bits. Given the 24 bit precision for the mantissa, the maximum value number of decimal digits is approximately 7.2 ($\log_{10}(2^{24}) \approx 7.2$). This limitation means that performing updates on the order of 10^{-8} fall below machine precision and could result in increasing imprecision over subsequent iterations as seen in Figure 3.25.

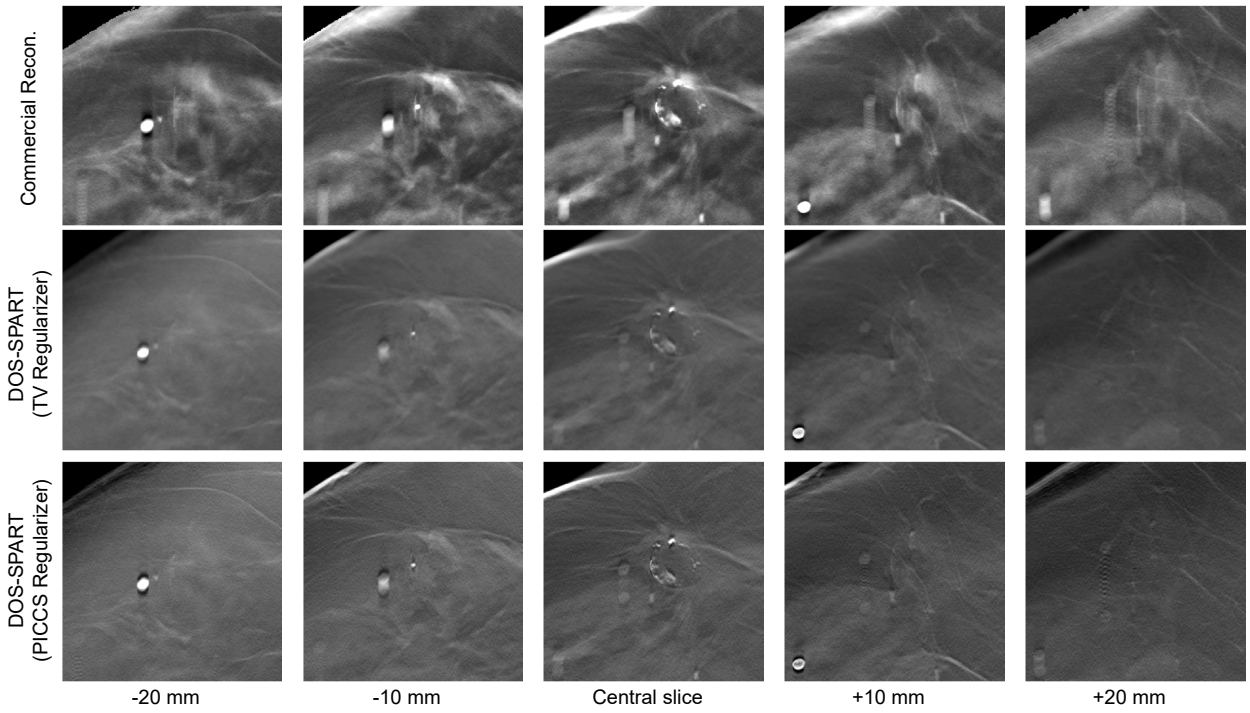

Figure 3.24: A boundary region in a clinical DBT exam reconstructed with the commercial reconstruction engine (top), DOS-SPART (TV Regularizer) (middle), and DOS-SPART (PICCS Regularizer) (bottom) is shown at different z locations. All image shown with the same W/L.

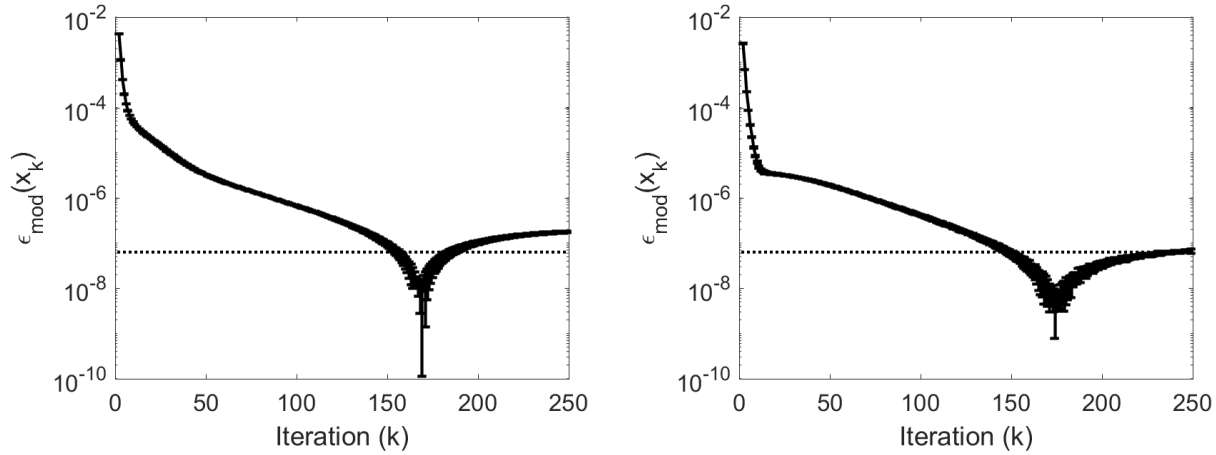

(a) TV Regularization ($\alpha = 0$) (b) PICCS Regularization ($\alpha = 0.5$)

Figure 3.25: Plots of the modified normalized convergence criteria (bottom) from Eq. 3.29 is shown for the TV (a) and PICCS (b) regularized implementations. Error bars denote the measured standard deviation between measured curves. The dashed line in the plots indicates $10^{-7.2}$.

Plenty of future work remains to improve the clinical implementation of the DOS-SPART reconstructions. So far, two regularizers, TV and PICCS, have been introduced, however the DOS-SPART framework is conducive to many possible regularization schemes. The introduction of a more advanced regularization scheme could permit more aggressive image denoising (and thus lower dose reconstructions) without sacrificing fine details such as calcifications or tumor margins. The addition of diffusion regularization is being explored currently. A derivation of the implementation of anisotropic diffusion as a regularizer is provided in Appendix A.2. In addition, an important step in the clinical processing currently is the introduction of an iterative contrast enhancement scheme. As a result, the contrast in the commercial images currently is typically higher than in pure FBP reconstructions. In the future, the introduction of such a tool would be helpful to clinicians who are accustomed to relatively high contrast images.

The unique features of DBT required several major modifications to the DOS-SPART algorithm for it to be applicable. First, a tomosynthesis FBP reconstruction was needed to generate a seed image for the DOS-SPART reconstructions that can also serve as a prior image for the PICCS regularized implementation. Second, a metal detection and compensation scheme was needed to provide reliable statistical weighting matrices for the reconstructions. Third, a 3D breast mask calculation method was introduced. This breast mask was used to constrain the reconstruction, providing substantially improved reconstruction speed and reduced artifacts at the object boundaries. Fourth, a projection matrix formalism was introduced to perform the forward and backprojection operations for the iterative procedure. With all of these modifications in place, the implementation was outlined and reconstructed images using the commercial reconstruction method were compared with the DOS-SPART reconstructions.

4 Truncation Artifacts in Digital Breast Tomosynthesis

4.1 Introduction

In this chapter, truncation artifacts for digital breast tomosynthesis are explored. Truncation artifacts are common in DBT images. In fact, in the MLO view, truncation artifacts are almost always unavoidable (see Figure 4.1). For DBT, filtered backprojection (FBP) is the standard reconstruction technique. In this method, projection data acquired at each angular position are first filtered by a kernel (typically the ramp kernel) before being backprojected to the tomographic image domain. Since the filtering operation introduces spatial correlations, spatial inconsistencies in the data due to the abrupt cutoff of the object at the edge of the field of view (FOV) of the system (viz. truncation) may produce strong artifacts in the reconstructed images, such as those seen in Figure 4.2. Specifically, two major types of artifacts due to truncation manifest themselves in tomosynthesis reconstructions: artifacts due to the discontinuity at the edge of the detector and artifacts due to an underestimation of the attenuation through the object by ignoring objects which intersect the beam, but lie outside the FOV [184].

Many established methods to correct for data truncation in CT using FBP reconstruction methods are based upon data extrapolation [185–192]. Several correction techniques for digital breast tomosynthesis (DBT) have been proposed for both analytical and iterative reconstruction methods [181,184,193], however an optimal method with physical grounding is still needed. The purpose of this work was to propose techniques with physical grounding to correct for data truncation

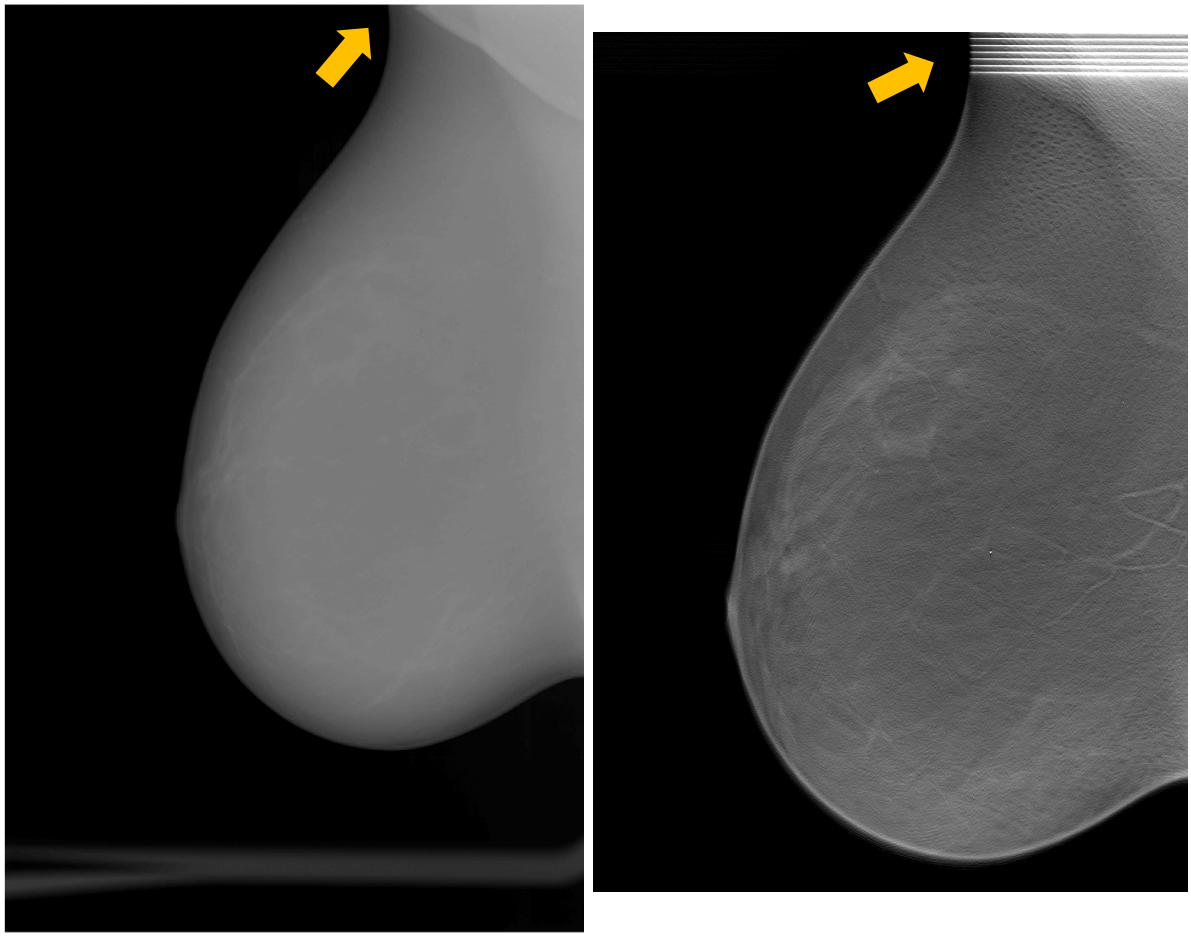

(a) Projection image

(b) Reconstructed slice
(z = 75 mm above detector)

Figure 4.1: An example of a clinical breast exam in the MLO projection. The truncation in the superior aspect of the breast is indicated with the golden arrow in the projection image (a) and the resulting artifacts in the FBP reconstruction are indicated in the reconstructed slice (b).

artifacts in breast tomosynthesis and determine which technique is best suited to alleviate truncation artifacts in DBT.

4.2 Methods

4.2.1 Acquisition parameters and equipment

Several image objects, including an American College of Radiology (ACR) mammography accreditation phantom (Fluke Biomedical, Everett, WA), two bovine udders, and several cadaver breast

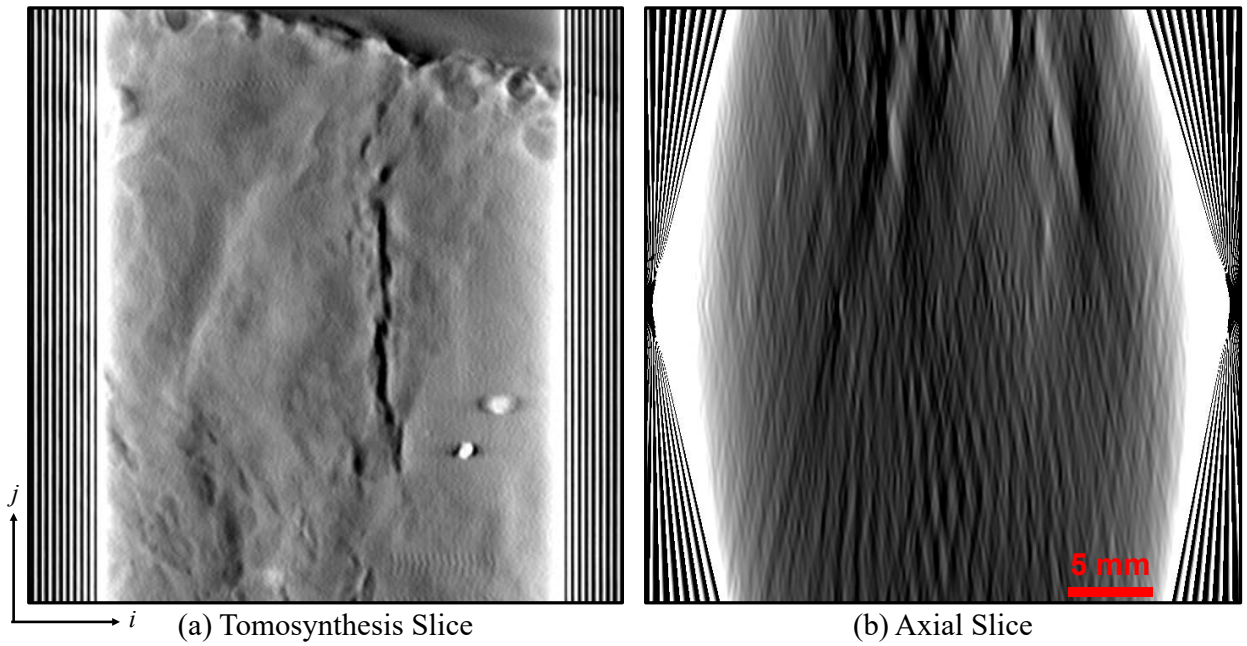

Figure 4.2: The manifestation of truncation artifacts in tomosynthetic reconstructions. The example here is a cadaver breast specimen imaged using our bench-top multi-contrast imaging system. A tomosynthesis slice (a) and the central axial slice (b) reconstructed through the object (ie. CT slice) are shown.

specimens were imaged for this work. For all objects, 15 projections with a 15° tomo angle were acquired using a bench-top imaging system (see Figure 4.3) with a rotary object stage. In order to investigate the impact of truncation on reconstruction artifacts with different tomo angles, two tomo angles (15° and 45°) with 15 and 45 views respectively were used to acquire cone beam projection data for the ACR accreditation phantom. The bench-top acquisition system used in this work includes a diagnostic x-ray tube (Varian G1582, Palo Alto, CA) operated at 40 kVp and 20 mA, and a CMOS flat panel detector with 48 μm isotropic pixel size (Rad-icon Shad-o-Box 2048, Sunnyvale, CA). The x-ray exposure time was 5 seconds per projection. For this work, we used a tube potential of 40 kVp, providing a mean energy of approximately 28 keV.

Tomosynthesis volumes were reconstructed through the image object using a 50×50 μm^2 in-plane pixel pitch and 0.5 mm nominal slice thickness. Each slice was 700×700 pixels and 140 slices were reconstructed along the z axis, resulting in a $3.5 \times 3.5 \times 7.5$ cm^3 ($i \times j \times z$) image volume. An FDK cone-beam CT reconstruction algorithm[194] implemented in Visual C++ (Microsoft Corporation, Redmond, WA) and CUDA (NVIDIA Corporation, Santa Clara, CA) was used to perform the

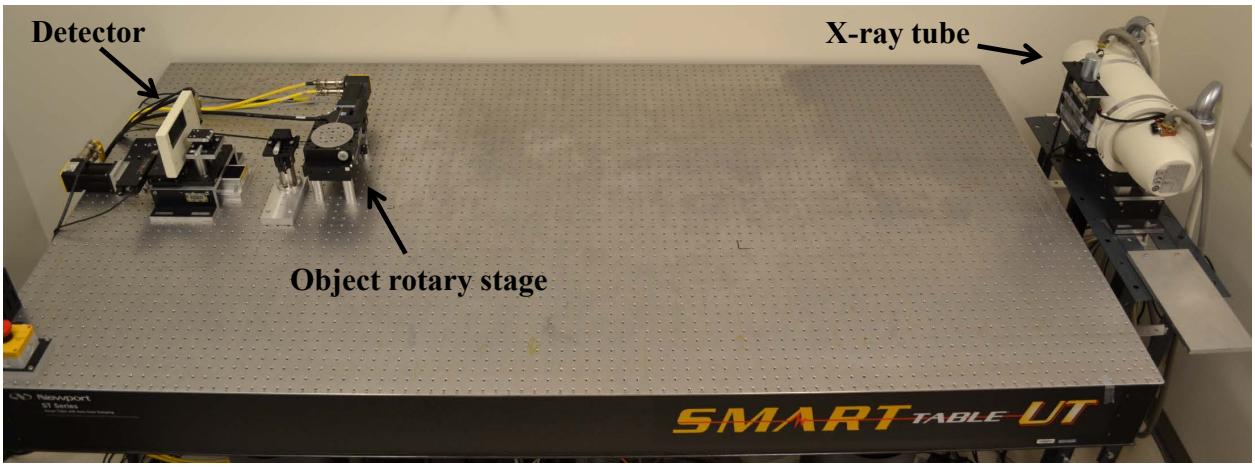

(a)

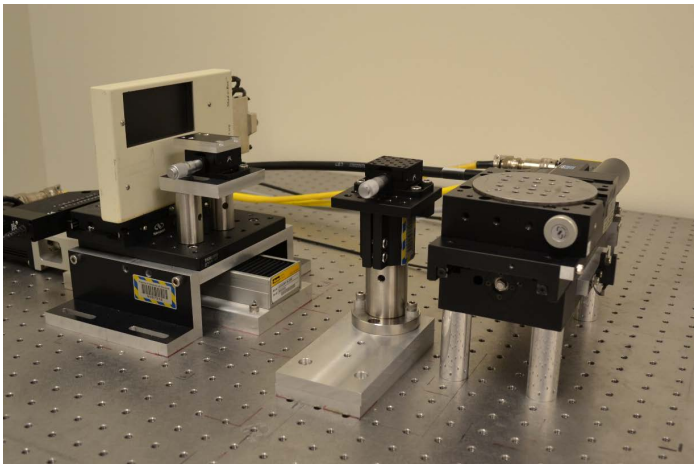

(b)

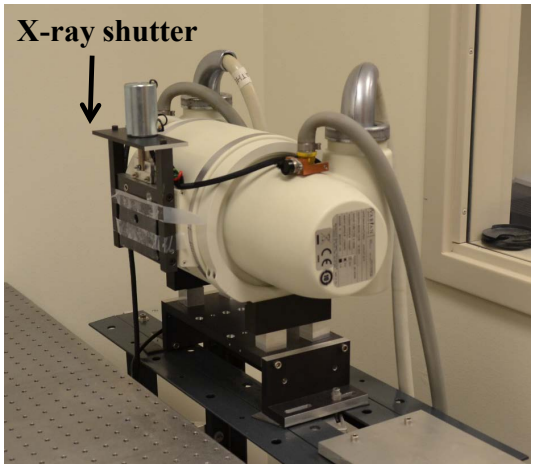

(c)

Figure 4.3: The bench-top system used to acquire all of the image data in this study (a). Close up images of the detector and object stage (b) and the x-ray tube (c) are shown below.

reconstructions with a ramp kernel.

Each reconstruction took about 10 seconds using a workstation equipped with a 6 core processor (Intel Xeon E5645, Intel Corporation, Santa Clara, CA) and an NVIDIA GTX Titan X GPU (NVIDIA Corporation, Santa Clara, CA).

4.2.2 Extrapolation Techniques

In order to mitigate data truncation, the projection data were extrapolated in the scanning direction (parallel to the surface of the table in Figure 4.3). Data extrapolation methods were used to mitigate

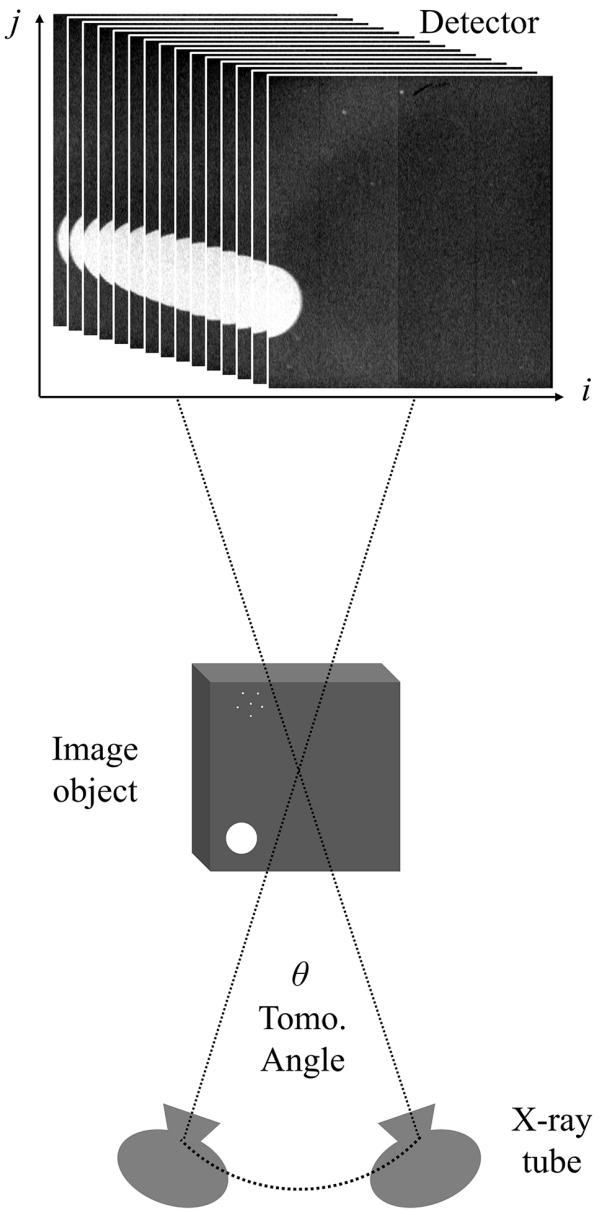

Figure 4.4: Imaging geometry used for these acquisitions. Extrapolations were performed along the i direction.

truncation artifacts in the x-ray CT reconstructions. To provide an intuitive argument to justify the use of the method, one fact is foundational: a real imaged object has compact support. That is to say, the object has some finite size and the entire object is enclosed by the x-ray source trajectory. By assuming this finite support, the measured data will eventually drop down to zero when the x-ray beam reaches the edge and ceases to pass through the finite image object. By assuming a smooth change of measurements from interior of image object to edge of the image object for a typical cone-beam data acquisition geometry, absorption projection data of the image object should smoothly drop to zero before reaching the edge of the image object and thus justify the use of the data extrapolation.

In the case of tomosynthesis, this justification no longer holds. Unlike CT, very large objects may be imaged with tomosynthesis, as the use of a limited angular span permits the gantry to rotate without colliding with the object. However, it doesn't make physical sense to assume the object has finite support in this case. Most clinical applications for tomosynthesis involve imaging large planar objects: the chest, extremities (planar along the limb), and the compressed breast. In all of these cases, the object extends more or less uniformly beyond the field of view rather than being bounded. As a result, we propose two different categories of extrapolation techniques for this work: "Tomo-like" (assuming uniform thickness and a uniform linear attenuation, μ, for the extrapolated data) and "CT-like" (assuming finite support).

Our hypothesis in this work was that the object should extend uniformly (in terms of thickness and linear attenuation or μ) beyond the field of view in tomosynthesis imaging to provide the best reconstruction results with mitigated data truncation artifacts.

For both Tomo-like extrapolation and CT-like extrapolation methods, we proposed two different specific data extrapolation schemes: 1) a true row-by-row extrapolation and 2) a low-pass filtered extrapolation for the entire truncated edge of the data. The proposed row-by-row extrapolation method can eliminate discontinuities at the boundary for each detector row while the variations across detector rows can be maintained in the reconstruction. Since the ramp filter is very sensitive to these discontinuities, it was thus expected that this method would be better for absorption tomosynthesis reconstruction. The performance for these proposed extrapolation methods were evaluated against the brute force method without any correction. Thus, there were a total of five

methods to be evaluated and these methods are described as follows (see Figure 4.4 for definition of i and j). An illustration of these methods with an example projection image is provided in Figure 4.5. Note that extrapolation was performed to double the field of view in this work with an extension of 50% of the detector width symmetrically on each side along the scanning direction.

Brute force method: No correction

1 In the first method, any values outside the active area of the detector were set to zero. Essentially, this is equivalent to performing no correction at all for data truncation. Mathematically this may be described as follows:

$$p_{i,j} = \begin{cases} 0 & : 0 < i < i_{\text{left}} \text{ or } i_{\max} > i > i_{\text{right}} \\ p_{i,j} & : \text{ otherwise} \end{cases}, \tag{4.1}$$

where $p_{i,j}$ is the pixel value in the ith row and jth column of the detector readout (see Figure 4.4 for definition of i and j). The index, $i_{\max}$, is the largest index in the extrapolated projection data.

Tomo-Like Extrapolation Methods

2 In the second method, the values at the edges of the active area of the detector were extended to fill the truncated areas on a row-by-row basis. This will be called a nearest neighbor extrapolation, since beyond the border of the object, the projection value is replaced by the value corresponding to the nearest true projection value. Mathematically, this may be described as follows:

$$p_{i,j} = \begin{cases} p_{i_{\text{left}},j} & : 0 < i < i_{\text{left}} \\ p_{i_{\text{right}},j} & : i_{\max} > i > i_{\text{right}} \\ p_{i,j} & : \text{ otherwise} \end{cases}, \tag{4.2}$$

where $p_{i,j}$ is the pixel value in the ith row and jth column of the detector readout and $p_{i_{\text{left/right}},j}$ denotes the nearest neighbor value on the left or right edge respectively.

3 In the third method, the mean value along the edge of the active area of the detector was calculated, and that value was used to fill out the truncated areas. In this case, rather than

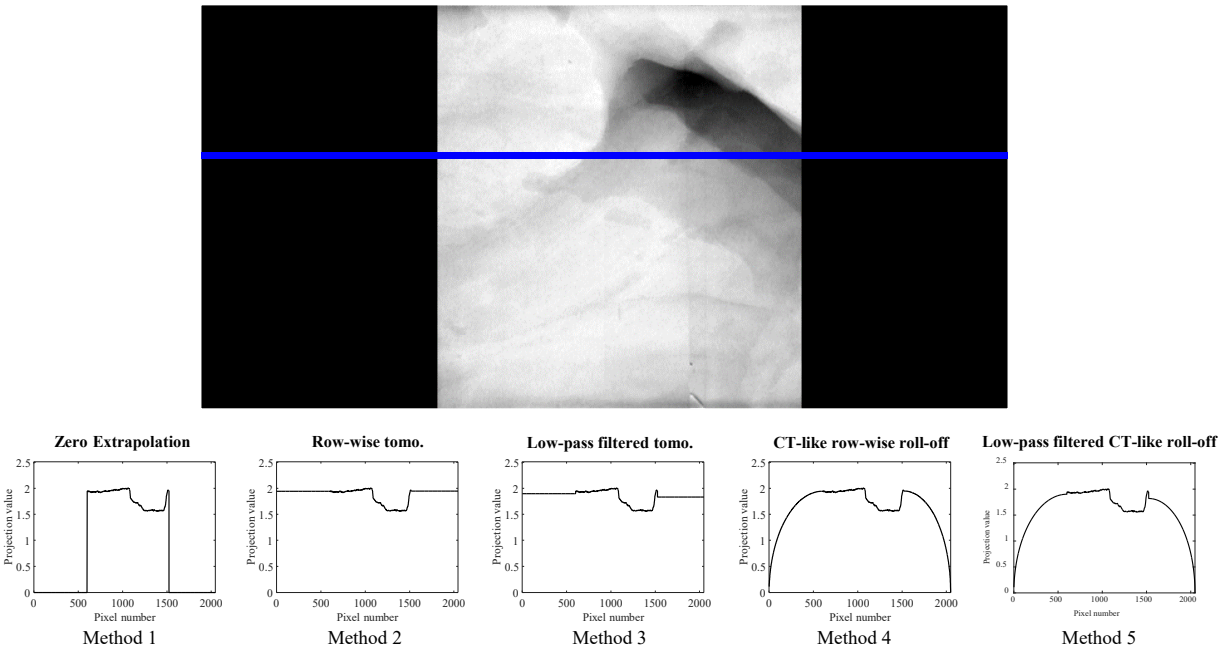

Figure 4.5: Example line profiles through a projection image of a cadaver breast specimen using the 5 extrapolation techniques.

extending values on a row-by-row basis, the same value was used to fill the truncated areas beyond each edge. Mathematically, this may be described as follows:

$$p_{i,j} = \begin{cases} \bar{p}_{i_{\text{left}}} & : 0 < i < i_{\text{left}} \\ \bar{p}_{i_{\text{right}}} & : i_{\text{max}} > i > i_{\text{right}} \\ p_{i,j} & : \text{ otherwise} \end{cases}, \tag{4.3}$$

where $p_{i,j}$ is the pixel value in the ith row and jth column of the detector readout, and $\bar{p}_{i_{\text{left/right}}}$ is the mean value along the left or right edge of the detector, defined as follows for p_n rows: $\bar{p}_{i_{\text{left/right}}} = \frac{1}{n}\sum_{j=1}^{n} p_{i_{\text{left}},j}$. This method is a low-pass filtered approximation of the second method.

CT-Like Extrapolation Methods

4 In the fourth method, the values at the edges of the active area of the detector were extended to fill the truncated areas on a row-by-row basis by following an elliptical curve such that the extrapolated value drops to zero at the edge of known boundary of the image support.

Mathematically, this may be described as follows:

$$p_{i,j} = \begin{cases} p_{i_{\text{left}},j}\sqrt{1-\left[\frac{(i_{\text{left}}-i)}{i_{\text{left}}}\right]^2} & : 0 < i < i_{\text{left}} \\ p_{i_{\text{right}},j}\sqrt{1-\left[\frac{(i-i_{\text{right}})}{i_{\text{max}}-i_{\text{right}}}\right]^2} & : i_{\text{max}} > i > i_{\text{right}} \\ p_{i,j} & : \text{ otherwise} \end{cases}, \tag{4.4}$$

where $p_{i,j}$ is the pixel value in the ith row and jth column of the detector readout.

5 In the fifth and final method, the mean value along the edge of the detector's active area was calculated and then used to extrapolate the truncated areas along an elliptical curve as well such that the value along the edge of the detector is the mean edge value and at the edge of the extrapolated projection data the value drops to zero. Mathematically this may be described as follows:

$$p_{i,j} = \begin{cases} \bar{p}_{i_{\text{left}},j}\sqrt{1-\left[\frac{(i_{\text{left}}-i)}{i_{\text{left}}}\right]^2} & : 0 < i < i_{\text{left}} \\ \bar{p}_{i_{\text{right}},j}\sqrt{1-\left[\frac{(i-i_{\text{right}})}{i_{\text{max}}-i_{\text{right}}}\right]^2} & : i_{\text{max}} > i > i_{\text{right}} \\ p_{i,j} & : \text{ otherwise} \end{cases}, \tag{4.5}$$

where $p_{i,j}$ is the pixel value in the ith row and jth column of the detector readout, and $\bar{p}_{i_{\text{left/right}}}$ is the mean value along the left or right edge of the detector. This method is a low-pass filtered approximation to the fourth method.

4.2.3 Quantitative evaluation methods

To quantitatively evaluate the performance of each technique, the signal difference to noise ratio (SDNR), relative root mean square error (rRMSE), and the universal quality index (UQI) [195] were used. The SDNR was defined as follows:

$$\text{SDNR} = \frac{\bar{s}_{obj} - \bar{s}_{bkg}}{\bar{\sigma}}, \tag{4.6}$$

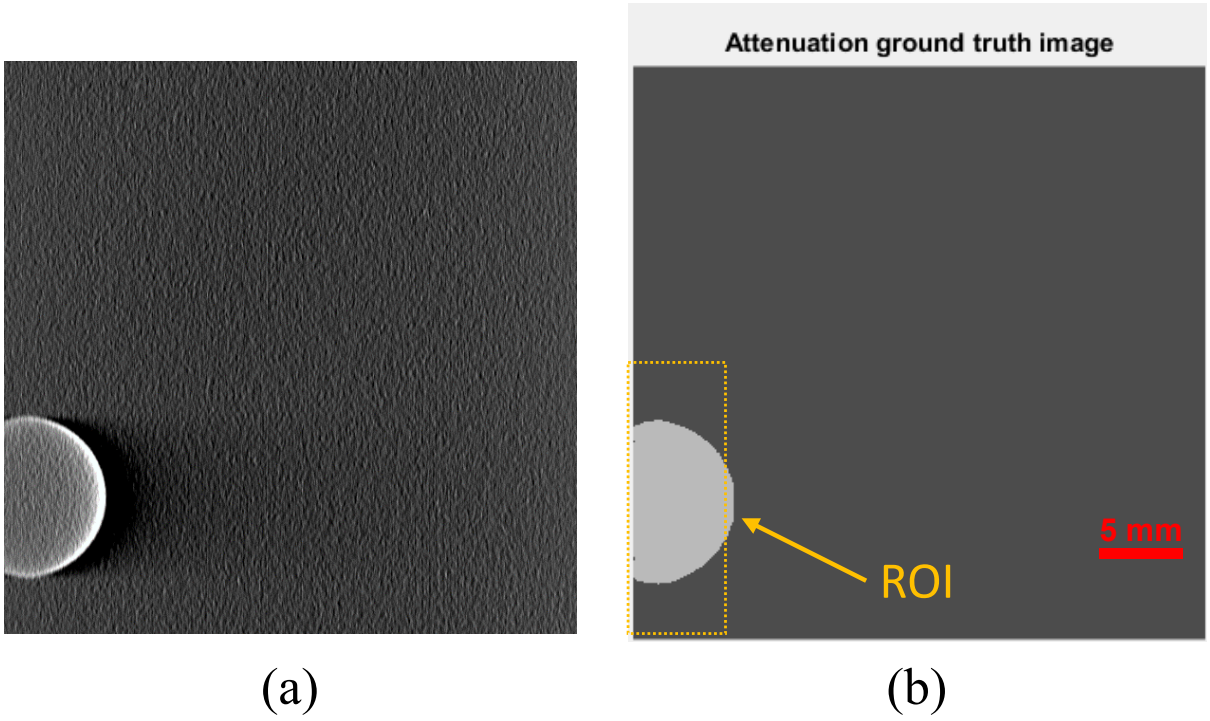

Figure 4.6: Example image reconstructions acquired with 45 projections over 45° (using method 2) the segmented ground truth mask (b) and the ROI for the measurement of rRMSE f

where $\bar{s}_{obj}$ is the mean signal in the object, $\bar{s}_{bkg}$ is the mean signal of the background, and $\bar{\sigma}$ is the mean of the noise standard deviation in the object and that in the background: $\bar{\sigma} = (\sigma_{obj} + \sigma_{bkg})/2$. In this work, the SDNR was measured for the same feature of the ACR phantom shown in Figure 4.6 (using 45° tomo angle) as well as for a low contrast vessel in a cadaver breast (Figure 4.7). The low contrast vessel was chosen due to its proximity to the border of the reconstruction volume (and the edge of the FOV), its low contrast, and the fact that it was clearly visible in both contrast mechanisms. The rRMSE is defined as follows:

$$\text{rRMSE} = \frac{\sqrt{\sum_i \left(I_i - I_i^{\text{truth}}\right)^2}}{\sum_i \left|I_i^{\text{truth}}\right|} \times 100\%, \tag{4.7}$$

where I is the image under evaluation, I^{truth} is the ground truth comparison image, and the subscript, i, denotes the pixel location i. This was measured for an ROI containing a high contrast object at the boundary of the object (see Figure 4.6). The ground truth was defined by segmenting the object out using a two-component segmentation method. A two-component segmentation method

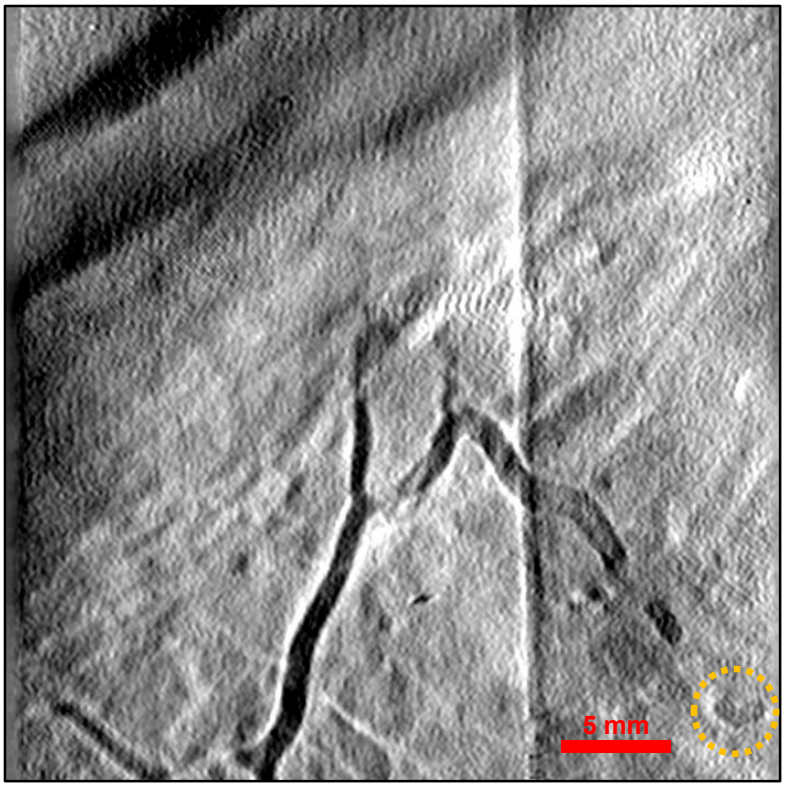

Figure 4.7: Tomosynthetic slices through a human cadaver breast volume reconstructed using FBP and method 2. The low-contrast portion of the vessel in the lower right of the image was the feature chosen for SDNR measurements as it is close to the boundary, low contrast, and visible in both image contrasts.

was chosen as the object of interest was uniform and in the region of interest the background was also uniform. Thus, a two-component model should be sufficient to model the object.

In addition, the UQI was measured for the same ROIs using the same segmented image as a reference. This provides a more general assessment of image quality, and is defined as follows[195]:

$$\text{UQI} = \frac{4\sigma_{xy}\bar{x}\bar{y}}{\left(\sigma_x^2 + \sigma_y^2\right)\left[(\bar{x})^2 + (\bar{y})^2\right]}, \tag{4.8}$$

where the subscripts x and y denote the input image (called I in Eq. 4.7) and the ground truth image for comparison (called I^{truth} in Eq. 4.7), respectively, $\sigma_{x/y}^2$ denotes the variance of x or y, $\bar{x}$ and $\bar{y}$ denote the mean values of x and y, respectively, and σ_{xy} denotes the covariance of x and y, defined as follows: $\sigma_{xy} = \frac{1}{N-1}\sum_{i=1}^{N}(x_i - \bar{x})(y_i - \bar{y})$. The UQI has a dynamic range of $[-1, 1]$ and is

Table 4.1: Measured SDNR values for ACR phantom. The highest (best) values are shown in bold.

		Tomo-like Methods			CT-like Methods	
Modality	Tomo-angle	1	2	3	4	5
Absorption	45°	0.10	0.96	0.63	**1.09**	0.73

Table 4.2: Measured SDNR values for cadaver vessel. The highest (best) values are shown in bold.

		Tomo-like Methods			CT-like Methods	
Modality	Tomo-angle	1	2	3	4	5
Absorption	15°	0.36	1.00	0.35	**1.09**	0.52

unitless.

4.3 Results

The proposed methods were used to correct truncation artifacts for tomosynthesis data acquisitions from both a bovine udder and cadaver breasts using our in-house bench-top data acquisition system. Figures 4.8 and 4.9 show tomosynthesis images of the ACR phantom acquired with 15 views over 15 degrees and 45 views over 45 degrees, respectively. With no correction (method 1), the bright bands at the edges of the absorption reconstruction volume can be clearly seen. With method 2, the image seems to be free of truncation artifacts. With method 3, the image has some residual vertical lines visible in the disk feature. In methods 4 and 5, similar results to method 2 and 3 are seen for the ACR phantom. The image results for the bovine udder and cadaver breast case are shown in Figures 4.10 and 4.11, respectively. These results are consistent with the phantom results, with even more pronounced artifacts in some cases (Methods 4 and 5 in Figure 4.10). The results of the SDNR measurements are shown for the ACR phantom and the cadaver vessel in tables 4.1 and 4.2, respectively, and the results from the rRMSE measurements are shown in table 4.3. As one can qualitatively observe in all figures, the row-by-row data extrapolation methods work well for tomosynthesis images.

Table 4.3: Measured rRMSE values (all in percent, %). The lowest (best) values are shown in bold.

		Tomo-like Methods			CT-like Methods	
Modality	Tomo-angle	1	2	3	4	5
Absorption	15°	1.0×10^{0}	$\mathbf{1.5 \times 10^{-1}}$	1.5×10^{-1}	1.5×10^{-1}	1.6×10^{-1}
	45°	4.7×10^{-1}	$\mathbf{6.6 \times 10^{-2}}$	6.6×10^{-2}	8.0×10^{-2}	8.0×10^{-2}

Table 4.4: Measured UQI values (unitless, ranging from $[-1, 1]$). The highest (best) values are shown in bold.

		Tomo-like Methods			CT-like Methods	
Modality	Tomo-angle	1	2	3	4	5
Absorption	15°	4.8×10^{-3}	1.2×10^{-1}	1.3×10^{-1}	1.2×10^{-1}	$\mathbf{1.4 \times 10^{-1}}$
	45°	-2.2×10^{-3}	$\mathbf{3.7 \times 10^{-1}}$	3.7×10^{-1}	3.6×10^{-1}	3.6×10^{-1}

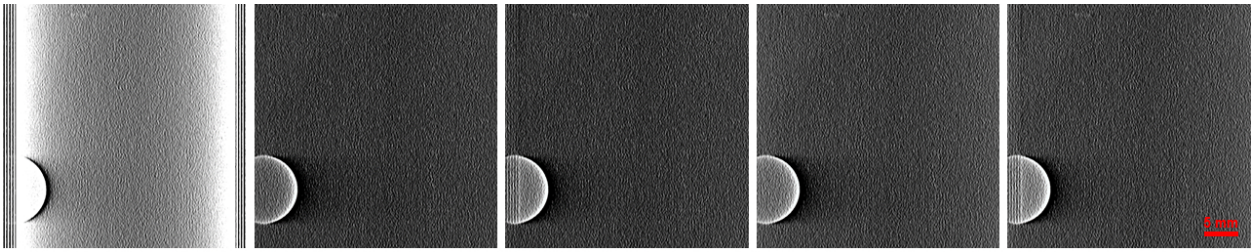

(a) Method 1 (b) Method 2 (c) Method 3 (d) Method 4 (e) Method 5

Figure 4.8: Example images of the ACR mammography phantom reconstructed using the 5 different extrapolation techniques to cope with data truncation. A 15° tomo angle (15 views) was used to acquire these images. All images are displayed with the same W/L.

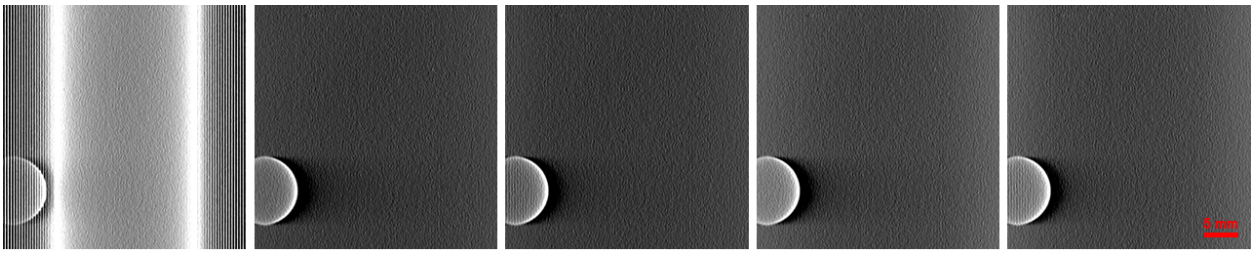

(a) Method 1 (b) Method 2 (c) Method 3 (d) Method 4 (e) Method 5

Figure 4.9: Example images of the ACR mammography phantom reconstructed using the 5 different extrapolation techniques to cope with data truncation. A 45° tomo angle (45 views) was used to acquire these images. All images are displayed with the same W/L.

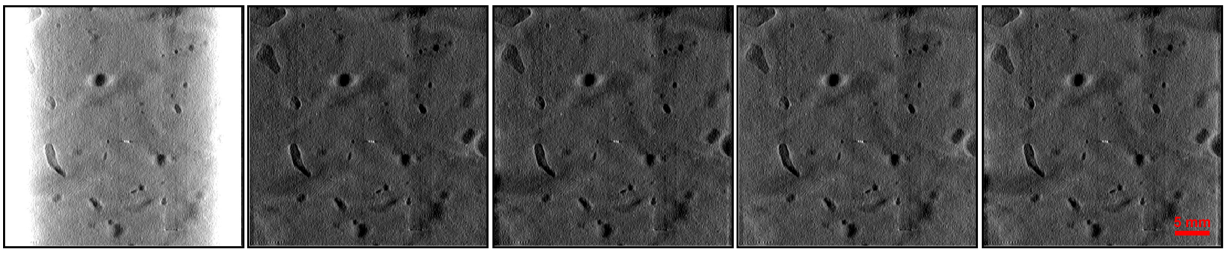

(a) Method 1 (b) Method 2 (c) Method 3 (d) Method 4 (e) Method 5

Figure 4.10: Example images of a bovine udder reconstructed using the 5 different methods. The same slice position was used for each contrast mechanism, and all images are displayed with the same W/L.

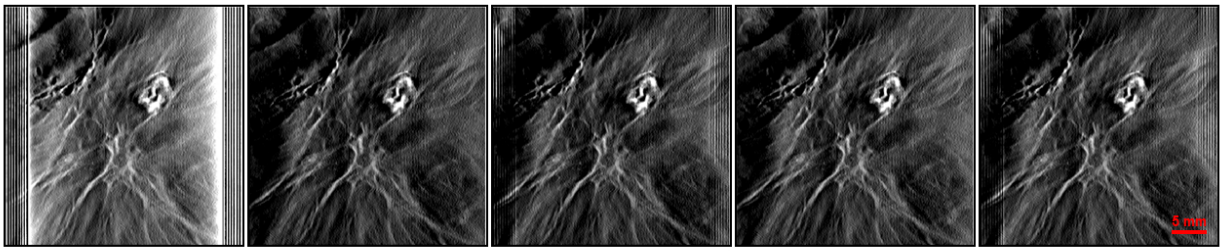

(a) Method 1 (b) Method 2 (c) Method 3 (d) Method 4 (e) Method 5

Figure 4.11: Example images of a cadaver breast reconstructed using the 5 different methods. The same slice position was used for each contrast mechanism, and all images with the same W/L.

4.4 Discussion and conclusions

The quantitative evaluations performed mostly agreed with subjective assessments of image quality. One exception, however, was that the "CT-Like" methods improved the CNR for imaging features at the cost of residual artifacts; this is a nice example of the limitations of a metric such as the CNR. On the other hand, the rRMSE metric accounted for both noise characteristics and image artifacts since the ground truth comparison was a noise-free image. Thus, the rRMSE measurements agree with the subjective image quality assessment. Similarly, the UQI also agreed nicely with subjective image quality assessment. It was found that the "tomo-like" methods gave the best overall results, and that the row-by-row method (method 2) worked best in all cases.

The tomo angle used for acquisition plays an important role as well. One can see in figures 4.8 and 4.9 that the extent of the artifacts depends heavily on the tomo angle, with the artifacts present in a much larger portion of the image acquired with a 45° tomo angle than those acquired with a

15° tomo angle in the case with no correction (method 1). It is worth pointing out that although the extent of the artifacts may be greater for a larger tomo angle, with proper correction we can expect better results with more view angles and a greater angular range.

In summary, we found that the method that provided the best image quality for truncated tomosynthesis images was a method which assumed a "tomo-like" (slab) image object and a row-by-row extrapolation (method 2). Using the appropriate method enables a reduction of artifacts in the reconstruction of tomosynthesis volumes in cases where data truncation is present.

5 Anatomical Noise

5.1 Introduction

In breast imaging, and in breast cancer screening in particular, the primary objective is to determine whether or not a malignancy is present. However, the anatomical background in images may significantly confound this imaging task. The impact of the anatomical background noise on detection performance has been quantified using several techniques[44,45,128–130] including a spatial frequency dependent power spectrum, viz., the anatomical background noise power spectrum[44,45,130]. In the presence of structure anatomical noise, the overall detectability for a specific imaging task is jointly impacted by a generalized noise power spectrum that consists of two major components: quantum and anatomical background noise[44,45,130]. The quantum noise depends on the imaging system itself (such as the quantum detection efficiency of the detector), the image acquisition parameters (such as the overall radiation exposure level and tube potential), and the breast itself (such as density, thickness, etc.). By comparison, the anatomical background noise is primarily dependent on the breast parenchymal structure, imaging conditions, and imaging geometry (compression, CC vs. MLO planar view, etc.), although the impact of acquisition parameters on image contrast may lead to some minor variation in the measured anatomical noise background[131]. It has been shown that the power spectrum of anatomical background noise may be empirically modeled as[44]:

$$\mathrm{NPS_a}(f) \approx \alpha f^{-\beta} \tag{5.1}$$

where f is the spatial frequency, and α and β are two parameters determined by fitting the measured and radially averaged $\mathrm{NPS_a}(f)$ to the model given in Eq. (5.1). In reality, the parameters α

and β may change from one imaging method to another and from patient to patient, but these deviations should fall within a range of typical values. Typical values for β in absorption x-ray mammography imaged using a cranio-caudal geometry with compression have been reported to be around $\beta_{\text{mammo}} \approx 3.2$. Recently, β has also been measured for digital breast tomosynthesis (DBT)[132] and breast cone-beam CT (BCT)[131,133], yielding values of $\beta_{\text{tomo}} \approx 3.1$, and $\beta_{\text{BCT}} \approx 2.0$. Not only does β depend on the imaging modality, but it also varies with the x-ray beam energy[131], the breast density[46], and even the imaging plane (e.g., CC vs. MLO for mammography and DBT)[133].

Despite its many dependencies on specific imaging conditions, it is well documented that β is strongly correlated with lesion detection performance[44,46,133–135]. Therefore, quantitative assessment and prediction of diagnostic performance for mammography should take into consideration not only imaging system/acquisition parameters, but also this beta-power law. As an example, the concept of a generalized NPS including the anatomical noise background has been developed and incorporated into the model observer framework[121]. With this framework, the knowledge of the typical range of β values for a given imaging method may help predict the lesion detection performance for that method. Understanding the anatomical noise background can be critically important for image task-orientated optimizations of determining system hardware and data acquisition parameters.

The purpose of this work was to explore the dependence of anatomical noise on reconstruction method (full model based iterative methods vs. FBP) as well as to propose and develop a method to simulate anatomical noise backgrounds realistically for model observer studies.

5.2 Method to determine the anatomical background noise power spectrum

As described in the literature[44,46,133,135,137], β can be estimated from local anatomical background power spectra for different regions of interest (ROIs) in a given breast, followed by an ensemble average over many local regions in many breast imaging datasets. The resulting power spectrum is then radially averaged and fitted to the model given in Eq. (5.1). From this fit, the value for β may be extracted. The steps of this process implemented experimentally here are presented as follows:

1. For a given breast image, square ROIs with the same size (128×128 pixels) were randomly

selected. The central coordinates of each ROI were randomized with the constraint that they must fall within the breast parenchyma without being too close to either the chest wall, nipple, or skin line. To ensure the ROIs were at an appropriate location, the center of mass of image intensity values of each breast was computed first and then each randomly-selected ROI was constrained to be within a certain distance (in pixels) from the center of mass of the breast.

2. A radial Hanning window was applied to each ROI to avoid discontinuities at the boundaries before the Fourier transform was performed for anatomical noise power analysis. This window was defined as:

$$W(r) = \begin{cases} 0.5 + 0.5\cos\left(\frac{\pi r}{R}\right) & : r \leq R \\ 0 & : r > R \end{cases}, \tag{5.2}$$

where r is the pixel location in the ROI ($r = \sqrt{x^2 + y^2}$, assuming the center of the ROI is $x = y = 0$) and R is half the width of the ROI in pixels ($R = 64$ here).

3. The Fourier transform of each ROI was then calculated using the fast Fourier transform (FFT); the square modulus of each of these Fourier transforms yielded a single realization of the power spectrum.

4. These individual power spectra were then averaged across ROIs, averaged radially, and fit to the function,

$$\mathrm{NPS_a}(f_r) = \alpha f_r^{-\beta}. \tag{5.3}$$

5. Finally the parameters, α and β, were extracted using a least squares fitting procedure.

Extremely low and extremely high frequencies do not correspond to the spatial scales of anatomical structures, and as a result the linear regression is performed over a limited range of frequencies. In this study, this range was typically determined to be $\approx [0.4, 3]$ mm^{-1} to provide the maximum r^2 value (coefficient of determination) for the least square fitting.

5.2.1 Validation of workflow

The workflow described in Section 5.2 is independent of imaging method, and thus can be used on breast images from any imaging modality. Our implementation of this workflow was used to estimate

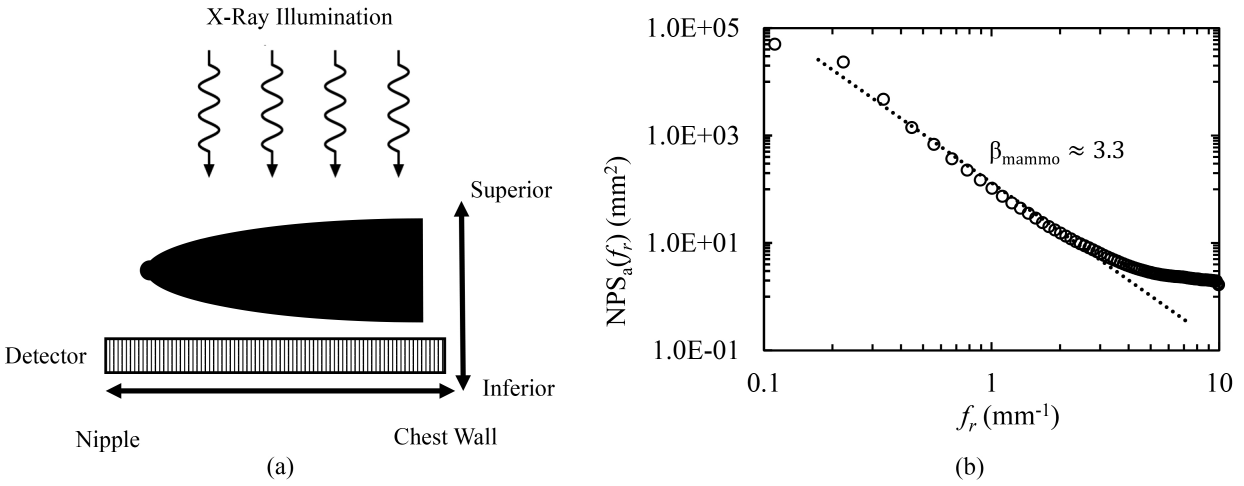

Figure 5.1: The imaging geometry (a) and the measured radial anatomical noise for clinical mammography used for validation (b).

β in clinical mammography with an IRB-approved patient cohort consisting of 56 anonymized mammograms. A clinical mammography system (Hologic Selenia Dimensions, Hologic Inc., Bedford, MA) was used and our measured values ($\beta = 3.3, r^2 = 0.99$) (Figure 5.1) were comparable to those values presented in the literature[46,133,135].

5.3 Anatomical noise and image reconstruction method

Previous work showed that moving from mammography to DBT resulted in a minimal reduction in anatomical noise[132]. This can be understood in large part as limited by anatomical noise from adjacent slices contaminating DBT reconstructions. In other words, even though DBT can provide focal planes at different heights above the detector, each of those focal planes is contaminated still with content from adjacent slices and the result is significant anatomical clutter. We saw in Chapter 3 that the introduction of a model-based iterative reconstruction method (DOS-SPART) was able to reduce the effective slice thickness for DBT acquisitions. Thus, we hypothesized that the introduction of DOS-SPART in addition to reducing the through plane blurring artifacts for objects of interest (thus improving object localization) may also reduce anatomical clutter in the reconstructed images.

5.3.1 Measurement

To test this hypothesis, the anatomical noise power spectra were measured in a large cohort of clinical breast exams ($N = 105$) using the method described previously in Section 5.2. The measurements were performed in volumes reconstructed using three methods: the commercial reconstruction (FBP+standard post-processing), DOS-SPART (TV regularization), and DOS-SPART (PICCS regularization). The parameters for the DOS-SPART reconstructions are provided in Table 3.2. The anatomical noise parameter, β, was measured in the central 25 slices of each reconstructed volume for a total of 2,625 measurements. At each slice position, the scaled pixel pitch (per the projective pixel grid in Figure 3.3) was used to determine the frequency sampling in the Fourier domain. As previously performed, the fitting of the NPS was performed over the frequency range that maximized the coefficient of correlation, r^2. This range was found by trying all possible frequency ranges and choosing the β value from the best fit. The measured β values were compared across methods, as well as between slices. A two-sample t-test was used to compare the means of the measured β values for each reconstruction method and determine statistical significance. In all cases, the null hypothesis was that the means were the same, $H_0 : \mu_1 = \mu_2$, and thus the alternative hypothesis was a difference in the mean measured value, $H_1 : \mu_1 > \mu_2$.

5.3.2 Results

The measured anatomical NPS for the three image reconstruction methods are shown in Figure 5.2. Previously, we found the range of frequencies which maximized the coefficient of correlation in mammographic images to be $\approx [0.4, 1]\text{mm}^{-1}$. For this large cohort of DBT slices, the frequency ranges used for the three reconstruction methods are shown in Figure 5.3 and summarized in Table 5.1. In all cases, the frequency range was consistent with published recommendations for fitting ranges. The corresponding r^2 values are shown in Figure 5.4; the linear fit was quite good in all cases (mean $r^2 > 0.99$ in each modality; $r^2 > 0.90$ for all measurements).

Figure 5.5 compares the measured β values using the DOS-SPART method with the measured values from the commercial reconstruction. A least squares linear fit was also performed and the fit is provided in the legend of each figure. In each case, the slope of the fit was close to one (0.96 and

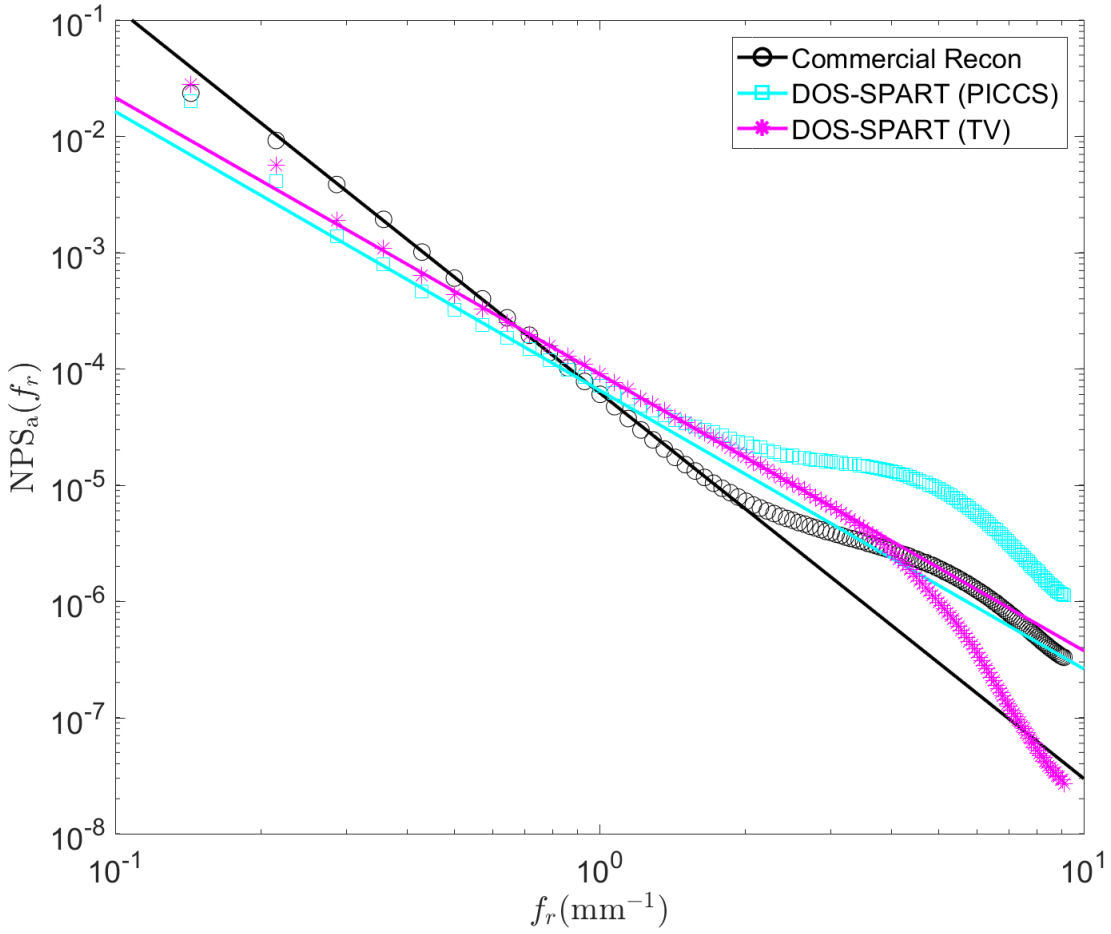

Figure 5.2: The measured anatomical noise power spectra for each reconstruction. The linear least squares fits are shown as well.

Table 5.1: The limits of the frequency range used to calculate β for the DBT reconstructions and the corresponding standard deviations for the different reconstruction methods.

	Commercial	DOS-SPART (TV)	DOS-SPART (PICCS)
$f_{min} \pm \sigma_f$ (mm^{-1})	0.25±0.06	0.24±0.08	0.24±0.08
$f_{max} \pm \sigma_f$ (mm^{-1})	1.24±0.25	1.25±0.24	1.17±0.22

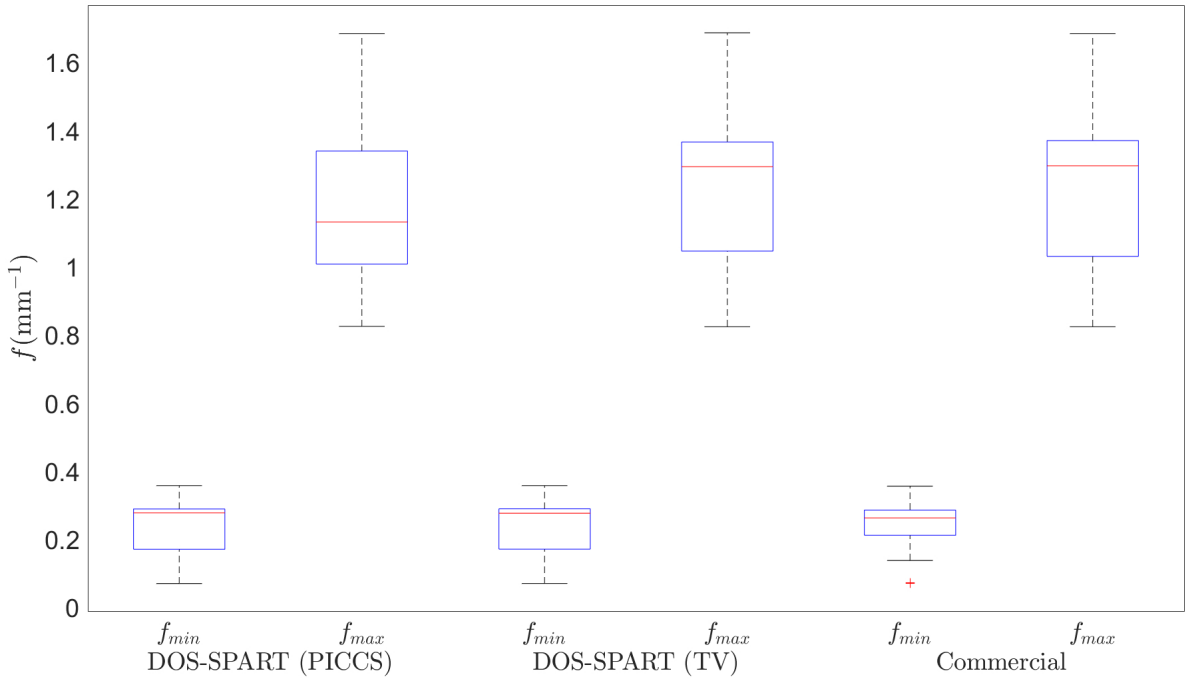

Figure 5.3: The frequency limits used for the fittings used to calculate β. The upper and lower limits were chosen such that the coefficients of correlation (Figure 5.4) were maximized.

0.99 for TV and PICCS regularizations, respectively), with a negative and non-zero offset. Figure 5.6 shows the measured β values for the three reconstruction methods. In addition, the mean measured values are compared in Table 5.2 with the statistical significance of the differences presented in Table 5.3. From the box and whisker plots we can see that both DOS-SPART implementations (TV regularized and PICCS regularized) have significantly reduced anatomical clutter compared with the commercial reconstruction. Figure 5.7 shows the average β for slices about the center. These curves are relatively flat, indicating that irrespective of reconstruction method the anatomical noise in the central slices about the center of the compressed breast is approximately the same.

In a clinical example shown in Figure 5.8, we can see the impact of reduced anatomical clutter on margin detection for a spiculated mass. The high-contrast calcification is clearly visible in all the reconstructions; however, the margins are much sharper and more well defined in different slices with the DOS-SPART reconstructions.

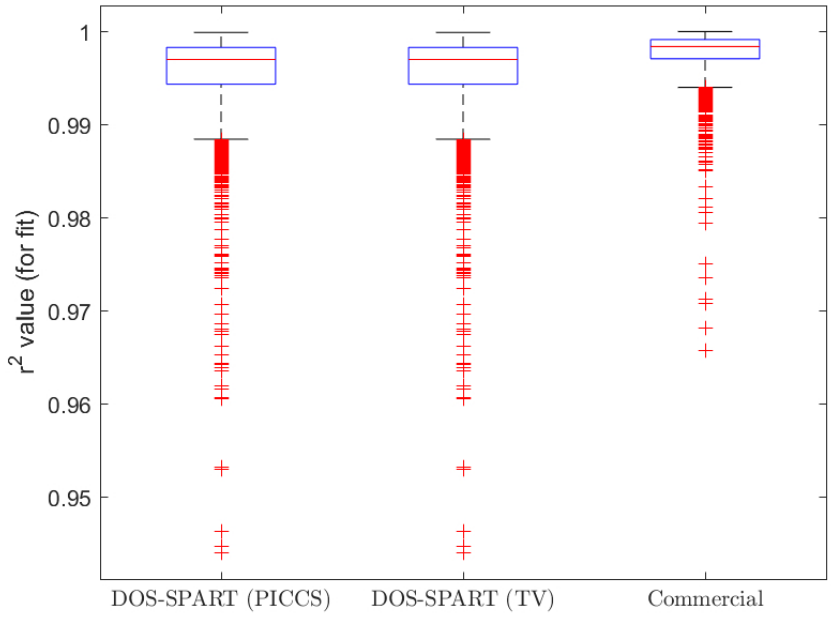

Figure 5.4: The measured coefficients of correlation for the fittings used to calculate β.

Table 5.2: The measured mean values of β, the corresponding standard deviations for the different reconstruction methods.

	Commercial	DOS-SPART (TV)	DOS-SPART (PICCS)
$\beta_{\text{mean}} \pm \sigma_\beta$	3.27±0.40	2.30±0.55	2.23±0.50

Table 5.3: The statistical significance of the differences in measured β values for the different reconstruction methods. The subscripts Comm., DS(TV), and DS(PICCS) indicate the commercial reconstruction method, DOS-SPART (TV regularizer), and DOS-SPART (PICCS regularizer), respectively.

$\left(\beta_{\text{Comm.}} > \beta_{\text{DS(TV)}}\right)$	$\left(\beta_{\text{Comm.}} > \beta_{\text{DS(PICCS)}}\right)$	$\left(\beta_{\text{DS(TV)}} > \beta_{\text{DS(PICCS)}}\right)$
p<<0.001	p<<0.001	**p > 0.05**

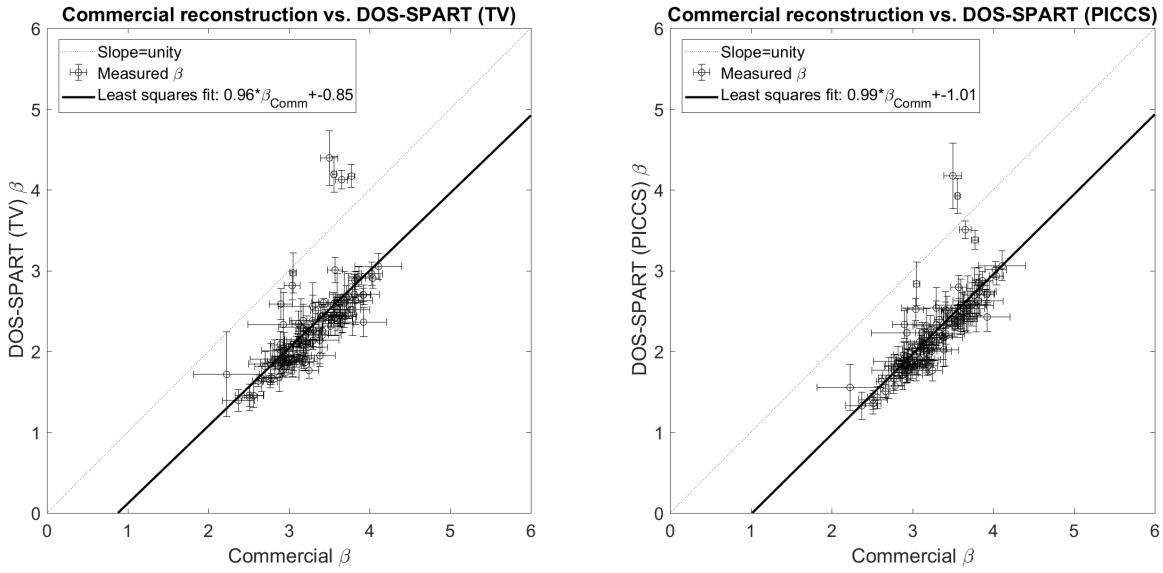

(a) (b)

Figure 5.5: The measured β values for the DOS-SPART DBT reconstructions plotted against the commercial reconstruction. The linear least squares fit is shown in the legend.

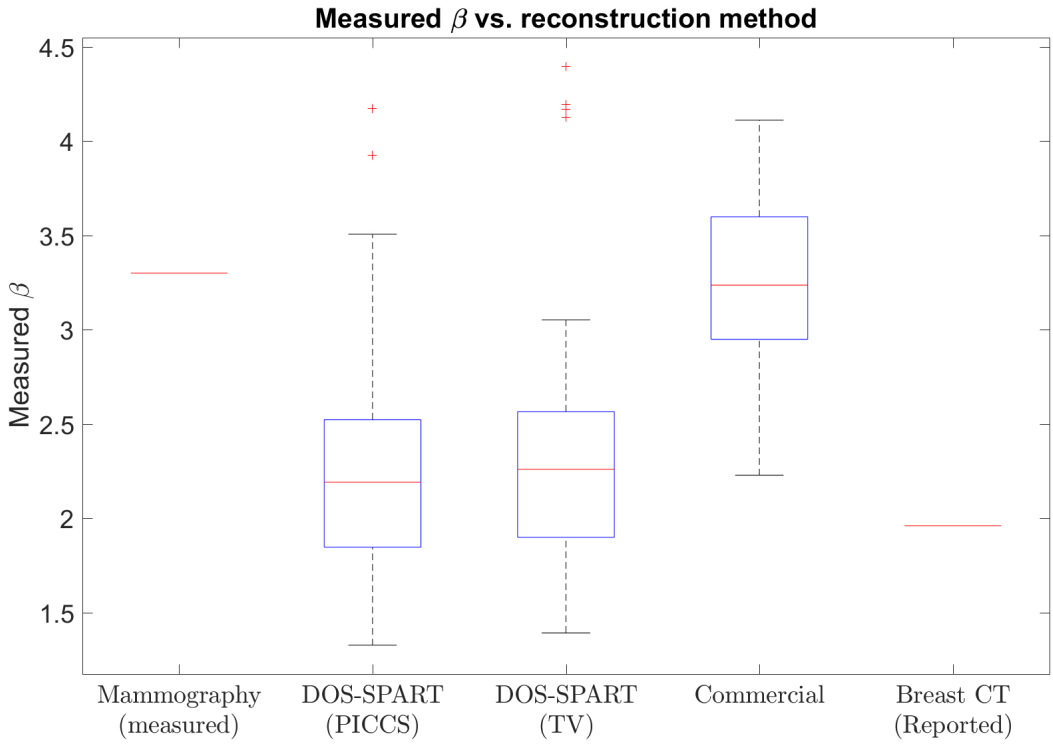

Figure 5.6: The measured β values for the DBT reconstructions.

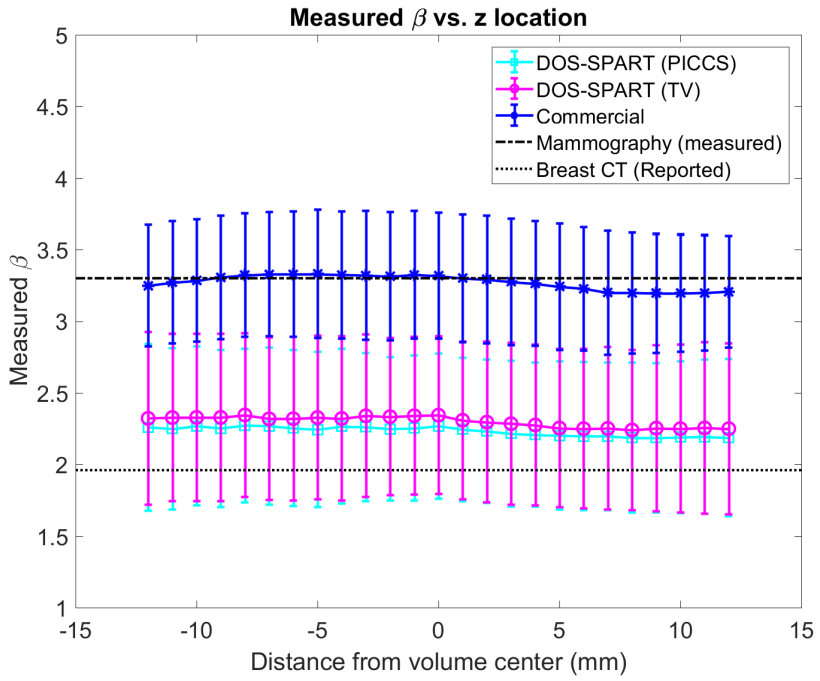

Figure 5.7: The average measured β value as a function of slice position for the two reconstruction methods.

5.4 Anatomical Noise Simulations

Understanding the anatomical background in new breast imaging techniques is a step towards understanding imaging performance, but we need to go further to understand its actual clinical impact. Traditional metrics, such as the CNR, are easy to calculate, but cannot account for aspects of an imaging system such as the anatomical noise. To rigorously quantify clinical imaging performance, we need a task-based metric that accounts for many different aspects of the imaging system. Such a metric can be used to predict system performance under a variety of conditions for a variety of imaging tasks. Using a model observer, a metric which meets our criteria, system parameters such as MTF, NPS, tube potential, dose, etc., may be incorporated along with actual observer performance (trained radiologist vs. physicist readers) and a specific imaging task to compare performance.

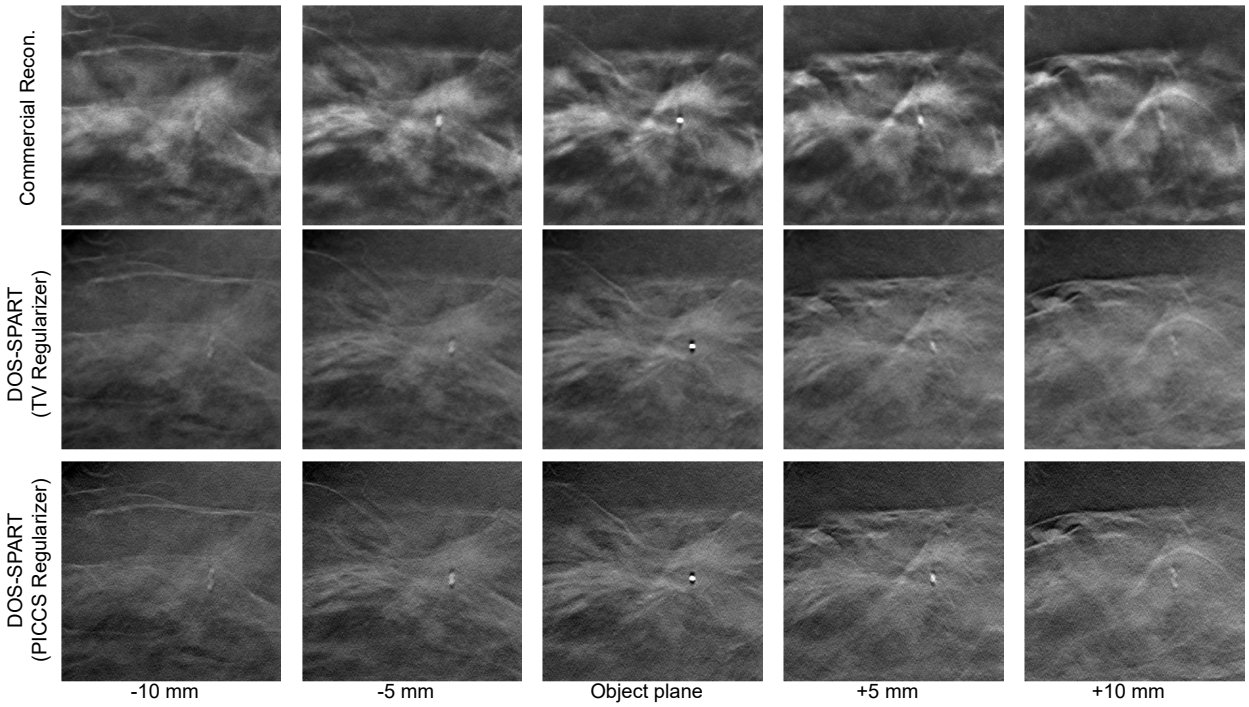

Figure 5.8: A clinical DBT exam reconstructed with the commercial reconstruction engine (top), DOS-SPART (TV Regularizer) (middle), and DOS-SPART (PICCS Regularizer) (bottom). A spiculated mass with a large calcification shown in focus and at locations above and below the focal plane. All image shown with the same W/L.

5.4.1 Methods

In order to use model observers, it may also be desirable to be able to simulate and recreate anatomical noise. To this end, we used our measured noise power spectrum to test such a framework. In this study we accounted for anatomical noise, both quantum and electronic noise, finite (100 μm) detector elements, as well as different mass objects sizes. Each noise instance was generated by adding the quantum NPS to a simulated NPS_a (including both α and β parameters). By scaling the quantum component, different dose levels could be simulated. The β parameter was varied to simulate different noise power shapes as well. An example simulated NPS is shown in Figure 5.9. Once a 1D NPS was simulated, it was used to generate a 2D NPS. Multiplicative random Gaussian noise with a mean of 1 was then introduced to generate a specific noise instance. One method that can be used to understand how anatomical noise impacts detection performance is a generalized ideal model observer. This model observer can account for anatomical noise and quantum noise in

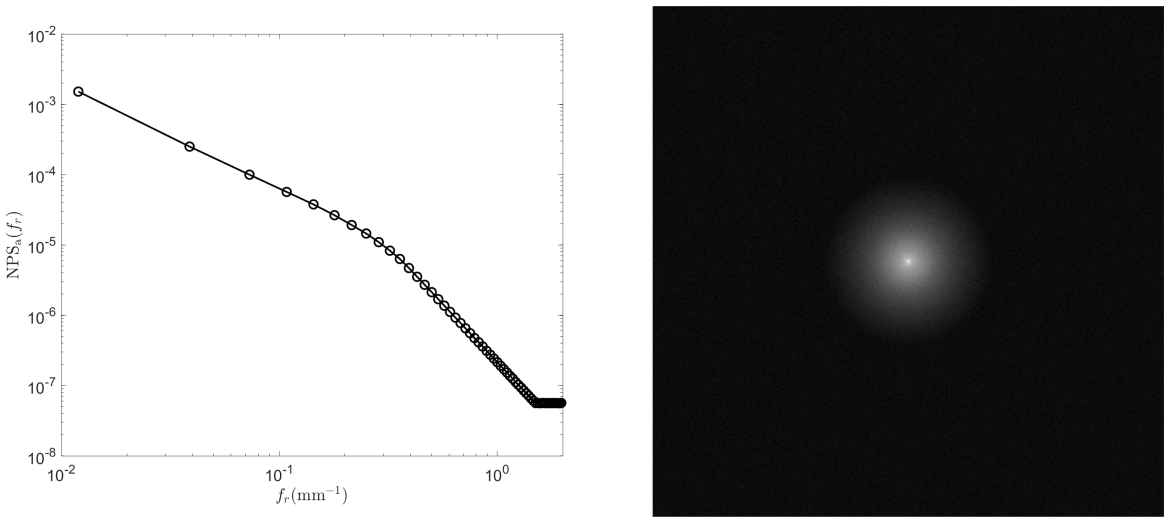

Figure 5.9: Example of a 1D (a) and 2D (b) simulated noise power spectrum for $\beta = 3.3$ (to simulate mammography).

assessing image quality[44]. This model observer is defined as follows:

$$(d')^2 = \int\int \frac{|T(f_x, f_y)|^2 \cdot [\mathrm{MTF}(f_x, f_y)]}{\mathrm{NPS}_a(f_x, f_y) + \mathrm{NPS}_q(f_x, f_y)} \mathrm{d}f_x \mathrm{d}f_y, \tag{5.4}$$

where T is the Fourier domain image task function, the MTF is the system modulation transfer function, NPS_a is the background anatomical noise power spectrum, and NPS_q is the quantum noise power spectrum. As it turns out, the model observer in Eq. 5.4 is a very simplified model, expected to provide an upper bound to observer performance. There are many other model observers, including: prewhitening observers with the eye filter and internal noise (PWEi)[196–198], nonprewhitening observers (NPW)[199,200], nonprewhitening observers with eye filter and internal noise (NPWEi)[201–203], and channelized Hotelling observers (CHO)[204–210]. With the exception of the CHOs, these are all frequency-domain analyses which modify the ideal observer laid out in Eq. 5.4 incorporating an observer's ability to prewhiten noise, including the frequency response of the eye, and internal observer noise.

While implementing these different observers can provide different performance estimates, on their own there is no way of knowing which of these estimates is the best indicator of actual observer

performance. A commonly used method to calibrate the model observers and identify the model observer which best represents human performance is to implement each of these families of observers and perform a two-alternative forced choice (2AFC) human reader study to tune the parameters of each model observer to best match human performance[126]. The proportion of correct responses from the 2AFC, P, is theoretically related to the model observer detectability as follows[211]:

$$P = \frac{1}{2}\left[1 + \mathrm{erf}\left(\frac{d'}{2}\right)\right], \tag{5.5}$$

where erf denotes the error function which is defined as $\mathrm{erf}(x) = (2/\sqrt{\pi})\int_0^x e^{-y^2}\mathrm{d}y$. Using this framework, P, obtained from human observer studies can be converted to d' values and compared to the model observer results. This can help us determine which model observer is the best choice to use for system optimization moving forward.

While it is beneficial to consider a model such as that provided in Eq. 5.4 in order to understand which aspects of the imaging system contribute to detectability, in practice the CHO models are very helpful for simulation studies. Since the framework proposed here to simulate anatomical noise backgrounds produces noise instances, the ability to work directly in the image domain is valuable. In addition, a CHO model utilizing Gabor channels has been validated and calibrated with human observers previously for breast mass detection tasks[126]. To that end, a preliminary study utilizing the simulated anatomical noise backgrounds and Gaussian masses with varying diameters (diameter was defined as $2\sqrt{2\log 2}\sigma$, the FWHM of the Gaussian distribution; see Figure 5.10) was performed. The goal of this study was to see subjectively how mass detectability changed as a function of lesion diameter and β. The CNR for the mass lesion was the same. We can see in Figure 5.11 several examples of these simulated noise backgrounds with a 10 mm Gaussian mass embedded. A CHO model was implemented using 50 Gabor channels, similar to those described and previously validated in Li *et al.*[126]. This model was then used to evaluate the detectability of the Gaussian lesions embedded in the simulated anatomical noise backgrounds.

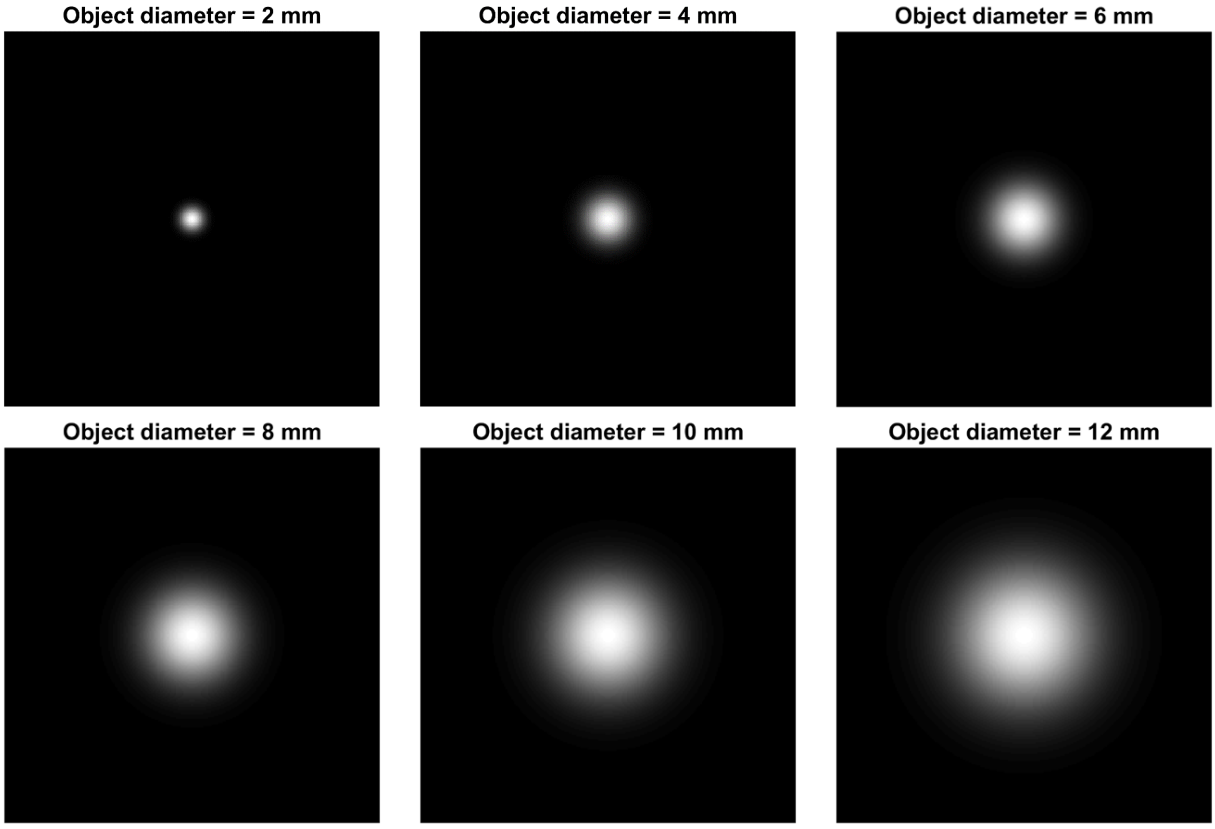

Figure 5.10: Simulated Gaussian mass lesions of different sizes.

5.4.2 Results

A contour plot of the measured (d‘) values for $\beta \in [0, 4]$ and objects with diameters ranging from 1 mm to 12 mm is shown in Figure 5.12. Detectability plots for a variety of β values (representing mammography, commercial DBT, DOS-SPART reconstructions, breast CT, and white noise) from the contour plot are shown in greater detail in Figure 5.13.

5.5 Discussion

The measured β values for the DOS-SPART images are important results, because they indicate that by modifying the reconstruction method, DBT images can achieve an anatomical background more similar to dedicated breast CT than mammography. In addition, this has been achieved using a clinical system with the smallest tomo angle of any clinical system. If human reader studies

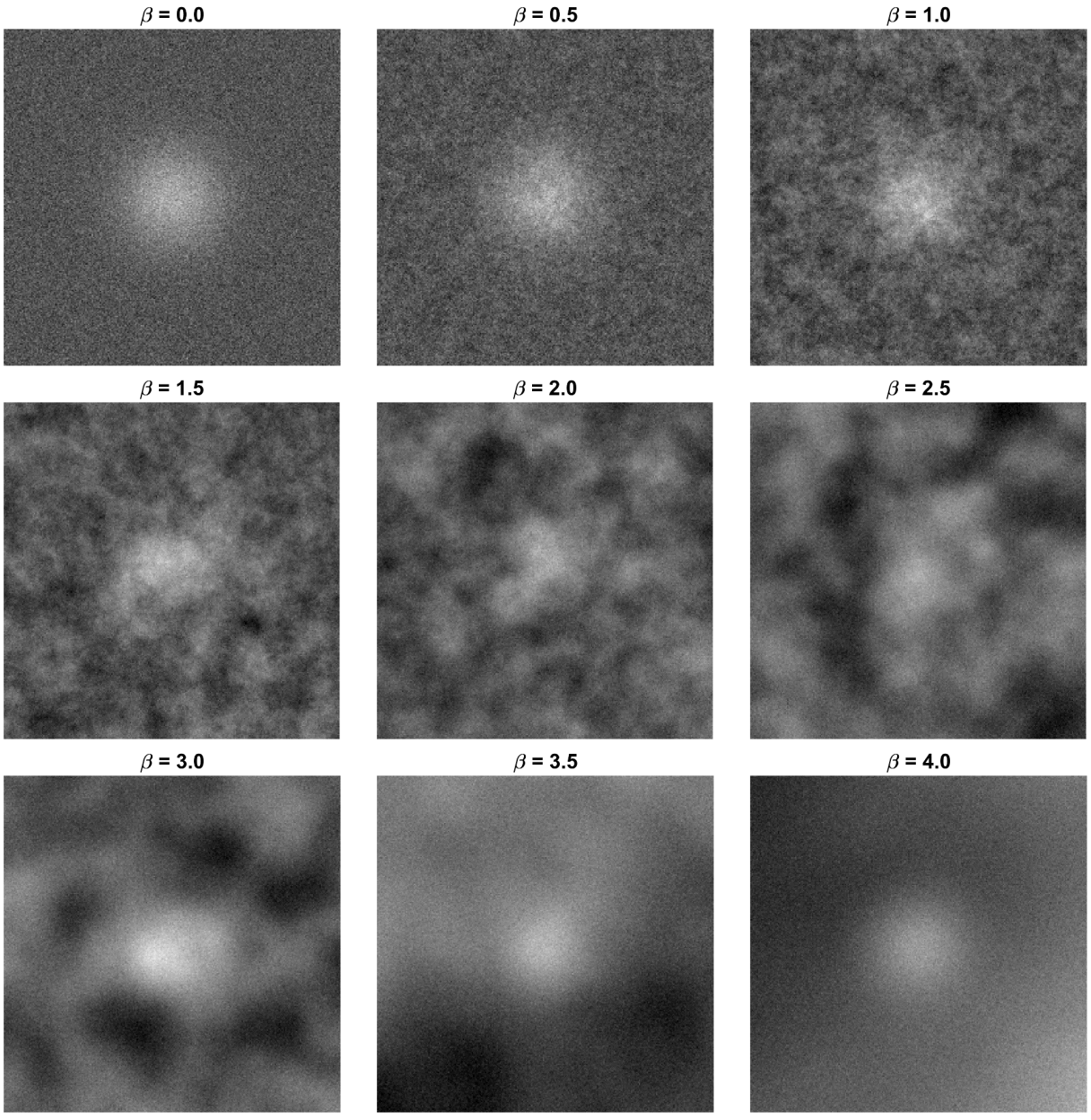

Figure 5.11: Examples of simulated noise instances for different β values with a 10 mm embedded Gaussian mass.

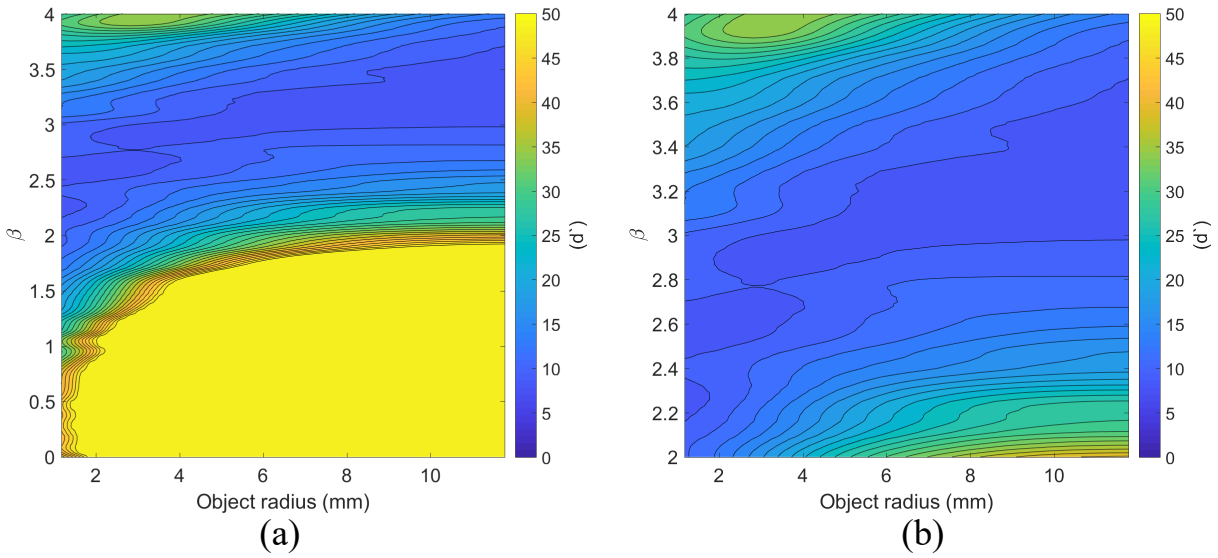

Figure 5.12: The measured CHO detectability for Gaussian lesions in simulated anatomical backgrounds. The full range ($\beta \in [0, 4]$) is shown in (a) with a reduced range ($\beta \in [2, 4]$ shown in (b) to emphasize the characteristics for real imaging modalities.

confirm the reduced anatomical clutter provides improved mass detection as predicted by observer theory, the introduction of DOS-SPART has the potential to make a significant impact in breast cancer detection.

In addition to the measured β values, the simulation results are very interesting for a few reasons as well. First and foremost, the β values corresponding to mammography reflect the human observer performance seen for similar mass lesions in work by Burgess *et al.*[44]. They found that the required contrast needed to detect mass lesions was reduced for smaller objects in anatomical backgrounds from mammography. An increasing detectability for smaller mass lesions found in our simulations conveys the same message: smaller objects are more conspicuous than large ones in mammographic backgrounds.

Second, there is an inflection point around $\beta = 2.8$ in the detectability maps shown in Figure 5.12 (clearly visible in (b)). At this point, the trend switches the conventional Rose model predictions (monotonically increasing detectability with increasing mass size) to the results discovered by Burgess *et al.*[44] (monotonically decreasing detectability with increasing mass size). Thus, for breast imaging modalities with β below this threshold we would expect reader results to follow a Rose modeltrend.

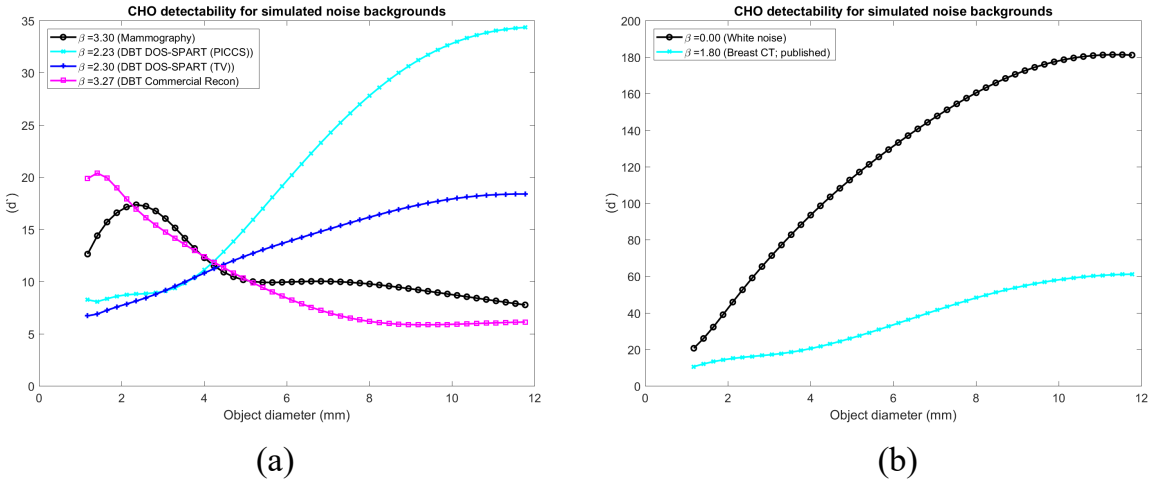

Figure 5.13: The measured CHO detectability for Gaussian lesions in simulated anatomical backgrounds for the modalities and reconstruction methods explored in this work.

However, for modalities where $\beta > 2.8$, we expect results consistent with clinical experience in mammography.

Third, the curve for breast CT (where anatomical noise is largely alleviated) and the curve for white noise (no anatomical contribution) shows a trend which matches our expectations from the Rose model quite well: increasing object size leads to increased detectability. Due to the finite size of the ROI used for simulation, there are diminishing returns as the objects get very large, as the largest objects occupy a substantial portion of the ROI, so the curves level off os the object diameter gets above ≈ 10 mm.

Fourth, the curve for commercial DBT reconstructions is inferior to mammography for both very small and larger masses and equivalent for masses between about 3 and 5 mm in diameter. This is somewhat surprising, however a major published advantage of DBT is its improvement in specificity (reducing false positive results) rather than sensitivity (mass detection) [212]. Thus, we might not expect a big boost in detection performance for DBT vs. mammography.

Finally, we can see the curve for DBT using DOS-SPART is similar to that of the commercial reconstructions for small objects, however it improves much more rapidly for larger masses, offering substantial improvement over mammography for masses larger than ≈ 5 mm in diameter. This may indicate the potential utility of DOS-SPART reconstruction in a clinical setting.

5.6 Conclusions

Understanding of the anatomical background noise spectrum in breast imaging can provide powerful insight into the ability of a given imaging technique to detect suspicious lesions or features. The NPS of this is often characterized by a power law, $\alpha f^{-\beta}$, where β characterizes the appearance and strength of anatomical noise. In this work we measured the anatomical noise in DBT reconstructions using both a commercial FBP-based reconstruction method and an in-house model-based iterative reconstruction method, DOS-SPART. We found the reduced slice thickness in the iterative reconstructions led to significantly reduced anatomic clutter in the reconstructed images. This has the potential to dramatically improve mass detection in DBT reconstructions. In addition, a framework to simulate anatomical backgrounds was proposed and utilized with a model observer to predict mass detection performance as a function of the anatomical noise parameter, β, and mass size. The data corresponding to $\beta \approx 3$ (close to traditional mammography and DBT with FBP) match previously published human studies, while the curves corresponding to the DOS-SPART reconstructions showed improved mass detection performance for masses larger than about 4 mm in diameter.

One interesting point to consider in this work is the following: with traditional mammography, it has been shown that anatomical noise is dominant, and that the dependence of the images on dose is minimal. However, in images with reduced anatomical noise, the quantum noise can again be a major contributor. As a result, exploring dose reduction potential is a very interesting topic, as current dose levels are determined using standard mammography or FBP images in current clinical practice.

6 Dose Reduction in Digital Breast Tomosynthesis with Prior Image Constrained Compressed Sensing (DR-PICCS)

As previously discussed, digital breast tomosynthesis (DBT) is an emerging breast imaging modality that builds on existing equipment and techniques used in mammography by incorporating three dimensional (3D) information[51]. DBT has been clinically available in the United States since 2011[8], and offers spatial resolution comparable to that of mammography while simultaneously alleviating two major problems inherent to two-dimensional (2D) imaging modalities: overlaying structures obscuring important pathology (false negatives leading to decreased sensitivity) and simulating pathology when none is present (false positives leading to decreased specificity)[49,90,98,99]. Although DBT is becoming more common in clinical practice, one major limitation is the concern of radiation exposure.

Ionizing radiation is used to generate endogenous image contrast in DBT, and as a result a balance between radiation exposure to the patient and image quality must be achieved. For many breasts, a DBT acquisition requires a radiation exposure similar to that of a mammogram on the same unit, however in some cases (such as thick or dense breasts) the exposure can be significantly higher[213]. In addition, current FDA-approved practice for some systems uses a "combo scan", in which both 2D mammographic and tomosynthesis acquisition are obtained and reviewed, requiring

two separate exposures and an increased dose for the exam[214]. This may be mitigated somewhat with the introduction of 2D synthesized mammograms generated from a tomosynthesis acquisition[68]. These synthesized mammograms use the acquired tomosynthesis data to generate a single 2D image similar to a mammogram. Since mammography and DBT are powerful tools that are used to screen a patient population consisting of healthy patients as well as cancer patients[8,215–217], maintaining a low radiation dose is especially important.

In x-ray based imaging techniques, the patient exposure can be reduced via several different techniques.[115] For tomographic imaging techniques, such as computed tomography (CT) or DBT, the number of view angles can be reduced while keeping other imaging parameters fixed. Although this reduces dose, it can result in image artifacts due to aliasing caused by angular under-sampling. In current DBT systems such as the one used in our studies, the number of projections is limited to fifteen. With so few projection views over a small angular range ($\approx [-7.5, 7.5]$), further reducing the number of views or decreasing the angular range will have a negative impact on the image quality and localization accuracy of the reconstructed images[48,139,140].

Another common technique is to reduce the x-ray tube current (and thus x-ray photon output) for the acquisition. This strategy reduces the x-ray fluence and results in a linear reduction in patient exposure[47]. However, a reduced x-ray fluence results in noisier images. Increased image noise results in potential degradation in diagnostic performance due to reduced detectability of masses, calcifications, and fine architectural detail. To reduce image noise, many post-processing techniques have been documented, however most conventional de-noising techniques inevitably blur the image (degrade spatial resolution) while removing noise from images. In breast imaging, spatial resolution is paramount to the identification of small clusters of microcalcifications or spiculated margins of lesions, key to the discovery of early stage breast cancers[8,47]. Therefore, any technique to reduce image noise in DBT must avoid the degradation of spatial resolution as much as possible to maintain the diagnostic performance of the DBT imaging system.

In this work, an image de-noising technique that was introduced to reduce image noise while retaining spatial resolution, viz., Dose Reduction with Prior Image Constrained Compressed Sensing algorithm (DR-PICCS)[142–145,175], was evaluated for its potential in radiation dose reduction in DBT imaging. The DR-PICCS technique has found several applications within diagnostic CT[143–146,177]

and cone beam CT [148] to demonstrate its potential in noise reduction while preserving spatial resolution. However, for DBT applications, the potential to retain spatial resolution and noise texture while reducing the overall image noise level must be carefully evaluated in phantom and human observer studies. Quantitative measurements of signal difference-to-noise ratio (SDNR), modulation transfer function (MTF), and noise power spectrum (NPS) have been performed to characterize the performance of DR-PICCS. Reader studies by experienced breast imaging radiologists have been performed in *ex vivo* breast cadaver and *in vivo* retrospective human subject studies to quantify the potential dose reduction in DBT using DR-PICCS.

The chapter is organized as follows: Section 6.1 describes the image acquisition techniques, the quantitative metrics to characterize the images, and the method of radiologist reader studies. Section 6.1 provides a description of all of the parameters used for image acquisition, a thorough description of the DR-PICCS method, as well as the parameters used to perform DR-PICCS reconstructions. A description of how the measurements were performed on the images is provided as well. Section 6.2 provides a summary of the results from quantitative measurements and the reader studies. Section 6.3 aims to interpret the results, provide a summary of the work completed, and provide the outlook of this work.

6.1 Materials and Methods

6.1.1 Data acquisition system and parameters

All data were acquired with a Selenia Dimensions DBT system (Hologic, Inc. Bedford, MA). The system geometry used in this work was a Cartesian coordinate system with the z-axis pointing vertically up from the detector surface (positive z towards the x-ray tube), the y-axis pointing away from the chest wall along the detector, and the x-axis pointing laterally along the detector edge (see Figure 3.2). All human subject data were acquired under the approval of an institutional review board (IRB).

6.1.2 Dose Reduction with Prior Image Constrained Compressed Sensing (DR-PICCS) Algorithm and Numerical Implementations

The Prior Image Constrained Compressed Sensing (PICCS) algorithm was developed initially as a reconstruction technique for highly under-sampled projection data sets in computed tomography (CT)[141], but it has been shown to have a variety of interesting clinical applications that do not have to be associated with the under-sampled reconstruction problems[142–146,178,179]. In the unconstrained framework used in this work, PICCS is performed by iteratively solving the following unconstrained minimization problem:

$$\tilde{\mathbf{x}} = \arg\min_{\mathbf{x}} \left[\frac{\lambda}{2} \frac{(\mathbf{A}\mathbf{x}-\mathbf{y})^T \mathbf{Q} (\mathbf{A}\mathbf{x}-\mathbf{y})}{||\mathbf{A}\mathbf{x}_p||^2} + \frac{f_{\text{PICCS}}(\mathbf{x})}{\text{TV}(\mathbf{x}_p)} \right], \tag{6.1}$$

$$f_{\text{PICCS}}(X) = \alpha\, \text{TV}(\mathbf{x}) + (1-\alpha)\, \text{TV}(\mathbf{x}-\mathbf{x}_p), \tag{6.2}$$

where $\mathbf{x} \in \mathbb{R}^{MN\times 1}$ is the vectorized representation a two-dimensional $M \times N$ image; $\mathbf{x}_p$ is a low noise prior image generated by a low-pass filter or other conventional denoising method. The vector, $\mathbf{y}$, is a synthetic projection dataset which will be described in detail below. $\mathbf{Q}$ is a diagonal matrix to introduce a pseudo-statistical weight to each synthetic datum. In non-CT applications, such as that proposed in this work, the matrix, $\mathbf{Q}$, should be the identity matrix since highly structured noise streaks are typically not present. $\mathbf{A}$ is the system matrix that defines the geometry used to generate synthetic projection data $\mathbf{y}$. The parameters α and λ are unitless scalars that determine the relative contribution of different terms in the optimization problem. Specifically, λ defines the relative weight of the PICCS and data-consistency terms and α defines the relative impact of the prior image in the PICCS term. The denominators in Eq. (6.1) the expression normalize the optimization problem such that selection of λ is nearly independent of application[147]. The total variation of the image matrix X which is defined as follows:

$$\text{TV}(\mathbf{x}) = \sum_{1<i<M(N-1)} \sqrt{(x_{i+1}-x_i)^2 + (x_{i+M}-x_i)^2}. \tag{6.3}$$

In this work, to solve the unconstrained optimization problem in Eq. (6.1) the non-linear conjugate

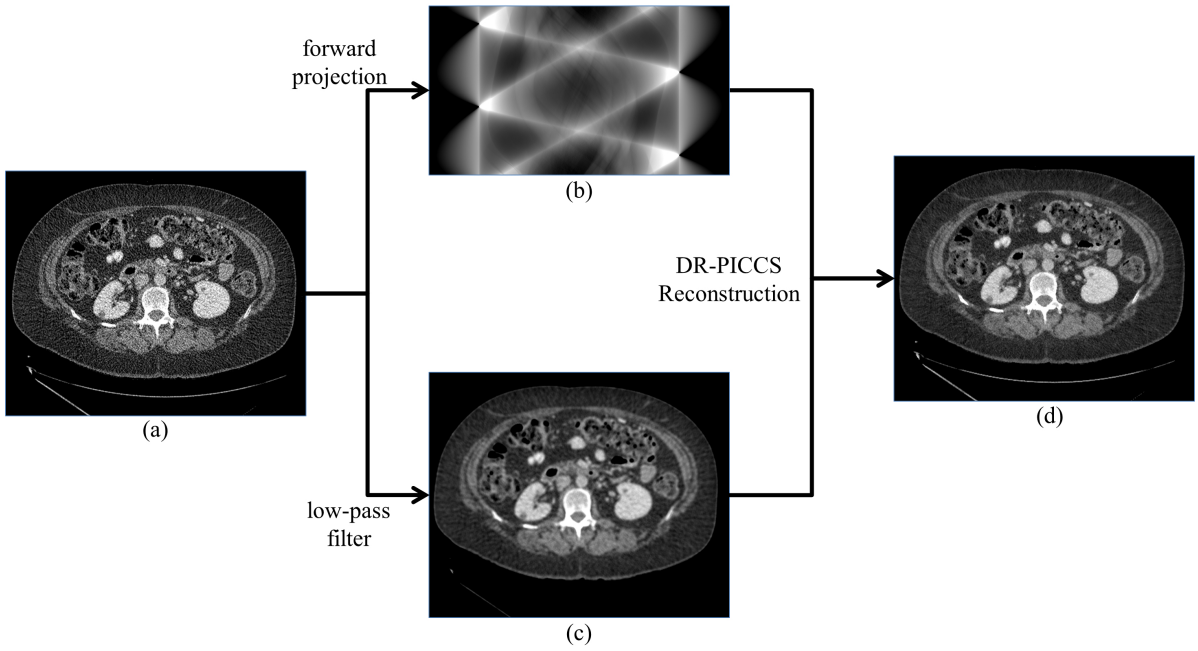

Figure 6.1: The DR-PICCS workflow shown with a clinical CT slice from a human abdomen.

gradient optimization method with Fletcher-Reeves updates and a backtracking line search subject to the Wolfe conditions for sufficient decrease was used[218].

The PICCS framework was originally intended to reconstruct CT datasets, however it has been shown that the adaptation of PICCS to dose reduction (DR-PICCS) can operate directly in the image domain to reduce noise while retaining important imaging features.[143,145] In this framework (see Figure 6.1) a noisy image of interest is forward projected to generate a synthesized projection dataset, $\mathbf{y}$, and a prior image can be generated by using a conventional image denoising technique over the noisy image. *The purpose of applying DR-PICCS, rather than a direct use of the conventional denoising technique, is to iteratively restore the loss of spatial resolution in conventional denoising techniques.*

6.1.2.1 Prior image generation

In this work, the prior image is generated using a 3D anisotropic diffusion filter and an automated slice-by-slice noise estimate.[149,150] This method uses a solution to a partial differential equation (PDE) modeling the physical diffusion process. This process is performed iteratively and each

iteration models the temporal evolution of a diffusive system. This process may be described as follows:[149]

$$I_{t+1} = I_t + \lambda \sum_k C_k \nabla_k I_t, \tag{6.4}$$

where I_t is the system (image) at the time point t, λ is a normalization factor, k denotes a spatial direction, C_k is the conduction coefficient in the direction, k, and $\nabla_k I_t$ is the directional gradient along the direction, k. Although there are many possible models, in this work, C_k, was defined as a function of the magnitude of $\nabla_k I_t$ as follows[150]:

$$C_k = \phi\left(||\nabla_k I_t||\right) = \frac{1}{1 + \left(\frac{||\nabla_k I_t||}{\kappa}\right)^2}, \tag{6.5}$$

where κ is determined by a local noise estimate calculated using the histogram threshold method described by Canny.[150] Due to the automation used to generate the prior image, the only free parameters available to the user were the total desired noise reduction and the noise estimation threshold value defined as $0.99 + \tau$. It should be noted that the value of τ depends on the number of histogram bins used in the estimation; in this work 2048 histogram values were used. These values were chosen subjectively. An example of prior images using a range of these values are shown in Fig. 6.2. A 75% noise reduction was used with $\tau = 5 \times 10^{-3}$ and provided sufficient noise reduction without severe distortion of small calcifications.

Finally, a brief summary of the working principles in DR-PICCS may be beneficial. The algorithm depends on two components: First, the prior image used in the PICCS reconstruction has excellent signal-to-noise ratio (SNR) characteristics, but limited spatial resolution. Second, the projection data have the desired high spatial resolution encoded, but also have the high image noise in the originally-reconstructed images that limits its utility. The goal of the algorithm is to produce an image with the desired characteristics from both the prior image and the original image. To accomplish this, a forward projection operation is used to encode the spatial resolution of the original noisy image in a synthetic projection dataset. The iterative reconstruction procedure of the PICCS implementation is then used to clone the high SNR nature of the prior image into the reconstructed image. The spatial resolution lost in the prior image is iteratively corrected

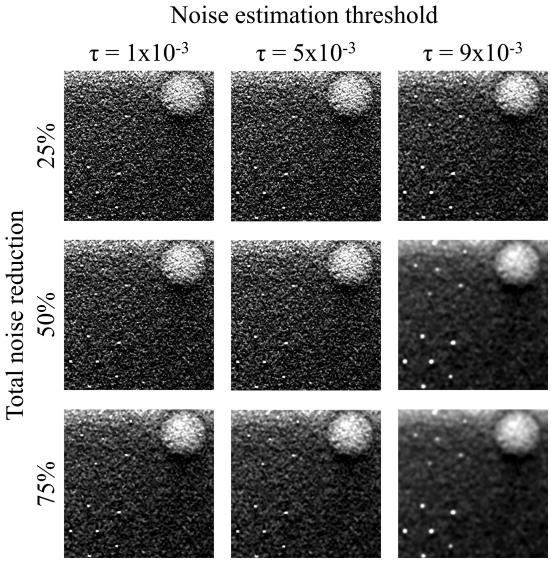

Figure 6.2: The two largest calcification clusters and the largest mass lesion from the ACR phantom are shown here in prior images generated using a range of parameters.

by matching the synthetic forward projection data with the high spatial resolution information encoded.[143] During the PICCS reconstruction, the local contrast is determined by the prior image and the "data consistency" updates are only used to update the spatial resolution, since with accurate local mean values the only inconsistencies in the projection data should be at boundaries. Since the prior image is generated using the 3D dataset, no inconsistency from slice to slice is introduced by this algorithm.

6.1.3 Reconstruction methods

In this work, three reconstruction methods were considered: (i) the commercial reconstruction method including filtered backprojection (FBP) and post-processing offered by the Hologic Selenia system; (ii) conventionally denoised reconstructions; and (iii) DR-PICCS reconstructions. For the DR-PICCS and conventionally denoised reconstructions, image volumes were first generated using FBP with no additional post-processing. These noisy volumes were then denoised either with the DR-PICCS algorithm (using $\alpha = 0.5$ and $\lambda = 10^4$ which consistently gave the best results) or via convolution with a 3×3 Gaussian kernel ($\sigma = 2$ pixels). These methods were compared using a variety of metrics as outlined below.

6.1.4 Performance evaluation of DR-PICCS: Measurement of the Impact of Radiation Dose on Signal Difference-to-Noise Ratio (SDNR)

A prospective dose reduction study using an American College of Radiology (ACR) mammography accreditation phantom (Fluke Biomedical, Cleveland, OH) was performed. In this study, the signal difference-to-noise ratio (SDNR) was measured for each reconstruction method for several different imaging features at different exposure levels (100%, 88%, 76%, 64%, 59%, 47%, 34%, and 22%; see Table 6.1 for acquisition parameters). A tube potential of 29 kVp was used for all phantom acquisitions. The SDNR of the largest three fibers, the largest three calcification groups, and the largest four lesions were measured (see Figure 6.3) for each of eight dose levels. For the calcifications, the SDNR of each calcification in the group was measured and an average SDNR for each group was calculated. The SDNR was defined as follows:

$$\text{SDNR} \equiv \frac{\mu_o - \mu_B}{\bar{\sigma}} \text{ with } \bar{\sigma} = \frac{\sigma_o + \sigma_B}{2} \tag{6.6}$$

where μ is the measured mean value in the given region of interest (ROI), $\bar{\sigma}$ is the mean standard deviation, σ_i is the measured standard deviation in the ROI, and the subscripts, O and B, represent the object and the background respectively. The SDNR was plotted as a function of dose and linear regressions were performed in each case to predict SDNR performance and to assess the correlation between SDNR and dose.

Table 6.1: ACR phantom image acquisition parameters

Parameter	Percent Dose (%)							
	100	88	76	64	59	47	34	22
mAs	51.5	45.3	39.9	33.2	30.2	24.2	17.7	11.3
Organ dose (mGy)	1.3	1.2	1.0	0.9	0.8	0.6	0.5	0.4

6.1.5 Performance evaluation of DR-PICCS: Noise Power Spectrum Measurements

The noise power spectrum (NPS) was calculated for each reconstruction method of a 4.1 cm thick anthropomorphic solid water phantom (see Figure 6.4). The data for this calculation were acquired

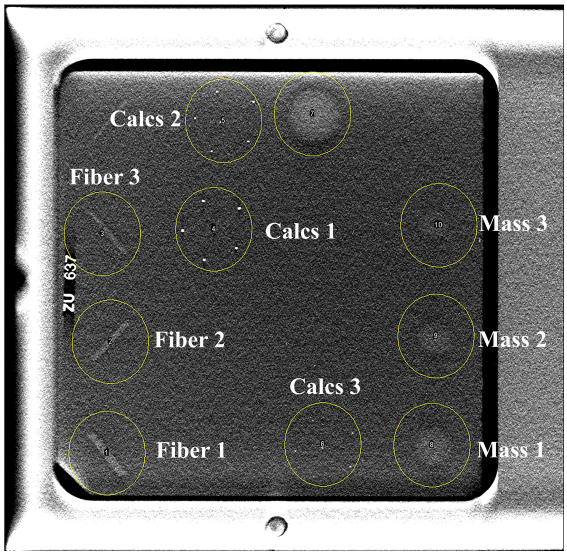

Figure 6.3: The imaging features of the ACR phantom used for SDNR measurements are shown circled here in the full dose commercial reconstruction of the phantom.

at 29 kVp and 30 mAs, providing a mean glandular dose of 0.8 mGy. The 3D NPS was measured as follows[127]:

$$\mathrm{S}\left(f_x, f_y, f_z\right) = \frac{\Delta_x \Delta_y \Delta_z}{N_x N_y N_z} \left\langle \left| \mathrm{DFT}\left\{ \mathrm{V}_i\left(x, y, z\right) \right\} \right|^2 \right\rangle, \tag{6.7}$$

where Δ_i is the pixel pitch in the i direction, N_i is the number of pixels in the volume of interest (VOI) used to estimate the NPS in the i direction, V_i is a noise instance, $\langle \cdot \rangle$ is the averaging operation, and DFT is the 3D discrete Fourier transform.

Three independent image volumes were acquired and used to generate three distinct noise-only images by subtracting the reconstructed volumes from one another and scaling by a factor of $1/\sqrt{2}$ to preserve the noise amplitude. In each of these noise instances, approximately 1500 overlapping $128 \times 128 \times 16$ volumes of interest (VOI) were extracted from the phantom image (see Figure 6.4) to simulate a large ensemble average. Each VOI had its mean subtracted and was used as a noise instance (V_i) to estimate the NPS using Eq. 6.7. The pixel size used for this estimate was $\Delta_x = \Delta_y = 0.110$ mm and Δ_z was 1 mm, resulting in $\Delta_{f_x} = \Delta_{f_y} = 0.04\mathrm{mm}^{-1}$ and $\Delta_{f_z} = 0.03\mathrm{mm}^{-1}$.

While the 3D NPS provides a comprehensive understanding of the system, the 1D NPS provides an opportunity to compare the NPS in the same plot. The 1D NPS is given by the following expression:

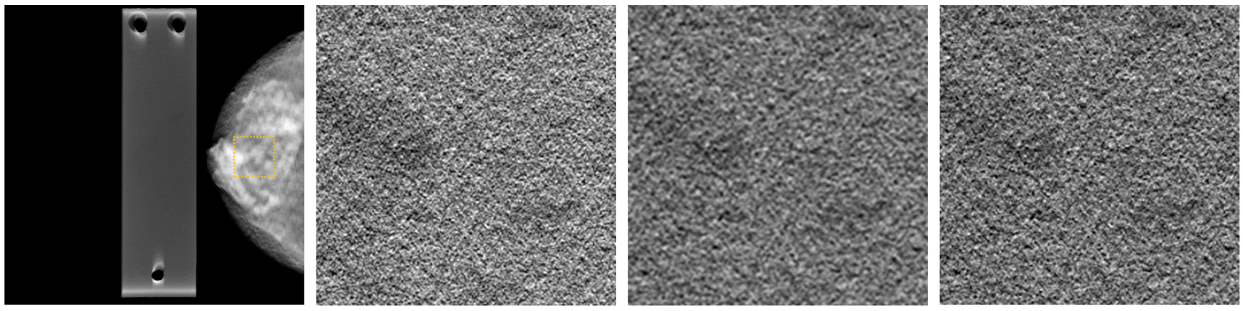

(a) (b) (c) (d)

Figure 6.4: The image object used in the NPS measurements is shown in (a). On the left is the solid water plate and on the right is an anthropomorphic phantom where the measurements were made (region denoted with the gold square). (b), (c), and (d) show an example of a noise instance reconstructed using the commercial reconstruction, conventional denoising, and with DR-PICCS, respectively.

$$\mathrm{S}_{1\mathrm{D}}\left(f_i\right) = \int\int \mathrm{S}\left(f_i, f_j, f_k\right) \mathrm{d}f_j \mathrm{d}f_k, \tag{6.8}$$

where the indices i, j, k can take x, y, z as their components in a non-repeated manner. The 3D NPS were normalized for comparison by dividing the NPS by the sum of all elements of the NPS:

$$\mathrm{S}_{norm} = \frac{\mathrm{S}\left(f_x, f_y, f_z\right)}{\sum_{f_x}\sum_{f_y}\sum_{f_z} \mathrm{S}\left(f_x, f_y, f_z\right)}. \tag{6.9}$$

6.1.6 Performance evaluation of DR-PICCS: Spatial Resolution Measurements

The spatial resolution was characterized via modulation transfer function (MTF) measurements. Since DBT does not necessarily provide uniform spatial resolution at different heights above the detector[57], the MTF was measured in the plane of the detector as well as at 2 cm intervals above the detector up to 8 cm (see Table 6.2 for acquisition parameters). These measurements were performed for the DR-PICCS reconstructions, filtered backprojection (FBP with no additional denoising), and the conventionally denoised reconstruction. The MTF was measured using an edge phantom (0.025 mm Pb) consisting of a square cutout (providing 4 edges per acquisition) and the method proposed by Fujita *et al.*[219]. Since an edge was measured rather than a slit or a wire, the measured edge profile was differentiated to generate a line profile. In order to generate an up-sampled line

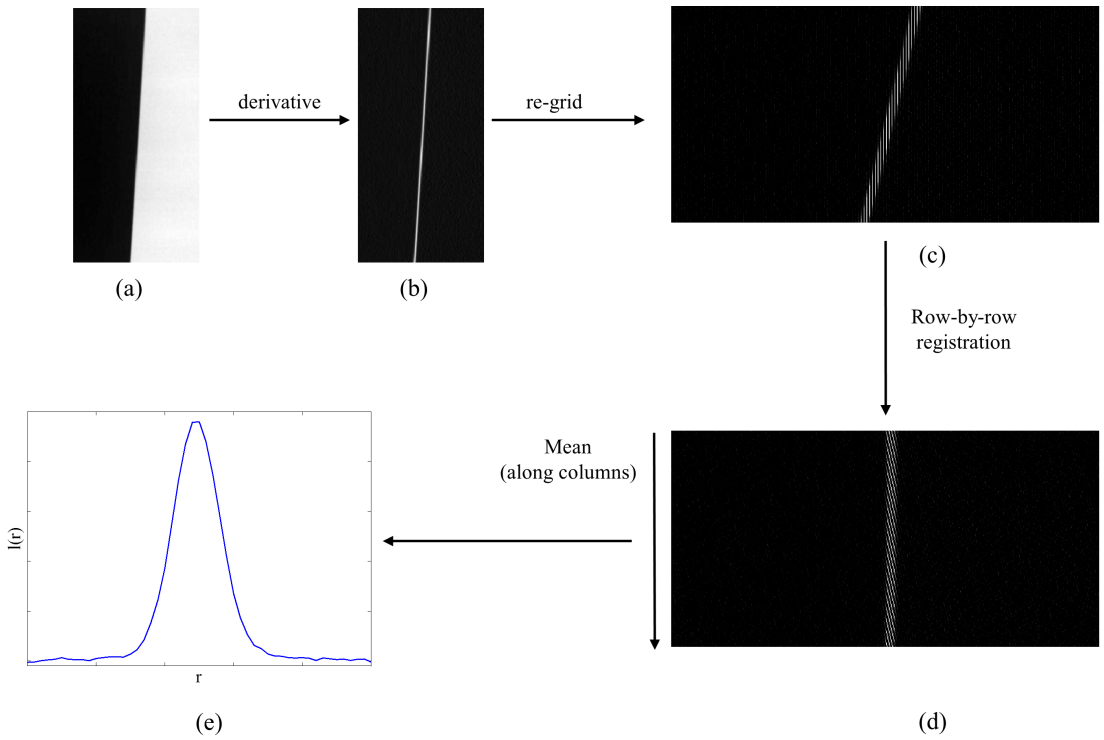

Figure 6.5: A workflow demonstrating how the presampled LSF was measured in this work. In (a) an image of an angled edge is shown as the starting point for the workflow.

spread function (LSF) and reduce aliasing in the MTF measurement, an angular registration and re-sampling was performed to generate an average line profile for each measured edge.

For each of these line profiles one tail corresponds to air and the other to lead. The tail corresponding to lead was much noisier than the air tail and typically didn't drop all the way to zero, but rather retained some small offset. In order to mitigate noise and ensure both tails fall to zero, the generated line profile was segmented at about 10% of the peak value on the lead tail side. This tail was then extrapolated to match the air side and both tails were then smoothed to remove the low-frequency-drop that characterizes noisy MTF measurements. The smooth line profiles acquired for each edge were averaged and re-normalized to generate an up-sampled LSF. The magnitude of the 1D discrete Fourier transform of the LSF was then taken to generate an MTF and at least two edges were measured in each plane. This procedure is summarized in Figures 6.5 and 6.6.

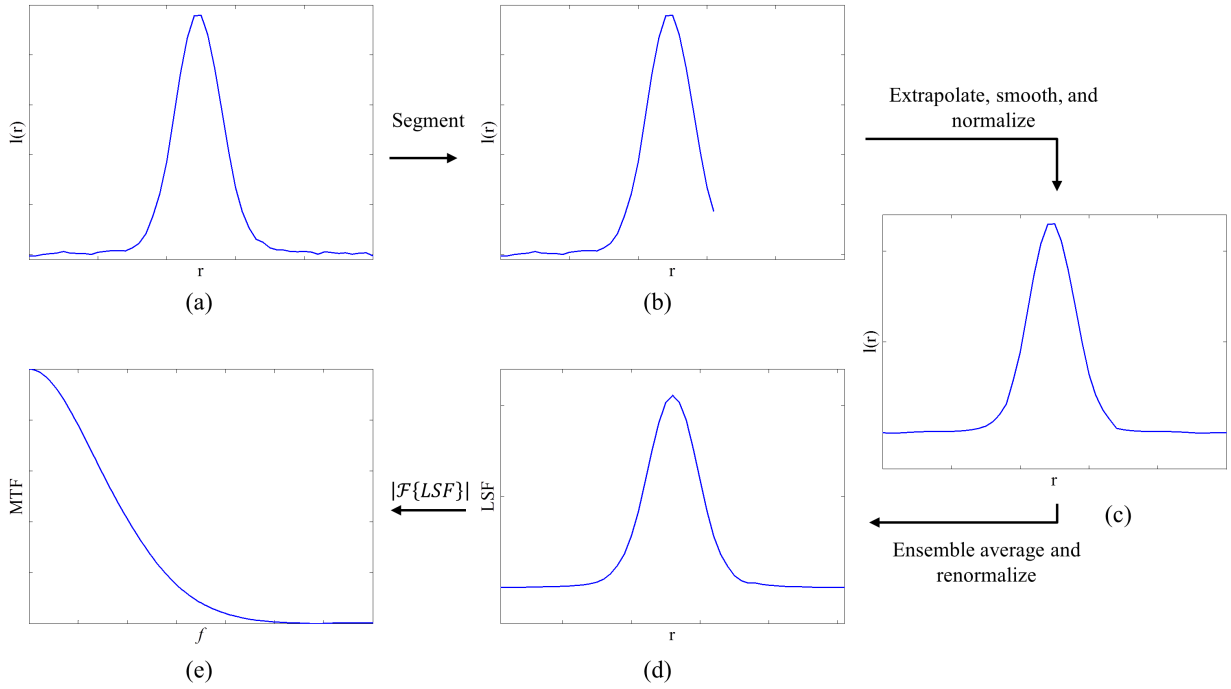

Figure 6.6: A workflow demonstrating how the MTF workflow from a presampled measured LSF shown in (a). The $\mathcal{F}$ symbol indicates a 1D discrete Fourier transform.

Table 6.2: MTF measurement image acquisition parameters

Parameter	MTF Phantom			
Edge height (cm)	2	4	6	8
Object thickness (cm)	2.2	4.3	6.4	8.4
kVp	26	29	33	38
mAs	30.3	48.2	66.6	84.5
Organ dose (mGy)	0.7	1.2	2.1	3.7

6.1.7 Performance evaluation of DR-PICCS: Human Observer Study

DBT data sets of the ACR breast accreditation phantom and two cadaver breasts were obtained at varying radiation exposure levels (see Table 6.3 for acquisition parameters). The cadaver breasts used were post-mastectomy breasts sealed in fiberglass containers. Five breast radiologists (4 with 20+ years experience, 1 with 5 years experience) performed a two alternative forced choice (2AFC) study on diagnostic mammography/DBT review stations with calibrated 5 MP monitors (Hewlett-Packard, Palo Alto, CA and Hologic, Inc., Bedford, MA) mammography review stations.

In each case, one image was a slice from a cadaver reconstruction acquired at full dose using the commercial reconstruction engine, while the other image was a DR-PICCS reconstruction of the same slice at 60% dose. The side of the screen displaying the DR-PICCS reconstruction was randomized for each slice shown. The radiologists were assigned the following task: when shown two similar images of the same slice of the same cadaver breast specimen, choose one of the two displayed images as diagnostically superior. The radiologists were not provided an opportunity to adjust the window/level for the images.

The radiologist reviewers' results were pooled into a single dataset for statistical analysis. If the full dose commercial reconstruction was chosen, that result was scored zero; if the reduced dose DR-PICCS reconstruction was chosen, that result was scored as 1. Two 1-tailed t-tests were used to determine a 95% confidence interval for the mean score. A mean score of one indicated the reduced dose DR-PICCS reconstruction was chosen all of the time, a mean score of zero indicated the full-dose commercial reconstruction was chosen all of the time. A mean score of 0.5 was considered to mean the two techniques were equivalent.

Table 6.3: Cadaver breast image acquisition parameters

Parameter	Cadaver 1 Percent Dose (%)		Cadaver 2 Percent Dose (%)	
	100	60	100	60
Object Thickness (cm)	— 6.2 —		— 6.3 —	
kVp	— 33 —		— 33 —	
mAs	67.0	39.4	69.7	42.4
Organ dose (mGy)	2.3	1.3	2.3	1.4

6.2 Results

6.2.1 Qualitative Comparison of Images from Two Image Reconstructions at Two Exposure Levels

A high-density mass with irregular margins is shown in Figure 6.7 at full dose using the commercial reconstruction technique as well with DR-PICCS denoising. This lesion appears in an 8.8 cm thick compressed breast, and was imaged at 40 kVp and 76.3 mAs resulting in a mean glandular dose of 3.9 mGy. In this case, important imaging features such as calcifications and margins have been well

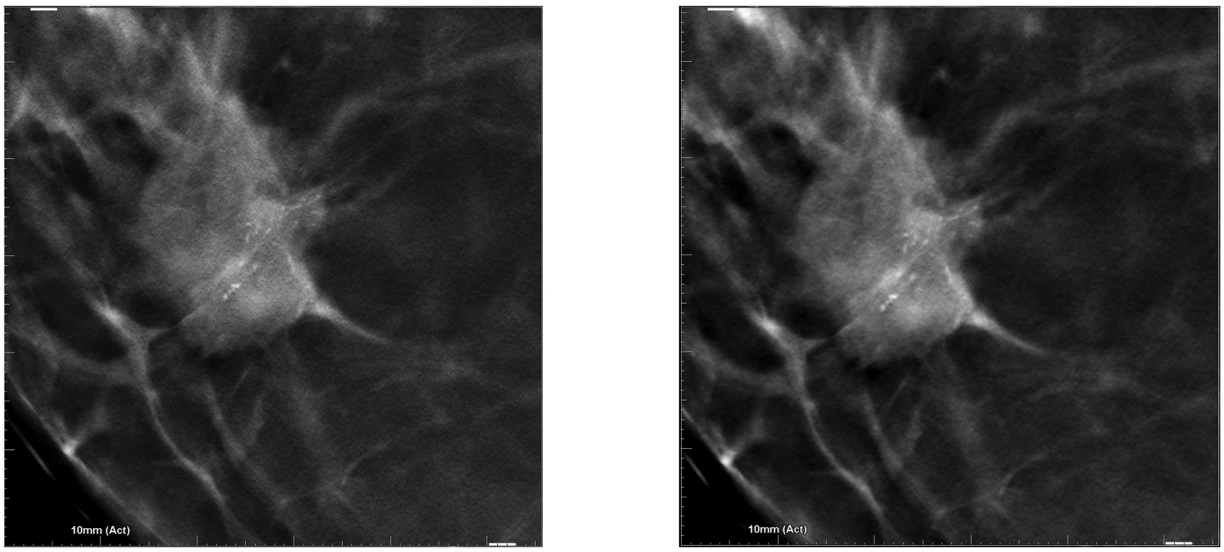

Figure 6.7: An example of a lesion with calcifications reconstructed (at the same dose level) using the commercial reconstruction (a) and the DR-PICCS reconstruction (b).

retained despite reduced noise. The background noise measured in the lesion was decreased by 20% (with the measured intensity standard deviation 26 with the commercial reconstruction and 20 with the DR-PICCS reconstruction).

A close up of the ACR accreditation phantom, including the fiber inserts, calcifications, and low contrast lesions, is shown in Figure 6.8 with the commercial reconstruction at 100% dose and the DR-PICCS reconstruction at 60% dose. All of the imaging features required to pass quality control procedures are visible in each case, namely the four largest fibers and 3 largest speck groups and masses should be visible in the acquired images.[220]

In addition to the phantom images, two examples of the cadaver breast images are shown in Figure 6.9. A cluster of microcalcifications and an area of architectural distortion are compared using the commercial reconstruction at 100% dose and the DR-PICCS reconstruction at 60% dose.

6.2.2 Experimental results of SDNR vs radiation exposure levels

The SDNR of the DR-PICCS reconstructions was higher for all of the ROIs using the commercial reconstruction at the same dose level (see Figures 6.10 and 6.11). In addition, using linear regression

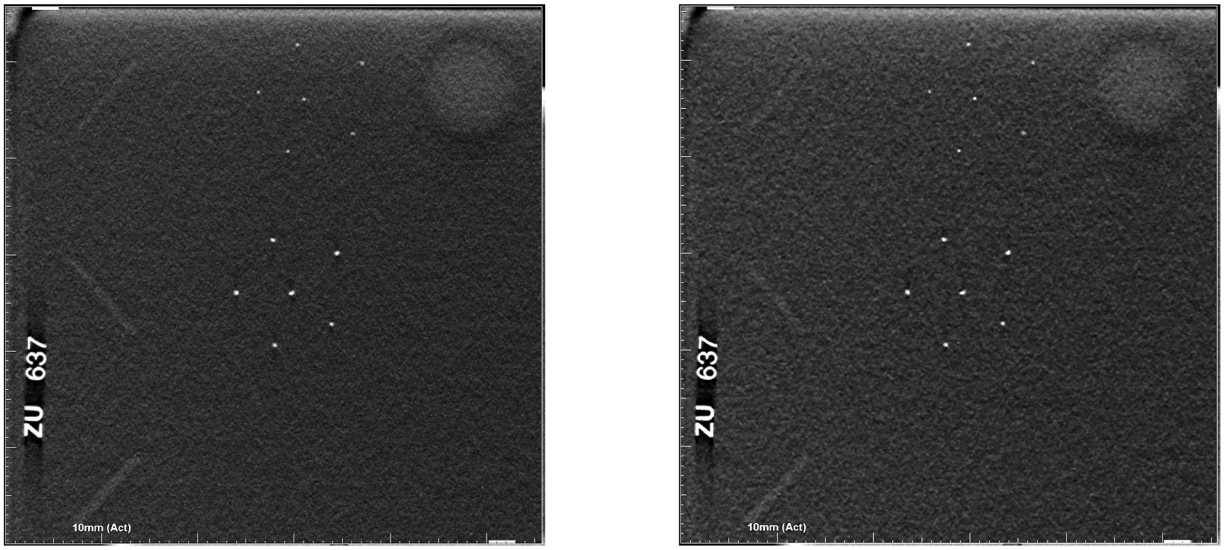

(a) (b)

Figure 6.8: A close up of the ACR accreditation phantom reconstructed at 100% dose using the commercial engine (a) and at 60% dose using DR-PICCS (b).

of the SDNR vs. dose data for each of the measured regions it was found that the average SDNR for all measured features for DR-PICCS was predicted to match that of the full dose commercial reconstruction at $68 \pm 8\%$ of the full dose. The correlation between the SDNR and dose was high with all three reconstruction methods, with an average correlation coefficient given by: $R^2 = 0.96 \pm 0.04$, $R^2 = 0.94 \pm 0.04$, and $R^2 = 0.95 \pm 0.04$ for the commercial reconstructions, the conventionally denoised reconstructions, and the DR-PICCS reconstructions, respectively. Although a linear regression does not match the physical model for these data, over the range of doses examined, this approximation seems to be sufficient.

6.2.3 Noise Power Spectrum

Five sample slices of the measured 32 slice 3D noise power spectrum are provided to compare the NPS of the commercial reconstruction, the conventionally denoised reconstruction, and the DR-PICCS reconstruction (see Figure 6.12). All three NPS are normalized and shown with the same window and level (W/L). Compared with the conventionally denoised reconstruction, the DR-PICCS reconstruction contains relatively more high frequency noise, and the overall shape of

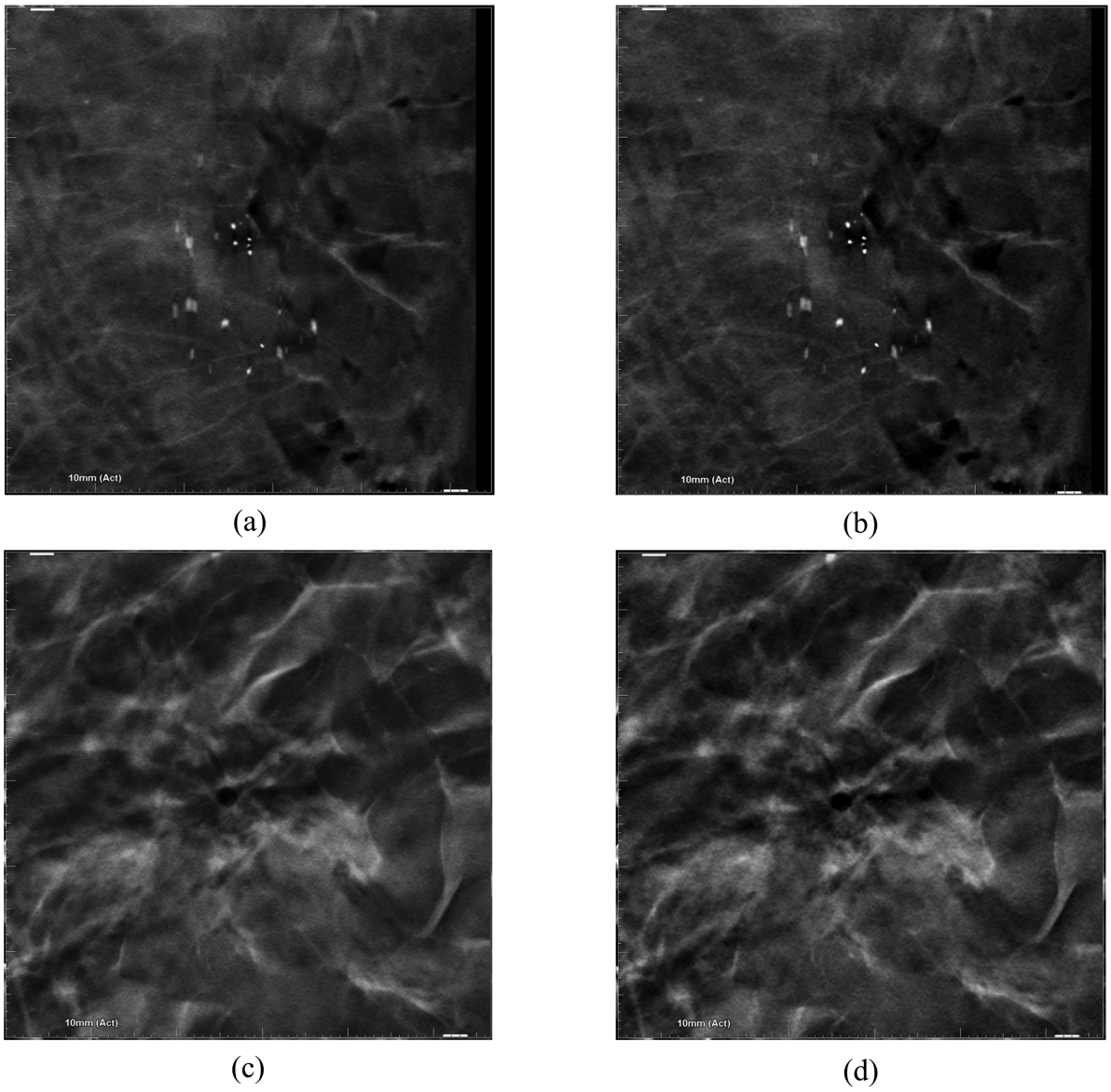

Figure 6.9: A close up of calcifications in one cadaver breast reconstructed at 100% dose using the commercial engine (a) and at 60% dose using DR-PICCS (b) and a close up of a heterogeneous density in one cadaver breast reconstructed at 100% dose using the commercial engine (c) and at 60% dose using DR-PICCS (d).

its 3D NPS is quite similar to that of the commercial reconstruction.

The 1D NPS is shown in the x- and y-directions in Figure 6.13. From these NPS we can compare the overall noise level of each method with the others. In addition, a significant low-frequency shift of the conventionally denoised NPS can be seen in Fig. 6.13(a) (x-direction), although we don't see

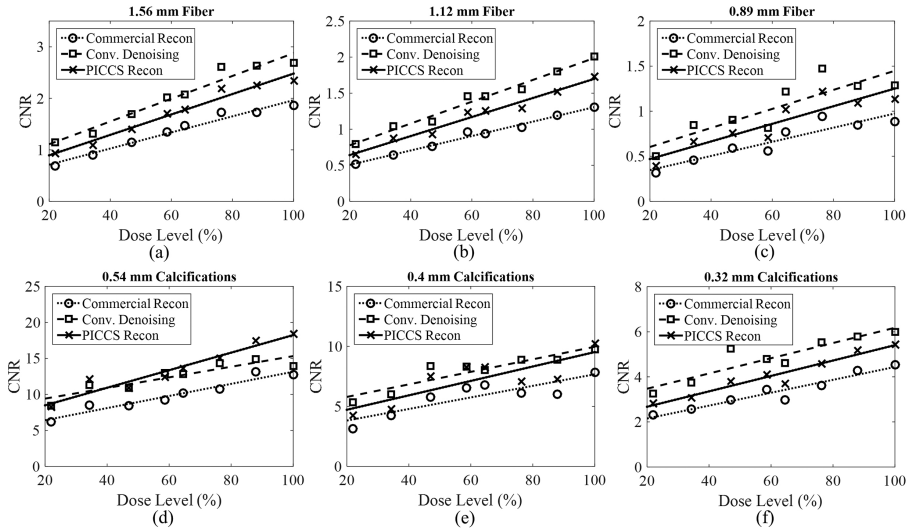

Figure 6.10: The measured SDNR for the fibers (a-c) and calcification clusters (d-f) in the ACR accreditation phantom at various dose levels. Shown are the measured values as well as linear fits to the data.

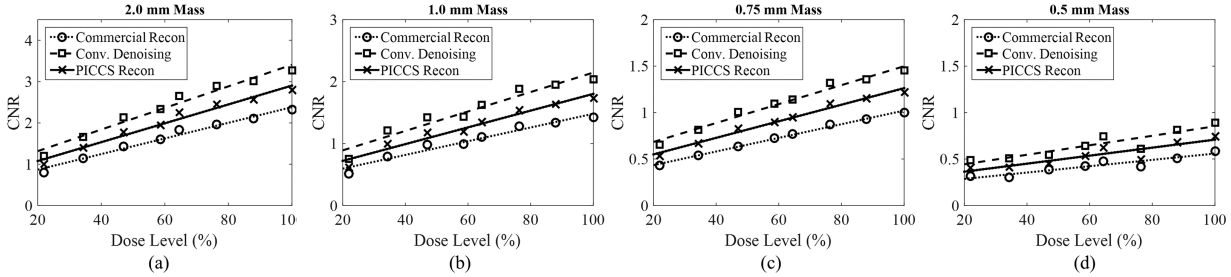

Figure 6.11: The measured SDNR for the lesions in the ACR accreditation phantom at various dose levels. Shown are the measured values as well as linear fits to the data.

the same shift in the y-direction.

The measured noise power spectra (NPS) show that the DR-PICCS reconstruction technique retains the shape of the NPS better than that of the conventional denoising method. Maintaining this frequency dependence results in images with which radiologists have grown more comfortable through review.

6.2.4 Modulation Transfer Function

A comparison of the MTF measurements for the commercial reconstruction, the conventionally-denoised reconstruction, and the DR-PICCS reconstruction at different depths are shown in Figures

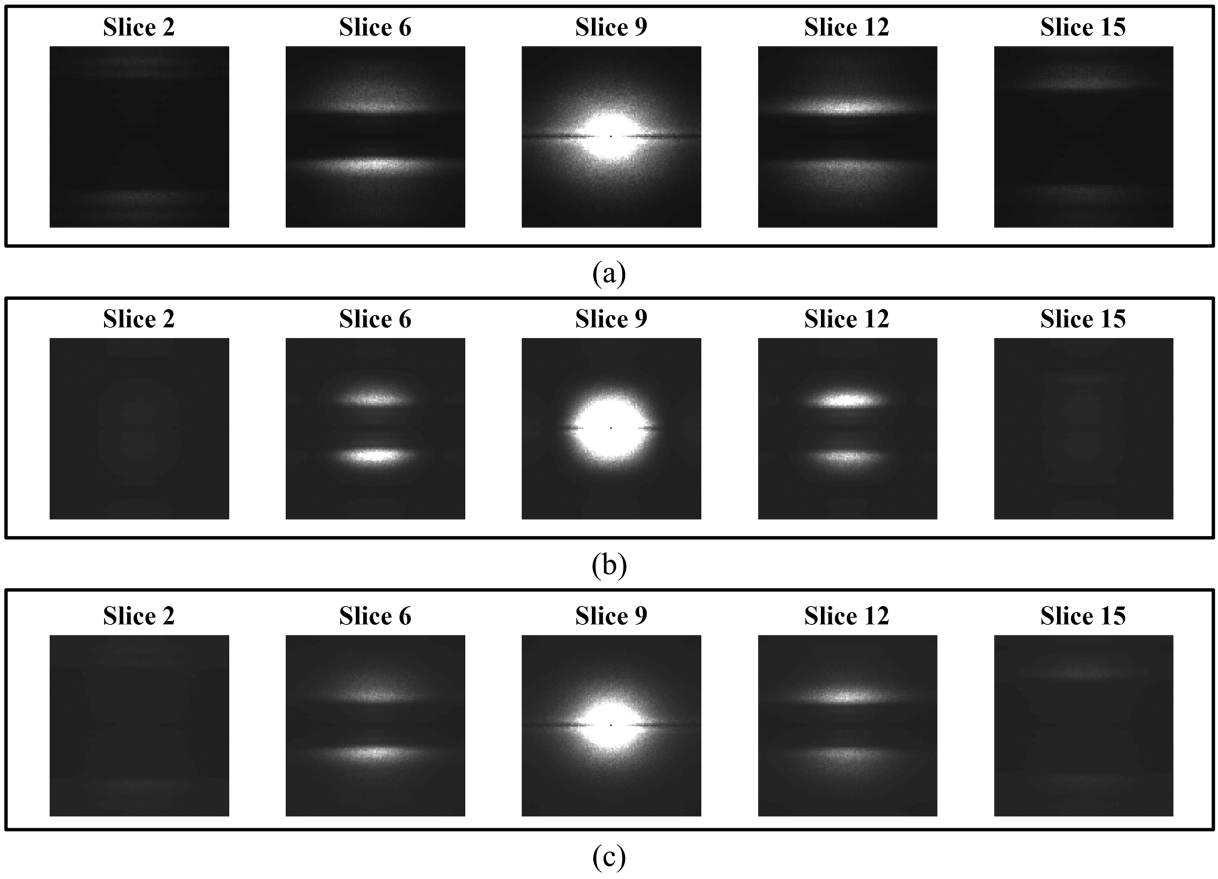

Figure 6.12: The measured 3D NPS using the commercial reconstruction (a), a conventional denoising technique (b), and DR-PICCS (c). all images shown with same window/level.

6.15 and 6.16. In these plots, the degradation in the MTF using the conventional denoising technique is clearly visible. These plots demonstrate the behavior of the MTF along the z-axis; separate plots for the x- and y-directions are shown as the performance (especially moving away from the detector) is not isotropic.

In Figure 6.14 an interesting trend is shown using the measured MTF at different heights above the detector with all three reconstruction methods (commercial, conventional denoising, and DR-PICCS). The further from the detector the reconstructed plane is, the more dramatic the blur in the x-direction. This is the direction of the x-ray tube's rocking, and the direction in which out-of-plane blurring artifacts occur. In the y-direction however, the MTF is highest at 4 and 8 cm above the detector. In Figures 6.15 and 6.16, it is clear that the DR-PICCS images have maintained

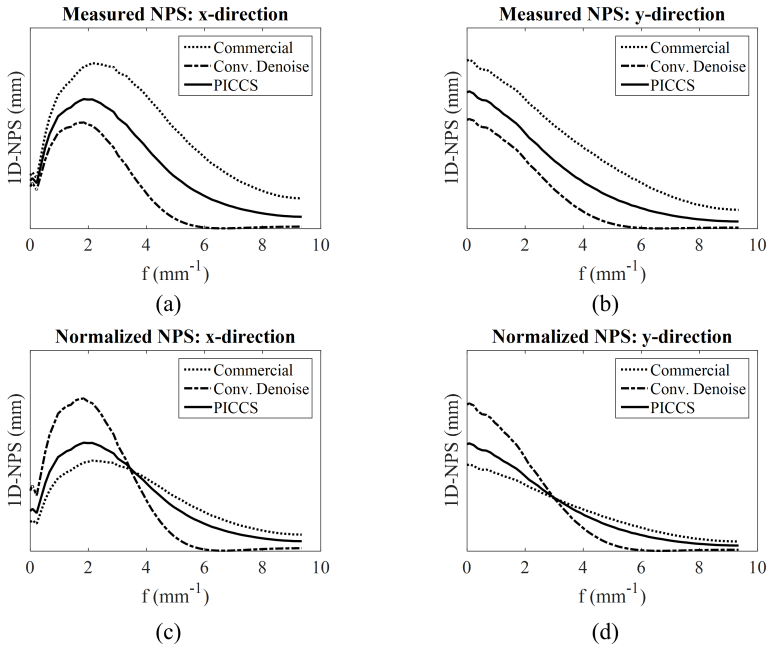

Figure 6.13: The measured 1D NPS in the x and y-directions ((a) and (b) respectively).

the MTF of the commercial (FBP) reconstruction, while the conventionally denoised images have dramatically reduced MTFs.

6.2.5 Results from the Radiologist Review

In the low dose cadaver breast study, radiologists chose the DR-PICCS reconstruction as superior to the full dose commercial reconstruction for 57% of the cases while choosing the full dose commercial reconstruction 43% of the time. The 95% confidence interval for the mean score was $[0.49, 0.66]$. Since 0.5 is included in our confidence interval, the two reconstructions can be considered equivalent ($p < 0.05$).

6.3 Discussion and conclusions

The SDNR measurements in Figures 6.10 and 6.11 show that using either DR-PICCS or a conventional denoising technique, the overall noise level in the images may be decreased, and the SDNR may be increased. In fact, in our results shown here, the conventional denoising method was able to

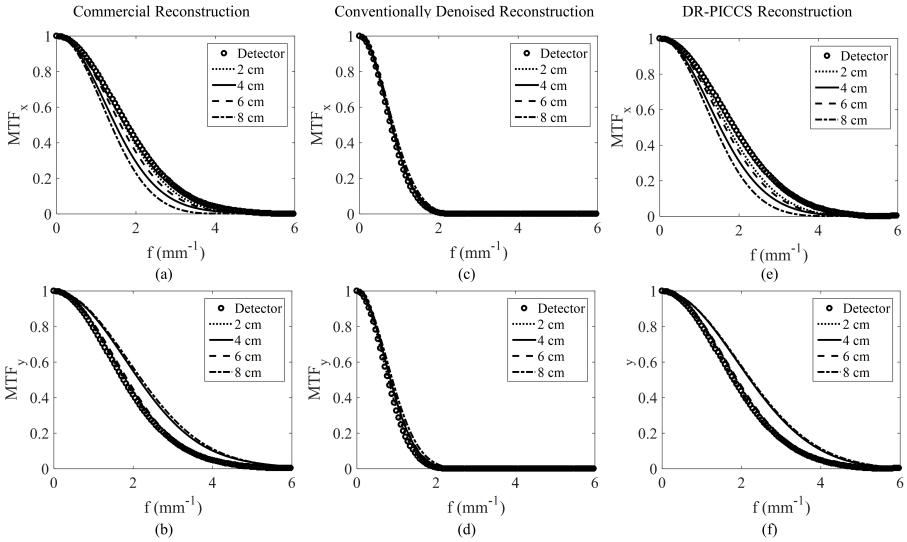

Figure 6.14: The measured MTF with the commercial reconstruction, conventionally denoised reconstruction, and DR-PICCS reconstructions (left to right) in the x and y planes (top row and bottom row respectively) at 0, 2, 4, 6, and 8 cm above the detector.

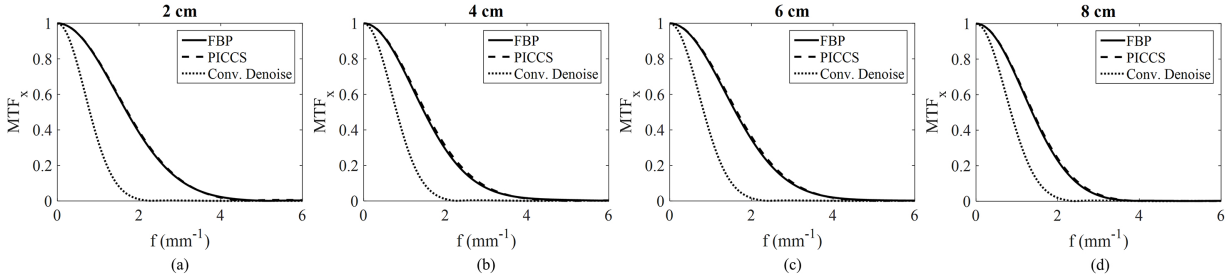

Figure 6.15: The measured MTF in the x-direction with FBP reconstruction, the conventionally denoised reconstruction, and the DR-PICCS reconstruction at 2 cm (a), 4 cm (b), 6 cm (c), and 8 cm (d) above the detector.

dramatically reduce image noise and increase the SDNR for all features. However, when we consider the more sophisticated metrics of the measured NPS and MTF, we see that this comes with a cost: the NPS demonstrate that the use of conventional Gaussian convolution kernel to low-pass filter the image volumes dramatically changes the frequency dependence of the noise and introduces highly correlated noise. In addition, we can see in the MTF measurements that spatial resolution is also degraded. In contrast, the peak of the NPS from DR-PICCS reconstruction and that of the commercial reconstruction are similar. This matched peak spatial frequencies for commercial reconstruction and DR-PICCS reconstruction explains why the noise texture in the DR-PICCS

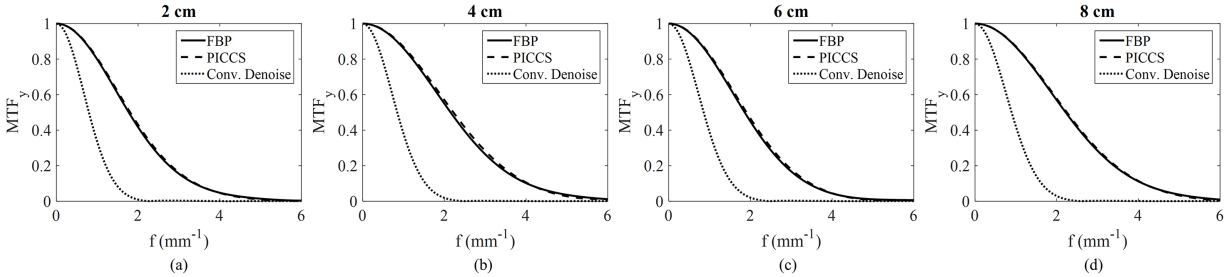

Figure 6.16: The measured MTF in the y-direction with FBP reconstruction, the conventionally denoised reconstruction, and the DR-PICCS reconstruction at 2 cm (a), 4 cm (b), 6 cm (c), and 8 cm (d) above the detector.

reconstructions is similar to that of the commercial reconstruction. Matching this peak is important because images reconstructed with the commercial technique are familiar to radiologists. Significant alteration in the shape of the NPS will produce images that appear "plastic" or artificial to trained eyes.

Although the SDNR measurements suggest a ≈30% dose reduction with DR-PICCS reconstruction, the visual evaluation of the reconstructed images suggests a more significant dose reduction with DR-PICCS is possible. This claim is supported by comparing the images of the ACR phantom and the cadavers as seen in Figures 6.8 and 6.9. When comparing the full-dose acquisitions with commercial reconstruction with the 60% dose acquisitions with the DR-PICCS reconstruction, all relevant imaging features are present at an acceptable noise level in both datasets. It may be the case that, despite a slightly lower SDNR at 60% dose, the minor edge enhancement inherent to the diffusion filter used to generate the prior image in the PICCS reconstruction boosts conspicuity [221].

Standard image quality metrics, such as the MTF, the NPS, and the SDNR, were used in this study to provide a quantitative comparison between different reconstruction methods and different dose levels, however there are several inherent limitations to this study. First, the use of SDNR is always questionable since SDNR doesn't account for noise correlation. It has been shown that noise correlation has a significant impact on detectability [200], and as a result the SDNR alone is not adequate to assess system performance. This motivated us to investigate the potential noise correlation by measuring NPS and introducing human observer studies to partially overcome this limitation. Second, although the authors have also measured and provided the NPS in an effort to alleviate any concern regarding the impact of possibly correlated noise, estimating the NPS in a

nonlinear imaging system (due to the nonlinearity of the PICCS reconstruction algorithm) poses some new challenges that must be carefully overcome. In this chapter, an anthropomorphic phantom was used to ensure the measured NPS and mimic the non-linear DR-PICCS algorithm's performance in clinical imaging scenarios. The same challenges stand for the MTF measurements. Despite these limitations, however, we found positive response from radiologist reviewers who confirmed the reconstructed clinical images had reduced noise (a visual appearance confirmed by quantitative measurements) and a clinically acceptable appearance.

The DR-PICCS algorithm was applied to digital breast tomosynthesis volume datasets acquired at a reduced dose (dose reduced by limiting tube current) to reduce image noise and enable reduced dose imaging. The SDNR, NPS, and MTF were all measured and used to assess image noise and spatial resolution quantitatively, and results were reviewed by radiologists to subjectively evaluate image quality.

Depending on the metric chosen, it was found that dose can be reduced by 30-40% in DBT with the use of DR-PICCS while producing satisfactory image quality. In the future, a prospective clinical study with ROC observer analysis could provide further insight into the clinical value of this method.

7 Summary and future research directions

In this dissertation, several different approaches to improve digital breast tomosynthesis were explored. Digital breast tomosynthesis is a young modality, but has already shown tremendous promise in breast imaging. That said, the technology is in many ways still immature. The overarching goal of this project was to improve image quality for DBT volumes and improve our ability to assess clinical breast images. This was accomplished by applying a variety of tools from CT research and image analysis, as well as developing new tools specifically for DBT reconstruction, processing, and assessment.

The first part of the project discussed several ways to reconstruct DBT volumes and mitigate artifacts. The focus of this section was largely on the introduction of a computationally-tractable iterative reconstruction method to alleviate some of the issues inherent to FBP reconstructed DBT images. The DOS-SPART algorithm was introduced with two different regularizers: TV and PICCS. In addition to introducing an iterative reconstruction method, a tomosynthesis-specific FBP method was presented along with a correction scheme for one of the most common artifacts in DBT images: truncation. The iterative reconstruction method introduced was able to maintain spatial resolution in DBT reconstructions while significantly reducing the through-plane resolution. Of the two regularizers, PICCS offered better spatial resolution and greater reduction of through-plane blurring compared with TV.

The second major section of the project focused on anatomical noise in the breast. In this section, a framework to measure anatomical noise in the breast was implemented and validated

using a cohort of clinical mammograms. This framework was then used to measure anatomical noise in DBT reconstructions generated using both the commercial reconstruction method as well as the iterative reconstruction methods introduced in the first section. The reduced through-plane blurring in the DOS-SPART image resulted in significantly reduced anatomical clutter, pushing the measured anatomical noise exponent, β, closer to the value found in CT than mammography. Finally, the measured anatomical NPS were introduced into a model observer framework and used to predict mass detection performance for the new reconstruction method using task-based model observers.

The third and final piece of the dissertation focused on exploring a method to reduce dose in DBT images. Previous human observer studies have shown the anatomical noise is dominant in mass detection in mammography, so reducing quantum noise is a problem with diminishing returns. Conventionally-reconstructed DBT images have been shown to have an anatomical noise background similar to mammography, so in DBT reducing quantum noise in an attempt to reduce dose has also offered diminishing returns. However, the introduction of a reconstruction method that significantly reduces the anatomical clutter means quantum noise is a relevant contributor. Thus, any attempts to further reduce dose need to account for the corresponding increase in quantum noise. The major advantages of the DR-PICCS method introduced here are that it can be applied to reconstructed images from any vendor with no prior knowledge of the system needed and it can preserve image spatial resolution and texture better than conventional denoising techniques.

Although several important areas have been explored in this work, there remains plenty of opportunity for future research. For starters, human reader studies are needed to validate the model observer studies and understand the true impact of the improved through-plane spatial resolution offered by DOS-SPART. In addition, current clinical reconstructions include significant post-processing to improve image contrast. Using these tools to further enhance the DOS-SPART reconstructions might offer further improvements in image quality. All of the work presented here (with the exception of the truncation studies) was performed using clinical equipment from a single vendor. Validating the reconstruction algorithms on other platforms from other vendors or utilizing the anatomical noise measurement framework on other platforms would offer valuable insight into their robustness and portability. Finally, one of the benefits of DOS-SPART discussed in this work

is its flexibility in incorporating a variety of different regularizers. In addition to the two introduced in this work, it would be very interesting to explore other more advanced regularization schemes, such as anisotropic diffusion, in the future. A derivation demonstrating the feasibility of introducing the anisotropic diffusion regularization into the framework is shown in Appendix A.2.

Overall, the work presented in this dissertation aims to solve a variety of problems in DBT image, with a strong emphasis on image reconstruction, post-processing, and assessment. Although DBT is a young modality, the future for it is bright.

A Appendices

A.1 Projection matrix implementation for Hologic Selenia Dimensions System

The purpose of this section is to derive the projection matrix (P-matrix) convention used for the Hologic Selenia Dimensions Tomosynthesis system. In addition, a derivation of the inverse P-Matrix convention needed to perform a forward projection of the image volumes generated using the P-Matrix backprojection is performed. This is crucial for any iterative reconstruction algorithm that we might choose to use as both a forward and back-projector are required in iterative reconstruction.

A.1.1 Notation

We will use the following conventions for this derivation:

1. The symbols u/v will refer to the x/y coordinates of the detector.

2. The symbols x_{pix}, y_{pix}, and z_{pix} will refer to voxels in the reconstructed volume in the x, y, and z planes respectively.

3. For each view angle, a 3x4 p-matrix is provided denoted here M_i. That matrix is given explicitly by

$$\mathbf{M_{i,BP}} = \begin{pmatrix} M_0 & M_1 & M_2 & M_3 \\ M_4 & M_5 & M_6 & M_7 \\ M_8 & M_9 & M_{10} & M_{11} \end{pmatrix}, \tag{A.1}$$

   where **i** indicates the view index, and **BP** indicates the transformation is a backprojection.

4. We can define another vector to describe the location in the image:

$$\begin{pmatrix} x_{pix} \\ y_{pix} \\ z_{pix} \\ 1 \end{pmatrix}. \tag{A.2}$$

5. We can also define a vector to describe the detector elements:

$$\begin{pmatrix} u \times s \\ v \times s \\ s \end{pmatrix}, \tag{A.3}$$

where s is a scalar.

A.1.2 Backprojection

Backprojection is performed simply by multiplying Equations A.1 and A.2 to solve for Equation A.3. That is:

$$\begin{aligned} \begin{pmatrix} u \times s \\ v \times s \\ s \end{pmatrix} &= \mathbf{M_{i,BP}} \begin{pmatrix} x_{pix} \\ y_{pix} \\ z_{pix} \\ 1 \end{pmatrix} \\ &= \begin{pmatrix} M_0 & M_1 & M_2 & M_3 \\ M_4 & M_5 & M_6 & M_7 \\ M_8 & M_9 & M_{10} & M_{11} \end{pmatrix} \begin{pmatrix} x_{pix} \\ y_{pix} \\ z_{pix} \\ 1 \end{pmatrix} \\ &= \begin{pmatrix} x_{pix}M_0 + y_{pix}M_1 + z_{pix}M_2 + M_3 \\ x_{pix}M_4 + y_{pix}M_5 + z_{pix}M_6 + M_7 \\ x_{pix}M_8 + y_{pix}M_9 + z_{pix}M_{10} + M_{11} \end{pmatrix}. \end{aligned} \tag{A.4}$$

Now that $u \times s$, $v \times s$, and s are known, we can solve for u and v:

$$u\frac{u \times s}{s} = \frac{x_{pix}M_0 + y_{pix}M_1 + z_{pix}M_2 + M_3}{x_{pix}M_8 + y_{pix}M_9 + z_{pix}M_{10} + M_{11}} \tag{A.5}$$

and

$$v = \frac{v \times s}{s} = \frac{x_{pix}M_4 + y_{pix}M_5 + z_{pix}M_6 + M_7}{x_{pix}M_8 + y_{pix}M_9 + z_{pix}M_{10} + M_{11}}. \tag{A.6}$$

These two equations allow backprojection on a voxel-by-voxel basis by identifying for each projection which detector element contains information regarding a specific voxel. In practice, the coordinates (u, v) often fall between true detector elements and a bilinear interpolation is used to estimate the correct value.

A.1.3 Forward-projection

Thus far, we have a framework for the backprojection of measured projection data. However, to perform iterative reconstruction methods we also need to be able to perform a forward projection operation. To accomplish this, we must solve Equations A.5 and A.6 for x_{pix} and y_{pix} as a function of the slice (z_{pix}) and detector elements (u and v). To simplify this process, we first make a few intermediate definitions:

$$a \equiv z_{pix}M_2 + M_3$$

$$b \equiv z_{pix}M_6 + M_7$$

$$c \equiv z_{pix}M_{10} + M_{11}$$

Using this notation, we can rewrite Equations A.5 and A.6 to get:

$$u = \frac{x_{pix}M_0 + y_{pix}M_1 + a}{x_{pix}M_8 + y_{pix}M_9 + c} \tag{A.7}$$

and

$$v = \frac{x_{pix}M_4 + y_{pix}M_5 + b}{x_{pix}M_8 + y_{pix}M_9 + c}. \tag{A.8}$$

We can rearrange these to find:

$$(x_{pix}M_8 + y_{pix}M_9 + c)u = x_{pix}M_0 + y_{pix}M_1 + a \tag{A.9}$$

and

$$(x_{pix}M_8 + y_{pix}M_9 + c)v = x_{pix}M_4 + y_{pix}M_5 + b \tag{A.10}$$

or alternatively:

$$(M_8u)x_{pix} + (M_9u)y_{pix} + cu = x_{pix}M_0 + y_{pix}M_1 + a \tag{A.11}$$

and

$$(M_8v)x_{pix} + (M_9v)y_{pix} + cv = x_{pix}M_4 + y_{pix}M_5 + b. \tag{A.12}$$

These can be further simplified to find:

$$(M_8u - M_0)x_{pix} + (M_9u - M_1)y_{pix} = (a - cu) \tag{A.13}$$

and

$$(M_8v - M_4)x_{pix} + (M_9v - M_5)y_{pix} = (b - cv). \tag{A.14}$$

We now have two linear equations and two unknowns. To simplify the algebra here, we can make the following substitutions:

$$C_1 \equiv (M_8u - M_0)$$
$$C_2 \equiv (M_9u - M_1)$$
$$C_3 \equiv (a - cu)$$
$$C_4 \equiv (M_8v - M_4)$$
$$C_5 \equiv (M_9v - M_5)$$
$$C_6 \equiv (b - cv)$$

With this notation we find:

$$C_1x_{pix} + C_2y_{pix} = C_3 \tag{A.15}$$

and

$$C_4x_{pix} + C_5y_{pix} = C_6. \tag{A.16}$$

We can multiply Equation A.15 by $-\frac{C_5}{C_2}$ and add it to Equation A.16 to find:

$$\begin{aligned}
C_4x_{pix} + C_5y_{pix} - \frac{C_5}{C_2}(C_1x_{pix} + C_2y_{pix}) &= C_6 - \frac{C_5}{C_2}C_3 \\
C_4x_{pix} - \frac{C_5C_1}{C_2}x_{pix} + C_5y_{pix} - C_5y_{pix} &= \frac{C_6C_2}{C_2} - \frac{C_5C_3}{C_2} \\
\left(\frac{C_4C_2 - C_5C_1}{C_2}\right)x_{pix} &= \frac{C_6C_2 - C_5C_3}{C_2} \\
\rightarrow x_{pix} &= \frac{C_6C_2 - C_5C_3}{C_4C_2 - C_5C_1}.
\end{aligned} \tag{A.17}$$

This can be used to solve for y_{pix} by inverting Equation A.15:

$$\begin{aligned} y_{pix} &= \frac{C_6 - C_4 x_{pix}}{C_5} \\ &= \frac{C_6}{C_5} - \frac{C_4}{C_5}\left(\frac{C_6C_2 - C_5C_3}{C_4C_2 - C_5C_1}\right) \\ &= \frac{C_6(C_4C_2 - C_5C_1) - C_4(C_6C_2 - C_5C_3)}{C_5(C_4C_2 - C_5C_1)} \\ &= \frac{C_6C_4C_2 - C_6C_5C_1 - C_4C_6C_2 + C_4C_5C_3}{C_5C_4C_2 - C_5^2C_1} \\ \rightarrow y_{pix} &= \frac{C_4C_3 - C_6C_1}{C_4C_2 - C_5C_1}. \end{aligned} \tag{A.18}$$

We can begin to substitute back into these equations to find x_{pix} and y_{pix} in terms of the detector elements and the given slice. First we can consider the shared denominator (here denoted s'):

$$\begin{aligned} s' = C_4C_2 - C_5C_1 &= (M_8v - M_4)(M_9u - M_1) - (M_9v - M_5)(M_8u - M_0) \\ &= M_8M_9uv - M_4M_9u - M_1M_8v + M_1M_4 - M_8M_9uv + M_5M_8u + M_0M_9v - M_0M_5 \\ &= (M_5M_8 - M_4M_9)u + (M_0M_9 - M_1M_8)v + (M_1M_4 - M_0M_5). \end{aligned} \tag{A.19}$$

We can also substitute into the numerator for x_{pix} to find:

$$\begin{aligned} C_6C_2 - C_5C_3 &= (b - cv)(M_9u - M_1) - (M_9v - M_5)(a - cu) \\ &= [z_{pix}M_6 + M_7 - (z_{pix}M_{10} + M_{11})v](M_9u - M_1) - (M_9v - M_5)[z_{pix}M_2 + M_3 - (z_{pix}M_{10} + M_{11})u] \\ &= (z_{pix}M_6 + M_7 - M_{10}vz_{pix} - M_{11}v)(M_9u - M_1) - (M_9v - M_5)(z_{pix}M_2 + M_3 - M_{10}uz_{pix} - M_{11}u) \\ &= M_6M_9uz_{pix} + M_7M_9u - M_9M_{10}uvz_{pix} - M_9M_{11}uv - M_1M_6z_{pix} - M_1M_7 + M_1M_{10}vz_{pix} + M_1M_{11}v \\ &\quad - M_2M_9vz_{pix} - M_3M_9v + M_9M_{10}uvz_{pix} + M_9M_{11}uv + M_2M_5z_{pix} + M_3M_5 - M_5M_{10}uz_{pix} - M_5M_{11}u \\ &= (M_7M_9 - M_5M_{11})u + (M_1M_{11} - M_3M_9)v + (M_6M_9 - M_5M_{10})uz_{pix} + (M_1M_{10} - M_2M_9)vz_{pix} \\ &\quad + (M_2M_5 - M_1M_6)z_{pix} + (M_3M_5 - M_1M_7). \end{aligned}$$

This can be further simplified as follows:

$$C_6C_2 - C_5C_3 = [(M_7M_9 - M_5M_{11}) + (M_6M_9 - M_5M_{10})z_{pix}]\,u + [(M_1M_{11} - M_3M_9) + (M_1M_{10} - M_2M_9)z_{pix}]\,v + (M_2M_5 - M_1M_6)z_{pix} + (M_3M_5 - M_1M_7) \tag{A.20}$$

Similar simplification can be done with y_{pix}:

$$\begin{aligned}
&C_4C_3 - C_6C_1 = (M_8v - M_4)(a - cu) - (b - cv)(M_8u - M_0)\\
&= (M_8v - M_4)[z_{pix}M_2 + M_3 - (z_{pix}M_{10} + M_{11})u] - [z_{pix}M_6 + M_7 - (z_{pix}M_{10} + M_{11})v](M_8u - M_0)\\
&= (M_8v - M_4)(z_{pix}M_2 + M_3 - M_{10}uz_{pix} - M_{11}u) - (z_{pix}M_6 + M_7 - M_{10}vz_{pix} - M_{11}v)(M_8u - M_0)\\
&= M_2M_8vz_{pix} + M_3M_8v - M_8M_{10}uvz_{pix} - M_8M_{11}uv - M_2M_4z_{pix} - M_3M_4 + M_4M_{10}uz_{pix} + M_4M_{11}u\\
&- M_6M_8uz_{pix} - M_7M_8u + M_8M_{10}uvz_{pix} + M_8M_{11}uv + M_0M_6z_{pix} + M_0M_7 - M_0M_{10}vz_{pix} - M_0M_{11}v\\
&= (M_4M_{11} - M_7M_8)u + (M_3M_8 - M_0M_{11})v + (M_4M_{10} - M_6M_8)uz_{pix} + (M_2M_8 - M_0M_{10})vz_{pix}\\
&\qquad + (M_0M_6 - M_2M_4)z_{pix} + (M_0M_7 - M_3M_4).
\end{aligned}$$

This can be further simplified as follows:

$$C_4C_3 - C_6C_1 = [(M_4M_{11} - M_7M_8) + (M_4M_{10} - M_6M_8)z_{pix}]\,u + [(M_3M_8 - M_0M_{11} + (M_2M_8 - M_0M_{10})z_{pix})]\,v + (M_0M_6 - M_2M_4)z_{pix} + (M_0M_7 - M_3M_4) \tag{A.21}$$

This allows us to write expressions for x_{pix} and y_{pix}:

$$x_{pix} = (s')^{-1}\,([(M_7M_9 - M_5M_{11}) + (M_6M_9 - M_5M_{10})z_{pix}]\,u + [(M_1M_{11} - M_3M_9) + (M_1M_{10} - M_2M_9)z_{pix}]\,v + (M_3M_5 - M_1M_7) + (M_2M_5 - M_1M_6)z_{pix}) \tag{A.22}$$

and

$$y_{pix} = \left(s'\right)^{-1}\left(\left[\left(M_4M_{11} - M_7M_8\right) + \left(M_4M_{10} - M_6M_8\right)z_{pix}\right]u \right.$$
$$\left. + \left[\left(M_3M_8 - M_0M_{11}\right) + \left(M_2M_8 - M_0M_{10}\right)z_{pix}\right)\right]v + \left(M_0M_7 - M_3M_4\right) + \left(M_0M_6 - M_2M_4\right)z_{pix}\right) \tag{A.23}$$

Although they are messy, these expressions provide a means of directly implementing P-matrix forward projection for a given view angle that is straightforward to code. Both x_{pix} and y_{pix} share a denominator, which we can label s' as indicated earlier. The choice of this notation is to match in backprojection P-matrix notation. This can be re-written in matrix form if desired; we'll call $\mathbf{M_{i,FP}}$ our forward projection P-matrix as shown here:

$$\begin{aligned}\begin{pmatrix} x_{pix}*s' \\ y_{pix}*s' \\ s' \end{pmatrix} &= \mathbf{M_{i,BP}} \begin{pmatrix} u \\ v \\ 1 \end{pmatrix} \\ &= \begin{pmatrix} M_{0,F} & M_{1,F} & M_{2,F} \\ M_{3,F} & M_{4,F} & M_{5,F} \\ M_{6,F} & M_{7,F} & M_{8,F} \end{pmatrix} \begin{pmatrix} u \\ v \\ 1 \end{pmatrix} \\ &= \begin{pmatrix} uM_{0,F}+vM_{1,F}+M_{2,F} \\ uM_{3,F}+vM_{4,F}+M_{5,F} \\ uM_{6,F}+vM_{7,F}+M_{8,F} \end{pmatrix},\end{aligned} \tag{A.24}$$

with

$$
\begin{aligned}
M_{0,F} &= (M_7M_9 - M_5M_{11}) + (M_6M_9 - M_5M_{10})z_{pix} \\
M_{1,F} &= (M_1M_{11} - M_3M_9) + (M_1M_{10} - M_2M_9)z_{pix} \\
M_{2,F} &= (M_3M_5 - M_1M_7) + (M_2M_5 - M_1M_6)z_{pix} \\
M_{3,F} &= (M_4M_{11} - M_7M_8) + (M_4M_{10} - M_6M_8)z_{pix} \\
M_{4,F} &= (M_3M_8 - M_0M_{11}) + (M_2M_8 - M_0M_{10})z_{pix} \\
M_{5,F} &= (M_0M_7 - M_3M_4) +_(M_0M_6 - M_2M_4)z_{pix} \\
M_{6,F} &= (M_5M_8 - M_4M_9) \\
M_{7,F} &= (M_0M_9 - M_1M_8) \\
M_{8,F} &= (M_1M_4 - M_0M_5)
\end{aligned}
\tag{A.25}
$$

A.2 Anisotropic diffusion regularization

While anisotropic diffusion has been used extensively for image denoising, in many applications (such as regularization in iterative reconstruction) it is also desirable to show that anisotropic diffusion denoising can be posed as a classical denoising problem, such that:

$$x^{k+1} = \arg\min_x \left[\frac{\lambda}{2} \left(x - u^{k+1} \right)^T P^{-1} \left(x - u^{k+1} \right) + R(\Psi x) \right], \tag{A.26}$$

where x^{k+1} is the denoised image, u^{k+1} is an image we want to stay close to (typically a data consistency updated image in image reconstruction), $R(\Psi x)$ is the a sparsifying regularizer that can take a variety of forms (most common is total variation), λ is a parameter describing the relative weight of the regularization term and the consistency term, and P is a weighting matrix matching the dimension of the image volume. While it has previously been shown that TV fits this form ($R(\Psi x) = TV(x)$), we want to show in this section that anisotropic diffusion also meets these criteria and is a suitable regularizer.

What we will show here (following a similar derivation in[222]) is that anisotropic diffusion denoising is equivalent to minimizing an energy functional, $E(x)$, of the image using a steepest descent technique as follows:

$$x_{\text{diff}} = \arg\min_x E(x) \tag{A.27}$$

solved iteratively as:

$$x_{\text{diff}}^{k+1} = x_{\text{diff}}^{k} - \nabla E(x), \tag{A.28}$$

where x_{diff}^{k} is the anisotropic diffusion denoised image at iteration, k, $\nabla E(x)$ is the gradient of the energy functional, and α is a step size parameter.

A.2.1 Energy minimization

The crucial first step in our proof here is to borrow a method from physics. We want to describe an energy functional (stationary integral) over the space of all possible smooth images, Ω:

$$E(x) = \int_{\Omega} f(|\nabla x|)\mathrm{d}\Omega, \tag{A.29}$$

where we claim $E(x)$ is the energy functional, f is a function of $|\nabla x|$, and Ω is the space of smooth images. To be explicit here, we claim smooth images are all possible images for which $|\nabla x|$ is finite. We can add a few additional constraints to our function, namely:

$$\begin{gathered} f(|\nabla x|) \geq 0 \\ f'(|\nabla x|) > 0 \end{gathered} \tag{A.30}$$

These constrains tell us our function (f) is positive and increasing. Now in physics we would commonly attempt to minimize this functional using the Euler equation (differential equation), however we can also consider a minimization by identifying the Gâteaux variation (directional derivative or $\mathrm{d}E(u,h) = \langle \nabla E(u), h \rangle$) for a direction, h:

$$\mathrm{d}E(x,h) = \lim_{\lambda \to 0} \frac{E(x+\lambda h) - E(x)}{\lambda}, \tag{A.31}$$

and identifying critical points where $\mathrm{d}E = 0$. If we recall, Ω is the space of smooth images; in addition we can identify a subspace, Ω_0, where it is not only true that $|\nabla x|$ is finite, but more strictly:

$$\Omega_0 = \{\omega : |\nabla x(\omega)| = 0, \omega \in \Omega\}, \tag{A.32}$$

in other words, Ω_0 is the set of images for which $|\nabla x| = 0$. With this definition, we can substitute Equuation A.29 into Equation A.31 to find the following expression for the Gâteaux variation:

$$\begin{aligned} dE(u,h) &= \lim_{\lambda\to 0} \frac{E(x+\lambda h) - E(x)}{\lambda} \\ &= \lim_{\lambda\to 0} \frac{\left(\int_{\Omega_0} f(|\nabla(x+\lambda h)|)\mathrm{d}\Omega + \int_{\Omega-\Omega_0} f(|\nabla(x+\lambda h)|)\mathrm{d}\Omega\right) - \left(\int_{\Omega_0} f(|\nabla x|)\mathrm{d}\Omega - \int_{\Omega+\Omega_0} f(|\nabla x|)\mathrm{d}\Omega\right)}{\lambda} \\ &= \lim_{\lambda\to 0} \frac{1}{\lambda}\left[\int_{\Omega_0} f(|\nabla(x+\lambda h)|)\mathrm{d}\Omega - \int_{\Omega_0} f(|\nabla x|)\mathrm{d}\Omega + \int_{\Omega-\Omega_0} f(|\nabla(x+\lambda h)|)\mathrm{d}\Omega - \int_{\Omega-\Omega_0} f(|\nabla x|)\mathrm{d}\Omega\right]. \end{aligned}$$

Since $f(|\nabla x|) \geq 0$ we can rearrange the integrals as follows:

$$dE(u,h) = \int_{\Omega_0} \lim_{\lambda\to 0} \frac{f(|\nabla(x+\lambda h)| - f(|\nabla x|)}{\lambda}\mathrm{d}\Omega + \int_{\Omega-\Omega_0} \lim_{\lambda\to 0} \frac{f(|\nabla(x+\lambda h)| - f(|\nabla x|)}{\lambda}\mathrm{d}\Omega.$$

If we recall $|\nabla x| = 0$ for Ω_0 the first term can be simplified yielding:

$$dE(u,h) = \int_{\Omega_0} \lim_{\lambda\to 0} \frac{f(\lambda|\nabla h|) - f(0)}{\lambda}\mathrm{d}\Omega + \int_{\Omega-\Omega_0} \lim_{\lambda\to 0} \frac{f(|\nabla x + \lambda\nabla h| - f(|\nabla x|)}{\lambda}\mathrm{d}\Omega. \tag{A.33}$$

Let's define two new variables: $\lambda\prime = \lambda|\nabla h|$ and $\lambda\prime\prime = \lambda\nabla h$, yielding:

$$dE(u,h) = \int_{\Omega_0} \lim_{\lambda\prime\to 0} \frac{f(0+\lambda\prime) - f(0)}{\lambda\prime}|\nabla h|\mathrm{d}\Omega + \int_{\Omega-\Omega_0} \lim_{\lambda\prime\prime\to 0} \frac{f(|\nabla x + \lambda\prime\prime|) - f(|\nabla x|)}{\lambda\prime\prime}\nabla h\mathrm{d}\Omega. \tag{A.34}$$

Here we recognize two derivatives and can rewrite these two terms:

$$dE(u,h) = f'(0)\int_{\Omega_0} |\nabla h|\mathrm{d}\Omega + \int_{\Omega-\Omega_0} f'(|\nabla x|)\frac{\nabla x}{|\nabla x|}\nabla h\mathrm{d}\Omega. \tag{A.35}$$

If we consider the set of directions, h, for which the following holds: $|\nabla h| \neq 0$ in Ω_0 and $|\nabla h| = 0$ otherwise, finding $\mathrm{d}E(u,h) = 0$ yields:

$$dE(u,h) = f'(0)\int_{\Omega_0} |\nabla h|\mathrm{d}\Omega = 0, \tag{A.36}$$

and thus, we require $f'(0) = 0$ for this to be true. The final constraint, $f'(0) = 0$, gives us a stationary point at $|\nabla x| = 0$. Thus, $E(x) \geq 0$, and a smooth image ($|\nabla x| = 0$) must minimize $E(x)$.

As a result, we can rewrite Equation A.35 as follows:

$$dE(u,h) = \int_{\Omega} f'(|\nabla x|)\frac{\nabla x}{|\nabla x|}\nabla h \mathrm{d}\Omega. \tag{A.37}$$

Let's take a moment to recall Green's theorem, which we can write as follows:

$$\oint_{\partial\Omega} u\nabla v \cdot \mathrm{d}\partial\Omega = \int_{\Omega} u\nabla^2 v \mathrm{d}\Omega + \int_{\Omega} \nabla u \cdot \nabla v \mathrm{d}\Omega. \tag{A.38}$$

If we use the following definitions: $\nabla u = \nabla h$ and $\nabla v = f'(|\nabla u|)\frac{\nabla u}{|\nabla u|}$, we can rearrange Green's theorem to give:

$$\mathrm{d}E(x,h) = -\int_{\Omega} \nabla \cdot \left[f'(|\nabla x|)\frac{\nabla x}{|\nabla x|}\right] h \mathrm{d}\Omega + \oint_{\partial\Omega} f'(|\nabla x|)\frac{\nabla x}{|\nabla x|} \cdot \hat{n} h \mathrm{d}\partial\Omega, \tag{A.39}$$

where $\hat{n}$ is the vector normal to the boundary, $\partial\Omega$. We are going to assume spherical boundary conditions, such that $\nabla x(\omega) \cdot \hat{n} = 0$ for $\omega \in \partial\Omega$. Under these conditions, the second term actually vanishes, leaving us with

$$\mathrm{d}E(x,h) = -\int_{\Omega} \nabla \cdot \left[f'(|\nabla x|)\frac{\nabla x}{|\nabla x|}\right] h \mathrm{d}\Omega, \tag{A.40}$$

which is an inner product:

$$\mathrm{d}E(x,h) = \left\langle -div\left[f'(|\nabla x|)\frac{\nabla x}{|\nabla x|}\right], h \right\rangle, \tag{A.41}$$

and since

$$\mathrm{d}E(x,h) = \langle \nabla E(x), h \rangle, \tag{A.42}$$

we're left with:

$$\nabla E(x) = -div\left[f'(|\nabla x|)\frac{\nabla x}{|\nabla x|}\right]. \tag{A.43}$$

Thus, as if we choose diffusion coefficients, $c(|\nabla x|) = \frac{f'(|\nabla x|)}{\nabla x}$ we find the following updated diffusion equation:

$$\frac{\partial u}{\partial t} = div\left[f'(|\nabla x|)\frac{\nabla x}{|\nabla x|}\right] = -\nabla E(u), \tag{A.44}$$

telling us we are performing a steepest descent energy minimization during the anisotropic diffusion denoising procedure.

A.2.2 Classical image denoising

Since we have shown anisotropic diffusion can be posed as the following minimization problem:

$$x_{\text{diff}} = \arg\min_{x} E(x), \tag{A.45}$$

solved using a steepest descent method, we still need to pose a classical image denoising problem using this. In other words, can we explicitly define a procedure to solve the following:

$$x^{k+1} = \arg\min_{x}\left[\frac{\lambda}{2}\left(x - u^{k+1}\right)^T P^{-1}\left(x - u^{k+1}\right) + E(x)\right] \tag{A.46}$$

in an iterative way? Since we know anisotropic diffusion attempts to minimize energy using a steepest descent, can we pose this entire classical denoising problem as a steepest descent problem? In this case, our cost function is:

$$f(x) = \left[\frac{\lambda}{2}\left(x - u^{k+1}\right)^T P^{-1}\left(x - u^{k+1}\right) + E(x)\right] \tag{A.47}$$

with a gradient defined as (recall P^{-1} is symmetric $\rightarrow (P^{-1})^T = P^{-1}$):

$$\begin{aligned}
\nabla f(x) &= \nabla \left[\frac{\lambda}{2} \left(x - u^{k+1} \right)^T P^{-1} \left(x - u^{k+1} \right) + E(x) \right] \\
&= \nabla \left[\frac{\lambda}{2} \left(x - u^{k+1} \right)^T P^{-1} \left(x - u^{k+1} \right) \right] + \nabla E(x) \\
&= \frac{\lambda}{2} \nabla \left[x^T P^{-1} x - (u^{k+1})^T P^{-1} x - x^T P^{-1} u^{k+1} + (u^{k+1})^T P^{-1} u^{k+1} \right] + \nabla E(x) \\
&= \frac{\lambda}{2} \nabla \left[x^T P^{-1} x - 2(u^{k+1})^T P^{-1} x + (u^{k+1})^T P^{-1} u^{k+1} \right] + \nabla E(x) \\
&= \frac{\lambda}{2} \left[2P^{-1} x - \nabla 2(u^{k+1})^T P^{-1} x \right] + \nabla E(x) \\
&= \frac{\lambda}{2} \left[2P^{-1} x - 2\nabla (P^{-1} u^{k+1})^T x \right] + \nabla E(x) \\
&= \frac{\lambda}{2} \left[2P^{-1} x - 2P^{-1} u^{k+1} \right] + \nabla E(x) \\
\nabla f(x) &= \lambda P^{-1} \left[x - u^{k+1} \right] + \nabla E(x)
\end{aligned} \tag{A.48}$$

Thus we can pose anisotropic diffusion as a classical image denoising problem which may be solved iteratively using a steepest descent method:

$$\begin{aligned}
x^{k+1} &= x^k - \alpha \nabla f(x^k) \\
x^{k+1} &= x^k - \alpha \left(\lambda P^{-1} \left[x^k - u^{k+1} \right] + \nabla E(x^k) \right),
\end{aligned} \tag{A.49}$$

where the first term of the gradient enforces consistency with the data and the second term is simply a single update of the anisotropic diffusion denoising procedure. The step-size (α) must be chosen carefully (per Wolfe conditions[218]) to ensure stability, and must be constrained s.t. $\alpha \in (0, 1]$. We should also note that $x^{k=0} = u^{k+1}$ at the beginning of the denoising procedure, so the first step of this procedure is always identical to a single anisotropic diffusion denoising iteration.

References

[1] World Cancer Research Fund International. Worldwide data, 2015. URL `http://www.wcrf.org/int/cancer-facts-figures/worldwide-data`.

[2] Centers for Disease Control and Prevention. Breast cancer trends, 2016. URL `https://www.cdc.gov/cancer/breast/statistics/trends.htm`.

[3] Donella Puliti, Lauro Bucchi, Silvia Mancini, Eugenio Paci, Susanna Baracco, Cinzia Campari, Debora Canuti, Claudia Cirilli, Natalina Collina, Giovanni Maria Conti, Enza Di Felice, Fabio Falcini, Maria Michiara, Rossella Negri, Alessandra Ravaioli, Priscilla Sassoli de' Bianchi, Monica Serafini, Manuel Zorzi, Adele Caldarella, Luigi Cataliotti, Marco Zappa, G. Manneschi, G. Miccinesi, N. Caranci, C. Naldoni, A.C. Finarelli, S. Ferretti, P. Pandolfi, L. Pizzi, C. Petrucci, P. Baldazzi, A. Pasquini, M. Manfredi, G. Saguatti, M. Zatelli, P. Sgargi, F. Bozzani, P. Giorgi Rossi, L. Mangone, S. Caroli, M. Vicentini, R. Vattiato, O. Giuliani, C. Balducci, B. Vitali, and G. Monticelli. Advanced breast cancer rates in the epoch of service screening: The 400,000 women cohort study from italy. *Eur. J. Cancer*, 75:109 – 116, 2017. ISSN 0959-8049. doi: 10.1016/j.ejca.2016.12.030.

[4] Centers for Medicare and Medicaid Services. Physician fee schedule search, 2017. URL `https://www.cms.gov/apps/physician-fee-schedule/`.

[5] L. Nystrom, I. Andersson, N. Bjurstam, J. Frisell, B. Nordenskjold, and L. E. Rutqvist. Long-term effects of mammography screening: updated overview of the Swedish randomised trials. *Lancet*, 359(9310):909–19, Mar 16 2002.

[6] American College of Radiology. ACR and SBI Continue to Recommend Regular Mammography Starting at Age 40 (News release), 2015.

[7] Oeffinger KC, Fontham EH, Etzioni R, and et al. Breast cancer screening for women at average risk: 2015 guideline update from the American Cancer Society. *JAMA*, 314(15):1599–1614, 2015. doi: 10.1001/jama.2015.12783.

[8] Ellen Warner. Breast-cancer screening. *N. Engl. J. Med.*, 365(11):1025–1032, 2011. doi: 10.1056/NEJMcp1101540. PMID: 21916640.

[9] U.S. Preventive Services Task Force. Final update summary: Breast cancer: Screening, 2015.

[10] Beatrice Lauby-Secretan, Chiara Scoccianti, Dana Loomis, Lamia Benbrahim-Tallaa, Véronique Bouvard, Franca Bianchini, and Kurt Straif. Breast-cancer screening - viewpoint of the IARC working group. *N. Engl. J. Med.*, 372(24):2353–2358, 2015. doi: 10.1056/NEJMsr1504363. PMID: 26039523.

[11] Philippe Autier, Mathieu Boniol, Michel Smans, Richard Sullivan, and Peter Boyle. Statistical analyses in swedish randomised trials on mammography screening and in other randomised trials on cancer screening: a systematic review. *J. R. Soc. Med.*, 2015. doi: 10.1177/0141076815593403.

[12] Sue M Moss, Christopher Wale, Robert Smith, Andrew Evans, Howard Cuckle, and Stephen W Duffy. Effect of mammographic screening from age 40 years on breast cancer mortality in the UK age trial at 17 years' follow-up: a randomised controlled trial. *The Lancet Oncology*, 2015. doi: 10.1016/S1470-2045(15)00128-X.

[13] C Harding, F Pompei, D Burmistrov, H Welch, R Abebe, and R Wilson. Breast cancer screening, incidence, and mortality across us counties. *JAMA Internal Medicine*, 2015. doi: 10.1001/jamainternmed.2015.3043.

[14] U.S. Preventive Services Task Force. Final recommendation statement: Breast cancer: Screening., 2016.

[15] J. A. Harvey and V. E. Bovbjerg. Quantitative assessment of mammographic breast density: relationship with breast cancer risk. *Radiology*, 230(1):29–41, Jan 2004. doi: 10.1148/radiol.2301020870.

[16] Archie Bleyer and H. Gilbert Welch. Effect of three decades of screening mammography on breast-cancer incidence. *NEJM*, 367(21):1998–2005, 2012. doi: 10.1056/NEJMoa1206809. PMID: 23171096.

[17] Regina J. Hooley. Breast density legislation and clinical evidence. *Radiol. Clin. North Am.*, pages –, 2017. ISSN 0033-8389. doi: 10.1016/j.rcl.2016.12.006.

[18] T. M. Kolb, J. Lichy, and J. H. Newhouse. Comparison of the performance of screening mammography, physical examination, and breast US and evaluation of factors that influence them: an analysis of 27,825 patient evaluations. *Radiology*, 225(1):165–75, Oct 2002. doi: 10.1148/radiol.2251011667.

[19] L. Irwig, N. Houssami, and C. van Vliet. New technologies in screening for breast cancer: a systematic review of their accuracy. *Br. J. Cancer*, 90(11):2118–2122, 2004. ISSN 0007-0920. doi: DOI10.1038/sj.bjc.6601836.

[20] W. A. Berg. Rationale for a trial of screening breast ultrasound: American College of Radiology Imaging Network (ACRIN) 6666. *AJR Am. J. Roentgenol.*, 180(5):1225–8, 2003. doi: 10.2214/ajr.180.5.1801225.

[21] M. Kriege, C. T. Brekelmans, C. Boetes, P. E. Besnard, H. M. Zonderland, I. M. Obdeijn, R. A. Manoliu, T. Kok, H. Peterse, M. M. Tilanus-Linthorst, S. H. Muller, S. Meijer, J. C. Oosterwijk, L. V. Beex, R. A. Tollenaar, H. J. de Koning, E. J. Rutgers, and J. G. Klijn. Efficacy of MRI and mammography for breast-cancer screening in women with a familial or genetic predisposition. *N. Engl. J. Med.*, 351(5):427–37, Jul 29 2004. doi: 10.1056/NEJMoa031759.

[22] E. Warner, D. B. Plewes, K. A. Hill, P. A. Causer, J. T. Zubovits, R. A. Jong, M. R. Cutrara, G. DeBoer, M. J. Yaffe, S. J. Messner, W. S. Meschino, C. A. Piron, and S. A. Narod. Surveillance of BRCA1 and BRCA2 mutation carriers with magnetic resonance imaging,

ultrasound, mammography, and clinical breast examination. *JAMA*, 292(11):1317–25, Sep 15 2004.

[23] M. O. Leach, C. R. Boggis, A. K. Dixon, D. F. Easton, R. A. Eeles, D. G. Evans, F. J. Gilbert, I. Griebsch, R. J. Hoff, P. Kessar, S. R. Lakhani, S. M. Moss, A. Nerurkar, A. R. Padhani, L. J. Pointon, D. Thompson, and R. M. Warren. Screening with magnetic resonance imaging and mammography of a UK population at high familial risk of breast cancer: a prospective multicentre cohort study (MARIBS). *Lancet*, 365(9473):1769–78, May 21-27 2005.

[24] I. Griebsch, J. Brown, C. Boggis, A. Dixon, M. Dixon, D. Easton, R. Eeles, D. G. Evans, F. J. Gilbert, J. Hawnaur, P. Kessar, S. R. Lakhani, S. M. Moss, A. Nerurkar, A. R. Padhani, L. J. Pointon, J. Potterton, D. Thompson, L. W. Turnbull, L. G. Walker, R. Warren, and M. O. Leach. Cost-effectiveness of screening with contrast enhanced magnetic resonance imaging vs x-ray mammography of women at a high familial risk of breast cancer. *Br. J. Cancer*, 95(7): 801–10, Oct 9 2006. doi: 10.1038/sj.bjc.6603356.

[25] L. Cortesi, D. Turchetti, I. Marchi, A. Fracca, B. Canossi, B. Rachele, R. Silvia, P. A. Rita, T. Pietro, and F. Massimo. Breast cancer screening in women at increased risk according to different family histories: an update of the Modena Study Group experience. *BMC Cancer*, 6: 210, 2006. doi: 10.1186/1471-2407-6-210.

[26] G. Trecate, D. Vergnaghi, S. Manoukian, S. Bergonzi, G. Scaperrotta, M. Marchesini, C. Ferranti, B. Peissel, G. Spatti, S. Bohm, A. Conti, C. Costa, M. Sporeni, F. Podo, and R. Musumeci. MRI in the early detection of breast cancer in women with high genetic risk. *Tumori*, 92(6): 517–23, Nov-Dec 2006.

[27] C. D. Lehman. Role of MRI in screening women at high risk for breast cancer. *J. Magn. Reson. Imaging*, 24(5):964–70, Nov 2006.

[28] A. Rieber, H. Schirrmeister, A. Gabelmann, K. Nuessle, S. Reske, R. Kreienberg, H. J. Brambs, and T. Kuehn. Pre-operative staging of invasive breast cancer with MR mammography and/or PET: boon or bunk? *Br. J. Radiol.*, 75(898):789–98, Oct 2002.

[29] U. Fischer, L. Kopka, and E. Grabbe. Breast carcinoma: effect of preoperative contrast-enhanced MR imaging on the therapeutic approach. *Radiology*, 213(3):881–8, Dec 1999.

[30] K. Schelfout, M. Van Goethem, E. Kersschot, C. Colpaert, A. M. Schelfhout, P. Leyman, I. Verslegers, I. Biltjes, J. Van Den Haute, J. P. Gillardin, W. Tjalma, J. C. Van Der Auwera, P. Buytaert, and A. De Schepper. Contrast-enhanced MR imaging of breast lesions and effect on treatment. *Eur. J. Surg. Oncol.*, 30(5):501–7, Jun 2004.

[31] H. Mumtaz, M. A. Hall-Craggs, T. Davidson, K. Walmsley, W. Thurell, M. W. Kissin, and I. Taylor. Staging of symptomatic primary breast cancer with MR imaging. *Am. J. Roentgenol.*, 169(2):417–24, Aug 1997.

[32] L. Esserman, N. Hylton, L. Yassa, J. Barclay, S. Frankel, and E. Sickles. Utility of magnetic resonance imaging in the management of breast cancer: evidence for improved preoperative staging. *J. Clin. Oncol.*, 17(1):110–9, Jan 1999.

[33] Y. Zhang, H. Fukatsu, S. Naganawa, H. Satake, Y. Sato, M. Ohiwa, T. Endo, S. Ichihara, and T. Ishigaki. The role of contrast-enhanced MR mammography for determining candidates for breast conservation surgery. *Breast Cancer*, 9(3):231–9, 2002.

[34] L. Liberman, E. A. Morris, D. D. Dershaw, A. F. Abramson, and L. K. Tan. MR imaging of the ipsilateral breast in women with percutaneously proven breast cancer. *Am. J. Roentgenol.*, 180(4):901–10, Apr 2003.

[35] I. Bedrosian, R. Mick, S. G. Orel, M. Schnall, C. Reynolds, F. R. Spitz, L. S. Callans, G. P. Buzby, E. F. Rosato, D. L. Fraker, and B. J. Czerniecki. Changes in the surgical management of patients with breast carcinoma based on preoperative magnetic resonance imaging. *Cancer*, 98(3):468–73, Aug 1 2003. doi: 10.1002/cncr.11490.

[36] G. N. Rodenko, S. E. Harms, J. M. Pruneda, Jr. Farrell, R. S., W. P. Evans, D. S. Copit, P. A. Krakos, and D. P. Flamig. MR imaging in the management before surgery of lobular carcinoma of the breast: correlation with pathology. *Am. J. Roentgenol.*, 167(6):1415–9, Dec 1996.

[37] P. J. Kneeshaw, L. W. Turnbull, A. Smith, and P. J. Drew. Dynamic contrast enhanced magnetic resonance imaging aids the surgical management of invasive lobular breast cancer. *Eur. J. Surg. Oncol.*, 29(1):32–7, Feb 2003. doi: 10.1053/ejso.2002.1391.

[38] C. D. Lehman, J. D. Blume, P. Weatherall, D. Thickman, N. Hylton, E. Warner, E. Pisano, S. J. Schnitt, C. Gatsonis, M. Schnall, G. A. DeAngelis, P. Stomper, E. L. Rosen, M. O'Loughlin, S. Harms, and D. A. Bluemke. Screening women at high risk for breast cancer with mammography and magnetic resonance imaging. *Cancer*, 103(9):1898–905, May 1 2005.

[39] E. R. Port, A. Park, P. I. Borgen, E. Morris, and L. L. Montgomery. Results of MRI screening for breast cancer in high-risk patients with LCIS and atypical hyperplasia. *Ann. Surg. Oncol.*, 14(3):1051–7, Mar 2007.

[40] J. Yu, A. Park, E. Morris, L. Liberman, P. I. Borgen, and T. A. King. MRI screening in a clinic population with a family history of breast cancer. *Ann. Surg. Oncol.*, 15(2):452–61, Feb 2008. doi: 10.1245/s10434-007-9622-2.

[41] R. Dent and E. Warner. Screening for hereditary breast cancer. *Semin. Oncol.*, 34(5):392–400, Oct 2007. doi: 10.1053/j.seminoncol.2007.07.002.

[42] Berg WA, Zhang Z, Lehrer D, and et al. Detection of breast cancer with addition of annual screening ultrasound or a single screening MRI to mammography in women with elevated breast cancer risk. *JAMA*, 307(13):1394–1404, 2012. doi: 10.1001/jama.2012.388.

[43] A. Becherer, T. Helbich, A. Staudenherz, R. Jakesz, E. Kubista, R. Lehner, M. Rudas, B. Teleky, K. Kletter, and T. Leitha. The diagnostic value of planar and SPECT scintimammography in different age groups. *Nucl. Med. Commun.*, 18(8):710–8, Aug 1997.

[44] A. E. Burgess, F. L. Jacobson, and P. F. Judy. Human observer detection experiments with mammograms and power-law noise. *Med. Phys.*, 28(4):419–37, Apr 2001. doi: 10.1118/1.1355308.

[45] Francois O. Bochud, Francis R. Verdun, Jean-Francois Valley, Christian Hessler, and Raphael Moeckli. Importance of anatomical noise in mammography. *Proc. SPIE*, 3036:74–80, 1997. doi: 10.1117/12.271313.

[46] Lin Chen, Craig K Abbey, and John M Boone. Association between power law coefficients of the anatomical noise power spectrum and lesion detectability in breast imaging modalities. *Phys. Med. Biol.*, 58(6):1663, 2013.

[47] Jerrold T. Bushberg, J. Anthony Seibert, Jr. Edwin M. Leidholdt, and John M. Boone. *The Essential Physics of Medical Imaging.* Lippincott Williams & Wilkins, 2nd edition, 2002.

[48] Yue-Houng Hu, Bo Zhao, and Wei Zhao. Image artifacts in digital breast tomosynthesis: Investigation of the effects of system geometry and reconstruction parameters using a linear system approach. *Med. Phys.*, 35(12):5242–52, December 2008. doi: 10.1118/1.2996110.

[49] L. T. Niklason, B. T. Christian, L. E. Niklason, D. B. Kopans, D. E. Castleberry, B. H. Opsahl-Ong, C. E. Landberg, P. J. Slanetz, A. A. Giardino, R. Moore, D. Albagli, M. C. DeJule, P. F. Fitzgerald, D. F. Fobare, B. W. Giambattista, R. F. Kwasnick, J. Liu, S. J. Lubowski, G. E. Possin, J. F. Richotte, C. Y. Wei, and R. F. Wirth. Digital tomosynthesis in breast imaging. *Radiology*, 205(2):399–406, 1997.

[50] A. Smith. Full-field breast tomosynthesis. *Radiol. Manage.*, 27(5):25–31, 2005.

[51] Baorui Ren, C. Ruth, J. Stein, A. Smith, I. Shaw, and Jing Zhenxue. Design and performance of the prototype full field breast tomosynthesis system with selenium based flat panel detector. *Proc. SPIE*, 5745:550–61, 2005.

[52] M. Bissonnette, M. Hansroul, E. Masson, S. Savard, S. Cadieux, P. Warmoes, D. Gravel, J. Agopyan, B. Polischuk, W. Haerer, T. Mertelmeier, J. Y. Lo, Y. Chen, III Dobbins, J. T., J. L. Jesneck, and S. Singh. Digital breast tomosynthesis using an amorphous selenium flat panel detector. *Proc. SPIE*, 5745:529–40, 2005. doi: 10.1117/12.601622.

[53] Tao Wu, Alexander Stewart, Martin Stanton, Thomas McCauley, Walter Phillips, Daniel B. Kopans, Richard Moore, Jeffrey W. Eberhard, Beale Opsahl-Ong, Loren Niklason, and Mark B. Williams. Tomographic mammography using a limted number of low-dose cone-beam projection images. *Med. Phys.*, 30(3):365–380, 2003. ISSN 00942405. doi: 10.1118/1.1543934.

[54] Jun Zhou, Bo Zhao, and Wei Zhao. A computer simulation platform for the optimization of a breast tomosynthesis system. *Med. Phys.*, 34(3):1098–1109, 2007. doi: 10.1118/1.2558160.

[55] Bo Zhao and Wei Zhao. Three-dimensional linear system analysis for breast tomosynthesis. *Med. Phys.*, 35(12):5219–32, December 2008. doi: 10.1118/1.2996014.

[56] Bo Zhao and Wei Zhao. Imaging performance of an amorphous selenium digital mammography detector in a breast tomosynthesis system. *Med. Phys.*, 35(5):1978–87, May 2008. doi: 10.1118/1.2903425.

[57] Bo Zhao, Jun Zhou, Yue-Houng Hu, Thomas Mertelmeier, Jasmina Ludwig, and Wei Zhao. Experimental validation of a three-dimensional linear system model for breast tomosynthesis. *Med. Phys.*, 36(1):240–51, January 2009. doi: 10.1118/1.3040178.

[58] J. M. Boone, A. L. C. Kwan, T. R. Nelson, N. Shah, G. Burkett, J. A. Seibert, K. K. Lindfors, and G. Roos. Performance assessment of a pendant-geometry CT scanner for breast cancer detection. *Proc. SPIE*, 5745:319–23, 2005. doi: 10.1117/12.595706.

[59] J. M. Boone, T. R. Nelson, K. K. Lindfors, and J. A. Seibert. Dedicated breast CT: radiation dose and image quality evaluation. *Radiology*, 221(3):657–67, Dec 2001. doi: 10.1148/radiol.2213010334.

[60] J. M. Boone, A. L. Kwan, K. Yang, G. W. Burkett, K. K. Lindfors, and T. R. Nelson. Computed tomography for imaging the breast. *J. Mammary Gland Biol. Neoplasia*, 11(2): 103–11, Apr 2006. doi: 10.1007/s10911-006-9017-1.

[61] J. M. Boone and K. K. Lindfors. Breast CT: potential for breast cancer screening and diagnosis. *Future Oncol.*, 2(3):351–6, Jun 2006. doi: 10.2217/14796694.2.3.351.

[62] K. K. Lindfors, J. M. Boone, T. R. Nelson, K. Yang, A. L. Kwan, and D. F. Miller. Dedicated breast CT: initial clinical experience. *Radiology*, 246(3):725–33, Mar 2008. doi: 10.1148/radiol.2463070410.

[63] Ruola Ning, David Conover, Yong Yu, Yan Zhang, Weixing Cai, Ricardo Betancourt-Benitez, and Xianghua Lu. A novel cone beam breast CT scanner: System evaluation. *Proc. SPIE*, 6510:SPIE, 2007. doi: 10.1117/12.710340.

[64] S.J. Glick, S. Thacker, X. Gong, and B. Liu. Evaluating the impact of x-ray spectral shape on image quality in flat-panel CT breast imaging. *Med. Phys.*, 34:5, 2007. doi: 10.1118/1.2388574.

[65] Biao Chen and Ruola Ning. Cone-beam volumetric CT breast imaging: feasibility study. *Med. Phys.*, 29:755, 2002. doi: 10.1118/1.1461843.

[66] Linyun Chen, Youtao Shen, Chao-Jen Lai, Tao Han, Yuncheng Zhong, Shuaiping Ge, Xinming Liu, Tianpeng Wang, Wei T. Yang, Gary J. Whitman, and Chris Shaw. Dual resolution cone beam breast CT: A feasibility study. *Med. Phys.*, 36:4007–4014, 2009. doi: 10.1118/1.3187225.

[67] Samantha P. Zuckerman, Emily F. Conant, Brad M. Keller, Andrew D. A. Maidment, Bruno Barufaldi, Susan P. Weinstein, Marie Synnestvedt, and Elizabeth S. McDonald. Implementation of synthesized two-dimensional mammography in a population-based digital breast tomosynthesis screening program. *Radiology*, 281(3):730–736, 2016. doi: 10.1148/radiol.2016160366. PMID: 27467468.

[68] Margarita L Zuley, Ben Guo, Victor J Catullo, Denise M Chough, Amy E Kelly, Amy H Lu, Grace Y Rathfon, Marion Lee Spangler, Jules H Sumkin, Luisa P Wallace, and Andriy I Bandos. Comparison of two-dimensional synthesized mammograms versus original digital mammograms alone and in combination with tomosynthesis images. *Radiology*, 271(3):664–671, June 2014. ISSN 0033-8419. doi: 10.1148/radiol.13131530.

[69] John M. Lewin, Pamela K. Isaacs, Virginia Vance, and Fred J. Larke. Dual-energy contrast-enhanced digital subtraction mammography: Feasibility. *Radiology*, 229(1):261–268, 2003. doi: 10.1148/radiol.2291021276.

[70] Roberta A. Jong, Martin J. Yaffe, Mia Skarpathiotakis, Rene S. Shumak, Nathalie M. Danjoux, Anoma Gunesekara, and Donald B. Plewes. Contrast-enhanced digital mammography: Initial clinical experience. *Radiology*, 228(3):842–850, 2003. doi: 10.1148/radiol.2283020961. PMID: 12881585.

[71] Florian F. Schmitzberger, Eva Maria Fallenberg, R udiger Lawaczeck, Magnus Hemmendorff, Elin Moa, Mats Danielsson, Ulrich Bick, Susanne Diekmann, Alexander Pöllinger, Florian J. Engelken, and Felix Diekmann. Development of low-dose photon-counting contrast-enhanced tomosynthesis with spectral imaging. *Radiology*, 259(2):558–564, 2011. doi: 10.1148/radiol.11101682.

[72] Felix Diekmann and Ulrich Bick. Tomosynthesis and contrast-enhanced digital mammography: recent advances in digital mammography. *Eur. Radiol.*, 17(12):3086–3092, 2007. ISSN 1432-1084. doi: 10.1007/s00330-007-0715-x.

[73] Sara C. Chen, Ann-Katherine Carton, Michael Albert, Emily F. Conant, Mitchell D. Schnall, and Andrew D. A. Maidment. Initial clinical experience with contrast-enhanced digital breast tomosynthesis. *Acad. Radiol.*, 14(2):229–238. ISSN 1076-6332. doi: 10.1016/j.acra.2006.10.022.

[74] John Garrett, Yongshuai Ge, Ke Li, and Guang-Hong Chen. Anatomical background noise power spectrum in differential phase contrast breast images. *Proc. SPIE*, 9412:94121J–94121J–6, 2015. doi: 10.1117/12.2081008.

[75] T. Morita, M. Yamada, A. Kano, S. Nagatsuka, C. Honda, and T. Endo. Subtle abnormalities in highly dense breasts detected by use of a digital phase contrast mammography system: A report of three invasive cancer cases in the early stage. *Lect. Notes Comput. Sci.*, 5116: 228–234, 2008. doi: 10.1007/978-3-540-70538-3.

[76] Srinivasan Vedantham and Andrew Karellas. X-ray phase contrast imaging of the breast: Analysis of tissue simulating materials. *Med. Phys.*, 40(4):041906, 2013. doi: 10.1118/1.4794503.

[77] Joseph Zambelli, Nicholas Bevins, Zhihua Qi, and Guang-Hong Chen. Measurement of contrast-to-noise ratio for differential phase contrast computed tomography. 7622:76224C, 2010. doi: 10.1117/12.844448.

[78] Zhentian Wang, Nik Hauser, Gad Singer, Mafalda Trippel, Rahel A. Kubik-Huch, Christof W. Schneider, and Marco Stampanoni. Non-invasive classification of microcalcifications with phase-contrast x-ray mammography. *Nat. Commun.*, 5, 2014. doi: 10.1038/ncomms4797.

[79] Tilman Donath, Franz Pfeiffer, Oliver Bunk, Christian Gruenzweig, Eckhard Hempel, Stefan Popescu, Peter Vock, and Christian David. Toward clinical x-ray phase-contrast CT demonstration of enhanced soft-tissue contrast in human specimen. *Invest. Radiol.*, 45(7):445–452, 2010. doi: 10.1097/RLI.0b013e3181e21866.

[80] F Gilbert, L Tucker, M Gillan, P Willsher, J Cooke, K Duncan, M Michell, H Dobson, Y Lim, H Purushothaman, S Strudley, C anbd Astley, O Morrish, K Young, and S Duffy. TOMMY trial: A comparison of TOMosynthesis with digital MammographY in the UK NHS Breast Screening Programme. *Health Technol Assess*, 19(4), 2015.

[81] Fiona J. Gilbert, Lorraine Tucker, Maureen G. C. Gillan, Paula Willsher, Julie Cooke, Karen A. Duncan, Michael J. Michell, Hilary M. Dobson, Yit Yoong Lim, Tamara Suaris, Susan M. Astley, Oliver Morrish, Kenneth C. Young, and Stephen W. Duffy. Accuracy of digital breast tomosynthesis for depicting breast cancer subgroups in a UK retrospective reading study (TOMMY trial). *Radiology*, 277(3):697–706, 2015. doi: 10.1148/radiol.2015142566. PMID: 26176654.

[82] U.S. Food & Drug Administration. MQSA National Statistics, 2017. URL `https://www.fda.gov/Radiation-EmittingProducts/MammographyQualityStandardsActandProgram/FacilityScorecard/ucm113858.htm`.

[83] Debra M. Ikeda. *Breast Imaging: The Requisites*. The Requisites. Elsevier, 3rd edition, 2017.

[84] The American College of Radiology. *ACR BI-RADS Atlas*. 5th edition, 2013.

[85] James T. Dobbins. Tomosynthesis imaging: At a translational crossroads. *Med. Phys.*, 36(6): 1956–1967, 2009. ISSN 2473-4209. doi: 10.1118/1.3120285.

[86] B. G. Ziedses Des Plantes. Eine neue methode zur differenzierung in der rontgenographie (planigraphies). *Acta Radiol.*, 13(2):182–192, 1932. doi: 10.3109/00016923209135135.

[87] D. G. Grant. Tomosynthesis: A three-dimensional radiographic imaging technique. *IEEE Trans. Biomed. Eng.*, BME-19(1):20–28, Jan 1972. ISSN 0018-9294. doi: 10.1109/TBME.1972.324154.

[88] P. Edholm, G. Granlund, H. Knutsson, and C. Petersson. Ectomography: A new radiographic method for reproducing a selected slice of varying thickness. 21(4):433–442, 1980.

[89] H. Becher, M. Schlüter, D. G. Mathey, W. Bleifeld, E. Klotz, P. Haaker, R. Linde, and H. Weiss. Coronary angiography with flashing tomosynthesis. *Eur. Heart J.*, 6(5):399, 1985. doi: 10.1093/oxfordjournals.eurheartj.a061878.

[90] James T Dobbins III and Devon J Godfrey. Digital x-ray tomosynthesis: current state of the art and clinical potential. *Phys. Med. Biol.*, 48(19):R65, 2003.

[91] James T. Dobbins III and H. Page McAdams. Chest tomosynthesis: Technical principles and clinical update. *Eur. J. Radiol.*, 72(2):244 – 251, 2009. ISSN 0720-048X. doi: 10.1016/j.ejrad.2009.05.054. Digital Radiography.

[92] David A. P. Dunkerley, Tobias Funk, and Michael A. Speidel. Method for dose-reduced 3D catheter tracking on a scanning-beam digital x-ray system using dynamic electronic collimation. *Proc. SPIE*, 9783:97831Y–97831Y–12, 2016. doi: 10.1117/12.2216892.

[93] Jordan M. Slagowski, Michael T. Tomkowiak, David A. P. Dunkerley, and Michael A. Speidel. Feasibility of CT-based 3D anatomic mapping with a scanning-beam digital x-ray (SBDX) system. *Proc. SPIE*, 9412:941209–941209–12, 2015. doi: 10.1117/12.2082052.

[94] David A. P. Dunkerley, Jordan M. Slagowski, Lindsay E. Bodart, and Michael A. Speidel. Automated 3D coronary sinus catheter detection using a scanning-beam digital x-ray system. *Proc. SPIE*, 10132:101321N–101321N–10, 2017. doi: 10.1117/12.2254443.

[95] Michael A. Speidel, Brian P. Wilfley, Josh M. Star-Lack, Joseph A. Heanue, and Michael S. Van Lysel. Scanning-beam digital x-ray (SBDX) technology for interventional and diagnostic cardiac angiography. *Med. Phys.*, 33(8):2714–2727, 2006. ISSN 2473-4209. doi: 10.1118/1.2208736. URL `http://dx.doi.org/10.1118/1.2208736`.

[96] Michael A. Speidel, Michael T. Tomkowiak, Amish N. Raval, and Michael S. Van Lysel. Three-dimensional tracking of cardiac catheters using an inverse geometry x-ray fluoroscopy system. *Med. Phys.*, 37(12):6377–6389, 2010. doi: http://dx.doi.org/10.1118/1.3515463.

[97] J Shan, A W Tucker, L R Gaalaas, G Wu, E Platin, A Mol, J Lu, and O Zhou. Stationary intraoral digital tomosynthesis using a carbon nanotube x-ray source array. *Dentomaxillofacial Radiology*, 44(9):20150098, 2015. doi: 10.1259/dmfr.20150098. PMID: 26090933.

[98] Loren T. Niklason, Daniel B Kopans, and Leena M. Hamberg. Digital breast imaging: Tomosynthesis and digital subtraction mammography. *Breast Disease*, 10(3):151–64, January 1998.

[99] Per Skaane, Andriy I. Bandos, Randi Gullien, Ellen B. Eben, Ulrika Ekseth, Unni Haakenaasen, Mina Izadi, Ingvild N. Jebsen, Gunnar Jahr, Mona Krager, Loren T. Niklason, Solveig Hofvind, and David Gur. Comparison of digital mammography alone and digital mammography plus tomosynthesis in a population-based screening program. *Radiology*, 267(1):47–56, 2013. doi: 10.1148/radiol.12121373.

[100] Yoshihiro Okada, Keiichiro Sato, Takaaki Ito, Yuichi Hosoi, and Toshiro Hayakawa. A newly developed a-Se mammography flat panel detector with high-sensitivity and low image artifact. *Proc. SPIE*, 8668:86685V–86685V–9, 2013. doi: 10.1117/12.2006530.

[101] Alistair Mackenzie, Nicholas W Marshall, Andria Hadjipanteli, David R Dance, Hilde Bosmans, and Kenneth C Young. Characterisation of noise and sharpness of images from four digital breast tomosynthesis systems for simulation of images for virtual clinical trials. *Phys. Med. Biol.*, 62(6):2376, 2017.

[102] A. Rodríguez-Ruiz, M. Castillo, J. Garayoa, and M. Chevalier. Evaluation of the technical performance of three different commercial digital breast tomosynthesis systems in the clinical environment. *Physica Med.*, 32(6):767 – 777, 2016. ISSN 1120-1797. doi: http://dx.doi.org/10.1016/j.ejmp.2016.05.001.

[103] U.S. Food & Drug Administration. Digital accreditation: FFDM and DBT Systems, 2017. URL `https://www.fda.gov/radiation-emittingproducts/mammographyqualitystandardsactandprogram/facilitycertificationandinspection/ucm114148.htm`.

[104] K. Yang, A. L.C. Kwan, SY. Huang, N. J. Packard, and J. M. Boone. Noise power properties of a cone-beam ct system for breast caner detection. *Med. Phys.*, 35:5317–5327, 2008. doi: 10.1118/1.3002411.

[105] Xin Qian, Andrew Tucker, Emily Gidcumb, Jing Shan, Guang Yang, Xiomara Calderon-Colon, Shabana Sultana, Jianping Lu, Otto Zhou, Derrek Spronk, Frank Sprenger, Yiheng Zhang, Don Kennedy, Tom Farbizio, and Zhenxue Jing. High resolution stationary digital breast tomosynthesis using distributed carbon nanotube x-ray source array. *Med. Phys.*, 39(4):2090–2099, 2012. ISSN 2473-4209. doi: 10.1118/1.3694667.

[106] Jabari Calliste, Andrew W. Tucker, Emily Gidcumb, Cherie M. Kuzmiak, Jianping Lu, Otto Zhou, and Yueh Z. Lee. Initial clinical evaluation of stationary digital breast tomosynthesis. *Proc. SPIE*, 9412:941228–941228–7, 2015. doi: 10.1117/12.2082090.

[107] William S. Ferris, Trevor L. Vent, Tristan D. Maidment, Raymond J. Acciavatti, David E. Wurtele, and Andrew D. A. Maidment. Geometric calibration for a next-generation digital breast tomosynthesis system. *Proc. SPIE*, 10132:101324C–101324C–10, 2017. doi: 10.1117/12.2255301.

[108] Björn Cederström, Erik Fredenberg, Karl Berggren, Klaus Erhard, Mats Danielsson, and Matthew Wallis. Lesion characterization in spectral photon-counting tomosynthesis. *Proc. SPIE*, 10132:1013205–1013205–10, 2017. doi: 10.1117/12.2253966.

[109] Heang K. Tuy. An inversion formula for cone-beam reconstruction. *SIAM Journal on Applied Mathematics*, 43(3):546–552, 1983. doi: 10.1137/0143035.

[110] I. A. Cunningham, M. S. Westmore, and A. Fenster. A spatial-frequency dependent quantum accounting diagram and detective quantum efficiency model of signal and noise propagation in cascaded imaging systems. *Med. Phys.*, 21(3):417–427, 1994. doi: 10.1118/1.597401.

[111] Ke Li, Nicholas Bevins, Joseph Zambelli, and Guang-Hong Chen. Fundamental relationship between the noise properties of grating-based differential phase contrast ct and absorption ct: Theoretical framework using a cascaded system model and experimental validation. *Med. Phys.*, 40(2):021908, 2013. doi: http://dx.doi.org/10.1118/1.4788647.

[112] Samuel Richard, Jeffrey H. Siewerdsen, and Daniel J. Tward. NEQ and task in dual-energy imaging: from cascaded systems analysis to human observer performance. *Proc. SPIE*, 6913 (1):691311, 2008. doi: 10.1117/12.772772.

[113] D.J. Tward and J.H. Siewerdsen. Cascaded systems analysis of the 3D noise transfer characteristics of flat-panel cone-beam CT. *Med. Phys.*, 35:5510, 2008.

[114] A. C. Kak and Malcolm Slaney. *Principles of Computerized Tomographic Imaging*. IEEE Press, New York, 1988.

[115] Jiang Hsieh. *Computed Tomography, Second Edition: Principles, Design, Artifacts, and Recent Advances*. SPIE and John Wiley & Sons, Inc., 2009. doi: 10.1117/3.817303.

[116] A. Rose. Television pickup tubes and the problem of vision. *Advances in Electronics and Electron Physics*, 1:131–166, 1948.

[117] A. Rose. The sensitivity performance of the human eye on an absolute scale. *J. Opt. Soc. Am.*, 38(2):196–208, 1948. doi: 10.1364/JOSA.38.000196.

[118] A. Rose. *Vision: human and electronic*. Plenum Press New York, 1973.

[119] A.E. Burgess. The Rose model, revisited. *JOSA A*, 16(3):633–646, 1999. doi: 10.1364/JOSAA.16.000633.

[120] Harrison H Barrett, Kyle J Myers, Christoph Hoeschen, Matthew A Kupinski, and Mark P Little. Task-based measures of image quality and their relation to radiation dose and patient risk. *Phys. Med. Biol.*, 60(2):R1, 2015.

[121] H H Barrett, J Yao, J P Rolland, and K J Myers. Model observers for assessment of image quality. *PNAS*, 90(21):9758–9765, 1993.

[122] S. Richard and J. H. Siewerdsen. Optimization of dual-energy imaging systems using generalized NEQ and imaging task. *Med. Phys.*, 34(1):127–139, 2007. doi: 10.1118/1.2400620.

[123] Adam Wunderlich and Frèdèric Noo. Image covariance and lesion detectability in direct fan-beam x-ray computed tomography. *Phys. Med. Biol.*, 53(10):2471, 2008. doi: 10.1088/0031-9155/53/10/002.

[124] Grace J. Gang, Junghoon Lee, J. Webster Stayman, Daniel J. Tward, W. Zbijewski, Jerry L. Prince, and Jeffrey H. Siewerdsen. Analysis of Fourier-domain task-based detectability index in tomosynthesis and cone-beam CT in relation to human observer performance. *Med. Phys.*, 38(4):1754–68, April 2011. doi: 10.1118/1.3560428.

[125] Samuel Richard, Daniela B. Husarik, Girijesh Yadava, Simon N. Murphy, and Ehsan Samei. Towards task-based assessment of CT performance: System and object MTF across different reconstruction algorithms. *Med. Phys.*, 39(7):4115–4122, 2012. doi: 10.1118/1.4725171.

[126] Ke Li, John Garrett, and Guang-Hong Chen. Correlation between human observer performance and model observer performance in differential phase contrast CT. *Med. Phys.*, 40(11):111905, 2013. doi: 10.1118/1.4822576.

[127] J. H. Siewerdsen, I. A. Cunningham, and D. A. Jaffray. A framework for noise-power spectrum analysis of multidimensional images. *Med. Phys.*, 29(11):2655–2671, 2002. doi: 10.1118/1.1513158.

[128] C B Caldwell, S J Stapleton, D W Holdsworth, R A Jong, W J Weiser, G Cooke, and M J Yaffe. Characterisation of mammographic parenchymal pattern by fractal dimension. *Phys. Med. Biol.*, 35(2):235, 1990.

[129] A. van der Schaaf and J.H. van Hateren. Modelling the power spectra of natural images: Statistics and information. *Vision Res.*, 36(17):2759 – 2770, 1996. ISSN 0042-6989. doi: 10.1016/0042-6989(96)00002-8.

[130] Francois O. Bochud, Jean-Francois Valley, Francis R. Verdun, Christian Hessler, and Pierre Schnyder. Estimation of the noisy component of anatomical backgrounds. *Med. Phys.*, 26(7):1365–1370, 1999. doi: 10.1118/1.598632.

[131] Srinivasan Vedantham, Linxi Shi, Stephen J. Glick, and Andrew Karellas. Scaling-law for the energy dependence of anatomic power spectrum in dedicated breast CT. *Med. Phys.*, 40(1):011901, 2013. doi: 10.1118/1.4769408.

[132] Yue-Houng Hu, Michael Masiar, and Wei Zhao. Breast structural noise in digital breast tomosynthesis and its dependence on reconstruction methods. In Joan Marti, Arnau Oliver, Jordi Freixenet, and Robert Marti, editors, *Digital Mammography*, volume 6136 of *Lecture Notes in Computer Science*, pages 598–605. Springer Berlin Heidelberg, 2010. doi: 10.1007/978-3-642-13666-5_81.

[133] Lin Chen, Craig K. Abbey, Anita Nosratieh, Karen K. Lindfors, and John M. Boone. Anatomical complexity in breast parenchyma and its implications for optimal breast imaging strategies. *Med. Phys.*, 39(3):1435–1441, 2012. doi: 10.1118/1.3685462.

[134] Arthur E. Burgess and Philip F. Judy. Signal detection in power-law noise: effect of spectrum exponents. *J. Opt. Soc. Am. A*, 24(12):B52–B60, Dec 2007. doi: 10.1364/JOSAA.24.000B52.

[135] Kathrine G. Metheany, Craig K. Abbey, Nathan Packard, and John M. Boone. Characterizing anatomical variability in breast CT images. *Med. Phys.*, 35(10):4685–4694, 2008. doi: 10.1118/1.2977772.

[136] John Garrett, Yongshuai Ge, Ke Li, and Guang-Hong Chen. Impact of anatomical noise on detection performance of microcalcifications in multi-contrast breast imaging. *AAPM Annual Meeting 2015, Anaheim, CA*, 2015.

[137] John Garrett, Yongshuai Ge, Ke Li, and Guang-Hong Chen. Anatomical background noise power spectrum in differential phase contrast and dark field contrast mammograms. *Med. Phys.*, 41(12):120701, 2014. doi: 10.1118/1.4901313.

[138] United States Nuclear Regulatory Commission. NRC Library, Basic References, Glossary, 2017. URL `https://www.nrc.gov/reading-rm/basic-ref/glossary/alara.html`.

[139] Yao Lu, Heang-Ping Chan, Jun Wei, MItch Goodsitt, Paul L. Carson, Lubomir Hadijiski, Andrea Schmitz, Jeffrey W Eberhard, and Bernhard E. H. Claus. Image quality of microcalcification in digital breast tomosynthesis: Effects of projection-view distributions. *Med. Phys.*, 38(10):5703–12, October 2011. doi: 10.1118/1.3637492.

[140] James G. Mainprize, Alli Bloomquist, Xinying Wang, and Martin J. Yaffe. Dependence of image quality on geometric factors in breast tomosynthesis. *Med. Phys.*, 38(6):3090–103, June 2011. doi: 10.1118/1.3591990.

[141] G. H. Chen and Z. Qi. Image reconstruction for fan-beam differential phase contrast computed tomography. *Phys. Med. Biol.*, 53(4):1015–25, Feb 21 2008. doi: 10.1088/0031-9155/53/4/013.

[142] Guang-Hong Chen, Jie Tang, Brian Nett, Zhihua Qi, Shuai Leng, and Timothy Szczykutowicz. Prior image constrained compressed sensing (PICCS) and applications in x-ray computed tomography. *Current Medical Imaging Reviews*, 6:119–34, 2010.

[143] J. Tang, P. Thèriault-Lauzier, and G.-H. Chen. Dose reduction using prior image constrained compressed sensing (DR-PICCS). *Proc. SPIE*, 7961:79612K, 2011. doi: 10.1117/12.878200.

[144] Meghan G. Lubner, Perry J. Pickhardt, Jie Tang, and Guang-Hong Chen. Reduced image noise at low-dose multidetector CT of the abdomen with prior image constrained compressed sensing algorithm. *Radiology*, 260(1):248–56, July 2011. doi: 10.1148/radiol.11101380.

[145] Pascal Thèriault-Lauzier and Guang-Hong Chen. Characterization of statistical prior image constrained compressed sensing (PICCS): II. application to dose reduction. *Med. Phys.*, 40(2): 021902, 2013. doi: 10.1118/1.4773866.

[146] Pascal Thèriault-Lauzier and Guang-Hong Chen. Characterization of statistical prior image constrained compressed sensing. I. applications to time-resolved contrast-enhanced CT. *Med. Phys.*, 39(10):5930–48, October 2012. doi: 10.1118/1.4748323.

[147] Pascal Thèriault-Lauzier, Jie Tang, and Guang-Hong Chen. Prior image constrained compressed sensing: Implementation and performance evaluation. *Med. Phys.*, 39(1):66–80, 2012. doi: 10.1118/1.3666946.

[148] Kai Niu, Jie Tang, Kevin Royalty, Orhan Ozkan, Charles Strother, Beverly Aagaard-Kienitz, Kari A. Pulfer, and Guang-Hong Chen. Radiation dose reduction and CNR enhancement in C-arm cone beam CT. *Proc. SPIE*, 8668:86682S–86682S–6, 2013. doi: 10.1117/12.2007736.

[149] Pietro Perona and Jitendra Malik. Scale-space and edge detection using anisotropic diffusion. *IEEE Trans. Pattern Anal. Mach. Intell.*, 12:629–39, July 1990. doi: 10.1109/34.56205.

[150] John Canny. A computational approach to edge detection. *IEEE Trans. Pattern Anal. Mach. Intell.*, 8(6):679–698, June 1986. ISSN 0162-8828. doi: 10.1109/TPAMI.1986.4767851.

[151] Ioannis Sechopoulos. A review of breast tomosynthesis. part i. the image acquisition process. *Med. Phys.*, 40(1):014301, 2013. doi: 10.1118/1.4770279.

[152] Tao Wu, Richard H Moore, Elizabeth a Rafferty, and Daniel B Kopans. A comparison of reconstruction algorithms for breast tomosynthesis. *Med. Phys.*, 31(9):2636–2647, 2004. ISSN 00942405. doi: 10.1118/1.1786692.

[153] Thomas Mertelmeier, Jasmina Orman, Wolfgang Haerer, and Mithun K. Dudam. Optimizing filtered backprojection reconstruction for a breast tomosynthesis prototype device. *Proc. SPIE*, 6142:61420F–61420F–12, 2006. doi: 10.1117/12.651380.

[154] Anna K. Jerebko and Thomas Mertelmeier. Evaluation and optimization of the maximum-likelihood approach for image reconstruction in digital breast tomosynthesis. *Proc. SPIE*, 7622:76220E–76220E–9, 2010. doi: 10.1117/12.844177.

[155] Yiheng Zhang, Heang-Ping Chan, Berkman Sahiner, Jun Wei, Mitchell M Goodsitt, Lubomir M Hadjiiski, Jun Ge, and Chuan Zhou. A comparative study of limited-angle cone-beam reconstruction methods for breast tomosynthesis. *Med. Phys.*, 33(10):3781–3795, 2006. ISSN 00942405. doi: 10.1118/1.2237543.

[156] Yiheng Zhang, Heang-Ping Chan, Berkman Sahiner, Yi-Ta Wu, Chuan Zhou, Jun Ge, Jun Wei, and Lubomir M Hadjiiski. Application of boundary detection information in breast tomosynthesis reconstruction. *Med. Phys.*, 34(9):3603–13, 2007. ISSN 0094-2405. doi: 10.1118/1.2761968.

[157] Shiyu Xu, Jianping Lu, Otto Zhou, and Ying Chen. Statistical iterative reconstruction to improve image quality for digital breast tomosynthesis. *Med. Phys.*, 42(9):5377–5390, 2015. doi: http://dx.doi.org/10.1118/1.4928603.

[158] Veronica Mejia Bustamante, James G. Nagy, Steve S. J. Feng, and Ioannis Sechopoulos. Iterative breast tomosynthesis image reconstruction. *SIAM J. Sci. Comput.*, 35(5):S192–S208, 2013. doi: 10.1137/120881440.

[159] Emil Y. Sidky, Xiaochuan Pan, Ingrid S. Reiser, Robert M. Nishikawa, Richard H. Moore, and Daniel B. Kopans. Enhanced imaging of microcalcifications in digital breast tomosynthesis through improved image-reconstruction algorithms. *Med. Phys.*, 36(11):4920–4932, 2009. ISSN 2473-4209. doi: 10.1118/1.3232211.

[160] Rongping Zeng, Aldo Badano, and Kyle J Myers. Optimization of digital breast tomosynthesis (DBT) acquisition parameters for human observers: effect of reconstruction algorithms. 62: 2598–2611, 2017. doi: 10.1088/1361-6560/aa5ddc.

[161] N. Navab, A. Bani-Hashemi, M. S. Nadar, K. Wiesent, P. Durlak, T. Brunner, K. Barth, and R. Graumann. *3D reconstruction from projection matrices in a C-arm based 3D-angiography system*, pages 119–129. Springer Berlin Heidelberg, Berlin, Heidelberg, 1998. ISBN 978-3-540-49563-5. doi: 10.1007/BFb0056194.

[162] G. Lauritsch and W.H. Haerer. Theoretical framework for filtered back projection in tomosynthesis. 3338:1127, 1998. doi: 10.1117/12.310839.

[163] Thomas Mertelmeier, Jasmina Ludwig, Bo Zhao, and Wei Zhao. *Optimization of Tomosynthesis Acquisition Parameters: Angular Range and Number of Projections*, pages 220–227. Springer Berlin Heidelberg, Berlin, Heidelberg, 2008. ISBN 978-3-540-70538-3. doi: 10.1007/978-3-540-70538-3_31.

[164] Yinsheng Li, Kai Niu, Jie Tang, and Guang-Hong Chen. Statistical image reconstruction via denoised ordered-subset statistically penalized algebraic reconstruction technique (DOS-SPART). *Proc. SPIE*, 9033:90330U–90330U–8, 2014. doi: 10.1117/12.2043491.

[165] John Garrett, Yinsheng Li, Ke Li, and Guang-Hong Chen. Denoised ordered subset statistically penalized algebraic reconstruction technique (DOS-SPART) in digital breast tomosynthesis. *Proc. SPIE*, 10132:101324F–101324F–7, 2017. doi: 10.1117/12.2255584.

[166] Ke Li, Jie Tang, and Guang-Hong Chen. Statistical model based iterative reconstruction (MBIR) in clinical CT systems: Experimental assessment of noise performance. *Med. Phys.*, 41(4):041906, 2014. doi: 10.1118/1.4867863.

[167] J. Cai, B. Dong, S. Osher, and Z. Shen. Image restoration: Total variation, wavelet frames, and beyond. *Journal of the American Mathematical Society*, 25(1):1033–1089, 2012.

[168] L. Ritschl, F. Bergner, C. Fleischmann, and M. Kachelrieß. Improved total variation-based CT image reconstruction applied to clinical data. *Phys. Med. Biol.*, 56:1545, 2011.

[169] L. I. Rudin, S. Osher, and E. Fatemi. Nonlinear total variation based noise removal algorithm. *Journal of Physica D*, 60(4):259 – 268, 1992.

[170] E.Y. Sidky and X. Pan. Image reconstruction in circular cone-beam computed tomography by constrained, total-variation minimization. *Phys. Med. Biol.*, 53:4777, 2008.

[171] J. Tang, B.E. Nett, and G.H. Chen. Performance comparison between total variation (TV)-based compressed sensing and statistical iterative reconstruction algorithms. *Phys. Med. Biol.*, 54:5781, 2009.

[172] C.R. Vogel and M.E. Oman. Iterative methods for total variation denoising. *SIAM J. Sci. Comput.*, 17(1):227–238, 1996. ISSN 1064-8275.

[173] C.R. Vogel and M.E. Oman. Fast, robust total variation-based reconstruction of noisy, blurred images. *IEEE Trans. Image Process.*, 7(6):813–824, 2002. ISSN 1057-7149.

[174] Yilun Wang, Junfeng Yang, Wotao Yin, and Yin Zhang. A new alternating minimization algorithm for total variation image reconstruction. *SIAM J. IMAGING SCI*, pages 248–272, 2008.

[175] G.H. Chen, J. Tang, and S. Leng. Prior image constrained compressed sensing (PICCS): a method to accurately reconstruct dynamic CT images from highly undersampled projection data sets. *Med. Phys.*, 35:660, 2008.

[176] P Lauzier and G.H. Chen. Characterization of statistical Prior Image Constrained Compressed Sensing (PICCS). I. Applications to Time-resolved Contrast-enhanced CT. *Med. Phys.*, 39 (10):5930–5948, 2012.

[177] Pascal Thériault Lauzier and Guang-Hong Chen. Characterization of statistical prior image constrained compressed sensing (PICCS): II. Application to dose reduction. *Med. Phys.*, 40 (2):021902, 2013. doi: 10.1118/1.4773866.

[178] G.H. Chen, J. Tang, B. Nett, S. Leng, J. Zambelli, Z. Qi, N. Bevins, S. Reeder, and H. Rowley. High temporal resolution cardiac cone-beam CT using a slowly rotating c-arm gantry. *Proc. SPIE*, 7258:72580C, 2009. doi: 10.1117/12.813810.

[179] Guang-Hong Chen, P. Theriault-Lauzier, Jie Tang, B. Nett, Shuai Leng, J. Zambelli, Zhihua Qi, N. Bevins, A. Raval, S. Reeder, and H. Rowley. Time-resolved interventional cardiac c-arm cone-beam ct: An application of the piccs algorithm. *IEEE Trans. Med. Imag.*, 31(4): 907–923, April 2012. ISSN 0278-0062. doi: 10.1109/TMI.2011.2172951.

[180] Zhihua Qi and Guang-Hong Chen. Extraction of tumor motion trajectories using piccs-4dcbct: A validation study. *Med. Phys.*, 38(10):5530–5538, 2011. ISSN 2473-4209. doi: 10.1118/1.3637501.

[181] Yiheng Zhang, Heang-Ping Chan, Yi-Ta Wu, Berkman Sahiner, Chuan Zhou, Jun Wei, Jun Ge, Lubomir M. Hadjiiski, and Jiazheng Shi. Truncation Artifact and Boundary Artifact Reduction in Breast Tomosynthesis Reconstruction. *SPIE Medical Imaging: Physics of Medical Imaging*, 6913:69132Y, 2008. ISSN 0277-786X. doi: 10.1117/12.769698.

[182] Pascal Theriault Lauzier, Jie Tang, and Guang-Hong Chen. Prior image constrained compressed sensing: Implementation and performance evaluation. *Med. Phys.*, 39(1):66–80, 2012.

[183] IEEE Standard for Floating-Point Arithmetic. *IEEE Std 754-2008*, pages 1–70, Aug 2008. doi: 10.1109/IEEESTD.2008.4610935.

[184] Y. Zhang, H. P. Chan, B. Sahiner, J. Wei, C. Zhou, and L. M. Hadjiiski. Artifact reduction methods for truncated projections in iterative breast tomosynthesis reconstruction. *J. Comput. Assist. Tomogr.*, 33(3):426–35, 2009. doi: 10.1097/RCT.0b013e3181838000.

[185] B. Ohnesorge, T. Flohr, K. Schwarz, J. P. Heiken, and K. T. Bae. Efficient correction for CT image artifacts caused by objects extending outside the scan field of view. *Med. Phys.*, 27(1): 39–46, 2000. doi: 10.1118/1.598855.

[186] J. Hsieh, E. Chao, J. Thibault, B. Grekowicz, A. Horst, S. McOlash, and T. J. Myers. A novel reconstruction algorithm to extend the CT scan field-of-view. *Med. Phys.*, 31(9):2385–2391, 2004. doi: 10.1118/1.1776673.

[187] Jared Starman, Norbert Pelc, Norbert Strobel, and Rebecca Fahrig. Estimating 0th and 1st moments in C-arm CT data for extrapolating truncated projections. *Proc. SPIE*, 5747: 378–387, 2005. doi: 10.1117/12.596041.

[188] Jens Wiegert, Matthias Bertram, Thomas Netsch, Jürg Wulff, Jürgen Weese, and Georg Rose. Projection extension for region of interest imaging in cone-beam CT. *Acad. Radiol.*, 12(8): 1010 – 1023, 2005. ISSN 1076-6332. doi: 10.1016/j.acra.2005.04.017.

[189] Ravishankar Chityala, Kenneth R. Hoffmann, Stephen Rudin, and Daniel R. Bednarek. Artifact reduction in truncated CT using sinogram completion. *Proc. SPIE*, 5747:2110–2117, 2005. doi: 10.1117/12.595450.

[190] Alexander A. Zamyatin and Satoru Nakanishi. Extension of the reconstruction field of view and truncation correction using sinogram decomposition. *Med. Phys.*, 34(5):1593–1604, 2007. doi: 10.1118/1.2721656.

[191] Daniel Kolditz, Michael Meyer, Yiannis Kyriakou, and Willi A Kalender. Comparison of extended field-of-view reconstructions in C-arm flat-detector CT using patient size, shape or attenuation information. *Phys. Med. Biol.*, 56(1):39, 2011.

[192] Y. Xia, S. Bauer, A. Maier, M. Berger, and J. Hornegger. Patient-bounded extrapolation using low-dose priors for volume-of-interest imaging in C-arm CT. *Med. Phys.*, 42(4):1787–1796, 2015. doi: 10.1118/1.4914135.

[193] Baojun Li, Gopal Avinash, Bernhard Claus, and Stephen Metz. 3D view weighted cone-beam backprojection reconstruction for digital tomosynthesis. *Proc. SPIE*, 6510:65104X–65104X–8, 2007. doi: 10.1117/12.708084.

[194] L. A. Feldkamp, L. C. Davis, and J. W. Kress. Practical cone-beam algorithm. *J. Opt. Soc. Am. A*, 1:612–9, 1984.

[195] Zhou Wang and A.C. Bovik. A universal image quality index. *Signal Processing Letters, IEEE*, 9(3):81–84, March 2002. ISSN 1070-9908. doi: 10.1109/97.995823.

[196] Arthur E. Burgess. Visual signal detection with two-component noise: low-pass spectrum effects. *J. Opt. Soc. Am. A*, 16(3):694–704, Mar 1999. doi: 10.1364/JOSAA.16.000694.

[197] Arthur E. Burgess, Xing Li, and Craig K. Abbey. Visual signal detectability with two noise components: anomalous masking effects. *J. Opt. Soc. Am. A*, 14(9):2420–2442, Sep 1997. doi: 10.1364/JOSAA.14.002420.

[198] A. E. Burgess and B. Colborne. Visual signal detection. IV. observer inconsistency. *J. Opt. Soc. Am. A*, 5(4):617–627, Apr 1988. doi: 10.1364/JOSAA.5.000617.

[199] Robert F. Wagner and Kenneth E. Weaver. An assortment of image quality indexes for radiographic film-screen combinations —can they be resolved? *Proc. SPIE*, 0035:83–94, 1972. doi: 10.1117/12.953665.

[200] K. J. Myers, H. H. Barrett, M. C. Borgstrom, D. D. Patton, and G. W. Seeley. Effect of noise correlation on detectability of disk signals in medical imaging. *J. Opt. Soc. Am. A*, 2(10): 1752–1759, October 1985. doi: 10.1364/JOSAA.2.001752.

[201] AE Burgess, RF Wagner, RJ Jennings, and HB Barlow. Efficiency of human visual signal discrimination. *Science*, 214(4516):93–94, 1981. doi: 10.1126/science.7280685.

[202] M Ishida, K Doi, L N Loo, C E Metz, and J L Lehr. Digital image processing: effect on detectability of simulated low-contrast radiographic patterns. *Radiology*, 150(2):569–575, 1984. doi: 10.1148/radiology.150.2.6691118.

[203] J. P. Rolland and H. H. Barrett. Effect of random background inhomogeneity on observer detection performance. *J. Opt. Soc. Am. A*, 9(5):649–658, May 1992. doi: 10.1364/JOSAA.9.000649.

[204] Kyle J. Myers and Harrison H. Barrett. Addition of a channel mechanism to the ideal-observer model. *J. Opt. Soc. Am. A*, 4(12):2447–2457, Dec 1987. doi: 10.1364/JOSAA.4.002447.

[205] Craig K. Abbey, Harrison H. Barrett, and Donald W. Wilson. Observer signal-to-noise ratios for the ML-EM algorithm. *Proc. SPIE*, 2712:47–58, 1996. doi: 10.1117/12.236860.

[206] Howard C. Gifford, Michael A. King, Daniel J. de Vries, and Edward J. Soares. Channelized Hotelling and human observer correlation for lesion detection in hepatic spect imaging. *J. Nucl. Med.*, 41(3):514–521, 2000.

[207] Brandon D. Gallas and Harrison H. Barrett. Validating the use of channels to estimate the ideal linear observer. *J. Opt. Soc. Am. A*, 20(9):1725–1738, Sep 2003. doi: 10.1364/JOSAA.20.001725.

[208] Scott Daly. Digital images and human vision. chapter The Visible Differences Predictor: An Algorithm for the Assessment of Image Fidelity, pages 179–206. MIT Press, Cambridge, MA, USA, 1993. ISBN 0-262-23171-9.

[209] Miguel Eckstein, Jay Bartroff, Craig Abbey, James Whiting, and Francois Bochud. Automated computer evaluation and optimization of image compression of x-ray coronary angiograms for signal known exactly detection tasks. *Opt. Exp.*, 11(5):460–475, Mar 2003. doi: 10.1364/OE.11.000460.

[210] Yani Zhang, B.T. Pham, and M.P. Eckstein. The effect of nonlinear human visual system components on performance of a channelized hotelling observer in structured backgrounds. *IEEE Trans. Med. Imag.*, 25(10):1348–1362, Oct 2006. ISSN 0278-0062. doi: 10.1109/TMI.2006.880681.

[211] J. A. Swets. *Signal Detection and Recognition by Human Observers*. Wiley, 1964.

[212] David Gur, Gordon S. Abrams, Denise M. Chough, Marie A. Ganott, Christiane M. Hakim, Ronald L. Perrin, Grace Y. Rathfon, Jules H. Sumkin, Margarita L. Zuley, and Andriy I. Bandos. Digital breast tomosynthesis: Observer performance study. *American Journal of Roentgenology*, 193(2):586–591, 2009. ISSN 0361-803X. doi: 10.2214/AJR.08.2031.

[213] Steve Si Jia Feng and Ioannis Sechopoulos. Clinical digital breast tomosynthesis system: Dosimetric characterization. *Radiology*, 263(1):36–42, April 2012. doi: 10.1148/radiol.11111789.

[214] David Gur, Margarita L. Zuley, Maria I. Anello, Grace Y. Rathfon, Denise M. Chough, Marie A. Ganott, Christiane M. Hakim, Luisa Wallace, Amy Lu, and Andriy I. Bandos. Dose reduction in digital breast tomosynthesis (DBT) screening using synthetically reconstructed projection images: An observer performance study. *Acad. Radiol.*, 19(2):166 – 171, 2012. ISSN 1076-6332. doi: 10.1016/j.acra.2011.10.003.

[215] Louise M. Henderson, Rebecca A. Hubbard, Tracy L. Onega, Weiwei Zhu, Diana S. M. Buist, Paul Fishman, and Anna N. A. Tosteson. Assessing health care use and cost consequences of a new screening modality the case of digital mammography. *Med. Care*, 50(12):1045–52, December 2012. doi: 10.1097/MLR.0b013e318269e0d1.

[216] Stefano Ciatto, Nehmat Houssami, Daniela Bernardi, Francesca Caumo, Marco Pellegrini, Silvia Brunelli, Paola Tuttobene, Paola Bricolo, Carmine Fantò, Marvi Valentini, Stefania Montemezzi, and Petra Macaskill. Integration of 3D digital mammography with tomosynthesis for population breast-cancer screening (STORM): a prospective comparison study. *The Lancet Oncology*, 14(7):583–89, June 2013. doi: 10.1016/S1470-2045(13)70134-7.

[217] Mark A. Helvie. Digital mammography imaging: Breast tomosynthesis and advanced applications. *Radiologic Clinics of North America: Breast Imaging*, 48(5):917–929, 2010. ISSN 0033-8389. doi: 10.1016/j.rcl.2010.06.009.

[218] Jorge Nocedal and Stephen J. Wright. *Numerical Optimization*. Springer, second edition, 2006.

[219] Hiroshi Fujita, Du-Yih Tsai, Takumi Itoh, Kunio Doi, Junji Morishita, Katsuhiko Ueda, and Akiyoshi Ohtsuka. A simple method for determining the modulation transfer function in digital radiography. *IEEE Trans. Med. Imag.*, 11(1):34–9, Mar 1992. doi: 10.1109/42.126908.

[220] Hologic, Inc. *Selenia Dimensions Quality Control Manual*. Hologic, Inc., Bedford, MA, August 2011. Part Number MAN-01965, Revision 003.

[221] Stephen L Keeling and Rudolf Stollberger. Nonlinear anisotropic diffusion filtering for multiscale edge enhancement. *Inverse Prob.*, 18(1):175, 2002.

[222] Yu-Li You, Wenyuan Xu, A. Tannenbaum, and M. Kaveh. Behavioral analysis of anisotropic diffusion in image processing. *IEEE Trans. Image Process.*, 5(11):1539–1553, Nov 1996. ISSN 1057-7149. doi: 10.1109/83.541424.